HOFSTADTER-HUBBARD PHYSICS

Dissertation
zur Erlangung des Doktorgrades
der Naturwissenschaften

vorgelegt beim Fachbereich Physik
Johann Wolfgang Goethe-Universität
in Frankfurt am Main

von
Bernhard Julius Irsigler
aus Berlin

Frankfurt 2020
(D30)

vom Fachbereich Physik der Johann Wolfgang Goethe-Universität als Dissertation angenommen.

Dekan: Prof. Dr. Michael Lang
Gutachter: Prof. Dr. Walter Hofstetter
Priv.-Doz. Dr. Axel Pelster
Prof. Dr. Antun Balaž

Datum der Disputation: 4.12.2020

Zusammenfassung

Die Topologie, als Disziplin der Mathematik, hat in der Physik der kondensierten Materie Einzug gehalten, da sich mit ihrer Hilfe bestimmte exotische quantenmechanische Phänomene beschreiben lassen. Zu diesen gehören die Zustände wie der Quanten-Hall-Effekt, der anomale Quanten-Hall-Effekt, der Quanten-Spin-Hall-Effekt und viele weitere. Die Aufgabe der Topologie besteht darin, die Zustände durch topologische Invarianten zu beschreiben; ganze Zahlen, die sich durch Beiträge von allen besetzten Moden im Vielteilchensystem berechnen lassen. Die topologischen Invarianten stehen damit im Kontrast zu konventionellen Ordnungsparametern, die sich lokal berechnen lassen, um beispielsweise Bose-Einstein-Kondensation oder Ferromagnetismus zu beschreiben.

Zwar existieren topologische Zustände auch in Materialien, tatsächlich haben sich aber solche Zustände als eine faszinierende Anwendung von Quantensimulatoren bewährt. Ein wichtiges Beispiel von Quantensimulatoren sind ultrakalte Quantengase in optischen Gittern. Ein direkter Vergleich zu elektronischen Systemen zeigt: Elektronen, als Quantenobjekte, beeinflussen durch ihre Dynamik im Ionengitter den makroskopischen Zustand des Materials. Das ist analog zu einzelnen Atomen in ultrakalten Quantengasen, die sich als Quantenobjekte im durch Laserfelder erzeugten, optischen Gitter bewegen. Ultrakalte Quantengase eignen sich dadurch als Simulatoren für elektronische Systeme. Tatsächlich aber sind ultrakalte Atome durch ihre gute Kontrollierbarkeit in der Lage, exotische Quantenzustände zu erzeugen, die weit über konventionelle elektronische Systeme hinausgehen. So lassen sich zum Beispiel auch diverse, in Materialien bisher unbeobachtete, topologische Zustände mit Hilfe von künstlichen Eichfeldern herstellen.

Ein weiterer, gut kontrollierter Parameter in ultrakalten Quantengasen ist die Wechselwirkung zwischen jeweils zwei Atomen. Systeme mit Wechselwirkungen zwischen den Teilchen sind schwierig zu lösen, da sogar schon im Fall von drei miteinander wechselwirkenden Teilchen in der klassischen Physik keine analytische Lösung vorliegt. In ultrakalten Quantengasen sind typischerweise zehntausende Teilchen beteiligt, in elektronischen Systemen liegt die Größenordnung sogar bei 10^{23}. Lösungen zu wechselwirkenden Problemen sind somit immer approximativ und es haben

sich viele Methoden für unterschiedliche Anwendungsfälle etabliert. Die dynamische Molekularfeldtheorie, kurz DMFT, ist beispielsweise in der Lage den gesamten Phasenübergang zwischen einem Metall und einem Mott-Isolator zu beschreiben. Das ist nur möglich, da in der DMFT Korrekturen von lokalen Quantenfluktuationen enthalten sind, die in der konventionellen, statischen Molekularfeldtheorie vernachlässigt werden.

Die vorliegende Arbeit widmet sich weitreichend der Physik des Hofstadter-Hubbard-Modells, das insbesondere für ultrakalte Quantengase in optischen Gittern relevant ist. Ursprünglich beschreibt das Hofstadter-Modell Elektronen in einem zweidimensionalen Gitter, auf das senkrecht ein starkes Magnetfeld ausgerichtet ist. Je nach Stärke des Magnetfelds nehmen die Elektronen Zustände ein, deren Energiespektrum ein selbstähnliches Muster bildet. Dieses Fraktal wird Hofstadter-Schmetterling genannt. Er wurde bisher nur in künstlichen Systemen beobachtet.

Die meisten topologischen Zustände sind isolierend in ihrem Inneren, aber dafür leitend an ihren Rändern. Diese Randzustände sind nicht nur leitend sondern auch robust. Das heißt, dass sie ihre Leitfähigkeiten nicht verlieren, wenn beispielsweise eine Störstelle vorliegt. Diese Eigenschaften machen topologische Zustände sehr interessant für zukünftige technische Anwendungen.

Topologische Randzustände wurden bisher noch nicht in zweidimensionalen ultrakalten Quantengasen beobachtet. Ein Grund hierfür ist die intrinsische Inhomogenität dieser Experimente, die es erschwert, eindeutig zwischen dem Inneren und dem Rand des Systems zu unterscheiden. Wir untersuchen in dieser Arbeit den Randzustand, der zwischen zwei topologisch unterschiedlichen Vielteilchen-Phasen des zweidimensionalen, zeitumkehrsymmetrischen Hofstadter-Hubbard-Modells entsteht. Der räumliche Übergang dieser beiden Phasen wird durch einen äußeren, räumlich variierenden Kontrollparameter erzeugt, in diesem Fall ein gestaffeltes Potential. Dieses kann in einem optischen Gitter durch ein Übergitter realisiert werden. Bei einem kritischen Wert des gestaffelten Potentials ist ein topologischer Phasenübergang zu erwarten, wodurch in dieser Stelle im Raum ein Randzustand entsteht. Randzustände oder die Grenze zwischen zwei topologisch verschiedenen Phasen sind nicht durch Unterschiede in der Dichteverteilung der Atome ablesbar, stattdessen geben verschiedene Transporteigenschaften Hinweise auf topologische Randzustände. Wir betrachten die räumlich aufgelöste Kompressibilität und beobachten einen Randzustand in der Mitte des Systems. Mit Hilfe der DMFT können wir die Kompressibilität auch für den wechselwirkenden Fall berechnen und finden, dass die Wechselwirkung den Randzustand nicht zerstört sondern lediglich seine Position verschiebt. Er ist folglich robust gegen die Wechselwirkung.

Wir charakterisieren die beiden Phasen, zwischen denen sich der topologische Randzustand befindet, durch topologisches Pumpverhalten. Dies ist äquivalent zur Hall-Spannung, die sich senkrecht zur ursprünglichen

Spannung in einem Hall-Zustand aufbaut. Das topologische Pumpen zeigt deutlich den topologischen Unterschied beider Phasen im System. Weiterhin berechnen wir einen topologischen Index im Konfigurationsraum, kurz LCM, wodurch wir die topologische Phasenseparation noch präziser charakterisieren können. Hierfür haben wir den LCM-Index generalisiert, um ihn auf zeitumkehrsymmetrische Systeme anwenden zu können. Dies ist jedoch nur für einen Spezialfall möglich. Das System erlaubt durch Spin-Bahn-Kopplung Prozesse, bei denen sich der Spinzustand eines sich bewegenden Teilchens im Gitter ändert. Dieser Prozess ist in ultrakalten Quantengasen ebenfalls von außen durch ein künstliches Eichfeld kontrolliert. Im Spezialfall maximaler Spinmischung lässt sich das System durch eine Transformation in zwei neue, virtuelle Spinzustände zerlegen. Diese Vereinfachung ermöglicht nun die Verallgemeinerung des LCM-Indexes auf zeitumkehrsymmetrische Systeme. In Fall der topologischen Phasenseparation zeigt diese Technik mit dem LCM-Index, dass der Sprung des topologischen Index an dem selben Raumpunkt eintritt, an dem sich auch der Randzustand befindet. Dies gilt auch für den wechselwirkenden Fall und bestätigt somit die Korrespondenz zwischen den topologischen Invarianten und den Transporteigenschaften am Rand für wechselwirkende Systeme im optischen Gitter.

Wir wenden die beschriebenen Techniken, die sich besonders für inhomogene, wechselwirkende Systeme eignen, auf ein typisches Problem der ultrakalten Quantengase an, auf die harmonische Falle. Es zeigt sich, dass sich abhängig von der Teilchenzahl im System topologische Phasen durch die Steigerung der Wechselwirkungsstärke in der Mitte der harmonischen Falle induzieren lassen. Ein Grund hierfür sind die beiden kompetitiven Energieskalen von der harmonischen Falle und von der Wechselwirkung. Die stärkere Wechselwirkung unterdrückt doppelt besetzte Gitterplätze im System und drängt somit Teilchen weiter nach außen an den Fallenrand. Dies verändert effektiv die Füllung des Gitters in der Mitte des Systems, wodurch topologische Phasenübergänge abhängig von der zugrunde liegenden Bandstruktur stattfinden. Die Ergebnisse lassen sich hier ebenfalls mit dem LCM-Index belegen.

Die Vielzahl von Anwendungen des LCM-Indexes führt zu der Frage der experimentellen Messbarkeit. Hierfür überführen wir den Ausdruck für den LCM-Index in eine Funktion von Ein-Teilchen-Dichtematrizen. Der LCM-Index an einem Raumpunkt lässt sich somit als die doppelte Summe aller Raumpunkte berechnen, die mit dem ursprünglichen Raumpunkt ein Dreieck mit endlicher Fläche bilden. Natürlich ist es experimentell unmöglich, die Beiträge aller Raumpunkte zu erfassen. Wir fokussieren uns daher auf den Beitrag der kleinsten Dreiecke und untersuchen diese Näherung in Hinblick auf die oben genannten Systeme, der topologischen Phasenseparation und der harmonischen Falle. Hierbei stellen wir fest, dass diese Näherung nur dann sinnvoll ist, wenn die Bandlücke der zu untersuchenden Phasen groß ist, wenn diese also weit von einem topologischen Phasenübergang entfernt sind.

Weiterhin diskutieren wir einen Vorschlag für die experimentelle Messung der Ein-Teilchen-Dichtematrizen im Konfigurationsraum und somit des LCM-Indexes. Dies wäre durch eine tomographische Messung des Quantenzustandes möglich. Hierfür wird das optische Gitter mit Hilfe der richtigen Laserkonfiguration plötzlich in ein Dimer-Gitter gewandelt, in dem jeweils nur zwei Gitterplätze miteinander gekoppelt sind. Die plötzliche Änderung des Gitterpotentials führt zu einem Nicht-Gleichgewichtszustand, bei dem zeitliche Oszillationen der lokalen Teilchendichte zu beobachten sind. Diese könnten im Experiment mit Hilfe eines Quantengas-Mikroskops sichtbar gemacht werden. Eine analytische Rechnung zeigt, dass man aus den zeitlichen Oszillationen Eigenschaften über die zu messende Ein-Teilchen-Dichtematrix extrahieren kann. In Kombination mit unseren Untersuchungen der topologischen Phasenseparation wäre es somit möglich, in einem System sowohl den Randzustand als auch die topologische Invariante genähert zu messen.

In einer weiteren Studie untersuchen wir die Auswirkungen von einem Ungleichgewicht der Populationen von den zwei Spinarten auf topologische Phasen unter starken, repulsiven Wechselwirkungen. Dieses Problem ist für ultrakalte Quantengase in optischen Gittern relevant, da sowohl Spin-Ordnungen durch starke Wechselwirkung mit Spin-Ungleichgewicht als auch topologische Phasen experimentell beobachtet wurden. Die Kombination beider Effekte wirft die Frage auf, inwieweit die beiden jeweiligen Grundzustände ineinander überführt werden können. Um diese Frage zu klären, führen wir zuerst klassische Monte-Carlo-Simulationen durch und finden einen neuen, exotischen Grundzustand, bei dem die makroskopische Magnetisierung endlich ist und einen Beitrag hat, der orthogonal zu allen äußeren Felder ausgerichtet ist. Der Grund hierfür liegt in den künstlichen Eichfeldern, die in Kombination mit dem Spin-Ungleichgewicht zu einer geometrischen Frustration des Gitters führen. Tatsächlich finden wir in dieser Form von geometrischer Frustration das theoretische frustrierte XY-Modell für die Spin-Komponenten in der Ebene wieder. Somit eröffnet dieses System einen unerwarteten und realistischen Weg zu einem bekannten, über Jahrzehnte ausführlich studierten Problem. Wir untersuchen weiterhin die Stabilität dieser Phase in Hinblick auf lokale Quantenfluktuationen mit Hilfe der DMFT. Hierbei finden wir, dass ein Teil der Phase aus dem Phasendiagramm verschwindet, also instabil hinsichtlich lokaler Quantenfluktuationen ist. Stattdessen bildet sich ein Ferrimagnet.

Das ursprünglich zweidimensionale Hofstadter-Modell lässt sich auch auf höhere Dimensionen verallgemeinern. Dies ist deshalb besonders interessant, da sich topologische Phasen in zwei Dimensionen extrem von denen in drei Dimensionen unterscheiden können. So gibt es beispielsweise nicht nur isolierende topologische Phasen sondern auch topologisch geschützte Semimetalle. Wir untersuchen das dreidimensionale, zeitumkehrsymmetrische Hofstadter-Hubbard-Modell für beliebige Ausprägung der Spin-Mischung. Wie bereits oben beschrieben, lässt sich der Spezialfall bei maximaler Spin-Mischung vereinfachen. Dies gilt nicht im allgemeinen Fall. Wir entwickeln drei unterschiedliche Methoden für die Berechnung von topologischen Invarianten in wechselwirkenden, dreidimensionalen, zeitumkehrsymmetrischen Systemen basierend auf gewundenen Randbedingungen, Wilson-Schleifen und auf dem LCM-Index. Mit Hilfe dieser Techniken lässt sich das gesamte Phasendiagramm charakterisieren, welches sowohl starke und schwache topologische Isolatoren ausweist als auch ein Nodallinien-Semimetall. Dieses exotische Semimetall entsteht in Bereichen im Phasendiagramm zwischen starken und schwachen topologischen Isolatoren bei bestimmten Werten der Spin-Mischung. Wir stützen unsere Resultate durch Berechnung der zugehörigen Randzustände, bei denen es sich im dreidimensionalen Fall um Oberflächenzustände handelt und finden die Übereinstimmung zwischen den topologischen Invarianten und den daraus resultierenden Eigenschaften für Oberflächenzustände.

In dieser Arbeit wird das Hofstadter-Hubbard-Modell in vielen Facetten mit Hilfe der DMFT analysiert, wobei das Hauptaugenmerk auf dem Kontext der ultrakalten Quantengase in optischen Gittern liegt. Das Hofstadter-Modell lässt sich in solchen Systemen realisieren und Hubbard-Wechselwirkungen können heutzutage routinemäßig implementiert werden. Der endgültigen Realisierung des Hofstadter-Hubbard-Modells steht allerdings noch ein Hindernis im Weg. Topologische Phasen werden in ultrakalten Quantengasen durch periodisch getriebene Systeme geschaffen, die im Hochfrequenzfall einen effektiven, statischen Hamilton-Operator erzeugen. Wechselwirkungen führen zu Multiphoton-Anregungen, wodurch letztendlich ein Heizeffekt entsteht, der das ultrakalte Quantengas zerstört. Trotzdem sind die Bestrebungen der aktuellen Forschung groß, solche Heizeffekte einzudämmen und es existieren die ersten experimentellen Studien zu wechselwirkenden, topologischen System in ultrakalten Quantengasen in optischen Gittern. Die in der vorliegenden Arbeit entwickelten Methoden lassen sich sehr allgemein auf weitere Systeme anwenden. Sie sind anwendbar auf topologische, zeitumkehrsymmetrische Systeme in zwei und drei Dimensionen, mit Hubbard-Wechselwirkung sowie möglicherweise gebrochener Translationssymmetrie. Weitere mögliche interessante Anwendungsgebiete für diese Methoden, die über das Hofstadter-Hubbard-Modell hinausgehen, sind unter anderem die verdrehte Graphen-Doppelschicht, die durch Moiré-Muster sowohl supraleitende als auch isolierende Phasen aufweist, und der topologische Proximity-Effekt, der dem gleichnamigen Effekt bei Supraleitern entlehnt ist. All dies sind Themen, die zur Zeit heiß diskutiert werden.

"I might indeed be crazy but this is not evidence for it."

– Steven H. Simon, Solvay workshop, Brussels 2019

Preface

My favorite word in English is *indistinguishability*. This is not only because it exhibits more syllabi than its German translation *Ununterscheidbarkeit* - which is rare - but also because it is a fundamental concept of quantum *many-body physics* leading to unbelievably fascinating consequences. Let us ask the question: What happens when we exchange two particles inside a collective of many indistinguishable particles? When we measure any physical *observable* on this collective before and after the exchange, nothing should have changed since we cannot tell which particle is which, they simply cannot be distinguished. However, the quantum state, or equivalently, the *wavefunction*, as they are not observables, may have changed. One would assume that this has no consequences as they are not observable. It turns out, however, that the square of the absolute value of the wavefunction is an observable, specifically, it is the density of particles. Because of the square, the wavefunction can change in two ways without changing the density of particles: Either it is multiplied by a plus sign or by a minus sign. What sounds rather dull right now, has vast consequences in the theory of many quantum particles and divides the world into two different types of particles: There are *bosons* and there are *fermions*. Light, e.g., consists of bosons while all matter is made of fermions. Bosons like to condense into a single state when it's cold, fermions always stay in different states. A boson can be made out of two fermions but not the other way around. These are just a few general examples of their extreme difference. Of course, the world is not only plus or minus and there are particles which are neither bosons nor fermions. But this simple consideration should elucidate what I love about theoretical physics. We started with a very simple question which boiled down to a simple minus sign, however, after decades or even a century of research such rich physics can evolve and blossom. For me this is pure elegance. Of course this elegance does not come for free and the present work is an example for that. Plenty of different theories, relevance for experiments, heavy numerical computations, and thousands of lines of coding are required just to take a small step forward in research.

The numerical part of this work is based on codes which were inherited and improved over many generations of postdocs and Ph.D. students in the Hofstetter group. I am thankful for being part of that. Moreover, I am

grateful for the excellent collaboration with Jun-Hui Zheng. Together we have published a number of interesting articles over the last three years. I also would like to thank Constantin Meyer-Grant, Jaromir Panas, and Irakli Titvinidze for their careful reading of the manuscript, their valuable comments, and their time. I would like to thank the German Research Foundation (DFG) as I am very grateful for their funding of my position as a Ph.D. student within the research unit FOR 2414 as well as the access to the supercomputing facilities at the Center for Scientific Computing Frankfurt. Finally, I would like to thank Walter Hofstetter as my supervisor in the last three years. He taught my precious skills in research, as well as academia in general, from which I will always benefit.

The last words within this manuscript were written down during the time when Covid-19 has become a part of everyone's life. The huge confusion of this new threat, however, slowly fades away and there is much hope for the return to the life we know, without pandemic.

to Ursula, to Gerlinde

Abstract

The Hofstadter model, besides the Haldane and Kane-Mele models, is the most common tight-binding model which hosts topologically nontrivial states of matter. In its time-reversal-symmetric formulation the model can even describe topological insulators. Experimentally, the Hofstadter model was realized with ultracold quantum gases in optical lattices which is a well-controlled way to engineer quantum states of tight-binding Hamiltonians. Another established control parameter in ultracold quantum gases are two-particle, on-site interactions, also known as Hubbard interactions. This work aims at introducing the reader to the concepts of topological states of matter, a collection of corresponding tight-binding models, and the methodology to treat interacting topological states with dynamical mean-field theory. We present recent results for inhomogeneous, interacting systems, spin-imbalanced magnetic systems, propose experimental detection methods, and extensions to three-dimensional topological states.

Publications

The following is a list of peer-reviewed journal articles and preprints which were published in the context of this work:

- “Interacting Hofstadter Interface”
  by Bernhard Irsigler, Jun-Hui Zheng, and Walter Hofstetter
  in *Phys. Rev. Lett.* **122**, 010406 (2019)

- “Spin-imbalance-induced transverse magnetization
  in the Hofstadter-Hubbard model”
  by Bernhard Irsigler, Jun-Hui Zheng, Mohsen Hafez-Torbati,
  and Walter Hofstetter
  in *Phys. Rev. A* **99**, 043628 (2019)

- “Microscopic characteristics and tomography scheme
  of the local Chern marker”
  by Bernhard Irsigler, Jun-Hui Zheng, and Walter Hofstetter
  in *Phys. Rev. A* **100**, 023610 (2019)

- “Measuring the topological phase transition
  via the single-particle density matrix”
  by Jun-Hui Zheng, Bernhard Irsigler, Lijia Jiang, Christof Weitenberg,
  and Walter Hofstetter
  in *Phys. Rev. A* **101**, 013631 (2020)

- “Z_2 characterization
  for three-dimensional multiband Hubbard models”
  by Bernhard Irsigler, Jun-Hui Zheng, Fabian Grusdt,
  and Walter Hofstetter
  in *Phys. Rev. Res.* **2**, 013299 (2020)

- “Local Chern marker of smoothly confined Hofstadter fermions”
  by Urs Gebert, Bernhard Irsigler, and Walter Hofstetter
  in *Phys. Rev. A* **101**, 063606 (2020)

- “Bulk topological proximity effect in multilayer systems”
  by Jaromir Panas, Bernhard Irsigler, Jun-Hui Zheng,
  and Walter Hofstetter
  in *Phys. Rev. B* **102**, 075403 (2020)

- “Interaction-driven topological phase transitions
  in fermionic SU(3) systems”
  by Mohsen Hafez-Torbati, Jun-Hui Zheng, Bernhard Irsigler,
  and Walter Hofstetter
  in *Phys. Rev. B* **101**, 245159 (2020)

Contents

1 Introduction 21
- 1.1 Family of quantum Hall effects 22
  - 1.1.1 Integer quantum Hall effect 22
  - 1.1.2 Quantum anomalous Hall effect 23
  - 1.1.3 Quantum spin Hall effect 23
  - 1.1.4 Further relatives 24
- 1.2 Topological states of matter 24
  - 1.2.1 Topology in condensed matter physics 25
  - 1.2.2 Topological invariants 26
  - 1.2.3 Boundary states 26
  - 1.2.4 Quantum Hall and Chern insulators 28
  - 1.2.5 Topological insulators 29
  - 1.2.6 Three-dimensional topological states 31
- 1.3 Quantum simulators 33
- 1.4 Cold atoms in optical lattices 34
- 1.5 Topological states in cold atomic gases 38
- 1.6 Driven systems and Floquet theory 39
- 1.7 Hubbard model in the context of dynamical mean-field theory 41

2 Topologically nontrivial tight-binding models 49
- 2.1 Hofstadter model 50
- 2.2 Time-reversal-symmetric Hofstadter model 54
- 2.3 Harper-Hofstadter-Hatsugai model 56
- 2.4 Haldane model 56
- 2.5 Kane-Mele model 58

3 Methods 61
- 3.1 Dynamical mean-field theory 61
  - 3.1.1 DMFT equations 62
  - 3.1.2 Anderson impurity model 67
  - 3.1.3 Real-space DMFT 68
  - 3.1.4 Solvers 69
- 3.2 Maximum entropy method 72

3.3 Topological Hamiltonian 74
3.4 Local Chern marker 77
3.5 Fukui's method and twisted boundary conditions 79
3.6 Wilson loops 82

4 Results 84
4.1 Interacting, inhomogeneous topological states in optical lattices 84
    4.1.1 Interacting Hofstadter interface 84
    4.1.2 Local Chern marker of smoothly confined, interacting Hofstadter fermions 96
4.2 Tomography of the local Chern marker 101
    4.2.1 Tomography of the topological Hamiltonian 111
4.3 Spin-imbalanced Hofstadter-Hubbard model 116
4.4 $\mathbb{Z}_2$ characterization of the three-dimensional time-reversal-symmetric Hofstadter-Hubbard model 125
    4.4.1 Topological proximity effect in layered systems . . . 139

5 Conclusion 146

Chapter 1

Introduction

There is a common perception of material properties: some materials can conduct current such as metals and some cannot, e.g., ceramics. Then there are semiconductors which relax the strict picture of *conductor* and *insulator*. The semiconductors opened a huge world of technological applications and are the reason for the high abundance of computers nowadays. Another state of matter, which exists in some materials and also has properties of both conductors as well as insulators, is the so-called topological insulator. It behaves like insulators in the *bulk*, i.e., the inner part of the material, but is conducting at its *boundary*. Boundary states are common since the physics at surfaces is intrinsically different compared to bulk physics. The crucial difference to the boundary states of topological insulators, however, is that the latter are robust. This means perturbations such as impurities cannot destroy them. If one cuts off a piece from a topological insulator the boundary changes. Subsequently, also the conducting boundary states are recovered at the new boundary. There is a deep mathematical reason for this behavior which will be discussed later in this chapter. Before we come to that, we introduce the *family of quantum Hall effects* which can be understood as the consequence of nontrivial topological properties of the physical state of matter.

We start this introduction with a historical overview of the different quantum Hall effects in Sec. 1.1 without going too much in-depth on the physical principles leading to the exciting field of Hall physics. Instead, we introduce the concept of topology in condensed matter physics in Sec. 1.2 and apply it to the Hall effects introduced in Sec. 1.1. In Sec. 1.3 we briefly review quantum simulators with a closer look on the field of cold atomic gases in optical lattices in Sec. 1.4. We then combine the topological states and the cold atom setups in Sec. 1.5. This is followed by an introduction to Floquet theory in Sec. 1.6 in order to connect the theory with the experimental implementation. Eventually, the Hubbard model in the context of dynamical mean-field theory is reviewed in Sec. 1.7.

1.1 Family of quantum Hall effects

The classical Hall effect was discovered by Edwin Hall in 1879 [1]. It arises from the electrodynamic equation of motion for a charged particle, e.g., an electron in a conductor, exposed to an electric field $\boldsymbol{E}$ and a magnetic field $\boldsymbol{B}$

$$M\frac{d\boldsymbol{v}}{dt} = -e\boldsymbol{E} - e\boldsymbol{v} \times \boldsymbol{B}, \tag{1.1}$$

where M, e, and $\boldsymbol{v}$ are the particle's mass, electric charge, and velocity, respectively, and t denotes time. To get an interpretation of this equation, we picture a two-dimensional (2d) material in the xy plane. An applied electric field $\boldsymbol{E} = E\hat{e}_x$ with $E > 0$ in x direction will accelerate the electron in x direction, where we denote unit vectors in μ direction as $\hat{e}_\mu$. From a finite perpendicular magnetic field $\boldsymbol{B} = B_\perp \hat{e}_z$, the electron will experience a force in y direction which is the origin of the measurable Hall voltage. This is associated with the Hall resistivity R_{xy} which is found to be proportional to $B_\perp$. The diagonal resistivity R_{xx}, on the other hand, is associated with currents along the electric field. Here, it vanishes in this simple vacuum description. Treating the Drude model would result in a finite constant resistivity. This very basic treatment of the classical Hall effect shows us the two relations $R_{xy} \propto B_\perp$ and $R_{xx} = 0$. In the following we will introduce the quantum-mechanical extensions of the Hall effect and will observe the severe deviations from these relations. We will follow the books by Ezawa [2] and by Bernevig and Hughes [3] as well as the lecture notes by Asbóth et al. [4] and by Tong [5].

1.1.1 Integer quantum Hall effect

At low temperatures T, typically quantum effects play an enhanced role which leads to experimental deviations from the classical theory. This is because the thermal energy $k_B T$ is much smaller than other energy scales in the system, where k_B is Boltzmann constant which we set to 1. In 1980 von Klitzing et al. [6] measured at a temperature $T = 1.8\,\mathrm{K}$ and a magnetic field strength of $13\,\mathrm{T}$ a plateau for the Hall resistivity in contrast to the proportional behavior as predicted by the classical theory discussed above. This suggests that the Hall resistivity is quantized. It turns out that it obeys $R_{xy} = 2\pi\hbar/(e^2\nu)$, where $\nu = 2\pi\hbar\rho_0/(eB_\perp)$ assumes integer values. Here, ρ_0 is the electron density in the sample. The effect is called integer Quantum Hall effect (IQH). The value of the plateau can be measured with extreme precision which stimulated the idea to measure the fine-structure constant [7] in the original experiment. In 1985 von Klitzing was awarded the Nobel Prize for these findings.

A paradigmatic lattice model for the IQH is the Hofstadter model published in 1976 [8] which is based on ideas by Harper from 1955 [9]. We will introduce the Hofstadter model, or sometimes Harper-Hofstadter model, in Sec. 2.1.

1.1.2 Quantum anomalous Hall effect

As a follow up, Edwin Hall published in 1881 his findings on the Hall effect in ferromagnetic materials and reports that the effect is 'several times greater' compared to paramagnetic materials [10]. It was then dubbed anomalous Hall effect. The naïve perception here, is that the finite magnetization of the material gives rise to an effective magnetic field which modifies the Hall effect. However, it is not sufficient to explain the huge increment of the Hall effect in ferromagnetic materials. In 1954 the first quantum mechanical theory involving spin-orbit coupling (SOC) to describe the anomalous Hall effect was published [11]. Today it is assumed that many effects are involved and cumulatively contribute to this phenomenon. The quantum anomalous Hall effect (QAH) in real materials roots in quantum mechanical as well as topological mechanisms [12]. The QAH has been measured in thin magnetic topological insulators in 2013 [13].

In 1988 Haldane proposed a 2d tight-binding model which possesses a nontrivial Chern number even though there is no net magnetic flux penetrating the 2d lattice [14]. The model is an approach to the nontrivial QAH. We will go into more detail of the Haldane model in Sec. 2.4.

1.1.3 Quantum spin Hall effect

The spin Hall effect (SHE) was introduced theoretically by Dyakonov and Perel in 1971 [15,16]. It corresponds to classical spin transport in conductors within an external magnetic field. In the SHE, SOC effects of the material will yield a finite spin polarization of the Hall effect. This makes the SHE intriguing for applications in spintronics reviewed in Ref. [17].

The quantum spin Hall effect (QSH) was theoretically introduced in the context of semiconductors [18, 19] and in graphene [20]. The latter established the so-called Kane-Mele model, see Sec. 2.5, which describes spinful electrons in graphene accompanied with SOC. It is regarded as a milestone for the field of topological insulators. The SOC opens a gap which is topologically nontrivial. However, it turns out that in real graphene the SOC is too small, which stimulated research in other systems like HgTe quantum wells. A tight-binding model here is the so-called BHZ model [21], which led to the experimental confirmation of the QSH in 2007 by König et al. [22] followed by a review on the QSH [23].

1.1.4 Further relatives

Besides the IQH, QAH, and QSH there are even more versions of the quantum Hall effect. The content of this work will be concerned with quantum states related to the former three, however, we will briefly mention some of the most intriguing other versions.

The fractional Quantum Hall effect (FQH) was discovered in 1982 by Tsui et al. [24] showing a plateau at fractional numbers of the transverse resistivity in contrast to the IQH. The so-called Laughlin wavefunction is an approximative analytic form for the groundstate of the FQH at odd fractional fillings of the lowest band [25]. A common modern framework is to explain the FQH in the composite particle picture where electrons and flux quanta combine to quasiparticles [26] following anyonic statistics [27]. This and the fact that FQH states exhibits long-range entanglement [28] is condensed in a new concept which is called topological order.

The quantum valley effect is a version of the Hall effect in which the transport properties are assigned to valleys in the Brillouin zone (BZ). In graphene, e.g., there are two valleys in the BZ. It is then possible to find a mapping between the QSH and the quantum valley effect [29].

We thus far discussed only Hall effects which occur in 2d. In fact, there is no limitation to the dimensionality. Depending on the symmetry of the system, topologically nontrivial states can emerge in any dimension [30]. The three- and four-dimensional generalizations to the quantum Hall effect exist, mostly theoretically. Recently, however, the 4d quantum Hall effect has been measured in 2018 with cold atoms [31] and the 3d quantum Hall effect in 2019 in $ZrTe_5$ [32].

1.2 Topological states of matter

We will try to introduce the concept of topology without mentioning the words ’coffee cup’ or ’doughnut’. Topology is a branch of mathematics which investigates mathematical objects in a very free abstraction. Topology is concerned with the preserved properties of objects under deformations, twistings, and stretchings. It stands in sharp contrast to geometry, which is concerned with measures of a shape such as lengths, angles, etc. The difference can be illustrated with an example. In Fig. 1.1(a) we show the surface of a polyhedron, a geometrical object which consists of v vertices, e edges, and f faces, which are all three integer numbers. Geometry would be interested in, e.g., its total surface area or its volume. In topology, this is different. A nice example from topology is the so-called Euler characteristics χ [33]:

$$\chi = v - e + f. \tag{1.2}$$

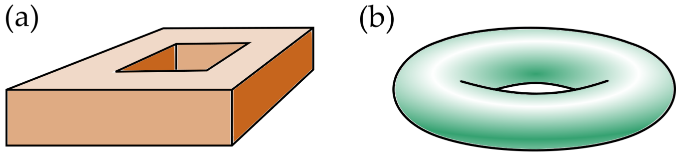

Figure 1.1: Example for topology: The polyhedron in (a) and the torus in (b) have the same genus, i.e., the same number of holes.

As we can see, no geometrical quantities such as surface areas or angles enter this equation, only numbers from counting appear. The value of χ is thus independent of the exact form of the polyhedron. It turns out that for any polyhedron the Euler characteristics is $\chi = 2 - 2g$, where g is called genus and represents the number of holes in the polyhedron, Fig. 1.1(a) has one hole $g = 1$. The Gauss-Bonnet theorem connects the Euler characteristics to a continuous quantity, the Gauss curvature. The Gauss curvature comes from the field of differential geometry and is a measure for the curvature of a 2d surface defined at each point of the surface in space. The 2d integral of the Gauss curvature over the entire closed surface yields the Euler characteristics. Thus also smooth surfaces such as the torus in Fig. 1.1(b) can be associated with an integer number. The genus, as such a number, is an example of a topological invariant. Both, the polyhedron and the torus exhibit the same topological invariant $g = 1$ even though their appearance is completely different.

1.2.1 Topology in condensed matter physics

The connection to condensed matter physics was first built up through the so-called TKNN invariant [34], see Sec. 1.2.4, which corresponds to the physical quantity of conductivity. In Sec. 1.1, we realized that conductivity, as it is the inverse of resistivity, is a central quantity in Hall effects. The TKNN invariant thus connects the mathematical concept of topology with Hall physics. Another closely related quantity is the Berry curvature introduced in 1984 by Berry [35], see Sec. 3.5. Berry investigated the quantum phase of a state which is changed on a closed path in the parameter space. In the adiabatic limit the so-called dynamical phase vanishes, however, a geometric phase remains which is now dubbed Berry phase. Via Stokes' theorem this quantity is then linked to a two-dimensional integral. It is the comment by Barry Simon in Berry's paper which provides the missing link to topology in math. He stated that the integrand in Berry's formula has the mathematical structure of a curvature. This reminds us of the discussion on the Gauss curvature in Sec. 1.2.

In the TKNN paper the Kubo formula was used to compute the conductivity of a quantum Hall system to find a quantized value [34]. This formula happens to be the equivalent to Berry's formula. Now the topological invariant obtains a physical meaning which is the quantization of the Hall conductivity.

1.2.2 Topological invariants

The TKNN invariant is the first example of a topological invariant in condensed matter systems. As it was applied to a 2d lattice pierced by a magnetic field, it describes the quantization of the IQH. This corresponds to the Hofstadter model, see Sec. 2.1. The conductivity assumes values of integer multiples of e^2/h where h is the Planck constant. The topological invariant here is an integer, or $\mathbb{Z}$ number. This is just an instance of a more general concept of the classification of topological states of matter. In fact, topologically nontrivial states like the IQH are not restricted to 2d and may obey certain symmetries. Ryu et al. [30] introduced a classification for topological states. Herein, the dimensionality and the symmetries of the system uniquely define the type of topological invariant which describes the physical state. The symmetries involve time-reversal symmetry (TRS), particle-hole symmetry, and the combination of both, the chiral symmetry. Other symmetries are expressed through unitary operations which always decouples the Hamiltonian into irreducible blocks. The classification aims at identifying these irreducible blocks. Time-reversal and particle-hole transformations, on the other hand, are anti-unitary operations and thus give rise to these fundamental symmetries. Translational symmetry is not involved since the classification should also apply to disordered systems. It turns out that the three mentioned symmetries give rise to ten symmetry classes. The classification thus consists of a table for the ten symmetry classes in all dimensions, see Ref. [30, Table 3.]. The entries then provide the type of topological invariant to characterize the corresponding state. These are either trivial or the classification obeys a $\mathbb{Z}$ or $\mathbb{Z}_2$ number. The IQH, e.g., has no symmetries and occurs in 2d. From the table one then finds a $\mathbb{Z}$ classification which is consistent with our discussion above. How to calculate a topological invariant in practice depends on the specific case and we will provide examples in Sec. 1.2.4 for the nonsymmetric case in 2d and Sec. 3 for the TRS case in 2d as well as 3d. It is important to note that topological invariants are only defined if a gap is open since all occupied eigenstates contribute to their calculation. Partially filled bands may fluctuate which cannot yield a quantized value.

1.2.3 Boundary states

In the last section, we manifested the concept of a topological invariant for a quantum many-body state. Let us consider a state with a $\mathbb{Z}$ classification where the topological invariant is an integer-valued constant assigned to

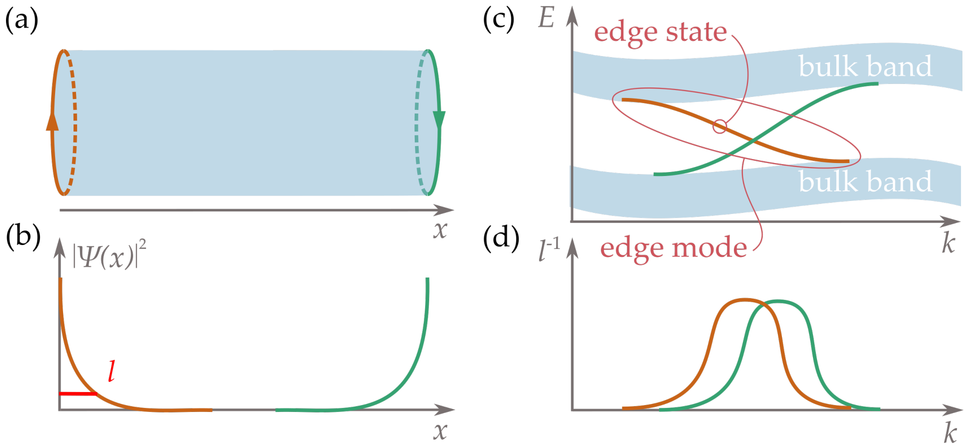

Figure 1.2: Schematic of topological edge states: (a) a topological phase in cylinder geometry (b) the wavefunction $\psi(x)$ of the chiral edge state resides at the boundaries of the cylinder with penetration depth l (c) the energy spectrum with the two edge modes crossing the band gap (d) inverse penetration depth as a function of momentum k.

an insulator and robust with respect to smooth deformations of the Hamiltonian. This is true as long as the gap is finite and has huge impact on the resulting state. There is an intuitive picture of what happens at the interface of two topologically distinct insulating phases with invariants ν_1 and ν_2, respectively. The topological invariants cannot change as long as the band gap remains open for both insulators. However, because the two phases are topologically different $\nu_1 \neq \nu_2$, there must be a change of the topologically invariant from ν_1 to ν_2. Yet, this is possible only if the gap is closed. As a result, there must exists at least one gapless state called boundary state. In 2d it is mostly dubbed edge state and in 3d surface state. The so-called bulk-boundary correspondence states that the difference of topological invariants $\nu_1 - \nu_2$ corresponds to the number of robust, gapless edge states sitting at the interface [36, 37]. In the interacting case, the bulk-boundary correspondence is expected to hold as well [38]. On the other hand, in non-hermitian systems the bulk-boundary correspondence is violated [39, 40]. Since we only cover hermitian systems in this work, we expect the bulk-boundary correspondence to hold.

In Fig. 1.2, we schematically present the edge states of a IQH state. The 2d state in cylinder geometry is shown in (a) where the chiral states sit at the edges of the system. The term 'cylinder geometry' refers to the boundary condition of the system. In the 2d cylinder geometry, one spatial direction exhibits periodic boundary conditions (PBC) and the other one exhibits open boundary conditions (OBC). As a counterexample, in torus geometry, both spatial variables have PBCs.

The wavefunction $\psi(x)$ of the edge state is localized at the edges as shown in Fig. 1.2(a) and decays into the bulk as shown in (b). Here, one can define a penetration depth l which measures the localization of the edge states at the boundary. In (c), we show the energy spectrum of this system. Considering the bulk bands only, with the lower band being completely filled and the upper band being empty, the system is an insulator. With edge states, however, the system becomes gapless at the boundary. The term 'edge states' is slightly misleading since a single state, associated with one k value, corresponds to just one point in the energy spectrum. What is usually meant is the edge mode which connects the upper and the lower bulk band, i.e., runs over many k values [41]. However, the name edge state is commonly used and for practical reasons we stick to this convention. An edge state crosses the whole band gap once. This means that we can assign a group velocity $\partial E/\partial k$ to the edge state at the Fermi energy. This group velocity is positive for the edge state at one edge and negative for the edge state at the other edge as highlighted in Fig. 1.2(a). Furthermore, we show the inverse penetration depth l^{-1} of the edge states in (d) which shows that the edge state is well localized as soon as it is energetically well separated from the bulk bands. For more introductory details on edge state spectra consult Refs. [42,43].

One of the most intriguing consequences of the described edge states stems from their chirality. In the most simple nontrivial scenario, there is one edge state per edge which has a certain chirality. If we focus on one edge only this means there is only one state at the Fermi energy and this state has a finite group velocity, say positive. This means there is no state with negative velocity, what implies that the state cannot backscatter at an impurity on that edge since there is no state to scatter into with a negative velocity. This feature is called robustness. Therefore, topological edge states are referred to as robust, gapless, conducting edge states.

1.2.4 Quantum Hall and Chern insulators

The *quantum Hall insulator* and the *Chern insulator* are both topologically nontrivial states. The quantum Hall insulator is achieved through a strong magnetic field which creates the quantum Hall effect, as it was introduced in Sec. 1.1.1. The topological properties of this state are characterized by the Chern number C, or originally called TKNN invariant, as described in Sec. 1.2. Let us think of a 2d lattice system in momentum space, so $\boldsymbol{k} = (k_x, k_y)$ is a good quantum number. The Chern number is defined as the integral of the Berry curvature over the whole BZ summed over all filled bands [4,34,35]:

$$C = \frac{i}{2\pi} \sum_{n=1}^{N_{\text{occ}}} \int dk_x dk_y \left[\langle \partial_{k_x} \psi_n(\boldsymbol{k}) | \partial_{k_y} \psi_n(\boldsymbol{k}) \rangle - \langle \partial_{k_y} \psi_n(\boldsymbol{k}) | \partial_{k_x} \psi_n(\boldsymbol{k}) \rangle \right] \tag{1.3}$$

Here, $|\partial_{k_\mu} \psi_n(\boldsymbol{k})\rangle$ is the k_μ derivative of the Bloch state of the nth band corresponding to the spatial direction $\mu = x, y$. Equation (1.3) is an example of a topological invariant. We observe that it is expressed by contributions from all N_{occ} occupied states. The contribution of all the occupied states makes it a global quantity, in fact, it is in general not possible to express it through local quantities. Besides its nontrivial Chern number, the IQH state also hosts chiral edge states, as explained in Sec. 1.2.3, where the number of edge states is equal to the Chern number.

The word Chern insulator is used for a topologically nontrivial state without an externally applied field, i.e., without net magnetic flux piercing the 2d plane. Thus it corresponds to the state of the QAH of Sec. 1.1.2. A Chern insulator is also characterized by the Chern number in Eq. (1.3) and, correspondingly, also hosts chiral edge states. Examples for tight-binding models which generate the quantum Hall insulator and the Chern insulator are the Hofstadter model in Sec. 2.1 and the Haldane model in Sec. 2.4, respectively.

1.2.5 Topological insulators

In the preceding section, we have understood that quantum Hall and Chern insulators are topologically protected, i.e., they carry a nontrivial Chern number which can only change upon a gap closing. They also host robust, gapless, conducting, chiral edge states which cannot backscatter as explained in Sec. 1.2.3. *Topological insulators*, on the other hand, are states which are not only topologically protected but also by symmetry, namely TRS. It thus corresponds to the QSH discussed in Sec. 1.1.3 and to the symmetry class AII recalling our discussion in Sec. 1.2.2. Until topological insulators were introduced [20, 44] it was believed that TRS breaking is necessary for nontrivial states such as the IQH. This triggered a huge excitement in the field [3, 45].

The most simple way to construct a TRS topologically nontrivial system is to think of two copies of a quantum Hall insulator each assigned to one spin-1/2 spin state with flipped magnetic field. This means that the spin-up particles are exposed to the positive magnetic field and the spin-down particles to the negative one of the same magnitude. Upon time reversion, the magnetic fields as well as the spin states flip and one obtains the same system. This is the spin conserving case, i.e., spin-up and down particles are not coupled and can be treated independently. Let us say the Chern number of the spin-up particle is $C_\uparrow = 1$. Then, because of the opposite magnetic fields due to TRS, the spin-down particles must have Chern number $C_\downarrow = -1$. We observe that the total Chern number $C_\uparrow + C_\downarrow$ vanishes even though there are edge states. These edge states, however, do not contribute to any mass transport, sometimes also called charge transport, but rather to spin transport. This is why these edge states are dubbed helical and a spin Chern number $(C_\uparrow - C_\downarrow)/2$ can be defined which equals to 1 in this case.

The concept of a topological insulator, however, is more general than just two copies of a quantum Hall insulator. To understand this concept, we have to look at the fundamental symmetry of the system, TRS, following Ref. [3] here. The time reversion operator is denoted $\hat{\Theta}$. Certainly, $\hat{\Theta}$ will not change a particle's position $\boldsymbol{r}$ but will reverse its motion, i.e., its momentum $\boldsymbol{p}$. In operator language this is expressed as

$$\hat{\Theta}\hat{\boldsymbol{r}}\hat{\Theta}^{-1} = \hat{\boldsymbol{r}}, \quad \hat{\Theta}\hat{\boldsymbol{p}}\hat{\Theta}^{-1} = -\hat{\boldsymbol{p}}, \tag{1.4}$$

where $\hat{\boldsymbol{r}}$ and $\hat{\boldsymbol{p}}$ stand for the position and the momentum operator, respectively. Looking at the commutator $[\hat{\boldsymbol{r}}, \hat{\boldsymbol{p}}] = i\hbar$, where $\hbar = h/(2\pi)$, we find $\hat{\Theta} i \hat{\Theta}^{-1} = -i$ which makes $\hat{\Theta}$ an anti-unitary operator. For spin-1/2 systems the time reversion operator can be represented as

$$\hat{\Theta} = e^{i\pi\sigma^y/2}\hat{K} = i\sigma^y\hat{K}, \tag{1.5}$$

where $\hat{K}$ is the complex conjugation operator, $\hat{K}i\hat{K}^{-1} = -i$ with $\hat{K}^2 = \mathbb{1}$. The square of the time reversion operator yields

$$\hat{\Theta}^2 = i\sigma^y\hat{K}i\sigma^y\hat{K} = i\sigma^y(-i)(\sigma^y)^*\hat{K}^2 = -(\sigma^y)^2 = -\mathbb{1}. \tag{1.6}$$

The property $\hat{\Theta}^2 = -\mathbb{1}$ puts 2d TRS topological states into the AII class within the ten-fold way of the symmetry classification [30], see Sec. 1.2. In 2d and 3d, this implies the characterization of topological states by $\mathbb{Z}_2$ numbers, what we will see in this and the following sections. In four dimensions the states are characterized by an integer number, i.e. a $\mathbb{Z}$ number, a fact that is later discussed in Sec. 4.1.1. Methods of how to compute the $\mathbb{Z}_2$ number to characterize topological insulators are presented in Sec. 3 and diverse generalizations to it are a substantial part of this work.

For a half-integer spin system, the Kramers theorem applies. Let us consider a Hamiltonian $\hat{H}(\boldsymbol{k})$ of a lattice system with quasimomentum $\boldsymbol{k}$. Upon time reversion the sign of the quasimomentum of the Hamiltonian flips $\boldsymbol{k}$ [3]:

$$\hat{\Theta}\hat{H}(\boldsymbol{k})\hat{\Theta}^{-1} = \hat{H}(-\boldsymbol{k}) \tag{1.7}$$

The TRS of the system then has the following implications on the energy spectrum $E(\boldsymbol{k})$ of the system. The spectrum is defined as $\hat{H}(\boldsymbol{k})|\psi(\boldsymbol{k})\rangle = E(\boldsymbol{k})|\psi(\boldsymbol{k})\rangle$. The energy of the time-reversed state $\hat{\Theta}|\psi(\boldsymbol{k})\rangle$ is computed as

$$\begin{aligned} \hat{H}(\boldsymbol{k})\hat{\Theta}|\psi(\boldsymbol{k})\rangle &= \hat{\Theta}\hat{H}(-\boldsymbol{k})\hat{\Theta}^{-1}\hat{\Theta}|\psi(\boldsymbol{k})\rangle = \hat{\Theta}\hat{H}(-\boldsymbol{k})|\psi(\boldsymbol{k})\rangle \\ &= \hat{\Theta}E(-\boldsymbol{k})|\psi(\boldsymbol{k})\rangle = E(-\boldsymbol{k})\hat{\Theta}|\psi(\boldsymbol{k})\rangle. \end{aligned} \tag{1.8}$$

Thus, we find that the time-reversed partner $\hat{\Theta}|\psi(\boldsymbol{k})\rangle$ at $\boldsymbol{k}$ has the same energy as the state $|\psi(-\boldsymbol{k})\rangle$ at $-\boldsymbol{k}$. This is illustrated in Fig. 1.3(a) where we

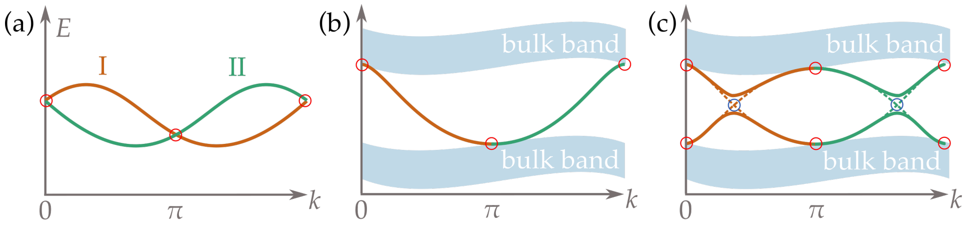

Figure 1.3: Schematic for edge states of topological insulators at one edge: (a) Kramer's degeneracy at $k = 0, \pi$ of time-reversed partners I and II, (b) edge state of a topological insulator, and (c) two edge states of a topological insulator which gap out at momenta not equal to 0 or π.

defined $|\psi_{II}(\boldsymbol{k})\rangle = \hat{\Theta}|\psi_I(\boldsymbol{k})\rangle$. Since the BZ is periodic, there exist two special points where we find degeneracies due to the above argument. These values are 0 and π, called time-reversal invariant momenta (TRIM). In 2d, e.g., the following four TRIM exist: $(0,0)$, $(\pi,0)$, $(0,\pi)$, and (π,π). We observe in Fig. 1.3(a) that at these special points there are degeneracies which are protected by the TRS, dubbed Kramers degeneracies.

In contrast to a quantum Hall state or a Chern insulator, a topological insulator hosts counter-propagating, helical edge states. This means that in principle back scattering could occur if spin mixing was present. However, since the TRS-protected degeneracies cannot be lifted, the state which crosses the band gap will not gap out. This is shown in Fig. 1.3(b) for one pair of edge states at one edge only. If a second pair of edge states exists, as shown in Fig. 1.3(c), band crossings can occur at quasimomenta not being equal to 0 or π. At these points, TRS is not protective against coupling of the crossing bands and they can hybridize and eventually gap out. The many-body state is then topologically equivalent to the topologically trivial state. In fact, only an odd number of edge state pairs per edge is topologically nontrivial. This emphasizes the characterization by a $\mathbb{Z}_2$ number as the topological invariant for topological insulators.

The quantum state of a topological insulator survives only if TRS is present, otherwise spin-mixing terms could gap out the nontrivial edge states. This is why they are sometimes called symmetry-protected topological states. Other symmetries can also protect the topologically nontrivial state. A further example is the topological crystalline insulator which incorporates mirror symmetries of the system [46].

1.2.6 Three-dimensional topological states

In the preceding section we have focused the 2d topological insulator state. Topological insulators are, however, not restricted to 2d and were generalized to 3d also exhibiting TRS [47–49], reviewed in Ref. [50]. From the

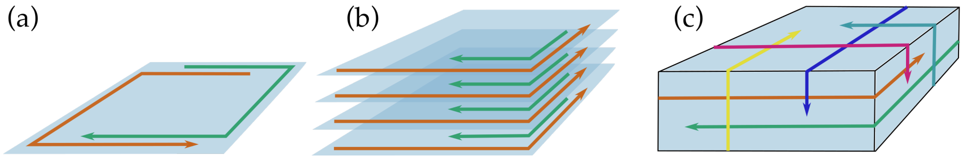

Figure 1.4: Schematic for three-dimensional topological insulators: (a) two-dimensional topological insulator $\nu = 1$ (b) weak topological insulator $(\nu_0; \nu_1, \nu_2, \nu_3) = (0; 0, 0, 1)$ as a stack of two-dimensional topological insulators (c) strong topological insulator $(\nu_0; \nu_1, \nu_2, \nu_3) = (1; 0, 0, 0)$ with colors representing different spin states.

topological classification [30] we understand that these states also obey a $\mathbb{Z}_2$ characterization. In contrast to the 2d equivalent, not a single $\mathbb{Z}_2$ number but four $\mathbb{Z}_2$ numbers are required for the full characterization of the 3d topological state. This comes from the fact that in 3d there exist eight TRIM. If one fixes one component k_i of the quasimomentum $\boldsymbol{k} = (k_x, k_y, k_z)$ to $k_i = 0, \pi$, we obtain a 2d plane. We recognize again a 2d BZ spanned by (k_j, k_l) with $i \neq j \neq l$. These 2d BZs again obey the characterization of a 2d topological insulator as explained before. There are six of such 2d planes in the 3d BZ each carrying a $\mathbb{Z}_2$ number. However, they are not entirely independent and one can reduce the number to four independent $\mathbb{Z}_2$ numbers $(\nu_0; \nu_1, \nu_2, \nu_3)$. Since a $\mathbb{Z}_2$ number can only assume two different values, this yields in total 16 possible many-body states including the topologically trivial state $(0; 0, 0, 0)$.

The most simple way to think of the 3d generalization is by coupling 2d topological insulators, depicted in Fig. 1.4(a), in order to achieve a 3d stack as shown in Fig. 1.4(b). The edge states are now surface states encircling the topological insulator around the stacking direction. This state is dubbed weak topological insulator (WTI) since is was assumed that it is sensitive to violations of the translational symmetry. However, the numerical study of Ref. [51] has shown robustness against surface disorder. We observe a clear anisotropy of the WTI which is determined by the three numbers ν_1, ν_2, ν_3. The stacking picture works only for weak coupling between the layers.

For strong inter-layer coupling, there is no equivalent to 2d such as stacking. Here, a very intriguing state can emerge which is called strong topological insulator (STI). The interesting feature of this state is, that it hosts a single Dirac cone [52] at its surface BZ. Due to TRS, this cone is spin-momentum locked, i.e., any value of the surface quasimomentum $\boldsymbol{k}_{\text{surf}}$, being element of the 2d surface BZ, is assigned to a fixed spin state. This means that a certain spin state has a determined propagation direction on the surface. We illustrate this phenomenon in Fig. 1.4(c) by assigning color to the spin state. The STI is characterized by the so-called strong invariant ν_0. Systems where the strong invariant together with the weak invariants are simultaneously nontrivial are studied in Refs. [53,54].

With the STI we encountered a 3d state which has no equivalent, i.e., adiabatic connection to a state, in 2d. But in 3d, even more fascinating states are revealed. Thus far, as in the 2d case, the states were insulating in the bulk but conducting at the boundaries. In 3d, however, there exist gapless bulk states which are topologically protected. Examples of which are Dirac, Weyl, and nodal-line semimetals [55,56]. In Sec. 4.4, we will go into detail of 3d topological states of matter with explicit application of the 3d generalization of the TRS Hofstadter model. The 2d version of which will be introduced in Sec. 2.2.

1.3 Quantum simulators

The idea of a *quantum simulator* goes back to Feynman in 1982 [57–60]. Quantum simulation is regarded as one of the four main quantum technologies, next to quantum computing, quantum communication, and quantum metrology [61]. Feynman proposed to simulate a quantum system with another equivalent quantum system, instead of a classical machine. The reason for that is the exponential growth of the Hilbert space with the system size and the subsequently increased demand of computational memory. Consider, e.g., a system of N quantum spins with two spin states. A state vector of this system is 2^N-dimensional. Handling a state vector like this on a classical machine restricts the number of quantum spins to small values. A system of N qubits on the other hand contains this amount of information in its very own quantum state.

Quantum simulations are nowadays conceptually divided into the so-called digital and analog quantum simulations. The former corresponds to a set of quantum objects like qubits which are assembled in circuits freely programmable to the specific problem to be investigated. This resembles the idea of the universal quantum simulator [62] and constitutes a very flexible concept. Its scaling is, however, problematic as reflected by the small number of fault-tolerant qubits in current quantum computers. Analog quantum simulations, on the other hand, are systems which obey a Hamiltonian which is as close as possible to the Hamiltonian of the system to be simulated. This makes analog quantum simulators a model-specific system, i.e., they are restricted to resemble a certain system. Approaches that combine the benefits from both concepts exist as well [63].

Physical realizations of quantum simulator candidates are manifold. Almost all of them rely on very low temperatures such that the physics is governed by quantum mechanics and the state is not destroyed by thermal fluctuations. They differ, however, by their type of quantum object, i.e., the carrier of information, and the respective confining potential. For example: *Cold atom* experiments are neutral atoms trapped in light fields. Trapped ion systems consist of ions in microwave fields. *Superconducting circuits* feature electrons in superconductors. Finally, *photonic lattices* constitute photonic excitations in optical media. We will go into depth of cold atoms in Sec. 1.4. In trapped ion setups, the Coulomb force can be exploited, in contrast to neutral atoms, to prepare well controllable arrays of laser-cooled trapped ions whose interactions and manipulation can be realized with different laser fields [64]. To realize superconducting circuits, well-developed chip fabrication methods can be used for creating structures of resonators which will then host electronic excitations [65]. Photonic lattices can be created by engineering structures inside optical media through local change of the refraction index. Photonic excitations then resemble the photonic quantum simulator [66, 67].

Applications for a quantum simulator range from condensed-matter physics [68–71] via high-energy physics [72,73] to quantum chemistry [74,75] and many more. Instances for quantum simulators for condensed matter physics exist numerously. A few examples of proposed and actually conducted experiments are: the bosonic [76] as well as the fermionic [77] Mott insulator, the BEC-BCS crossover [78,79], the Fermi pressure [80], the fermionic antiferromagnet (AFM) [81], lattice gauge theories [82], high-temperature superconductivity [83] with cold atoms, spin systems [84] and entangled states with trapped ions [85], many-body localization in superconducting circuits [86], or the relativistic Zitterbewegung in photonic lattices [87]. Of course, this is just a small fraction of successful applications for quantum simulators.

1.4 Cold atoms in optical lattices

As we have mentioned in the last section, cold atomic gases [88–90], or ultracold quantum gases, in optical lattices are a popular candidate for quantum simulators with a multitude of applications. The foundation for ultracold quantum gases in optical lattices is the interaction between atoms and photons. Light fields are used to both trap the atoms, which is necessary to avoid reheating of the atoms at any kind of container wall, and cool the atoms to temperatures low enough to reveal quantum effects. The origin of state-of-the-art cold atom experiments has led to a Nobel Prize in physics [91–93]. But the real kick off for cold atom experiments was the first observation of the 1925 proposed Bose-Einstein condensation [94, 95] in 1995 [96–99] which again led a Nobel Prize in 2001.

Trapping

The trapping of atoms, as already proposed in Ref. [100], relies on the effective force field $\boldsymbol{F}(\boldsymbol{r})$ acting on the atom which stems from the light field.

Let us consider the atom on a semi-classical level as a simple harmonic oscillator with resonance frequency ω_0, i.e., the atom is a two-level system with excitation energy $\hbar\omega_0$ [101]. The atom is now exposed to a driving light field with frequency ω. In the dipole approximation the respective force is then proportional to the gradient of the intensity field $I(\boldsymbol{r})$ of the driving light field:

$$\boldsymbol{F}(\boldsymbol{r}) = \frac{\omega_0^2 - \omega^2}{(\omega_0^2 - \omega^2)^2 + \omega^2\Gamma} \nabla I(\boldsymbol{r}). \tag{1.9}$$

We note that the sign of the force depends on the two frequencies ω and ω_0. If the light field frequency is tuned below the resonance frequency, i.e., $\omega < \omega_0$, the light field is dubbed red-detuned. The force field points along the gradient of the intensity field towards the maxima of the intensity field. Effectively, the atoms will then align at the intensity maxima of the light field. A red-detuned trap can readily be engineered with a tightly focused laser beam. Analogously, in a blue-detuned light field the atoms will align at the intensity minima of the light field. The endeavor here, is to surround the atomic cloud with a blue-detuned laser field. Since the intensity is low in the center of this kind of trap, unwanted atom-photon interactions can be minimized [101]. The potential profile of traps originating from Gaussian beam shapes is approximately harmonic, i.e., quadratic in the leading order of the spatial variables.

By imposing two counter-propagating laser beams one can create standing wave potentials with a spatially periodic profile. These periodic lattices can be used to simulate tight-binding models. This applies if the potential depth of the lattice is sufficiently deep such that the Wannier functions are well localized and the occupation of higher bands is suppressed [102, 103]. The lattice structure makes the so-called optical lattices an ideal candidate for simulating solid state systems [70, 71, 104–106]. On the one hand, in optical lattices, atoms obey a tight-binding Hamiltonian within a laser potential, while on the other hand, in solid state systems electrons obey a tight-binding Hamiltonian within the ionic background potential. Moreover, since cold atoms in optical lattices are extremely versatile, the achieved states can go way beyond the simulation of electronic systems: It is possible to create quantum gases made out of fermions [107], bosons, or even mixtures of them [108, 109]. Their internal degrees of freedom can represent almost arbitrarily many spin degrees of freedom [110]. The interaction strength can be tuned through Feshbach resonances [111]. Topologically nontrivial gauge fields [112–115] and spin-orbit coupling [116] can be engineered. Disorder can be imposed [117]. Long-range interactions through Rydberg excitations can be created [118], and much more is possible.

As we mentioned above, trapping potentials possess an approximately harmonic profile. However, recent experiments have shown uniform ultracold Bose [119] as well as Fermi [120] gases created with so-called light sheets. An even more exciting development is the application of digital mirror devices (DMD) [121]. Here, almost any potential landscape can be realized, however, a resolution better than a typical lattice constant of an optical lattice is not yet achievable.

Cooling

In order to reveal the interesting quantum physics with ultracold quantum gases, one has to reach temperatures below a few nano Kelvin. This is because for these quantum gases, critical temperatures for, e.g, the condensation of bosons or degenerate fermions, lie in the micro to nano Kelvin regimes [105]. To achieve ultracold quantum gases within optical lattice potentials, typically the quantum gas is cooled to very low temperatures without the potential, i.e., only with the confining trapping potential being present. Subsequently, the optical lattice potential is ramped up in an adiabatic fashion [122]. For the cooling of atomic quantum gases [91–93, 101, 123, 124], many different techniques exist which make use of different effects: there is *Doppler cooling* which exploits the Doppler effect leading to a steady and selective absorption of photons of momentum pointing against the propagation direction of the atoms. Randomly directed emission of photons then leads to an effective slow down of the atoms. With this cooling technique one can achieve temperatures down to the so-called Doppler limit. To reach temperatures below this limit, further cooling techniques have to be applied. Within *Sisyphos cooling* the atoms have to climb a potential which is constantly tuned to slow down the atoms. For *evaporative cooling* the trapping potential is modulated such that particles with large velocity will escape from the trap but slow particles remain inside the trap. In order to cool fermions down to very low temperatures, even more advanced cooling techniques like *sympathetic cooling* are required since at very low temperatures single-state fermions cannot interact and thus they cannot thermalize [125]. These techniques are nowadays established. A more recent method to reach very low temperatures is the so-called entropy extraction scheme [126]. The idea of that scheme is to have a system which consists of two parts. The first part is the region of interest where the quantum gas should reach very low temperatures and will eventually be probed. The second region serves as a reservoir into which entropy will be redistributed. To this end, one uses a *dimple trap* which consists of an ordinary harmonic trap and an additional dimple in the trap center. The dimple serves as the region of interest. The chemical potential is tuned such that the dimple is filled with particles as well as parts of the remaining region of the harmonic trap. Now the harmonic trap is expanded while the dimple itself remains unchanged. Subsequently, this draws energetic particles out of the dimple into the expanded regions while lowering the entropy within the dimple. This techniques has been successfully applied in an experiment to create an antiferromagnet with fermions in an optical lattice [81].

Probing

To measure ultracold quantum gases, one utilizes many different detection techniques. A standard method is the time-of-flight imaging which can be used to measure the temperature [91–93] or correlations [106] of the quantum gas. Here, the atoms are released from the trap by suddenly switching it off. After a hold time t_{TOF}, a snapshot of the expanding atom cloud is taken through absorption imaging. The obtained spatial density distribution $n(\boldsymbol{r})$ is directly related to the momentum distribution in the cloud $n(\boldsymbol{k})$ and thus reveals information about its state and the temperature.

Quantum gas microscopes are another powerful method for the investigation of cold atoms in optical lattices which were realized for bosons [127] as well as fermions [128] and are now an established method used to detect, e.g., the Fermi-Hubbard AFM [81]. A quantum gas microscope, as the name suggests, indeed, combines an optical microscope and a cold atom setup. Typically, the microscope points on a 2d quantum gas, however, 3d configurations are possible [129]. Atoms which occupy different lattice sites are then fixed by ramping up the lattice depth such that they do not escape the lattice during the detection. Then the atoms are illuminated by a near-resonant laser beam. The optical setup, the microscope supported by a semi-spherical lense inside the vacuum chamber, is optimized to reach resolution length scales which are just below the lattice constant of the optical lattice. This high resolution can even be used for single-site addressing within the optical lattice [130]. Also, it is possible to create arbitrary potentials such as optical lattice potentials with a short lattice spacing which is independent of the laser frequency. This is done by projecting a mask through the microscope [127]. A quantum gas microscope can thus detect with single-site resolution, address with single-site resolution, and create arbitrary potential landscapes similar to the DMD explained above.

Interactions

Interactions between particles in cold atom setups can be tuned in a flexible manner via so-called Feshbach resonances [111, 131]. We consider two particles which scatter with a background s-wave scattering length a_{BG}, where we assume that the temperatures are sufficiently low such that only s-wave scattering takes place. A possible bound state between the two particles would host different vibrational excitations. The Feshbach resonances then occur if the energy of the separated particles matches the energy of a vibrational state. By applying an external magnetic field with magnitude B the coupling between the separated state and the vibrational states can be tuned. This is represented by the resonance formula for the s-wave scattering length of ultracold collisions

$$a(B) = a_{\mathrm{BG}} \left(1 - \frac{\Delta}{B - B_0}\right), \tag{1.10}$$

introduced in Ref. [132], where B_0 and Δ are atom-specific parameters. The resonances occur at $B = B_0$ where $a(B)$ diverges and another transition from repulsive to attractive particle interaction happens at $B = B_0 + \Delta$. It is therefore in principle possible to achieve any interaction strength as, e.g, shown in the BEC-BCS crossover [78,79].

1.5 Topological states in cold atomic gases

Topological states of matter are nowadays routinely engineered in cold atomic setups [133–136]. This is only possible by overcoming a huge obstacle: Cold atoms are charge neutral. Therefore, they do not couple to a magnetic field, in stark contrast to electrons in materials. There exist different methods to solve this problem. Common experimental approaches are rotating quantum gases, laser-assisted tunneling, lattice shaking, and synthetic dimensions. Rotating quantum gases resemble the physics of a charged particle within a magnetic field since the Coriolis force and the Lorentz force are mathematically equivalent [137]. Experimental realizations, however, are hard to control [138–140]. Synthetic dimensions [141] use the internal degree of the atoms of the ultracold quantum gas, i.e., the hyperfine states [142]. Through appropriate laser coupling of these states, excitations can, hop between different hyperfine states. With this, one can engineer a synthetic dimension with a finite number of lattice sites corresponding to the finite number of accessible hyperfine states. Synthetic dimensions can be very versatile as it will become apparent further below. A drawback, however, is the implementation of interactions since local interactions in the real dimension become nonlocal in the synthetic dimensions.

We will go into more detail of the techniques of laser-assisted tunneling and lattice shaking in the specific examples of the realizations of the Hofstadter and Haldane models in Secs. 2.1 and 2.4, respectively. The following little excerpt demonstrates the development of topological states in cold atom setups which is of course not exhaustive: In 2013, groups in Munich [112] as well as at MIT [113] both independently realized the Hofstadter Hamiltonian using laser-assisted tunneling. In 2014, the Haldane Hamiltonian on a brick-wall lattice was realized at ETH Zurich [114]. In 2015, the Chern number was measured from the Hall response in the Hofstadter model [143]. The same year, two groups independently engineered topological states with synthetic dimensions [144,145]. A year later tomographic schemes to measure Chern numbers were independently implemented by groups in Munich [146] and Hamburg [115]. Topological states were first combined with a quantum gas microscope in 2017 at MIT [147] including two-body interactions. In 2018, driven interacting topological states were realized [148] at ETH and in Munich, the 4d quantum Hall effect was explored with synthetic dimensions [31]. In 2019, the first three-dimensional topological state, a nodal-line semimetal, was realized in Hong-Kong [149]. This year a group in Paris performed an experiment with synthetic dimensions measuring the local Chern marker [150], a local topological indicator in real space, see Sec. 3.4.

It is important to mention that both lattice shaking as well as laser-assisted tunneling are methods which drive the system since both rely on time-periodic modulation of the laser fields. The high frequency limit, however, can be static. In some cases, the realized Hamiltonians in the experiment happen to be effective high-frequency Hamiltonians. We will discuss more about that in the next section and in Secs. 2.1 as well as 2.4.

1.6 Driven systems and Floquet theory

As mentioned in the preceding section, topologically nontrivial states are engineered by periodically driving systems of ultracold quantum gases. Periodically driven systems can exhibit interesting phases. If the driving frequency is much higher than all other energy scales in the system, the high oscillations can be integrated out leaving behind an effective system. An impressive example in classical physics is the Kapitza pendulum [151]. It consists of a normal pendulum which is fixed to a periodically driven mounting. In parameter regimes, where the driving frequency scales with the driving amplitude, the pendulum can oscillate upside down. Its motion is not anymore governed only by gravity but rather is subject to an effective force which points in the opposite direction.

The theory of dynamical systems is of course more involved than the static case. Here, we provide a brief introduction to Floquet theory which is an established framework to investigate periodically driven quantum systems. In general, the time-evolution operator from time t_1 to t_2 of a system with a time-dependent Hamiltonian $\hat{H}(t)$ is given by

$$\hat{U}(t_2, t_1) = \mathcal{T}_t \exp\left[-i \int_{t_1}^{t_2} \hat{H}(t')dt'\right], \tag{1.11}$$

where $\mathcal{T}_t$ is the real-time ordering operator and $\hbar = 1$. Floquet theory can be regarded as the analog of Bloch theory for the time domain. It can be applied if $\hat{H}(t)$ is periodic in time with a period T [151–153]. The so-called stroboscopic Floquet Hamiltonian $\hat{H}_F[t_0]$ is defined for the evolution of one period as

$$\hat{U}(t_0 + T, t_0) = e^{-i\hat{H}_F[t_0]T}, \tag{1.12}$$

where t_0 is the onset time of the periodic drive. We find that $\hat{H}_F[t_0]$ is time-independent, in contrast to the original Hamiltonian $\hat{H}(t)$. Hence $\mathcal{T}_t$ of Eq. (1.11) is obsolete. The dynamics of $\hat{H}_F[t_0]$ is stroboscopic, i.e., only time steps of multiples n of the period T are described. For a general time evolution, we can use Eq. (1.12) in combination with two additional time evolution operators:

$$\begin{aligned}\hat{U}(t_2,t_1) =&\hat{U}(t_2,t_0+nT)\hat{U}(t_0+nT,t_0)\hat{U}(t_0,t_1)\\ =&\hat{U}(t_2,t_0+nT)e^{-i\hat{H}_F[t_0]nT}\hat{U}(t_0,t_1)\\ =&e^{-i\hat{K}_F[t_0](t_2)}e^{-i\hat{H}_F[t_0](t_2-t_1)}e^{i\hat{K}_F[t_0](t_1)}\end{aligned} \tag{1.13}$$

This can be justified from the property $\hat{U}(t_2,t_1)=\hat{U}(t_2,t')\hat{U}(t',t_1)$ of the time evolution operator for arbitrary t'. In the last equation of Eq. (1.13), we have defined the so-called stroboscopic kick operator $\hat{K}_F[t_0](t)$.

The stroboscopic Floquet Hamiltonian $\hat{H}_F[t_0]$ and the associated stroboscopic kick operator $\hat{K}_F[t_0](t)$ are not unique and depend on t_0. Every choice of t_0, however, is only a gauge choice and the solutions for different t_0 are equivalent. In particular, they should all be equivalent to a solution which is independent of t_0 as

$$\hat{H}_{\text{eff}}=e^{i\hat{K}_{\text{eff}}(t_0)}\hat{H}_F[t_0]e^{-i\hat{K}_{\text{eff}}(t_0)}. \tag{1.14}$$

Here, we have defined the effective Hamiltonian $\hat{H}_{\text{eff}}$ and the effective kick operator $\hat{K}_{\text{eff}}(t)$. Both the stroboscopic Floquet Hamiltonian and the effective Hamiltonian carry the same amount of information about the system. In general, their construction is demanding. Therefore, expansions are necessary. We will first present the Magnus expansion of $\hat{H}_F[t_0]$ and then the high-frequency expansion of $\hat{H}_{\text{eff}}$.

The stroboscopic Floquet Hamiltonian in Eq. (1.12) and the stroboscopic kick operator can both be expanded in powers of the inverse frequency Ω^{-1}.

$$\hat{H}_F[t_0]=\sum_{n=0}^{\infty}\hat{H}_F^{(n)}[t_0] \quad \text{and} \quad \hat{K}_F[t_0]=\sum_{n=0}^{\infty}\hat{K}_F^{(n)}[t_0], \tag{1.15}$$

where the superscript (n) denotes that the term scales with the nth power in Ω^{-1}. The expansion is done by rewriting $\hat{H}_F[t_0]$ as a function of $\hat{H}(t)$ using Eqs. (1.11) and (1.12). Subsequently, the expansion can be performed using the Baker-Campbell-Hausdorff formula. The stroboscopic kick operator $\hat{K}_F[t_0](t)$ can be expanded in a similar way. This yields for the zeroth order terms

$$\hat{H}_F^{(0)}[t_0]=\frac{1}{T}\int_{t_0}^{t_0+T}\hat{H}(t')dt' \quad \text{and} \quad \hat{K}_F^{(0)}[t_0](t)=0. \tag{1.16}$$

This procedure for the stroboscopic Floquet Hamiltonian is called *Magnus expansion*. The effective Hamiltonian in Eq. (1.14) can either be obtained from the Magnus expansion and a subsequent gauge transformation or directly by the *high-frequency expansion of the effective Hamiltonian*. The zeroth order terms here read

$$\hat{H}_{\text{eff}}^{(0)} = \frac{1}{T}\int_0^T \hat{H}(t')dt' \quad \text{and} \quad \hat{K}_{\text{eff}}^{(0)}(t) = 0, \tag{1.17}$$

which is the same results as the zeroth order term of the Magnus expansion. For higher order terms, however, the two approaches differ, i.e., they coincide only in the infinite-frequency limit.

1.7 Hubbard model in the context of dynamical mean-field theory

This section is dedicated to the Hubbard model and the applied dynamical mean-field theory (DMFT) without gauge fields. The aim is to provide a basic understanding of interacting tight-binding models and to introduce dynamical quantities necessary in the context of this work. In 1963, Hubbard, Kanamori, and Gutzwiller independently simplified the problem of interacting electrons in a solid by restricting the system to the lowest energy band and neglecting all electron-electron interactions which are not on-site [154–156]. The resulting tight-binding model is called Hubbard model. Even though the original model includes only two terms, any model including extensions to these is normally also called a Hubbard model. We now consider the 3d Hubbard model for spin-1/2 fermions on a simple cubic lattice. The Hamiltonian in second quantization reads

$$\hat{H} = -t \sum_{\langle \boldsymbol{ij} \rangle \sigma} \hat{c}_{\boldsymbol{i}\sigma}^{\dagger} \hat{c}_{\boldsymbol{j}\sigma} + U \sum_{\boldsymbol{i}} \hat{n}_{\boldsymbol{i}\uparrow} \hat{n}_{\boldsymbol{i}\downarrow}, \tag{1.18}$$

where the first term describes hopping in the lattice with t being the hopping energy and the second term describes on-site, two-particle interactions with interaction strength U. Here, $\boldsymbol{i} = (x, y, z)$ stands for a lattice site vector and the $\langle \ldots \rangle$ denotes nearest neighbors. The creation and annihilation operators of a fermion in spin state σ at site $\boldsymbol{i}$ are $\hat{c}_{\boldsymbol{i}\sigma}^{\dagger}$ and $\hat{c}_{\boldsymbol{i}\sigma}$, respectively. Eventually, the particle number operator is defined as $\hat{n}_{\boldsymbol{i}\sigma} = \hat{c}_{\boldsymbol{i}\sigma}^{\dagger} \hat{c}_{\boldsymbol{i}\sigma}$.

There is no exact solution known to the model in Eq. (1.18), at least in 3d, and the model has kept theoretical physicists busy since its first mention. A successful approximate method, however, is DMFT, which becomes more reliable in higher dimensions. We will introduce DMFT in Sec. 3.1 and will now focus only on its results with regard to the model in Eq. (1.18).

Interacting systems can be described by means of Green's functions. On a single-particle level, the Green's function is a two-point correlator, i.e., it is a correlation function of two field operators. The correlator is then computed over the quantum statistical ensemble of the many-body states.

The attribute 'single-particle' refers to the propagation of one particle being surrounded by all other particles in the system statistically interacting with this particle. At zero temperature, the Green's function can be expressed as [157, Eq. (2.116)]

$$G(\boldsymbol{k},\omega) = \frac{1}{\omega + i\eta - E(\boldsymbol{k}) - \Sigma(\boldsymbol{k},\omega) + \mu} \tag{1.19}$$

where $\boldsymbol{k}$ is the momentum, ω is the frequency, and μ is the chemical potential. $E(\boldsymbol{k})$ are the eigenenergies of the noninteracting Hamiltonian and $\Sigma(\boldsymbol{k},\omega)$ is the selfenergy. The sign of the infinitesimal number η determines whether (1.19) is the retarded or advanced Green's function. We will omit η and always refer to the retarded Green's function. The negative imaginary part of the Green's function yields the spectral function

$$A(\boldsymbol{k},\omega) = -\frac{1}{\pi}\mathrm{Im}G(\boldsymbol{k},\omega), \tag{1.20}$$

which is a generalization of the energy spectrum of noninteracting systems to interacting systems. It provides information about the existence of quantum states as a function of ω and $\boldsymbol{k}$. The spectral function is normalized according to $\int d\omega A(\boldsymbol{k},\omega) = 1$. Performing the $\boldsymbol{k}$-space integration of $A(\boldsymbol{k},\omega)$ results in the density of states (DOS).

Two natural quantities which appear in the study of fermionic Hubbard models are the antiferromagnetic (AFM) order parameter, or staggered magnetization, m and the double occupancy n_D. On a cubic lattice, they are defined as

$$m = \frac{1}{N_s}\sum_{\boldsymbol{i}}(-1)^{x+y+z}\langle \hat{n}_{\boldsymbol{i}\uparrow} - \hat{n}_{\boldsymbol{i}\downarrow}\rangle, \quad n_D = \frac{1}{N_s}\sum_{\boldsymbol{i}}\langle \hat{n}_{\boldsymbol{i}\uparrow}\hat{n}_{\boldsymbol{i}\downarrow}\rangle. \tag{1.21}$$

Here, $\langle \dots \rangle$ denotes the quantum-statistical average in equilibrium and N_s is the number of lattice sites. Here, m is expressed for a polarization of magnetic moments in z direction. The model in Eq. (1.18), on the other hand, exhibits a SU(2) spin-rotation symmetry. However, the spins can always be rotated into the z direction because of this symmetry and therefore the expression in Eq. (1.21) is sufficient. In the half-filled, noninteracting case n_D is strictly equal to 0.25 since there is a probability of 0.5 for each spin state to occupy a site.

In general, the selfenergy $\Sigma(\boldsymbol{k},\omega)$ in Eq. (1.19) is a complex-valued function of $\boldsymbol{k}$ and ω. In mean-field theories, with the exception of cluster mean-field theories, the selfenergy is momentum-independent $\Sigma(\boldsymbol{k},\omega) = \Sigma(\omega)$. In contrast to static mean-field theories, where the selfenergy Σ_{MF} is a constant and real-valued, in DMFT, the selfenergy is frequency-dependent. In the limit of infinite frequency, both selfenergies coincide $\Sigma(\omega \to \infty) = \Sigma_{\mathrm{MF}}$.

Deviations from that can be quantified through the so-called correlation strength Ξ [54,158,159]

$$\Xi = \frac{\Sigma(\omega = 0) - \Sigma_{\mathrm{MF}}}{\Sigma_{\mathrm{MF}}}. \tag{1.22}$$

This quantity measures the deviation from the static mean-field result and thus can be regarded as a quantification of local quantum fluctuations.

Finally, we introduce the quasiparticle weight as a measure for Fermi liquid behavior. It is a useful quantity in the context of Mott insulators. Following Ref. [160], we perform a low-energy expansion of the selfenergy in Eq. (1.19) as $\Sigma(\boldsymbol{k},\omega) \approx \Sigma(\boldsymbol{k},0) + \omega[\partial_\omega \Sigma(\boldsymbol{k},\omega)]_{\omega=0}$ such that we find

$$G(\boldsymbol{k},\omega) = \frac{Q_{\boldsymbol{k}}}{\omega + i\eta - \tilde{E}(\boldsymbol{k}) + \mu} + G'(\boldsymbol{k},\omega), \tag{1.23}$$

where $G'(\boldsymbol{k},\omega)$ contains the deviations from the expansion. The first term has the structure of a noninteracting Green's function with the weight $Q_{\boldsymbol{k}}$. The so-called quasiparticle weight $Q_{\boldsymbol{k}}$ and the renormalized energies $\tilde{E}_{\boldsymbol{k}}$ are defined as

$$Q_{\boldsymbol{k}} = \left(1 - \left.\frac{\partial \Sigma(\boldsymbol{k},\omega)}{\partial \omega}\right|_{\omega=0}\right)^{-1}, \quad \tilde{E}_{\boldsymbol{k}} = Q_{\boldsymbol{k}}[E_{\boldsymbol{k}} - \Sigma(\boldsymbol{k},0)]. \tag{1.24}$$

For a $\boldsymbol{k}$-independent selfenergy $\Sigma(\boldsymbol{k},\omega) = \Sigma(\omega)$, it follows that the quasiparticle weight becomes a constant $Q_{\boldsymbol{k}} = Q$. This is indeed the case in DMFT which we will introduce in Sec. 3.1. In order to get an intuition for the quasiparticle weight, we compute the effective mass

$$M^* \propto \left(\frac{\partial^2 \tilde{E}_{\boldsymbol{k}}}{\partial \boldsymbol{k}^2}\right)^{-1} \tag{1.25}$$

The attribute 'effective' here refers to the renormalization through interactions in contrast to the effective mass renormalized through an optical lattice potential [85]. Originally, the analog with the physical mass works at energy minima where the nonconstant leading term is quadratic. The effective mass, however, can also be defined elsewhere in the energy landscape and thus can assume even negative values. From Eqs. (1.24) and (1.25), we find that $Q = M/M^*$ which suggests that the quasiparticle weight is a measure for the modification of the mobility of the particles due to interactions. $Q = 1$ means there is no decrease of mobility compared to the noninteracting case and $Q = 0$ signifies that the particles are localized due to their infinite effective mass arising from inter-particle interaction.

In Fig. 1.5 we show the phase diagrams of the cubic Hubbard model defined in Eq. (1.18). We show the staggered magnetization in (a) as the order parameter for AFM. We observe the immediate onset of AFM as U is

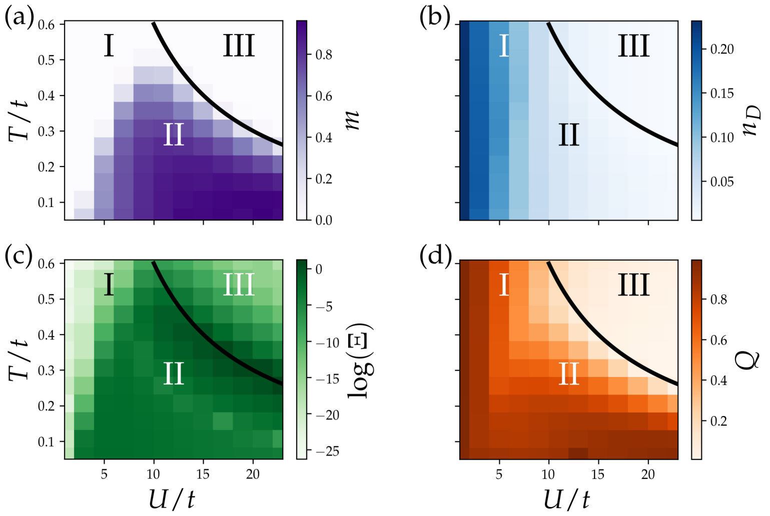

Figure 1.5: Phase diagrams of the cubic Hubbard model defined in Eq. (1.18): (a) the staggered magnetization m and (b) the double occupancy both defined in Eq. (1.21), (c) the correlation strength Ξ defined in Eq. (1.22), as well as (d) the quasiparticle weight Q defined in Eq. (1.24) as a function of the temperature T and the interaction strength U . Superexchange temperature of the cubic lattice is shown as thick black line $T = 6t^2/U$. We also highlight three instances of many-body phases of the cubic Hubbard model for different values of (U, T): the paramagnetic metal (I) for $(5, 0.11)$, the antiferromagnet (II) for $(11, 0.26)$, and the Mott insulator (III) for $(21, 0.51)$. Results were obtained from real-space DMFT with a two-site unit cell combined with an exact diagonalization solver with four bath sites.

finite for zero temperature. The critical temperature for the phase transition between paramagnetic and AFM phases is called Néel temperature T_N. The Néel temperature of the Hubbard model is an intensely studied quantity. It is strongly dependent on the method since fluctuations play an important role here. DMFT mostly overestimates the Néel temperature compared to quantum Monte Carlo results [161–163], since it neglects to some degree nonlocal fluctuations. Moreover, within DMFT the choice of the specific solver can lead to different results [164]. For the strongly interacting limit the many-body state of the Hubbard model in Eq. (1.18) maps to an effective Heisenberg spin model. This is because at half filling and low enough temperatures the many-body state will be part of a subspace with one particle per lattice site. Excitations will occur as hopping processes to nearest neighbors and back. This is expressed through the Heisenberg Hamiltonian

$$\hat{H} = J \sum_{\langle ij \rangle} \hat{S}_i \cdot \hat{S}_j, \tag{1.26}$$

where we defined spin operators as $\hat{\boldsymbol{S}}_i = \hat{\boldsymbol{c}}_i^\dagger \boldsymbol{\sigma} \hat{\boldsymbol{c}}_i$ with $\boldsymbol{\sigma} = (\sigma^x, \sigma^y, \sigma^z)$ being the Pauli vector. The effective spin interaction origins from second-order hopping processes, i.e., the forth-and-back hopping or exchange mechanisms with nearest neighbors in the Hubbard model. These processes scale with the superexchange energy $J = t^2/U > 0$. AFM ordering is anticipated to occur if the superexchange energy is equal to the temperature. In a cubic lattice the number of partners for the superexchange is six, i.e., the Néel temperature becomes $T_N \sim 6J = 6t^2/U$ in the cubic lattice in the strong interaction limit. We plot this simple relation in Fig. 1.5 as a thick black line. It coincides with the phase transition of the DMFT results, however, this is again an overestimation as a reduced value for the Néel temperature of $T_N = 3.83J$ is known in the literature, e.g., in Refs. [165–167]. Since this value is just shown in these references, but does not appear explicitly in Ref. [168] which is commonly cited for this value, we take a moment to understand where it comes from. Reference [168] is an exhaustive collection of results for the Heisenberg model using the high-temperature expansion technique. The Heisenberg model therein without external field reads [168, Eqs. (1.1), (1.3), and (1.4)]

$$\hat{H} = -2J_1 s^2 \sum_{\langle ij \rangle} \hat{\boldsymbol{S}}_i \cdot \hat{\boldsymbol{S}}_j. \tag{1.27}$$

This relates to our definition of the spin coupling energy as $J = |2J_1|s^2$, where s is the spin, being $1/2$ in our case. For $J_1 > 0$, the system becomes ferromagnetic for temperatures below the Curie temperature T_C. For $J_1 < 0$, the Néel temperature can be related to the corresponding Curie temperature for the same value of $|J_1|$ through Ref. [168, Eq. (5.6)]:

$$\frac{T_N - T_C}{T_C} \approx \frac{0.63}{qX}, \tag{1.28}$$

where q is the coordination number and $X = s(s+1)$ is equal to $3/4$ in our case of a spin-$1/2$ system. In a simple cubic lattice the coordination number is $q = 6$ and we find with Eq. (1.28) that $T_N \approx 1.14 T_C$. In [168, Table III.] an estimate for the Curie temperature is given for the simple cubic lattice of $T_C = 1.68 J_1$. Finally, with the conversion above this yields a Néel temperature of $T_N \approx 1.915|J_1| = 3.83J$.

The double occupancy n_D is sometimes used as an order parameter to characterize the Mott insulator phase. However, the Mott insulator is more complex than just a suppressed value for n_D. Additionally, not every insulator which emerges from increasing interaction is a Mott insulator. We show the double occupancy in Fig. 1.5(b). We observe a clear decrease for increasing interaction strength. This is consistent with the notion that the energy penalty for doubly occupied sites scales with U. The temperature dependence, on the other hand, seems to be rather week. In Ref. [169] the double occupancy as a function of the temperature for the cubic Hubbard model has been investigated and shows a rather flat behavior. We made sure that the results of Ref. [169] are consistent with our results.

In contrast to static mean-field theories, the DMFT yields a selfenergy which is frequency-dependent $\Sigma(\omega)$. As described above, the correlation strength is a measure for the frequency-dependent features of the selfenergy solution. We show the correlation strength Ξ in Fig. 1.5(c). We observe that Ξ is largest at the phase transition between the AFM and the paramagnetic, strongly interacting phase which coincides with the black thick line as described above in the discussion on the Néel temperature.

The last phase diagram in Fig. 1.5(d) shows the quasiparticle weight which we introduced in Eq. (1.24). In the weakly interacting and in the AFM regime, the quasiparticle weight is almost 1. Only in the remaining regime, we observe that the quasiparticle weight vanishes for the paramagnetic region above the black line for strong interaction strength and high temperature. As discussed above, if the selfenergy is $\boldsymbol{k}$-independent, a vanishing quasiparticle weight $Q = 0$ is equivalent to a divergent effective mass. Figuratively speaking, the particles are localized because of their infinite effective mass.

In discussing the four quantities of Fig. 1.5, we have identified three different many-body phases of the cubic Hubbard model of Eq. (1.18) which we label I, II, and III. Phase I is a paramagnetic phase with finite double occupancy and finite quasiparticle weight and is metallic since it persists at small U and the noninteracting case is metallic. Phase II is an AFM, since only here we find finite staggered magnetization. In fact, this AFM phase splits up into subphases. For small U, one finds a Slater insulator [170]. This is because on bipartite lattices, like the cubic lattice, infinitesimal U will cause a translational symmetry breaking. The unit cell doubles and thus the BZ is reduced by a factor of 2. This leads to two bands in the reduced BZ. These bands can hybridize and open a gap of size U. In the large U limit, one finds a Heisenberg AFM which we discussed above. Furthermore, the single-particle DOS of the AFM phase is always gapped [171]. Eventually, phase III is identified as the Mott insulator [172]. It is a paramagnetic phase and the only phase where the quasiparticle weight vanishes such that the particles become localized through strong interactions. We also observe that the double occupancy is strongly suppressed suggesting that there is one particle per site, a property which is typical for a Mott insulator.

Let us go into more detail on these three phases and investigate the corresponding selfenergy which is of course local within our DMFT results. It is to say that the selfenergy as output from DMFT, in most cases, is a function of imaginary Matsubara frequencies as most of the solvers work in imaginary time. We will discuss more on that in Sec. 3.1.4. In Fig. 1.6, column (a) we show the real part in blue and the imaginary part in orange of the on-site selfenergy $\Sigma(i\omega_n)$ as a function of the fermionic Matsubara

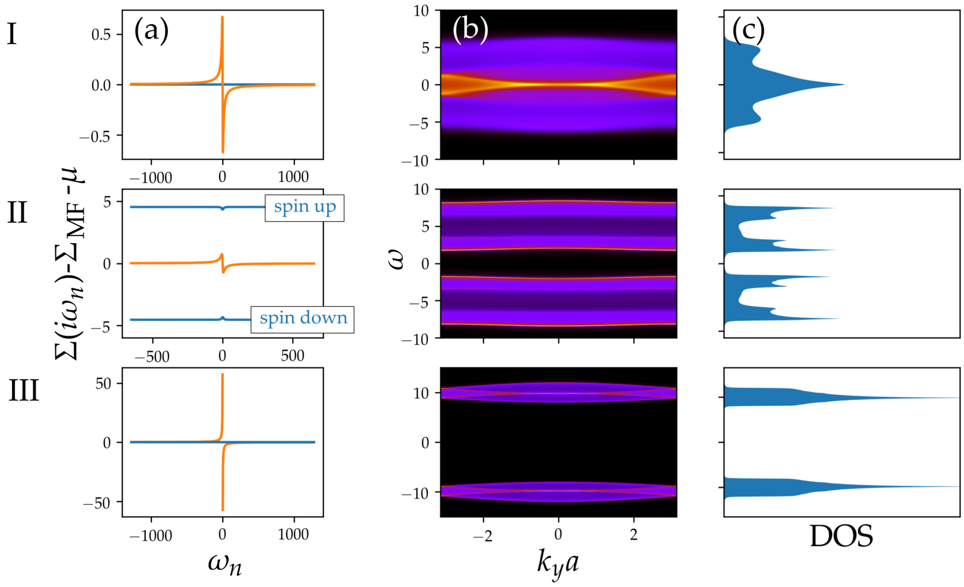

Figure 1.6: Dynamical quantities of the three phases in Fig. 1.5: paramagnetic metal (I), antiferromagnet (II), Mott insulator (III). Column (a) shows the real (imaginary) part of the selfenergy in blue (orange) as a function of Matsubara frequencies ω_n, column (b) shows the k_x-k_z-integrated spectral function $\int dk_x dk_z A(\boldsymbol{k}, \omega)$ with the definition in Eq. (1.20) as a function of k_y and as a function of the real frequencies ω, and column (c) shows the density of states DOS $= \int d\boldsymbol{k} A(\boldsymbol{k}, \omega)$ as a function of ω. Energies are measured in units of the hopping energy t.

frequencies:

$$\omega_n = \frac{(2n+1)\pi}{\beta} \quad \text{with} \quad n \in \mathbb{Z}. \tag{1.29}$$

In Matsubara frequencies the selfenergy has the following symmetry:

$$\mathrm{Re}\Sigma(-i\omega_n) = \mathrm{Re}\Sigma(i\omega_n) \quad \text{and} \quad \mathrm{Im}\Sigma(-i\omega_n) = -\mathrm{Im}\Sigma(i\omega_n), \tag{1.30}$$

which can be deduced from the Lehmann representation of the Green's function and its hermiticity condition. Using the Cauchy-Riemann equations, these symmetry conditions can be transferred to the selfenergy as a function real frequencies $\Sigma(\omega)$. Therein, real and imaginary part will exchange their roles, i.e., the real part of $\Sigma(\omega)$ is antisymmetric and the imaginary part is symmetric. These symmetries have also an impact on the computation of the quasiparticle weight defined in Eq. (1.24). Since only the derivative at zero frequency contributes to Q_k, we conclude that only the antisymmetric part of the selfenergy is required, i.e., either $\mathrm{Re}\Sigma(\omega)$ or $\mathrm{Im}\Sigma(i\omega_n)$. The exact analytical form for the latter can be obtained from the Kramers-Kronig relations.

Coming back to our results in Fig. 1.6, we observe in column (a) that indeed the real part is always symmetric while the imaginary part is always antisymmetric with respect to ω_n. In phase I and III, the real part is constantly zero, in contrast to phase II, where we find for the spin-up state an approximately constant value of 5 and for the spin-down state a value of -5. This corresponds to a spin-selective on-site potential. Note, that on the nearest-neighbor sites, these values are flipped, which corresponds to the AFM order. The imaginary part of the selfenergy has some features around $\omega_n = 0$ in the cases I and II, which will slightly rescale the value of the quasiparticle weight defined in Eq. (1.24). However, a drastic difference is visible for the case III. Here, the imaginary part of the selfenergy is discontinuous and even divergent. It is of course not possible to show real divergence in numerics, however, we observe that the magnitude of the selfenergy is much larger than any energy scale in the system except U.

From Figs. 1.6(b) and (c), we see that phase I is a metal, in phase II we observe two bands each associated with one spin state. At half filling the lower band is completely filled leading to an insulating state with spin polarization at one site. This is exactly the scenario of a Slater insulator [170]. Therein, the noninteracting band splits into two spin-associated bands by increasing the interaction strength. This eventually yields magnetic order. In the phase III in Fig. 1.6(b) and (c), we again find two bands dubbed Hubbard bands, but this time they are not associated with a certain spin state. In fact, the phase is a paramagnetic insulator, a Mott insulator [172]. Let us consider the transition from phase I to phase III by increasing U and fixing T. In order to split the metallic band of the case I, the spectral function defined in Eq. (1.20) has to vanish for all $\boldsymbol{k}$. Via Eq. (1.19) this translates into a divergence of the selfenergy at zero frequency, see Fig. 1.6(a), row III. This would not be possible to describe with a constant selfenergy Σ_{MF}. We like to point out that this scenario is one of the highlights of DMFT since it is capable of describing this metal-to-Mott-insulator transition. The full range of this transition cannot be described in, e.g., static mean-field or Fermi liquid theory. In real materials this is of interest, e.g, in transition metal oxides, in which the d orbitals are partially filled. The resulting orbitals in the compound narrow the wavefunctions of the electrons' overlap and their repulsive interaction becomes important [173]. A prototypical example of a transition metal oxide and the corresponding DMFT calculations is Vanadium Sesquioxide V_2O_3 [174]. The transition can be tuned through applied pressure or doping [175]. In synthetic systems, cold atomic setups are the ideal platform to study the metal-to-Mott-insulator transition [76,77].

Chapter 2

Topologically nontrivial tight-binding models

Generally, the many-body systems in the context of this thesis can be described by a real-space Hamiltonian, whose parameter space includes the continuous space of d-dimensional vectors in real space. The Hilbert space is thus infinite dimensional, so discretization is required to make the problem numerically manageable. However, the Hilbert space is still huge in most instances. A successful simplification for lattice problems is the tight-binding approximation. Herein, the wavefunction of particles, like electrons in solids or atoms in optical lattices, is bound very closely to the potential minima. These minima of the potential landscape constitute the lattice sites. The potential itself corresponds to the ionic potential in solids or the optical lattice for ultracold quantum gases. With the tight-binding approximation it is then possible to energetically restrict the Hilbert space to a discrete set of lattice sites. Tunnel couplings between the sites and on-site potentials can then be conveniently expressed in matrix elements, being just numbers.

Cold atom experiments are well controllable configurations. With the help of optical lattices it is possible to engineer very closely tight-binding models in real setups. This is nicely reflected by the following statement in Ref. [176]: “To study material systems, theorists create ‘spherical-cow’ models of real materials, whereas in cold atom physics experimentalists can actually make spherical cows.”

In this chapter, we list the most common tight-binding models which reveal nontrivial topological states. Even though this work is mainly dedicated to the generalizations of the famous Hofstadter model, we will also introduce other models to provide a broader perspective for the field by showing differences and similarities between them. In Fig. 2.1, we show schematic pictures of three spinless tight-binding models, the Hofstadter, the Harper-Hofstadter-Hatsugai (HHH), and the Haldane model.

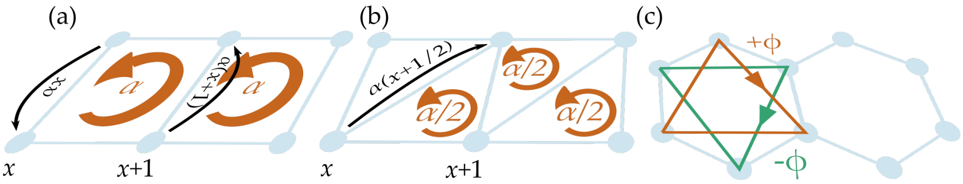

Figure 2.1: Spinless tight-binding models for topologically nontrivial states: (a) Hofstadter model with a square plaquette flux of α, (b) HHH model with the hopping matrix elements of (a) and one additional diagonal hopping matrix element leading to a plaquette flux per triangle of $\alpha/2$, and (c) Haldane model particles, which hop along the orange (green) links, acquire a phase ϕ ($-\phi$).

2.1 Hofstadter model

The quantum-mechanical problem of electrons confined to a 2d lattice and exposed to a perpendicular magnetic field stimulated research over many decades. This generated, among others, three famous publications which appeared in a periodic manner of approximately 22 years after another. Peierls first came up with the idea for the substitution of the momentum operator in a system exposed to a magnetic field in 1933 [177]. Then Harper used this in 1955 to study the case of a lattice structure exposed to small magnetic field strength of 10^4 Oe which corresponds to 1 T in vacuum [9]. Finally, in 1976, Hofstadter investigated energy levels of electrons in strong magnetic fields [8] giving rise to what is nowadays called *Hofstadter butterfly*. He estimated that field strengths of around 10^9 G would be required in real materials to observe this effect which corresponds to 10^5 T. For comparison, the magnetic field record set in 2018 is 1200 T [178]. The story, however, does not end here as it turns out that synthetic realizations of the IQH enable the creation of such high field equivalents which we have discussed in Sec. 1.5.

The Hofstadter Hamiltonian, sometimes Harper-Hofstadter Hamiltonian, in the Landau gauge and in second quantization reads

$$\hat{H} = -t \sum_{x,y} \left[\hat{c}^{\dagger}_{x+1,y} \hat{c}_{x,y} + \hat{c}^{\dagger}_{x,y+1} e^{2\pi i \alpha x} \hat{c}_{x,y} + \text{h.c.} \right], \tag{2.1}$$

where $\hat{c}_{x,y}$ is the annihilation operator of a spinless fermion on site (x, y). Of course, the Hofstadter model can also be constructed for bosons [112, 179], but we treat solely fermions in this work. In Eq. (2.1), as shown schematically in Fig. 2.1(a), a fermion can hop along the x direction with energy t but acquires a complex quantum phase when hopping in the y direction. Through this phase, the vector potential $\boldsymbol{A}(x, y)$ enters in the Peierls' substitution as

$$\frac{e}{\hbar} \int \boldsymbol{A} \cdot d\boldsymbol{l} = \frac{eBax}{\hbar} \int_{y}^{y+1} a dy' = \frac{eBxa^2}{\hbar} = 2\pi\alpha x, \tag{2.2}$$

where we have used the Landau gauge $\boldsymbol{A}(x,y) = Bax\hat{e}_y$ for the second equation and the lattice constant is a. Note that x and y denote dimensionless indices rather than coordinates. The corresponding real-space coordinate is obtained through multiplication with a. We thus find the so-called plaquette flux to be $\alpha = eBa^2/h = \Phi_B/\Phi_0$. Here, $\Phi_B = a^2B$ is the magnetic flux and $\Phi_0 = e/h$ is known as the flux quantum. The plaquette flux is proportional to the magnetic field strength B and to the penetrated area a^2. This squared lattice constant is a main reason why the Hofstadter model cannot be realized in real materials since a here is of the order of $1\,\text{Å} = 10^{-10}\,\text{m}$. In contrast, in cold atom setups, a is of the order of a few 100 nm. However, it is possible to control the magnitude of α directly as explained in Sec. 1.5.

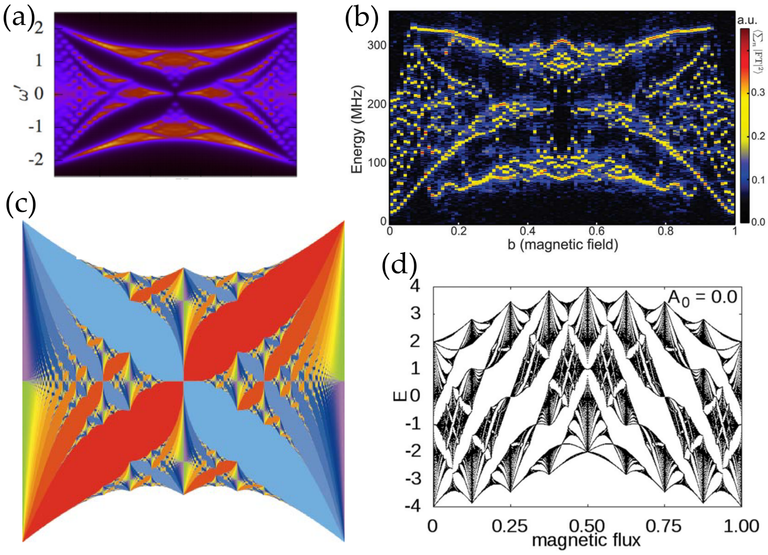

Figure 2.2: Hofstadter butterflies: (a) For a driven optical lattice. Reprinted with permission from Ref. [180]. Copyright (2020) by the American Physical Society. (b) Hofstadter butterfly from an experiment with superconducting qubits. From Ref. [181]. Reprinted with permission from AAAS. (c) Hofstadter butterfly colored by the respective Chern number. Reprinted from Ref. [182], with the permission of AIP Publishing. (d) Hofstadter butterfly in the Kagomé lattice. Reprinted with permission from Ref. [183]. Copyright (2020) by the American Physical Society.

Hofstadter solved the Harper equation [9] without restrictions for the field strength and revealed the fascinating fractal structure of the energy levels [8]. This is to be understood in the following way. Let us restrict to the case of rational values for the plaquette flux $\alpha = p/q$ where p and q are integers. If p is a multiple of q or if $p = 0$, the phase is trivial as it then yields $e^{2\pi i \alpha x} = 1$. In the remaining cases, we find a periodicity of the

Hamiltonian in Eq. (2.1) along the x direction with a period of q sites. We deduce that this q-site unit cell yields q bands in the band structure. Plotting the $\boldsymbol{k}$-integrated bands as a function of α from 0 to 1, one finds the fractal structure, the Hofstadter butterfly, also known as Hofstadter moth.

This structure is also found in related systems as we show in Fig. 2.2. In Fig. 2.2(a), the butterfly appears in the theoretical calculation of a Floquet system and in (b) it is detected experimentally with a system of superconducting qubits [184]. Figure 2.2(c) shows the Chern numbers [34], see Sec. 1.2.2, of the different energy gaps in the butterfly [182] and (d) confirms that the fractal structure is not restricted to square lattices as it appears, e.g., also in the Kagomé lattice penetrated by a flux [183].

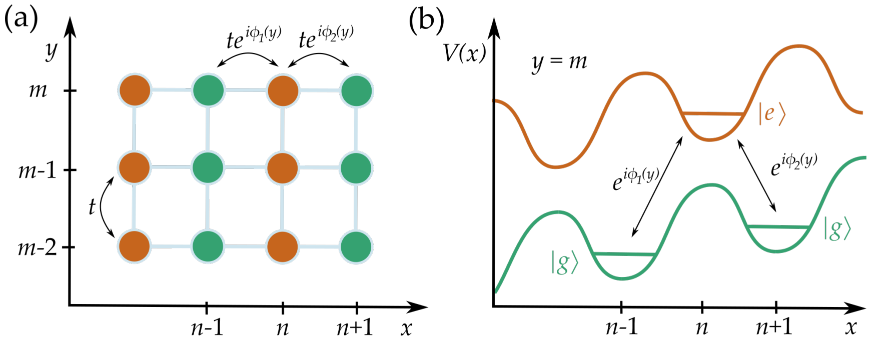

Figure 2.3: Anti-magic lattice with the two states $|g\rangle$ and $|e\rangle$ corresponding to even and odd sites, respectively. Resonant laser couplings between $|g\rangle$ and $|e\rangle$ impose a y-dependent quantum phase $\phi_i(y)$.

Let us take a look at the connection between the Hofstadter model and actual experiments. As discussed before, solid state systems are not expected to show Hofstadter physics since this would require very strong magnetic fields. These strong magnetic fields, however, can be simulated in, e.g., cold atom setups. For the Hofstadter model, the proposal by Jaksch and Zoller [185] has proven successful since it has been realized in experiments [112, 113]. We schematically depict this in Fig. 2.3. Within this approach the Hamiltonian in Eq. (2.1) is engineered using anisotropic hopping shown in Fig. 2.3(a). Normal hopping, i.e., no additional phase is acquired, is used along the y direction. But this normal hopping is suppressed in the x direction either through lattice acceleration, a static electric field [185], or a superlattice [186]. The hopping in the x direction is then restored through laser-assisted tunneling, i.e., via an intermediate state which locally resides between the original lattice sites in the x direction. This is achieved through a so-called anti-magic lattice shown in Fig. 2.3(b) with the additional static electric field. An anti-magic lattice is tuned such that the polarizabilities of two internal states of the atom $|g\rangle$ and $|e\rangle$ are exactly opposite, i.e., they have the same magnitude but a different sign. This results in a lattice where the states $|g\rangle$ sit on the even sites, while the states $|e\rangle$ sit on the odd sites. Coming back to the laser-assisted tunneling process, one laser couples $|g\rangle$ at site n with state $|e\rangle$ at site $n+1$, another laser couples $|e\rangle$ at site $n+1$ with state $|g\rangle$ at site $n+2$. These laser couplings are used to impose the complex phases.

These phases, however, are the results of a more complex configuration. In fact, the Hamiltonian achieved in the experiment, which resembles the Hofstadter Hamiltonian in Eq. (2.1), is an effective Hamiltonian of a periodically driven system. Let us go into more detail following Refs. [151,187]. In this experiment, the system, which consists of a 2d optical lattice, is driven trough running-wave laser beams which create an on-site potential of the form

$$V(\boldsymbol{r},t) = V_0 \sin(\delta\boldsymbol{k}\cdot\boldsymbol{r} + \Omega t + \phi_0), \tag{2.3}$$

where Ω is the periodic driving frequency, $\delta\boldsymbol{k}\cdot\boldsymbol{r} = \phi_{xy}$ is a spatially inhomogeneous phase, and ϕ_0 is a phase shift which will be important later on. The amplitude $V_0 = \eta\Omega$ should scale with the driving frequency. The time-dependent driven Hamiltonian has the form

$$\begin{aligned}\hat{H}(t) = &- t\sum_{x,y}\left[\hat{c}^{\dagger}_{x+1,y}\hat{c}_{x,y} + \hat{c}^{\dagger}_{x,y+1}\hat{c}_{x,y} + \text{h.c.}\right]\\ &+\sum_{x,y}\left[V(\boldsymbol{r},t) + \Delta x\right]\hat{n}_{x,y}\end{aligned} \tag{2.4}$$

where Δ corresponds to the static electric field in x direction. A unitary transformation is used to eliminate the time dependence of the on-site terms which are linear in $\hat{n}_{x,y}$ [113,151]:

$$\hat{U}(t) = \exp\left\{-i\int_{t_0}^{t} dt'\,\left[V(\boldsymbol{r},t') + \Delta x\right]\right\}. \tag{2.5}$$

The Hamiltonian in the rotating frame is found through

$$\hat{H}_{\text{rot}}(t) = \hat{U}(t)\hat{H}(t)\hat{U}^{\dagger}(t) - i\hbar\hat{U}(t)\frac{d}{dt}\hat{U}(t). \tag{2.6}$$

If the linear potential Δx is resonant, i.e., $\Delta = \hbar\Omega$, the on-site terms cancel out exactly and one is left with hopping terms only:

$$\begin{aligned}\hat{H}_{\text{rot}}(t) = -t\sum_{x,y}\Big[&e^{-i\zeta\sin(\Omega t-\phi_{xy})+i\Omega t}\hat{c}^{\dagger}_{x+1,y}\hat{c}_{x,y}\\ &+e^{-i\zeta\sin(\Omega t-\phi_{xy})}\hat{c}^{\dagger}_{x,y+1}\hat{c}_{x,y} + \text{h.c.}\Big],\end{aligned} \tag{2.7}$$

where we defined $\zeta = 2\eta\sin(\phi_0/2)$, where $V_0 = \eta\Omega$. As we have discussed in Sec. 1.6, the zeroth order contributions of the stroboscopic Floquet

Hamiltonian and the effective Hamiltonian coincide and can be found as the time-averaged Hamiltonian. The time integral of Eq. (2.7) leads to Bessel functions of the first kind with the integral representation:

$$J_n(x) = \frac{1}{2\pi} \int_{-\pi}^{\pi} dt e^{i(x \sin t - nt)} \tag{2.8}$$

such that we finally arrive at the Hamiltonian

$$\hat{H} = -t \sum_{x,y} \left[J_1(\zeta) e^{-i\phi_{xy}} \hat{c}^\dagger_{x+1,y} \hat{c}_{x,y} + J_0(\zeta) \hat{c}^\dagger_{x,y+1} \hat{c}_{x,y} + \text{h.c.} \right], \tag{2.9}$$

which corresponds to the Hofstadter Hamiltonian in Eq. (2.1) up to a 90° rotation and the subsequent identification $\phi_{xy} = 2\pi\alpha x$. This can be achieved by tuning the spatial modulation $\phi_{xy} = \delta \boldsymbol{k} \cdot \boldsymbol{r}$. The hopping anisotropy $J_0(\zeta)/J_1(\zeta)$ in Eq. (2.9) can be lifted through the tuning of the laser amplitudes [188].

2.2 Time-reversal-symmetric Hofstadter model

As generalization to the Hofstadter model in Sec. 2.1, the TRS Hofstadter model was introduced in 2010 [189]. Here, the field operators of Eq. (2.1) are replaced through spinful field operators in the spinor representation $\hat{\boldsymbol{c}}_{x,y} = (\hat{c}_{\uparrow,x,y}, \hat{c}_{\downarrow,x,y})$ such that

$$\begin{aligned} \hat{H} = &- t \sum_{x,y} \left[\hat{\boldsymbol{c}}^\dagger_{x+1,y} e^{2\pi i \gamma \sigma^x} \hat{\boldsymbol{c}}_{x,y} + \hat{\boldsymbol{c}}^\dagger_{x,y+1} e^{2\pi i \alpha x \sigma^z} \hat{\boldsymbol{c}}_{x,y} + \text{h.c.} \right] \\ &+ \lambda \sum_{x,y} \left[(-1)^x \hat{\boldsymbol{c}}^\dagger_{x,y} \hat{\boldsymbol{c}}_{x,y} \right]. \end{aligned} \tag{2.10}$$

The Peierls phase is now spin-dependent as it is proportional to σ^z, where σ^k is the kth Pauli matrix. Furthermore in Eq. (2.10) a spin-flip factor is introduced for the hopping term in the x direction. Its magnitude is controlled by the parameter γ which we call spin mixing. The last term in Eq. (2.10) is a staggered potential along the x direction which controls the topological state. For large λ a topologically trivial band insulator is expected at half filling. In cold atoms, a staggered potential can be realized with a laser beam of double the wavelength compared to the original optical lattice wavelength.

In Fig. 2.4, we show different instances of the TRS Hofstadter model in the literature. Figure 2.4(a) is a band structure for the case $\alpha = 1/6$, $\gamma = 1/4$, and $\lambda = 0.5$. Here, we find many different insulating many-body states depending on the filling fraction, e.g., a QSH state at half filling or a band insulator at 2/3 filling, taken from [189]. Fig. 2.4(b) is the phase diagram of the TRS Hofstadter model taken from Ref. [190] for $\alpha = 1/6$ at half filling as a function of the spin mixing γ and the staggered potential λ. We observe

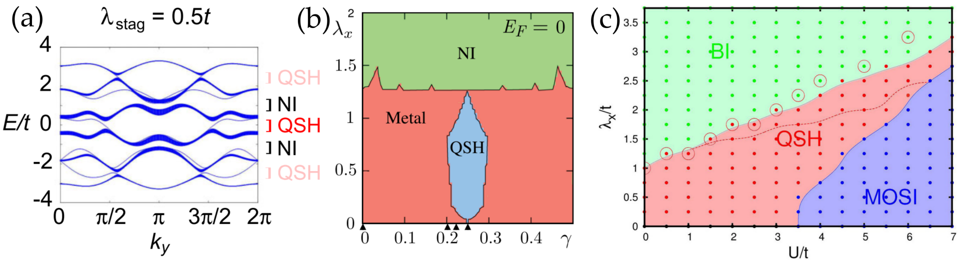

Figure 2.4: Instances in the literature on the TRS Hofstadter model showing regimes of the QSH phase: (a) Example band structure of the TRS Hofstadter model with finite staggered potential and spin mixing. Reprinted with permission from Ref. [189]. Copyright (2020) by the American Physical Society. (b) Phase diagram of the TRS Hofstadter model at half filling as a function of the staggered potential and the spin mixing. Reprinted with permission from Ref. [190]. Copyright (2020) by the American Physical Society. (c) Phase diagram of the TRS Hofstadter-Hubbard model for finite spin mixing as a function of the staggered potential and the interaction strength. Reprinted with permission from Ref. [193]. Copyright (2020) by the American Physical Society.

that there is a QSH phase in the regime of maximal spin-mixing $\gamma = 1/4$ and for $0 < \lambda < \sqrt[3]{2} \approx 1.25$ [191]. The staggered potential λ can thus be used as a control parameter for the QSH phase since for $\lambda > \sqrt[3]{2}$ the system is in a topologically trivial, insulating state. In fact, it is found that the parameter set $\alpha = 1/6$, $\gamma \approx 1/4$, and $\lambda > \sqrt[3]{2}$ is the most simple setting to achieve a QSH state in the TRS Hofstadter model at half filling [192]. This is interesting for us because at half filling the influence of Hubbard interactions has the highest impact and interaction effects are most pronounced.

Time-reversal-symmetric Hofstadter-Hubbard model

Coming to the interacting physics, the fermionic TRS Hofstadter-Hubbard model was intensively studied by means of dynamical mean-field theory [190,192,193]. It is obtained from adding the interaction term proportional to U of the Hubbard model in Eq. (1.18) to the noninteracting TRS Hofstadter Hamiltonian in Eq. (2.10). In Fig. 2.4(c) we show the phase diagram from Ref. [193] for $\alpha = 1/6$ and $\gamma = 1/4$ as a function of λ and U. It exhibits a QSH state as well as a band insulating and a magnetically ordered phase labeled MOSI in this figure. The QSH phase is most stable for $\lambda \approx 2U$. This can be understood from the competition between the staggered potential and the Hubbard interaction. The staggered potential energetically favors double occupancy while the Hubbard interaction favors either a Mott insulator or an AFM, see Sec. 1.7, leading to singly occupied sites. Interactions thus effectively reduce the staggered potential, thus stabilizing the QSH state. This is dubbed interaction-induced topological phase transition.

2.3 Harper-Hofstadter-Hatsugai model

From the Hofstadter butterfly, we see that the Hofstadter model never exhibits a gap at half filling. In the TRS Hofstadter model, we have discussed that a finite gap can be opened at half filling if spin mixing is present. Another way to open a gap at half filling relies on the following extension to the Hofstadter model. The Harper-Hofstadter-Hatsugai model [194] is often abbreviated as HHH model. It generalizes the Hofstadter model by introducing next-nearest neighbor hopping terms, i.e., particles can now tunnel along the diagonals of the square lattice. This is schematically depicted in Fig. 2.1(b) and yields the HHH Hamiltonian

$$\begin{aligned}\hat{H} = -t\sum_{x,y}\Big[&\hat{c}^\dagger_{x+1,y}\hat{c}_{x,y} + \hat{c}^\dagger_{x,y+1}e^{2\pi i\alpha x}\hat{c}_{x,y} \\ &+ \hat{c}^\dagger_{x+1,y+1}e^{2\pi i\alpha(x+1/2)}\hat{c}_{x,y} + \hat{c}^\dagger_{x+1,y-1}e^{2\pi i\alpha(x+1/2)}\hat{c}_{x,y} + \text{h.c.}\Big]\,.\end{aligned} \tag{2.11}$$

The next-nearest-neighbor hopping terms open a gap at half filling for values of the flux α with even denominators. This is in contrast to the Hofstadter model which is in the semi-metallic phase and has the advantage that one can study topologically non-trivial phases of a two-band model. The Hofstadter model, on the other hand, requires a minimum of three bands $\alpha = 1/3$ to find topologically nontrivial states. Concerning the nontrivial diagonal hopping elements, we will notice the similarity to the Haldane model in the next section. Another benefit of introducing the diagonal hopping term becomes apparent in the case with interactions because there is a gapped phase at half filling without the need for spin-mixing terms [195].

2.4 Haldane model

In 1988, Haldane introduced a model which, in contrast to the Hofstadter model, yields a topologically nontrivial state without a net magnetic field [14]. This corresponds to the anomalous Hall effect. Within the tight-binding model, this is achieved on a honeycomb lattice with a complex-valued hopping matrix element between next-nearest neighbors, as shown schematically in Fig. 2.1(c). The Hamiltonian reads [196]

$$\hat{H} = -t\sum_{\langle ij\rangle}\hat{c}^\dagger_i\hat{c}_j - t'\sum_{\langle\langle ij\rangle\rangle}\hat{c}^\dagger_i e^{i\phi}\hat{c}_j + \lambda\sum_i v_i\hat{c}^\dagger_i\hat{c}_j. \tag{2.12}$$

Here, the first term corresponds to the usual nearest-neighbor hopping in Hubbard models and the second term describes the next-nearest-neighbor hopping accompanied by a nontrivial phase ϕ, which breaks TRS. The honeycomb lattice exhibits two sites per unit cell corresponding to two sublattices A and B. The last term in Eq. (2.12) corresponds to a staggered potential of amplitude λ. The staggering is introduced through the function $v_{\boldsymbol{i}} = 1$ if $\boldsymbol{i} \in A$ and $v_{\boldsymbol{i}} = -1$ if $\boldsymbol{i} \in B$. The two-site structure of the unit cell can conveniently be represented in a pseudo spin-1/2 basis by means of Pauli matrices. This convenient form is achieved by Fourier transforming the Hamiltonian in Eq. (2.12). The corresponding momentum-space Hamiltonian matrix in this representation reads [14]

$$\begin{aligned} H(\boldsymbol{k}) = &- 2t' \cos(\phi) \sum_i \cos(\boldsymbol{k} \cdot \boldsymbol{a}_i) \mathbb{1} \\ &- t \sum_i \cos(\boldsymbol{k} \cdot \boldsymbol{a_i}) \sigma^x \\ &- t \sum_i \sin(\boldsymbol{k} \cdot \boldsymbol{a_i}) \sigma^y \\ &+ \left[\lambda - 2t' \sin(\phi) \sum_i \sin(\boldsymbol{k} \cdot \boldsymbol{b}_i) \right] \sigma^z \end{aligned} \tag{2.13}$$

where $\mathbb{1}$ is the 2×2 identity matrix, the $\boldsymbol{a}_i$ are three 2d real-space vectors pointing to the nearest neighbor sites, and the $\boldsymbol{b}_i$ are six real-space vectors to the next-nearest-neighbor sites [197]. For $t' = 0$, one recovers a model for a honeycomb, or hexagonal, lattice, i.e., the most simple form of graphene [197].

The Haldane model yields a nontrivial Chern number of 1 in some regimes in the phase diagram as a function of λ and ϕ [14]. Since there is no net flux piercing the 2d lattice, the Haldane model is a Chern insulator in these regimes, see Sec. 1.2.4. Interestingly, the Haldane model is a theoretical model to yield a Chern insulator, however, we will see in the next section that is has relevance in graphene and thus, in actual materials.

The fermionic Haldane-Hubbard model incorporating two decoupled spin species was studied in Ref. [198] leading to a phase diagram which is qualitatively similar to that of the Hofstadter-Hubbard model at maximal spin mixing as seen in Fig. 2.4(c). An explanation for this could be that at maximal spin mixing the two spin species can be decoupled into two new species. Each of them is exposed to a gauge field which does not show a net magnetic field as in the Haldane model. We will go into more detail of that spin decoupling in Sec. 4.1.

In Sec. 2.1 we have introduced the periodic driving protocol of an experimental system in order to achieve the Hofstadter Hamiltonian as the Floquet or effective Hamiltonian in the infinite-frequency limit. In the Hofstadter case, this is done through time-periodic modulation of the on-site potential by means of a running wave laser beam. In contrast, the Haldane model was realized through a periodic shaking of the lattice in which the relative lattice position changes in time as [114]

$$\boldsymbol{r}_{\mathrm{lat}}(t) = V_0[\cos(\Omega t)\hat{e}_x + \cos(\Omega t + \varphi)\hat{e}_y], \tag{2.14}$$

where the amplitude should again scale with the frequency $V_0 = \eta\Omega$. The lattice shaking in Eq. (2.14) can be achieved through retro-reflecting the laser beams which build up the optical lattice. The reflection mirrors are mounted on piezo-electric devices which are provided with an oscillatory voltage. This results in an oscillatory spatial shift of the retro-reflected standing wave laser beams. Tuning the phase shift ϕ of the lattice laser beams hence yields the time-dependent lattice position of Eq. (2.14). In the Hamiltonian, this drive couples to the atoms in the quantum gas as

$$\sum_{\boldsymbol{i}} f_{\boldsymbol{i}}(t)\hat{n}_{\boldsymbol{i}}, \quad \text{with} \quad f_{\boldsymbol{i}}(t) = \boldsymbol{i} \cdot \boldsymbol{E}_0|_{\boldsymbol{i}=\boldsymbol{r}_{\mathrm{lat}}(t)} = \boldsymbol{E}(t) \cdot \boldsymbol{r}. \tag{2.15}$$

The last equation shows that this protocol in ultracold quantum gases is equivalent to a drive with circularly polarized light $\boldsymbol{E}(t)$ [199–202]. To treat the driven Hamiltonian, one follows the same steps as we have discussed them for the Hofstadter model in detail, see Sec. 2.1. This includes the transformation to the rotating frame, the Magnus expansion of the stroboscopic Floquet Hamiltonian, and the high-frequency expansion of the effective Hamiltonian. Here, the zeroth order reveals real-valued rescaled hopping amplitudes. The first order contribution provides a nearest-neighbor complex-valued hopping amplitude. This is in contrast to the inverse frequency expansion of the Hofstadter model. We observe a clear difference in the engineering between both models. In the driving protocol for the Hofstadter model, the infinite-frequency Hamiltonian already features complex-valued hopping amplitude, i.e., an artificial gauge field. For the driving protocol for the Haldane model, the Ω^{-1} contributions is necessary to engineer an artificial gauge field.

2.5 Kane-Mele model

The Kane-Mele model [20] is an exciting model and is sometimes regarded as the discovery of topological insulators. The authors introduced SOC terms in the tight-binding model for the electrons of graphene. Graphene is treated as a flat, 2d honeycomb lattice which, as explained in the preceding section, contains two sites in the unit cell corresponding to two sublattices A and B [197]. We write the Kane-Mele Hamiltonian as

$$\hat{H} = -t\sum_{\langle \boldsymbol{i}\boldsymbol{j}\rangle} \hat{c}_{\boldsymbol{i}}^\dagger \hat{c}_{\boldsymbol{j}} - t' \sum_{\langle\langle \boldsymbol{i}\boldsymbol{j}\rangle\rangle} \hat{c}_{\boldsymbol{i}}^\dagger e^{i\phi\sigma^z} \hat{c}_{\boldsymbol{j}} - i\sum_{\langle \boldsymbol{i}\boldsymbol{j}\rangle} \hat{c}_{\boldsymbol{i}}^\dagger (d_1\sigma^y - d_2\sigma^x)\hat{c}_{\boldsymbol{j}}, \tag{2.16}$$

where we used again the spinor representation of the field operators as in Sec. 2.2. Originally, in graphene, only the first term is present. The second term corresponds to next-nearest-neighbor hopping along with a nontrivial phase ϕ. This resembles the Haldane model introduced in Sec. 2.4 for each of the two spin states separately in a TRS manner which means that the acquired phase is proportional to the σ^z Pauli matrix in spin space. This is a fascinating reappearance of the Haldane model. The Kane-Mele model, however, also covers possible spin-mixing processes through σ^x and σ^y with amplitudes d_1 and d_2, respectively, described by the third term. For finite d_1 or d_2, we cannot reduce the model to two separate Haldane models. Eventually, it turns out that the SOC in graphene is very small [203, 204]. Thus, the QSH effect was not found in graphene but in HgTe quantum wells instead [22]. Another candidate material is borophene, an analogous 2d material made from boron, which is much less understood than graphene but may give rise to interesting topological properties [205–207].

Chapter 3

Methods

This chapter represents the theoretical toolbox which we utilize to address the interacting topologically nontrivial tight-binding models we have introduced in the section before. Throughout this work, we tackle interacting systems by means of DMFT in its real-space version. We will introduce DMFT including spin-mixing processes and pay particular attention to those parts in the derivation that differ from standard DMFT, i.e., without spin mixing. We continue with a brief review of the two solvers we used within DMFT. These are the exact diagonalization solver and the continuous-time quantum Monte Carlo solver in the auxiliary-field expansion. We then review the maximum entropy method which is used to extract the dynamical properties from the quantum Monte Carlo results. Eventually, we introduce three methods for the computation of topological invariants, the local Chern marker, Fukui's method, and the Wilson loop technique.

3.1 Dynamical mean-field theory

DMFT in its original form is a nonperturbative and self-consistent method for solving Hubbard models, see Sec. 1.7, approximately. The attribute 'nonperturbative' means that DMFT does not rely on expansion parameters. This is in contrast to, e.g., a high-temperature expansion or an expansion for weak interaction strengths. The term 'self-consistent' refers to the iterative process to find a solution. Starting from an initial guess, the same quantity is successively reinserted until convergence is reached. The name DMFT prominently features 'mean-field theory' which refers to one of the most widespread class of theories in physics and chemistry to describe interacting particles. Instead of computing explicitly the interactions between all the particles, the problem is reduced to a single particle moving inside an effective field. The field is called mean field because it resembles the mean of all the individual fields created by each particle. As the name states, a mean field is a statistical average and does, by itself, not fluctuate.

The extension 'dynamical' to the mean-field theory employs the inclusion of dynamical fluctuations in DMFT. These fluctuations are purely quantum in nature which will be justified in the following. DMFT is rooted in the limit of infinite dimensions $d \to \infty$ [208,209] in which the nonlocal fluctuations vanish. The limit of infinite dimensions reduces the complexity of the full quantum problem and will be discussed further below in this section. The only remaining fluctuations are local and can only be temporal, i.e., dynamical. 'Temporal' does not refer to real time in the sense of time-dependent Hamiltonians. Rather it is to be understood from the Wick rotation which states that statistical mechanics in $d + 1$ dimensions, i.e., d spatial dimensions and one temporal dimension, is equivalent to quantum mechanics in d dimensions. The rotation is performed by transforming real time t to imaginary time $\tau = it$. A figurative way to think of the quantum fluctuations is that they occur on the imaginary time axis [210].

Since the first mention of the benefit of infinite dimensions, research shows immense output during the early 90ies. The advances made during that time are collected in the famous review by Georges et al. [211]. DMFT in its original form is formulated for periodic boundary conditions. In this work, we are interested in inhomogeneous system which brings us to the real-space formulation of DMFT. In order to study interface systems, Potthoff and Nolting used in 1999 [212] so-called inhomogeneous DMFT where one spatial direction is treated in real space. Inhomogeneous DMFT then was established for general layered systems [213]. The pure real-space DMFT was applied in 2008 to cold atoms confined to a harmonic trap [214,215]. For more overview on the developments of real-space DMFT consult Refs. [216–218].

Before we discuss real-space DMFT, we introduce DMFT for extended systems, such that $\boldsymbol{k}$ is a good quantum number and we can use the mathematical advantages of momentum space.

3.1.1 DMFT equations

We consider the Hubbard model with a general hopping amplitude $t_{ij}^{\sigma\sigma'}$ which can couple the two spin-1/2 states σ and σ' upon hopping from site $\boldsymbol{i}$ to site $\boldsymbol{j}$. This extends the standard Hubbard model in Eq. (1.18):

$$\hat{H} = \sum_{\langle \boldsymbol{ij}\rangle\sigma\sigma'} t_{\boldsymbol{ij}}^{\sigma\sigma'} \hat{c}_{\boldsymbol{i}\sigma}^{\dagger} \hat{c}_{\boldsymbol{j}\sigma'} + U \sum_{\boldsymbol{i}} \hat{c}_{\boldsymbol{i}\uparrow}^{\dagger} \hat{c}_{\boldsymbol{i}\uparrow} \hat{c}_{\boldsymbol{i}\downarrow}^{\dagger} \hat{c}_{\boldsymbol{i}\downarrow}. \tag{3.1}$$

The system is fully described by the partition function expressed in the path integral formalism as

$$\mathcal{Z} = \int \prod_{\boldsymbol{i}\sigma} Dc_{\boldsymbol{i}\sigma}^{*} Dc_{\boldsymbol{i}\sigma} \exp\left\{-S[c_{\boldsymbol{i}\sigma}^{*}, c_{\boldsymbol{i}\sigma}]\right\}. \tag{3.2}$$

Here, the action $S[c^*_{i\sigma}, c_{i\sigma}]$ is a functional of the Grassmann variables $c_{i\sigma}$ and $c^*_{i\sigma}$, such that

$$S[c^*_{i\sigma}, c_{i\sigma}] = \int_0^\beta d\tau \left\{ c^*_{i\sigma}(\tau) \left(\partial_\tau - \mu\right) c_{i\sigma}(\tau) + H[c^*_{i\sigma}(\tau), c_{i\sigma}(\tau)] \right\}, \tag{3.3}$$

where $\beta = 1/T$ is the inverse temperature and $H[c^*_{i\sigma}, c_{i\sigma}]$ corresponds to the Hamiltonian with the field operators $\hat{c}_{i\sigma}$ ($\hat{c}^\dagger_{i\sigma}$) being replaced by the corresponding Grassmann variables $c_{i\sigma}$ ($c^*_{i\sigma}$). Note that even though the Grassmann variables $c_{i\sigma}$ ($c^*_{i\sigma}$) describe annihilation (creation) of particles, they are treated as independent variables. In the following, we drop the imaginary time argument for the sake of readability.

We can define an effective action $S_{\text{eff}}[c^*_{o\sigma}, c_{o\sigma}]$ which is a functional of Grassmann variables at site $\boldsymbol{o}$ only. This can be achieved by integrating out all other Grassmann variables $c_{i\sigma}$ and $c^*_{i\sigma}$ with $\boldsymbol{i} \neq \boldsymbol{o}$:

$$\frac{1}{\mathcal{Z}_{\text{eff}}} \exp\left\{-S_{\text{eff}}[c^*_{o\sigma}, c_{o\sigma}]\right\} = \frac{1}{\mathcal{Z}} \int \prod_{i \neq o, \sigma} Dc^*_{i\sigma} Dc_{i\sigma} \exp\left\{-S[c^*_{i\sigma}, c_{i\sigma}]\right\} \tag{3.4}$$

where we introduced

$$\mathcal{Z}_{\text{eff}} = \int \prod_{\sigma} Dc^*_{o\sigma} Dc_{o\sigma} \exp\left\{-S_{\text{eff}}[c^*_{o\sigma}, c_{o\sigma}]\right\}. \tag{3.5}$$

In order to find a formal expression for the effective action we split the original action $S[c^*_{i\sigma}, c_{i\sigma}]$ into three parts:

$$S = S_{\boldsymbol{o}} + S^{(\boldsymbol{o})} + \Delta S, \tag{3.6}$$

where we omitted the functional arguments to have a compact form of the equation. Therein,

$$S_{\boldsymbol{o}} = \int_0^\beta d\tau \left[\sum_\sigma c^*_{o\sigma}(\partial_\tau - \mu) c_{o\sigma} + U c^*_{o\uparrow} c_{o\uparrow} c^*_{o\downarrow} c_{o\downarrow} \right] \tag{3.7}$$

is the local action which only contains Grassmann variables associated with the site $\boldsymbol{o}$. Both $S_{\boldsymbol{o}}$ and the effective action are local. The latter, however, contains the information of the rest of the lattice due to the integration of the respective Grassmann variables. In the cavity action

$$S^{(\boldsymbol{o})} = -\int_0^\beta d\tau \sum_{i \neq o, \sigma} \sum_{j \neq o, \sigma'} \left(t^{\sigma\sigma'}_{ij} c^*_{i\sigma} c_{j\sigma'} + t^{\sigma'\sigma}_{ji} c^*_{j\sigma'} c_{i\sigma} \right) \tag{3.8}$$

there are only Grassmann variables of the lattice excluding the site $\boldsymbol{o}$. Finally, the coupling between site $\boldsymbol{o}$ and the rest of the lattice is described by the action

$$\Delta S = -\int_0^\beta d\tau \sum_{i \neq o, \sigma} \sum_{\sigma'} \left(t^{\sigma\sigma'}_{io} c^*_{i\sigma} c_{o\sigma'} + t^{\sigma'\sigma}_{oi} c^*_{o\sigma'} c_{i\sigma} \right). \tag{3.9}$$

After integrating out the Grassmann variables of the sites $\boldsymbol{i} \neq \boldsymbol{o}$, we find for the effective action [211, 219–221]:

$$\begin{aligned} S_{\text{eff}}[c^*_{\boldsymbol{o}\sigma}, c_{\boldsymbol{o}\sigma}] = &\sum_{n=1}^{\infty} \sum_{\substack{\boldsymbol{i}_1,\dots\boldsymbol{i}_n \\ \sigma_1,\dots\sigma_n}} \sum_{\substack{\boldsymbol{j}_1,\dots\boldsymbol{j}_n \\ \sigma'_1,\dots\sigma'_n}} \int d\tau_1 \dots d\tau_n d\tau'_1 \dots d\tau'_n \\ &\times \eta^*_{\boldsymbol{i}_1,\sigma_1}(\tau_1) \dots \eta^*_{\boldsymbol{i}_n,\sigma_n}(\tau_n) \eta_{\boldsymbol{j}_1,\sigma'_1}(\tau'_1) \dots \eta_{\boldsymbol{j}_n,\sigma'_n}(\tau'_n) \\ &\times G^{(\boldsymbol{o})}{}^{\sigma_1,\dots\sigma_n,\sigma'_1,\dots\sigma'_n}_{\boldsymbol{i}_1,\dots\boldsymbol{i}_n,\boldsymbol{j}_1,\dots\boldsymbol{j}_n}\left(\tau_1, \dots \tau_n, \tau'_1, \dots \tau'_n\right) + S_{\boldsymbol{o}} + \text{const.} \end{aligned} \tag{3.10}$$

where $\eta_{\boldsymbol{i},\sigma}(\tau) = \sum_{\sigma'} t^{\sigma\sigma'}_{\boldsymbol{io}} c_{\boldsymbol{o}\sigma'}(\tau)$ acts as a source field coupled to the Grassmann variables $c_{\boldsymbol{i}\sigma}(\tau)$ in the rest of the system $\boldsymbol{i} \neq \boldsymbol{o}$. The $2n$-point correlator $G^{(\boldsymbol{o})}{}^{\sigma_1,\dots\sigma_n,\sigma'_1,\dots\sigma'_n}_{\boldsymbol{i}_1,\dots\boldsymbol{i}_n,\boldsymbol{j}_1,\dots\boldsymbol{j}_n}(\tau_1, \dots \tau_n, \tau'_1, \dots \tau'_n)$ is the connected Green's function associated with the cavity Hamiltonian. The cavity Hamiltonian corresponds to the full Hamiltonian with the site $\boldsymbol{o}$ and all couplings to it being removed.

Up to Eq. (3.10) the theory is valid in any dimension d. Computing a $2n$-point correlator with n going to infinity is of course not feasible. In the following, we show that Eq. (3.10) simplifies in the limit of infinite dimensions, i.e., $d \to \infty$, according to the original works in Refs. [208, 209]. The noninteracting density of states is given as

$$\rho(\epsilon) = \sum_{\boldsymbol{k}} \delta(\epsilon - E(\boldsymbol{k})), \tag{3.11}$$

where $E(\boldsymbol{k})$ corresponds to the energy spectrum of the lattice system. Here, we assume a d-dimensional hyper-cubic dispersion with generalized hopping amplitudes $E(\boldsymbol{k}) = -2\sum_{m=1}^{d} t_m \cos(k_m)$. The Fourier transform of $\rho(\epsilon)$ with respect to the energy ϵ yields

$$\begin{aligned} \Phi(s) &= \int d\epsilon e^{is\epsilon} \rho(\epsilon) = \int d\epsilon e^{is\epsilon} \sum_{\boldsymbol{k}} \delta(\epsilon - E(\boldsymbol{k})) \\ &= \sum_{\boldsymbol{k}} \int d\epsilon e^{is\epsilon} \delta(\epsilon - E(\boldsymbol{k})) = \sum_{\boldsymbol{k}} e^{isE(\boldsymbol{k})} = \sum_{\boldsymbol{k}} e^{-2is\sum_m t_m \cos(k_m)} \\ &= \sum_{\boldsymbol{k}} \prod_m e^{-2ist_m \cos(k_m)} = \prod_m \sum_{k_m} e^{-2ist_m \cos(k_m)} \end{aligned} \tag{3.12}$$

where we have used the hyper-cubic lattice dispersion $E(\boldsymbol{k})$ and the fact that it factorizes. We now utilize $\sum_{k_m} \to 1/(2\pi) \int_{-\pi}^{\pi} dk_m$ and find

$$\Phi(s) = \frac{1}{(2\pi)^d} \prod_m \int_{-\pi}^{\pi} dk_m e^{-2ist_m \cos(k_m)} = \prod_m J_0(2st_m), \tag{3.13}$$

where $J_0(x)$ is the Bessel function of the first kind. Expanding the Bessel function around $s = 0$, we find

$$J_0(2st_m) \approx 1 - \frac{(st_m)^2}{4} \approx e^{-(st_m/2)^2} \tag{3.14}$$

and thus

$$\Phi(s) \approx \prod_{m=1}^{d} e^{-(st_m/2)^2} = \exp\left\{-d\left(\frac{st}{2}\right)^2\right\}, \tag{3.15}$$

where we have used in the second equation the average of generalized hoppings $t^2 = \sum_m t_m^2/d$ [209]. Taking into account the proper normalization, the back transform of Eq. (3.15) yields

$$\rho(\epsilon) = \frac{1}{\sqrt{2\pi(t^2 d/2)}} \exp\left\{\frac{-\epsilon^2}{2(t^2 d/2)}\right\}. \tag{3.16}$$

Here, we observe that a nontrivial expression for the density of states is achieved only if we fix the value for $t^* = \sqrt{2d}t$ when performing the limit $d \to \infty$. Thus, we find that the physical hopping energy must scale as $t \sim d^{-1/2}$.

Coming back to Eq. (3.10), it turns out that there are three instances which determine the scaling in d of a term of order n [41]: The first instance is the number of independent summations which scales as d^m, where $0 \leq m \leq 2n$. The second instance is the connected Green's function which scales as d^{1-m}. Eventually, since the $2n$ source fields are proportional to the hopping t, they contribute as $t^{2n} \sim d^{-n}$. We conclude that the scaling of a term of order n is $d^m \times d^{1-m} \times d^{-n} \sim d^{1-n}$. Thus, in the limit $d \to \infty$, only the first term $n = 1$ will survive. Applying this limit, the effective action reads

$$\begin{aligned} S_{\text{eff}}[c^*_{\boldsymbol{o}\sigma}, c_{\boldsymbol{o}\sigma}] = \\ &\sum_{\sigma\sigma'} \int_0^\beta d\tau_1 \int_0^\beta d\tau_2\, c^*_{\boldsymbol{o}\sigma}(\tau_1)\, (\partial_\tau - \mu)\, \delta(\tau_1 - \tau_2)\delta_{\sigma,\sigma'} c_{\boldsymbol{o}\sigma'}(\tau_2) \\ &+ \sum_{\sigma\sigma'} \int_0^\beta d\tau_1 \int_0^\beta d\tau_2\, c^*_{\boldsymbol{o}\sigma}(\tau_1) \sum_{\boldsymbol{ij}\tilde{\sigma}\tilde{\sigma}'} t^{\tilde{\sigma}\sigma}_{\boldsymbol{io}} t^{\sigma'\tilde{\sigma}'}_{\boldsymbol{oj}} G^{(o)}{}^{\tilde{\sigma}\tilde{\sigma}'}_{\boldsymbol{ij}}(\tau_1 - \tau_2) c_{\boldsymbol{o}\sigma'}(\tau_2) \\ &+ U \int_0^\beta d\tau c^*_{\boldsymbol{o}\uparrow}(\tau) c_{\boldsymbol{o}\uparrow}(\tau) c^*_{\boldsymbol{o}\downarrow}(\tau) c_{\boldsymbol{o}\downarrow}(\tau) \end{aligned} \tag{3.17}$$

where $\delta(\tau)$ and $\delta_{\sigma,\sigma'}$ are the Dirac distribution function and the Kronecker delta, respectively. Furthermore, $G^{(o)}{}^{\tilde{\sigma}\tilde{\sigma}'}_{\boldsymbol{ij}}(\tau)$ denotes the single-particle cavity Green's function which includes the whole lattice except the lattice site $\boldsymbol{o}$. After applying a Fourier transformation

$$f(\tau) = \frac{1}{\beta}\sum_n f(i\omega_n) e^{-i\tau\omega_n}, \tag{3.18}$$

with the fermionic Matsubara frequencies $\omega_n = 2\pi(2n+1)/\beta$, we find the so-called dynamical Weiss field

$$\mathcal{G}^{-1}{}^{\sigma\sigma'}(i\omega_n) = (i\omega_n + \mu)\delta_{\sigma,\sigma'} + \sum_{\boldsymbol{ij}\tilde{\sigma}\tilde{\sigma}'} t^{\tilde{\sigma}\sigma}_{\boldsymbol{io}} t^{\sigma'\tilde{\sigma}'}_{\boldsymbol{oj}} G^{(o)}{}^{\tilde{\sigma}\tilde{\sigma}'}_{\boldsymbol{ij}}(i\omega_n). \tag{3.19}$$

We express the Matsubara cavity Green's function ${G^{(o)}}_{\boldsymbol{ij}}^{\tilde\sigma\tilde\sigma'}(i\omega_n)$, in terms of the lattice Green's function which can be achieved by expanding around the atomic limit of the site $\boldsymbol{o}$ [211], such that

$$ {G^{(o)}}_{\boldsymbol{ij}}^{\tilde\sigma\tilde\sigma'}(i\omega_n) = \left[\boldsymbol{G_{ij}}(i\omega_n) - \boldsymbol{G_{io}}(i\omega_n)\boldsymbol{G_{oo}}^{-1}(i\omega_n)\boldsymbol{G_{oj}}(i\omega_n)\right]^{\tilde\sigma\tilde\sigma'}, \tag{3.20} $$

where we introduced the spin notation with the bold-face quantities being 2×2 matrices in spin space:

$$ \boldsymbol{G_{ij}} = \begin{pmatrix} G_{\boldsymbol{ij}}^{\uparrow\uparrow} & G_{\boldsymbol{ij}}^{\uparrow\downarrow} \\ G_{\boldsymbol{ij}}^{\downarrow\uparrow} & G_{\boldsymbol{ij}}^{\downarrow\downarrow} \end{pmatrix} \quad \text{and} \quad \boldsymbol{T_{ij}} = \begin{pmatrix} t_{\boldsymbol{ij}}^{\uparrow\uparrow} & t_{\boldsymbol{ij}}^{\uparrow\downarrow} \\ t_{\boldsymbol{ij}}^{\downarrow\uparrow} & t_{\boldsymbol{ij}}^{\downarrow\downarrow} \end{pmatrix}. \tag{3.21} $$

We focus on the last term of Eq. (3.19):

$$ \sum_{\boldsymbol{ij}\tilde\sigma\tilde\sigma'} t_{\boldsymbol{io}}^{\tilde\sigma\sigma} t_{\boldsymbol{oj}}^{\sigma'\tilde\sigma'} {G^{(o)}}_{\boldsymbol{ij}}^{\tilde\sigma\tilde\sigma'}(i\omega_n) = \sum_{\boldsymbol{ij}} \left[\boldsymbol{T_{io}G_{ij}T_{oj}} - \boldsymbol{T_{io}G_{io}G_{oo}}^{-1}\boldsymbol{G_{oj}T_{oj}}\right]^{\sigma\sigma'} \tag{3.22} $$

where we dropped the Matsubara frequency argument of the $\boldsymbol{G_{ij}}$ for better readability. The Green's function is Fourier transformed between real and momentum space as

$$ \boldsymbol{G_{ij}} = \frac{1}{2\pi}\sum_{\boldsymbol{k}} e^{i\boldsymbol{R_{ij}k}}\boldsymbol{G_k}, \tag{3.23} $$

where $\boldsymbol{R_{ij}}$ is the real-space vector connecting site $\boldsymbol{i}$ and $\boldsymbol{j}$. In order to simplify Eq. (3.22), we compute

$$ \begin{aligned} \sum_{\boldsymbol{i}} \boldsymbol{T_{io}G_{io}} &= \frac{1}{2\pi}\sum_{\boldsymbol{k}}\left[\sum_{\boldsymbol{i}} e^{i\boldsymbol{R_{io}k}}\boldsymbol{T_{io}}\right]\boldsymbol{G_k} = \frac{1}{2\pi}\sum_{\boldsymbol{k}}\boldsymbol{E_k G_k} \\ &= \frac{1}{2\pi}\sum_{\boldsymbol{k}}\left(\boldsymbol{\xi} - \boldsymbol{G_k}^{-1}\right)\boldsymbol{G_k} = \frac{1}{2\pi}\sum_{\boldsymbol{k}}\left(\boldsymbol{\xi G_k} - \mathbf{1}\right) = \boldsymbol{\xi G_{oo}} - \mathbf{1}. \end{aligned} \tag{3.24} $$

Here, $\boldsymbol{E_k}$ is the 2×2 energy spectrum which results from the Fourier transform of the hopping matrix element representing the noninteracting Hamiltonian. We have also introduced the abbreviation $\boldsymbol{\xi} = (i\omega_n + \mu)\mathbf{1} - \boldsymbol{\Sigma}(i\omega_n)$ according to Eq. (1.19), where $\boldsymbol{\Sigma}(i\omega_n)$ is the 2×2 matrix of the local selfenergies $\Sigma^{\sigma\sigma'}(i\omega_n)$. Analogously, we find

$$ \sum_{\boldsymbol{j}} \boldsymbol{G_{oj}T_{oj}} = \boldsymbol{G_{oo}\xi} - \mathbf{1} \tag{3.25} $$

and

$$\begin{aligned}\sum_{ij} \boldsymbol{T}_{io}\boldsymbol{G}_{ij}\boldsymbol{T}_{oj} &= \sum_{ij} \boldsymbol{T}_{io}\left[\frac{1}{2\pi}\sum_k e^{iR_{ij}k}\boldsymbol{G}_k\right]\boldsymbol{T}_{oj} \\ &= \frac{1}{2\pi}\sum_k\left[\sum_i e^{iR_{io}k}\boldsymbol{T}_{io}\right]\boldsymbol{G}_k\left[\sum_i e^{iR_{oj}k}\boldsymbol{T}_{oj}\right] \\ &= \frac{1}{2\pi}\sum_k \boldsymbol{E}_k\boldsymbol{G}_k\boldsymbol{E}_k = \frac{1}{2\pi}\sum_k\left(\boldsymbol{\xi}-\boldsymbol{G}_k^{-1}\right)\boldsymbol{G}_k\boldsymbol{E}_k \\ &= \frac{1}{2\pi}\boldsymbol{\xi}\sum_k \boldsymbol{G}_k\boldsymbol{E}_k - \frac{1}{2\pi}\sum_k \boldsymbol{E}_k = \boldsymbol{\xi}(\boldsymbol{G}_{oo}\boldsymbol{\xi}-\mathbf{1}),\end{aligned} \tag{3.26}$$

where we have used Eq. (3.25) in the last equation and the fact that the term $1/(2\pi)\sum_k \boldsymbol{E}_k$ can be absorbed into the chemical potential. Plugging Eqs. (3.24)–(3.26) into Eq. (3.22) yields

$$\boldsymbol{\xi}(\boldsymbol{G}_{oo}\boldsymbol{\xi}-\mathbf{1}) - (\boldsymbol{\xi}\boldsymbol{G}_{oo}-\mathbf{1})\boldsymbol{G}_{oo}^{-1}(\boldsymbol{G}_{oo}\boldsymbol{\xi}-\mathbf{1}) = \boldsymbol{\xi} - \boldsymbol{G}_{oo}^{-1}, \tag{3.27}$$

and we find for the dynamical Weiss field in Eq. (3.19) that

$$\begin{aligned}[\mathcal{G}^{-1}(i\omega_n)]^{\sigma\sigma'} &= (i\omega_n+\mu)\delta_{\sigma\sigma'} - \xi^{\sigma\sigma'}(i\omega_n) + [G_{\boldsymbol{oo}}^{-1}(i\omega_n)]^{\sigma\sigma'} \\ &= \Sigma^{\sigma\sigma'}(i\omega_n) + [G_{\boldsymbol{oo}}^{-1}(i\omega_n)]^{\sigma\sigma'},\end{aligned} \tag{3.28}$$

which is named the local Dyson equation and is one of the DMFT equations. The mapping to an impurity model yields the next DMFT equation.

3.1.2 Anderson impurity model

The Anderson impurity model (AIM) is known since 1961 [222]. It describes an impurity coupled to a bath of fermions. The fermions can only interact at the impurity site and are noninteracting in the bath. The models, we are interested in, feature a spin-mixing hopping amplitude which is not considered in the original AIM. The Hamiltonian of the generalized AIM reads

$$\begin{aligned}\hat{H}_{\text{AIM}} = &\sum_{k\sigma\sigma'}\epsilon_k^{\sigma\sigma'}\hat{a}^\dagger_{k\sigma}\hat{a}_{k\sigma'} - \mu\sum_\sigma \hat{c}^\dagger_\sigma\hat{c}_\sigma + U\hat{c}^\dagger_\uparrow\hat{c}_\uparrow\hat{c}^\dagger_\downarrow\hat{c}_\downarrow \\ &+ \sum_{k\sigma}\left[V_{k\sigma}\hat{a}^\dagger_{k\sigma}\hat{c}_\sigma + V^*_{k\sigma}\hat{a}_{k\sigma}\hat{c}^\dagger_\sigma + W_{k\sigma}\hat{a}^\dagger_{k\sigma}\hat{c}_{\bar{\sigma}} + W^*_{k\sigma}\hat{a}_{k\sigma}\hat{c}^\dagger_{\bar{\sigma}}\right],\end{aligned} \tag{3.29}$$

where the noninteracting fermions in the bath are described by the operators $\hat{a}_{k\sigma}$ and dispersion $\epsilon_k^{\sigma\sigma'}$. At the impurity, the fermions interact and are described by the operators $\hat{c}_\sigma$. The amplitudes $V_{k\sigma}$ and $W_{k\sigma}$ describe the spin-conserving and spin-mixing coupling between bath and impurity, respectively. The bar notation applies as $\bar{\uparrow}=\downarrow$ and $\bar{\downarrow}=\uparrow$.

As in Sec. 3.1.1, we construct the partition function as a path integral and compute a local effective action

$$\begin{aligned}\mathcal{Z} &= \int \left(\prod_{i\sigma} Da^*_{i\sigma} Da_{i\sigma}\right)\left(\prod_{\sigma} Dc^*_{\sigma} Dc_{\sigma}\right) \exp(-S[a^*_{i\sigma}, a_{i\sigma}, c^*_{\sigma}, c_{\sigma}]) \\ &= \int \prod_{\sigma} Dc^*_{\sigma} Dc_{\sigma} \exp(-S_{\text{eff}}[c^*_{\sigma}, c_{\sigma}]),\end{aligned} \tag{3.30}$$

where the effective action for the AIM reads

$$\begin{aligned}S_{\text{eff}}[c^*_{\sigma}, c_{\sigma}] = &\sum_{\sigma\sigma'} \int_0^{\beta} d\tau_1 \int_0^{\beta} d\tau_2 \left\{ c^*_{\sigma}(\tau_1) \mathcal{G}^{-1^{\sigma\sigma'}}(\tau_1 - \tau_2) c_{\sigma'}(\tau_2) \right\} \\ &+ U \int_0^{\beta} d\tau c^*_{\uparrow}(\tau) c_{\uparrow}(\tau) c^*_{\downarrow}(\tau) c_{\downarrow}(\tau),\end{aligned} \tag{3.31}$$

where eventually the dynamical Weiss field is given as [190]:

$$\mathcal{G}^{-1^{\sigma\sigma}}(i\omega_n) = i\omega_n + \mu - \sum_{\boldsymbol{k}} \frac{|V_{\boldsymbol{k}}|^2 + |W_{\boldsymbol{k}}|^2}{i\omega_n - \epsilon^{\sigma\sigma}_{\boldsymbol{k}}} \tag{3.32}$$

$$\mathcal{G}^{-1^{\sigma\bar{\sigma}}}(i\omega_n) = -\sum_{\boldsymbol{k}} \frac{V^*_{\boldsymbol{k}} W_{\boldsymbol{k}} + W^*_{\boldsymbol{k}} V_{\boldsymbol{k}}}{i\omega_n - \epsilon^{\sigma\bar{\sigma}}_{\boldsymbol{k}}} \tag{3.33}$$

These equations define an impurity problem which is solved by methods reviewed in Sec. 3.1.4. The solution manifests in the selfenergy $\Sigma(i\omega_n)$. Solving an inhomogeneous system or a system with an extended unit cell provides different local selfenergies $\Sigma_{\boldsymbol{i}}(i\omega_n)$ for each site $\boldsymbol{i}$. These can be handled in the real-space DMFT algorithm.

3.1.3 Real-space DMFT

Let us consider a set of local selfenergies $\Sigma_{\boldsymbol{i}}(i\omega_n)$ as an initial guess for the real-space DMFT procedure. This is inserted into the lattice Dyson equation which contains the interacting and the noninteracting single-particle Green's functions:

$$G^{-1}{}_{\boldsymbol{ij}}(i\omega_n) = G_0^{-1}{}_{\boldsymbol{ij}}(i\omega_n) - \delta_{\boldsymbol{ij}} \Sigma_{\boldsymbol{i}}(i\omega_n). \tag{3.34}$$

Here, $G_0^{-1}{}_{\boldsymbol{ij}}(i\omega_n)$ denotes the noninteracting lattice Green's function which is constructed from the noninteracting Hamiltonian via Eq. (1.19) and zero selfenergy. The resulting Green's function from Eq. (3.34) is inverted to obtain the local Green's functions as $G(i\omega_n)|_{\boldsymbol{ii}} = G_{\boldsymbol{ii}}(i\omega_n)$. Using the local Dyson equation defined in Eq. (3.28) we find again a dynamical Weiss field which maps onto an impurity problem through Eqs. (3.32) and (3.33). From these impurity problems, we obtain a new set of local selfenergies with which we start over from the beginning. This self-consistent procedure is repeated until convergence. Computationally the most expensive steps are the matrix inversion of the lattice Green's function and solving the AIM which we will review in the next section. The inversion can become costly since a full lattice Green's function has to be inverted. One has to be careful in choosing a proper system size since matrix inversion of an $n \times n$ matrix scales with the third power in n. This scaling can of course be optimized depending on the properties of the specific case.

3.1.4 Solvers

In DMFT solvers are used to solve the AIM which appears once per site per iteration. Common solvers are the iterative perturbation theory [223], numerical renormalization group [224,225], exact diagonalization [226], and quantum Monte Carlo [227,228]. We will only review the last two methods since they have applications in this work.

Exact diagonalization

The AIM, as introduced in Eq. (3.29), features a bath with infinitely many sites. In exact diagonalization (ED) the AIM is approximated by an impurity interacting with a bath with a finite number of bath sites N_b [226]. The procedure works as follows: For a given set of data for the Weiss field as a function of frequency, one performs a numerical fit with the fit functions in Eqs. (3.32) and (3.33). From this, one obtains the coefficients for the AIM, i.e., $\{V_{\boldsymbol{k}}, W_{\boldsymbol{k}}, \epsilon_{\boldsymbol{k}}^{\sigma\sigma'}\}$. This can be a numerical bottleneck since the fitting procedure might suffer from bad convergence. In the present case, this means the following. The parameters $V_{\boldsymbol{k}}$ and $W_{\boldsymbol{k}}$ are both complex-valued leading to four free variables. In the parameter $\epsilon_{\boldsymbol{k}}^{\sigma\sigma'}$ there are four variables encoded due to hermiticity. For systems with balanced hopping amplitudes between the two spin states, we can assume that $\epsilon_{\boldsymbol{k}}^{\uparrow\uparrow} = \epsilon_{\boldsymbol{k}}^{\downarrow\downarrow}$. This leads to a total number of seven free variables per bath site. Consequently, the fitting function is a function of $7N_b$ variables. This large number diminishes the success of a converged fit. Additionally, fitting routines depend on an initial guess for the parameter set. In most of the calculations in the context of this work we choose a random initial guess of a uniform distribution between 0 and 1. Depending on the system of interest, one should use more elaborate initial guesses in order to work out a numerically stable algorithm.

For a given N_b, we can choose an occupation number basis to represent the state vector of our approximate impurity problem

$$|\Psi_l\rangle = |n_0^{\uparrow}, n_0^{\downarrow}, n_1^{\uparrow}, n_1^{\downarrow}, \ldots, n_{N_b}^{\uparrow}, n_{N_b}^{\downarrow}\rangle, \tag{3.35}$$

where $n_i^{\sigma} = 0, 1$ is the occupation number of a fermion on site i with spin σ [211]. We observe that the Hilbert space of the basis in Eq. (3.35) has dimension 4^{N_b+1} since there are four fermionic states per site and the system contains N_b bath sites and one impurity site. The index l labels these 4^{N_b+1} states. The Hamiltonian matrix H_{AIM} is then constructed through the matrix elements

$$H_{\mathrm{AIM}}|_{lm} = \langle \Psi_l | \hat{H}_{\mathrm{AIM}} | \Psi_m \rangle, \tag{3.36}$$

and can be diagonalized using standard routines. Note, that the basis in Eq. (3.35) cannot be factorized in the spin degree of freedom as for example in Ref. [211]. This is because our system allows for spin mixing in contrast to the usually discussed spin-conserving Hubbard model. The drawback is that a larger Hamiltonian has to be diagonalized. Since dense diagonalization routines scale approximately with the third power in n for $n \times n$ matrices, the slow down is of factor eight. After diagonalization, we are left with the eigenvectors $|E_p\rangle$ and their associated energies E_p. The impurity Green's function is now computed as [157,211]

$$G(i\omega_n) = \sum_{pq} \frac{(\langle E_p | \hat{c}^\dagger | E_q \rangle)^2}{E_p - E_q - i\omega_n} \left[e^{-\beta E_p} + e^{-\beta E_q} \right] / \sum_{pq} \left[e^{-\beta E_p} + e^{-\beta E_q} \right]. \tag{3.37}$$

Here, the operator $\hat{c}^\dagger$ connects an N-particle state with an $N+1$-particle state. The impurity Green's function is then used to compute the selfenergy through the local Dyson equation in Eq. (3.28).

Throughout this work, we solely perform finite-temperature calculations. This means, that we need the full set of eigenvectors from the ED algorithm. If one is interested in zero-temperature results only, the Lanczos algorithm is commonly used to find the groundstate of a Hamiltonian matrix numerically [229].

Continuous-time quantum Monte Carlo

In the quantum Monte Carlo technique (QMC) the AIM problem is solved numerically exactly and thereby differs from ED where an approximation of a finite bath is made. The Monte Carlo sampling, which is rooted in the famous Metropolis algorithm [230], is applied to the effective action of the AIM in Eq. (3.31). For a long time, the best method was the Hirsch-Fye algorithm [231]. It introduces an equidistant discretization of the imaginary time variable τ and a subsequent Hubbard-Stratonovich transformation. This decouples the original fermionic degrees of freedom and introduces new Ising-type spin degrees of freedom. These variables are then sampled during the Monte Carlo process. The drawback of the Hirsch-Fye algorithm is its equidistant discretization since the Green's function, as a function of imaginary time, evolves features, e.g., spikes at $\tau = 0, \beta$. These features are hard to capture at low temperatures which makes the algorithm inefficient under such circumstances.

Continuous-time quantum Monte Carlo (CT-QMC) methods [228,232, 233] do not base on an equidistant discretization of the time axis but rather allow for time steps of arbitrary size. We follow Ref. [228] which will suffice for an overview on the CT-QMC methods. For a more detailed description consult, e.g., the theses by Buchhold [234] or Panas [235]. In this work, only the auxiliary field expansion of CT-QMC (CT-AUX) [236,237] will be used which we will recapitulate in the following. Two other expansions are the interaction expansion (CT-INT) which is a weak-coupling expansion in the interaction term. *Weak* coupling, in this case, does not imply that the algorithm fails at describing strong interactions. It rather becomes inefficient at strong interactions since numerous terms have to enter the expansion. The third expansion is the hybridization expansion (CT-HYB) where the expansion is performed in the hybridization function. All variations have different advantages depending on the very system. CT-AUX is also a weak coupling expansion, however, a Hubbard-Stratonovich transformation is applied to decouple the interaction term first such that one is left with auxiliary fields from the transformation. We start with the partition function for a system with Hamiltonian $\hat{H}_0 + \hat{H}_1$ with $\hat{H}_0$ being the diagonal part of the Hamiltonian. The interaction representation of the partition function is [238]

$$\mathcal{Z} = \mathrm{Tr} e^{-\beta \hat{H}_0} \sum_{k=0}^{\infty} (-1)^k \int_{\tau_{k-1}}^{\beta} d\tau_k \cdots \int_0^{\beta} d\tau_1 \hat{H}_1(\tau_k) \ldots \hat{H}_1(\tau_1), \tag{3.38}$$

where $\hat{H}_1(\tau) = e^{\tau \hat{H}_0} \hat{H}_1 e^{-\tau \hat{H}_0}$. We set $\hat{H}_1 = \hat{V} - K/\beta$, where K is a constant, i.e., a shift of the chemical potential, and

$$\hat{V} = U \sum_{\boldsymbol{i}} \left(\hat{n}_{\uparrow \boldsymbol{i}} \hat{n}_{\downarrow \boldsymbol{i}} - \frac{\hat{n}_{\uparrow \boldsymbol{i}} + \hat{n}_{\downarrow \boldsymbol{i}}}{2} \right) \tag{3.39}$$

is equivalent to to the Hubbard interaction up to another shift of the chemical potential by the average filling. For the AIM the sum over all lattice sites is obsolete, so we drop the index $\boldsymbol{i}$. We find for the partition function

$$\begin{aligned} \mathcal{Z} = \sum_{k=0}^{\infty} (-1)^k \int_{\tau_{k-1}}^{\beta} d\tau_k \cdots \int_0^{\beta} d\tau_1 \\ \times \mathrm{Tr} e^{-\beta \hat{H}_0} e^{\tau_k \hat{H}_0} \left(\hat{V} - K/\beta \right) e^{-\tau_k \hat{H}_0} \ldots e^{\tau_1 \hat{H}_0} \left(\hat{V} - K/\beta \right) e^{-\tau_1 \hat{H}_0} \end{aligned} \tag{3.40}$$

and subsequently

$$\begin{aligned} \mathcal{Z} = \sum_{k=0}^{\infty} \left(\frac{K}{\beta} \right)^k \int_{\tau_{k-1}}^{\beta} d\tau_k \cdots \int_0^{\beta} d\tau_1 \\ \times \mathrm{Tr} e^{-(\beta - \tau_k)\hat{H}_0} \left(1 - \frac{\beta \hat{V}}{K} \right) e^{-(\tau_k - \tau_{k-1})\hat{H}_0} \ldots \\ e^{-(\tau_2 - \tau_1)\hat{H}_0} \left(1 - \frac{\beta \hat{V}}{K} \right) e^{-\tau_1 \hat{H}_0}. \end{aligned} \tag{3.41}$$

The interaction terms are then decoupled through [236]

$$1-\frac{\beta\hat{V}}{K}=\frac{1}{2}\sum_{s=-1,1}e^{\gamma s(\hat{n}_\uparrow-\hat{n}_\downarrow)}\quad\text{with}\quad\cosh\gamma=1+\frac{\beta U}{2K}. \tag{3.42}$$

This leads us to

$$\mathcal{Z}=\sum_{k=0}^{\infty}\sum_{q=0}^{k}\sum_{s_q=-1,1}\int_{\tau_{k-1}}^{\beta}d\tau_k\cdots\int_0^{\beta}d\tau_1\left(\frac{K}{2\beta}\right)^k Z_k(\{s_q,\tau_q\}), \tag{3.43}$$

with

$$Z_k(\{s_q,\tau_q\})=\mathrm{Tr}\prod_{q=1}^{k}e^{-(\tau_q-\tau_{k-1})\hat{H}_0}e^{\gamma s_q(\hat{n}_\uparrow-\hat{n}_\downarrow)}. \tag{3.44}$$

Monte Carlo sampling can now be performed on the variables $\{s_q,\tau_q\}$. The procedure works as follows. At first, it is initialized with a random configuration of $\{s_q,\tau_q\}$. The configuration is then updated with probability of 0.5 by an insertion or with probability of 0.5 by a removal of a so-called vertex, i.e., a new spin s is inserted at imaginary time τ or an existing spin is removed. The update is accepted with a probability determined by the Metropolis algorithm [230]. The process is repeated until the desired tolerance of the observable is reached.

The perturbation order $\langle k\rangle$ which is the mean number of vertices introduced in the sampling is linear in the interaction strength U [237]. This makes the CT-AUX algorithm computationally more demanding for larger U. Thus, for large U the CT-HYB is the better choice [239].

3.2 Maximum entropy method

The maximum entropy method to analytically continue QMC data was introduced by Jarrell and Gubernatis in 1996 [240]. As discussed above, observables, e.g., the Green's function $G(\tau)$, computed by QMC methods usually are functions of imaginary time τ since the sampling of the imaginary time axis is restricted to the interval $[0,\beta]$. However, the dynamical, physical properties are embedded in the Green's function as function of real frequencies $G(\omega)$, especially, in the spectral function $A(\omega)=-\mathrm{Im}G(\omega)/\pi$. It is connected to the imaginary-time Green's function through

$$G(\tau)=\int d\omega\frac{e^{-\tau\omega}}{1\pm e^{-\beta\omega}}A(\omega), \tag{3.45}$$

where the positive (negative) sign applies for fermions (bosons). The aim is to invert this equation, i.e., to find $A(\omega)$ in terms of a given $G(\tau)$. This could be done with standard fitting methods. This means one has to minimize a likelihood function which measures the distance between the numerical data for $G(\tau)$ and the prescription in Eq. (3.45) as a function of $A(\omega)$. Starting from an initial guess for $A(\omega)$ one would then iteratively minimize the likelihood function until convergence. This would be a simple approach, however, the exponential $e^{-\tau\omega}$ in Eq. (3.45) suppresses the large frequency behavior of $A(\omega)$. This results in a noisy and nonunique result for $A(\omega)$ since $G(\tau)$ already comes with noise due to the QMC sampling. Thus, inverting Eq. (3.45) even with small noise in $G(\tau)$ is an ill-defined problem because it is not uniquely defined. In order to solve this, certain assumptions are required. The maximum entropy method utilizes Bayesian statistical interference for analytic continuation of the Green's function and achieves a smooth functional behavior. The problem is consequently restated as: What is the most probable $A(\omega)$ given $G(\tau)$ which solves Eq. (3.45)? This translates into finding $A(\omega)$ which maximizes the conditional probability with a given $G(\tau)$. Bayes' theorem puts conditional probabilities into relation, it reads

$$p(a|b) = \frac{p(b|a)p(a)}{p(b)}, \tag{3.46}$$

where $p(a)$ and $p(b)$ are the probabilities for event a and b, respectively. Furthermore, $p(a|b)$ and $p(b|a)$ are the conditional probabilities of a given b and b given a, respectively. By identifying $a = A(\omega) \equiv A$ and analogously $b = G(\tau) \equiv G$ and assuming that G is given, we find

$$p(A|G) \propto p(G|A)p(A), \tag{3.47}$$

where we have dropped $p(G)$ since it is a constant with regard to finding the correct $A(\omega)$. Of the two remaining probabilities, $p(G|A)$ is interpreted as the *likelihood function* and $p(A)$ as the *prior*. The likelihood function is expressed by a least-square form $p(G|A) \propto e^{-\chi^2/2}$. In the simplest case of a diagonal covariance matrix $\mathrm{cov}(\omega, \omega') = \mathrm{cov}(\omega)$, where 'matrix' refers to the frequency space, we find

$$\chi^2 = \int d\omega \mathrm{cov}(\omega)(G - \bar{G})^2, \tag{3.48}$$

where $\bar{G} = \bar{G}(\omega)$ is the back-transformed $A(\omega)$ according to Eq. (3.45). Usually, $\mathrm{cov}(\omega)$ is kept constant. Minimizing Eq. (3.48) corresponds to a least-square fit. As discussed above, a simple least-square fit would yield a noisy, unusable result. Additional information is added through the prior $p(A)$ in the following way: The spectral density itself can be interpreted as a probability density function since $\int d\omega A(\omega) = 1$. The principle of maximum entropy states that this probability function maximizes an associate entropy

$$S = -\int d\omega A(\omega) \ln \frac{A(\omega)}{m(\omega)}, \tag{3.49}$$

which measures the similarity between $A(\omega)$ and $m(\omega)$. $m(\omega)$ is the *default model* which is also normalized to 1. In this similarity condition, the additionally required information about the spectral function $A(\omega)$ enters, e.g., $A(\omega)$ should be a smooth function of ω, so $m(\omega)$ should be a smooth function of ω as well. With the entropic prior $p(A) \propto e^{\alpha S}$ we find for Eq. (3.47)

$$p(A|G) \propto e^{-\chi^2/2+\alpha S}, \tag{3.50}$$

which is to be maximized by $A(\omega)$. The factor α balances the two contributions. For small α the contribution of the likelihood function is dominant and the result for $A(\omega)$ will become noisy without any physical information. For large α the contribution of the entropic prior is dominant and the result will be equal to the default model $A(\omega) = m(\omega)$. There are different methods to determine the best choice for α [241]. In this work, we use the *classic* maximum entropy method which finds an optimal α by using again Bayesian interference and maximizing

$$p(\alpha|G, m) = \int p(A, \alpha|G, m) dA \tag{3.51}$$

and

$$p(A, \alpha|G, m) \propto p(A|G, m, \alpha)p(\alpha) \propto e^{-\chi^2/2+\alpha S} p(\alpha). \tag{3.52}$$

For $p(\alpha)$ an analytic form like $p(\alpha) = 1/\alpha$ is chosen. The algorithm maximizes Eq. (3.50) iteratively while finding a new value for α in each iteration.

3.3 Topological Hamiltonian

The topological Hamiltonian approach is a powerful method to compute topological invariants of physical systems with many-body interactions. Here, we follow Ref. [242] to derive the topological Hamiltonian. The original idea was applied to inversion-symmetric systems [243], however, the method is more general and does not depend on the symmetry of the system. The field-theoretical generalization of the TKNN invariant or Chern number, which is discussed in Sec. 1.2, to the interacting case is given by the Ishikawa-Matsuyama formula [244]

$$C_{\mathrm{IM}} = \frac{1}{24\pi^2} \int dk_0 d\boldsymbol{k} \mathrm{Tr} \left[\epsilon^{\mu\nu\rho} \left(\hat{G} \partial_{k_\mu} \hat{G}^{-1} \right) \left(\hat{G} \partial_{k_\nu} \hat{G}^{-1} \right) \left(\hat{G} \partial_{k_\rho} \hat{G}^{-1} \right) \right], \tag{3.53}$$

where $\hat{G} = \hat{G}(i\omega_n, \boldsymbol{k})$ is the operator associated with the single-particle Green's function. It is constructed through Eq. (1.19) by replacing the energy values $E(\boldsymbol{k})$ with the Hamiltonian $\hat{H}(\boldsymbol{k})$. The arguments of the operator are the Matsubara frequencies $\omega_n = -ik_0$ and the 2d quasimomentum $\boldsymbol{k} = (k_x, k_y)$. Note that we take the zero-temperature limit in which the Matsubara frequency becomes a continuous quantity. Throughout this work, topological invariants will be computed in the zero-temperature limit. The topological classification at finite temperatures is a challenging topic. An example is the breakdown of the Hall conductivity at finite temperatures. More general concepts like the Uhlmann number or the ensemble geometric phase have to be used [245–248]. We assume that $\hat{G}(i\omega_n, \boldsymbol{k})$ can be diagonalized:

$$\hat{G}(i\omega_n, \boldsymbol{k})|\alpha(i\omega_n, \boldsymbol{k})\rangle = g_\alpha(i\omega_n, \boldsymbol{k})|\alpha(i\omega_n, \boldsymbol{k})\rangle \tag{3.54}$$

with normalized eigenstates $|\alpha(i\omega_n, \boldsymbol{k})\rangle$. Let us look at the Green's function operator at zero frequency $\hat{G}(0, \boldsymbol{k})$. Since the Green's function is expressed in terms of Matsubara frequencies, this is strictly speaking only valid at zero temperature. However, approximate solutions of the finite-temperature results can be used, see Sec. 4.1.

Since the imaginary part of the selfenergy is anti-symmetric with respect to the frequency $\mathrm{Im}\Sigma(-i\omega_n) = -\mathrm{Im}\Sigma(i\omega_n)$, it follows from Eq. (1.19) that the Green's function operator is hermitian at zero frequency. Thus, the eigenvalues of $\hat{G}(0, \boldsymbol{k})$ are all real. We assume that $\hat{G}(0, \boldsymbol{k})$ has no zero eigenvalue so we can group them into positive $g_\alpha(0, \boldsymbol{k}) > 0$ and negative $g_\alpha(0, \boldsymbol{k}) < 0$ eigenvalues. This is reminiscent of a gapped spectrum of a Hamiltonian with energies $g_\alpha^{-1}(0, \boldsymbol{k})$ and one can associate states with $g_\alpha(0, \boldsymbol{k}) < 0$ with the notion of occupied bands in topological band theory, see Sec. 1.2. A Chern number associated with these effective Hamiltonian states is then computed as

$$C_{\mathrm{TH}} = \frac{i}{2\pi} \sum_{\alpha: g_\alpha < 0} \int d\boldsymbol{k} \left[\langle \partial_{k_x} \alpha(0, \boldsymbol{k}) | \partial_{k_y} \alpha(0, \boldsymbol{k}) \rangle - \langle \partial_{k_y} \alpha(0, \boldsymbol{k}) | \partial_{k_x} \alpha(0, \boldsymbol{k}) \rangle \right] . \tag{3.55}$$

Our aim is to show that $C_{\mathrm{IM}} = C_{\mathrm{TH}}$ for certain conditions. To this end, we consider the parametrized deformation of the Green's function operator $\hat{G}(i\omega_n, \boldsymbol{k})$

$$\hat{G}(i\omega_n, \boldsymbol{k}, \lambda) = (1 - \lambda)\hat{G}(i\omega_n, \boldsymbol{k}) + \lambda \left[i\omega_n + \hat{G}^{-1}(0, \boldsymbol{k}) \right]^{-1} \tag{3.56}$$

where λ runs from 0 to 1. Changing λ corresponds to a smooth deformation of the Green's function operator. Topological phase transitions can only take place if the Green's function has a zero or pole [249]. Topological phase transitions at a pole of the Green's function correspond to a gap closing of the spectrum. This is analogous to the noninteracting case. Here, we are interested in the case of a zero, i.e., a topological phase transition occurs if $\hat{G}(i\omega_n, \boldsymbol{k}, \lambda)$ has a zero eigenvalue at any frequency. We now show that the deformation in Eq. (3.56) has no zero eigenvalues. For zero frequency, we find $\hat{G}(0, \boldsymbol{k}, \lambda) = \hat{G}(0, \boldsymbol{k})$ which has no zero eigenvalue by assumption. For finite frequencies, it can be shown that for the sign of the imaginary part of the Green's function the following applies:

$$\mathrm{sgn}\langle a|\mathrm{Im}\hat{G}(i\omega_n,\boldsymbol{k})|a\rangle = -\mathrm{sgn}(\omega_n). \tag{3.57}$$

Note that away from zero frequency the eigenvalues are not strictly real anymore. Moreover, for a divergent selfenergy which occurs, e.g., in Mott insulators, see Sec. 1.7, the imaginary part of the Green's function vanishes and the left-hand-side of Eq. (3.57) becomes meaningless. Therefore, the argument is not applicable in Mott-insulating regimes.

For the sake of readability, we omit the arguments of the states, i.e., we write $|\alpha\rangle = |\alpha(i\omega_n,\boldsymbol{k},\lambda)\rangle$. We compute the imaginary part of the eigenvalue $g_\alpha(i\omega_n,\boldsymbol{k},\lambda)$ of the operator $\hat{G}(i\omega_n,\boldsymbol{k})$ which is defined analogously to Eq. (3.54) as

$$\begin{aligned}\mathrm{Im}g_\alpha(i\omega_n,\boldsymbol{k},\lambda) =&\mathrm{Im}\langle\alpha|\hat{G}(i\omega_n,\boldsymbol{k},\lambda)|\alpha\rangle\\ =&\mathrm{Im}\langle\alpha|\Big\{(1-\lambda)\hat{G}(i\omega_n,\boldsymbol{k})\\ &+\lambda\left[i\omega_n+\hat{G}^{-1}(0,\boldsymbol{k})\right]^{-1}\Big\}|\alpha\rangle\end{aligned} \tag{3.58}$$

where we inserted Eq. (3.56) in order to achieve the last equation. Let us consider the last term, proportional to λ, in Eq. (3.58)

$$\begin{aligned}&\mathrm{Im}\langle\alpha|\left[i\omega_n+\hat{G}^{-1}(0,\boldsymbol{k})\right]^{-1}|\alpha\rangle &(3.59)\\ &=\mathrm{Im}\langle\alpha|\left[i\omega_n+\hat{G}^{-1}(0,\boldsymbol{k})\right]^{-1}\sum_\nu|s_\nu\rangle\langle s_\nu|\alpha\rangle &(3.60)\\ &=\mathrm{Im}\langle\alpha|\sum_\nu\langle s_\nu|\alpha\rangle\left[i\omega_n+\hat{G}^{-1}(0,\boldsymbol{k})\right]^{-1}|s_\nu\rangle &(3.61)\end{aligned}$$

$$\begin{aligned}&=\mathrm{Im}\langle\alpha|\sum_\nu\langle s_\nu|\alpha\rangle\left[i\omega_n+\epsilon_\nu\right]^{-1}|s_\nu\rangle &(3.62)\\ &=\mathrm{Im}\sum_\nu\langle s_\nu|\alpha\rangle\langle\alpha|s_\nu\rangle\left[i\omega_n+\epsilon_\nu\right]^{-1} &(3.63)\\ &=\mathrm{Im}\sum_\nu|\langle s_\nu|\alpha\rangle|^2\left[i\omega_n+\epsilon_\nu\right]^{-1} &(3.64)\\ &=-\omega_n\sum_\nu\frac{|\langle s_\nu|\alpha\rangle|^2}{\omega_n^2+\epsilon_\nu^2}, &(3.65)\end{aligned}$$

where we inserted a complete set of eigenstates of the inverse Green's function at zero frequency $G^{-1}(0,\boldsymbol{k})|s_\nu\rangle = \epsilon_\nu|s_\nu\rangle$ in Eq. (3.59). Thus, we find for the imaginary part of the eigenvalue $g_\alpha(i\omega_n,\boldsymbol{k},\lambda)$

$$\mathrm{Im}g_\alpha(i\omega_n,\boldsymbol{k},\lambda) = (1-\lambda)\langle\alpha|\mathrm{Im}\hat{G}(i\omega_n,\boldsymbol{k})|\alpha\rangle - \lambda\omega_n\sum_\nu\frac{|\langle s_\nu|\alpha\rangle|^2}{\omega_n^2+\epsilon_\nu^2}. \tag{3.66}$$

As we discussed above for finite frequencies, the sign of the imaginary part of the Green's function obeys Eq. (3.57), thus Eq. (3.66) is a sum of two terms which are both finite and which both have the same sign. This leads to a finite value of Eq. (3.66) for all values of λ for finite frequencies. For zero frequency the eigenvalues are real and nonzero as it was discussed above. Consequently, there is no topological phase transition in the full range of λ. We conclude that, if we compute Eq. (3.53) for the Green's function operator in Eq. (3.56), we find $C_{\mathrm{IM}}[\hat{G}(i\omega_n, \boldsymbol{k}, \lambda = 1)] = C_{\mathrm{TH}}$. Thus, the zero frequency Green's function is sufficient to compute topological invariants since it contains all the information about the topological properties of the full Green's function. This is an enormous simplification for investigating interacting topological states. We emphasize that the assumption was that $\hat{G}(i\omega_n, \boldsymbol{k})$ does not have a zero eigenvalue at any frequency. An effective Hamiltonian, which is dubbed topological Hamiltonian, is constructed [250] as

$$H_{\mathrm{top}}(\boldsymbol{k}) = -G^{-1}(0, \boldsymbol{k}) = H_0(\boldsymbol{k}) + \Sigma(\omega = 0, \boldsymbol{k}), \tag{3.67}$$

which is in matrix form. All methods which are used to compute topological invariants in the noninteracting case can also be applied to the effectively noninteracting Hamiltonian in Eq. (3.67). In Eq. (3.67), the selfenergy is $\boldsymbol{k}$-dependent. This is of course not the case for DMFT, see Sec. 3.1. In the DMFT + topological Hamiltonian approach we find the very convenient expression:

$$H_{\mathrm{top}}(\boldsymbol{k}) = H_0(\boldsymbol{k}) + \Sigma(\omega = 0). \tag{3.68}$$

We also note that the above derivation is independent of the symmetries of the system and is thus not restricted to Chern numbers but can also be applied to $\mathbb{Z}_2$ numbers in the TRS case. Generalizations to 3d and 4d as well as the TRS case of Eq. (3.53) are given in Ref. [242].

3.4 Local Chern marker

The local Chern marker (LCM) was introduced in 2011 by Bianco and Resta [251]. It is a quasi-local topological marker, which makes it possible to distinguish topological phases in inhomogeneous systems. Here, the term 'marker' instead of 'number' emphasizes that this quantity is not a topological invariant since those are nonlocal. Since its first mention, the LCM has gained increased interest, especially, in the cold atoms community. The main reason for that is the intrinsic inhomogeneity of cold atom setups. Applications of the LCM range from topological quasi-crystals [252], interacting, spin-conserving, fermionic Hubbard models [253], and nonequilibrium, topological marker currents [254] to topological traps and interfaces which will be discussed in this work [255–257] in Sec. 4.1. Here, we will follow the derivation of Ref. [251] for the LCM, for more details consult

Refs. [258,259]. The Chern number can be written as

$$C = \frac{i}{2\pi} \sum_{n\in O} \int d\boldsymbol{k} \left[\langle \partial_{k_x} u_n(\boldsymbol{k}) | \partial_{k_y} u_n(\boldsymbol{k}) \rangle - \text{c.c.} \right], \tag{3.69}$$

where we insert an identity operator $\mathbb{1} = \sum_m |u_m(\boldsymbol{k})\rangle\langle u_m(\boldsymbol{k})|$ and find that

$$C = \frac{i}{2\pi} \sum_{n\in O} \sum_{m} \int d\boldsymbol{k} \left[\langle \partial_{k_x} u_n(\boldsymbol{k}) | u_m(\boldsymbol{k}) \rangle \langle u_m(\boldsymbol{k}) | \partial_{k_y} u_n(\boldsymbol{k}) \rangle - \text{c.c.} \right]. \tag{3.70}$$

Here, O stands for the set of occupied bands. The derivative with respect to k_i can be exchanged between the bra and the ket state according to

$$\langle \partial_{k_i} u_n(\boldsymbol{k}) | u_m(\boldsymbol{k}) \rangle = -\langle u_n(\boldsymbol{k}) | \partial_{k_i} u_m(\boldsymbol{k}) \rangle, \tag{3.71}$$

which follows from

$$\begin{aligned} 0 = \partial_{k_i} \delta_{nm} &= \partial_{k_i} \langle u_n(\boldsymbol{k}) | u_m(\boldsymbol{k}) \rangle \\ &= \langle \partial_{k_i} u_n(\boldsymbol{k}) | u_m(\boldsymbol{k}) \rangle + \langle u_n(\boldsymbol{k}) | \partial_{k_i} u_m(\boldsymbol{k}) \rangle. \end{aligned} \tag{3.72}$$

Thus, for $m \in O$ the derivatives in Eq. (3.70) can be exchanged. Also, the indices n and m can be exchanged for $m \in O$. We find that all terms for $m \in O$ cancel with the complex conjugate, so they are real. Hence, this yields

$$C = \frac{i}{2\pi} \sum_{n\in O} \sum_{m\notin O} \int d\boldsymbol{k} \left[\langle \partial_{k_x} u_n(\boldsymbol{k}) | u_m(\boldsymbol{k}) \rangle \langle u_m(\boldsymbol{k}) | \partial_{k_y} u_n(\boldsymbol{k}) \rangle - \text{c.c.} \right]. \tag{3.73}$$

Next, we use

$$\langle u_n(\boldsymbol{k}) | \nabla_{\boldsymbol{k}} u_m(\boldsymbol{k}) \rangle = -i \langle \psi_n(\boldsymbol{k}) | \hat{\boldsymbol{r}} | \psi_m(\boldsymbol{k}) \rangle \quad n \neq m \tag{3.74}$$

which can be regarded as a basis change from momentum to position basis [258]. We furthermore find

$$C = \frac{i}{2\pi} \sum_{n\in O} \sum_{m\notin O} \int d\boldsymbol{k} \left[\langle \psi_n(\boldsymbol{k}) | \hat{x} | \psi_m(\boldsymbol{k}) \rangle \langle \psi_m(\boldsymbol{k}) | \hat{y} | \psi_n(\boldsymbol{k}) \rangle - \text{c.c.} \right] \tag{3.75}$$

$$= \frac{i N_x N_y}{(2\pi)^3} \sum_{n\in O} \sum_{m\notin O} \int d\boldsymbol{k} \int d\boldsymbol{k}' \left[\langle \psi_n(\boldsymbol{k}) | \hat{x} | \psi_m(\boldsymbol{k}') \rangle \langle \psi_m(\boldsymbol{k}') | \hat{y} | \psi_n(\boldsymbol{k}) \rangle - \text{c.c.} \right]. \tag{3.76}$$

In the last equation, we have introduced another integration over $\boldsymbol{k}'$ according to

$$\frac{N_i}{2\pi} \int dk_i = 1, \tag{3.77}$$

where N_i is the number of lattice sites in i direction. Changing the arguments in Eq. (3.76) from $\boldsymbol{k}$ to $\boldsymbol{k}'$ is justified since the position operator does not couple states with different $\boldsymbol{k}$ [259]:

$$\langle \psi_n(\boldsymbol{k})|\hat{r}|\psi_m(\boldsymbol{k}')\rangle \propto \delta_{\boldsymbol{k}\boldsymbol{k}'}. \tag{3.78}$$

Now we define the projectors

$$\hat{P} = \frac{N_x N_y}{(2\pi)^2} \sum_{n\in O} \int d\boldsymbol{k} |\psi_n(\boldsymbol{k})\rangle\langle\psi_n(\boldsymbol{k})| \tag{3.79}$$

$$\hat{Q} = 1 - \hat{P} = \frac{N_x N_y}{(2\pi)^2} \sum_{m\notin O} \int d\boldsymbol{k}' |\psi_m(\boldsymbol{k}')\rangle\langle\psi_m(\boldsymbol{k}')|. \tag{3.80}$$

Then Eq. (3.76) can be expressed as a trace

$$\begin{aligned} C &= \frac{2\pi i}{N_x N_y}\mathrm{Tr}\left[\hat{P}\hat{x}\hat{Q}\hat{y} - \hat{Q}\hat{y}\hat{P}\hat{x}\right] = -\frac{2\pi i}{N_x N_y}\mathrm{Tr}\left[\hat{P}\hat{x}\hat{P}\hat{y} - \hat{P}\hat{y}\hat{P}\hat{x}\right] \\ &= -\frac{2\pi i}{N_x N_y}\mathrm{Tr}\left[\hat{P}^2\hat{x}\hat{P}^2\hat{y} - \hat{P}^2\hat{y}\hat{P}^2\hat{x}\right] = -\frac{2\pi i}{N_x N_y}\mathrm{Tr}\left[\hat{P}\hat{x}\hat{P}, \hat{P}\hat{y}\hat{P}\right] \\ &= -2\pi i \int d\boldsymbol{r} \langle \boldsymbol{r}| \left[\hat{P}\hat{x}\hat{P}, \hat{P}\hat{y}\hat{P}\right] |\boldsymbol{r}\rangle = -4\pi \mathrm{Im} \int d\boldsymbol{r} \langle \boldsymbol{r}|\hat{P}\hat{x}\hat{P}\hat{y}\hat{P}|\boldsymbol{r}\rangle \end{aligned} \tag{3.81}$$

where we exploited the invariance of the trace under cyclic permutation. We also used $\hat{Q} = 1 - \hat{P}$ and $\hat{P}^2 = \hat{P}$ as well as $[\hat{x}, \hat{y}] = 0$. We further defined the eigenstates of the position operator $\hat{r}|\boldsymbol{r}\rangle = r|\boldsymbol{r}\rangle$. By omitting the final position integration, one is left with a locally resolved quantity which is dubbed local Chern marker, $C = \int d\boldsymbol{r} C(\boldsymbol{r})$

$$C(\boldsymbol{r}) = -2\pi i \langle \boldsymbol{r}| \left[\hat{P}\hat{x}\hat{P}, \hat{P}\hat{y}\hat{P}\right] |\boldsymbol{r}\rangle = -4\pi \mathrm{Im}\langle \boldsymbol{r}|\hat{P}\hat{x}\hat{P}\hat{y}\hat{P}|\boldsymbol{r}\rangle. \tag{3.82}$$

3.5 Fukui's method and twisted boundary conditions

Fukui's method [260] is a numerical technique to compute the Chern number of a system on a discretized BZ. First, we present the straightforward way of discretizing the continuum formula for the Chern number. This, however, has shown to be computationally inefficient. Fukui's method, which we show subsequently, resolves that and provides an alternative approach for computing the Berry curvature in a discrete BZ. Finally, we will treat the generalization to TRS systems which is possible through twisted boundary conditions.

The Berry curvature of a single band reads

$$\Omega(\boldsymbol{k}) = \partial_{k_x} A_y(\boldsymbol{k}) - \partial_{k_y} A_x(\boldsymbol{k}) \tag{3.83}$$

with the Berry connection

$$A_\mu(\boldsymbol{k}) = i\langle u(\boldsymbol{k})|\partial_{k_\mu}|u(\boldsymbol{k})\rangle. \tag{3.84}$$

With the discrete difference operator $\Delta_{k_\mu} f(\boldsymbol{k}) = f(\boldsymbol{k} + \delta k_\mu) - f(\boldsymbol{k})$, where δk_μ is the step size in μ direction on the discrete grid, the discretized expression for the Berry connection reads

$$A_\mu(\boldsymbol{k}) = i\langle u(\boldsymbol{k})|\Delta_{k_\mu}|u(\boldsymbol{k})\rangle = i\langle u(\boldsymbol{k})|u(\boldsymbol{k} + \delta k_\mu)\rangle - i \tag{3.85}$$

which yields

$$\Omega(\boldsymbol{k}) = \Delta_{k_x} A_y(\boldsymbol{k}) - \Delta_{k_y} A_x(\boldsymbol{k}), \tag{3.86}$$

and finally

$$\begin{aligned}\Omega(\boldsymbol{k}) =& i\langle u(\boldsymbol{k} + \delta k_x)|u(\boldsymbol{k} + \delta k_x + \delta k_y)\rangle - i\langle u(\boldsymbol{k})|u(\boldsymbol{k} + \delta k_y)\rangle \\ &+ i\langle u(\boldsymbol{k} + \delta k_y)|u(\boldsymbol{k} + \delta k_x + \delta k_y)\rangle - i\langle u(\boldsymbol{k})|u(\boldsymbol{k} + \delta k_x)\rangle.\end{aligned} \tag{3.87}$$

This can be evaluated on a discrete grid of $\boldsymbol{k}$ values in the BZ denoted by $\{k_l\}$. The Chern number is then computed through

$$C = \frac{1}{2\pi i} \sum_l \Omega(k_l). \tag{3.88}$$

In practice, this has proven to be numerically costly if one aims for a well quantized result. The alternative approach of Ref. [260] is to define

$$\tilde{\Omega}(k_l) = \ln \left[U_x(k_l) U_y(k_l + \delta k_x) U_x^{-1}(k_l + \delta k_y) U_y^{-1}(k_l) \right] \tag{3.89}$$

with

$$U_\mu(k_l) = \frac{\langle u(k_l)|u(k_l + \delta k_\mu)\rangle}{|\langle u(k_l)|u(k_l + \delta k_\mu)\rangle|}. \tag{3.90}$$

Now, the Chern number is computed through

$$C = \frac{1}{2\pi i} \sum_l \tilde{\Omega}(k_l). \tag{3.91}$$

We arrive at the expression in Eq. (3.89) by identifying a new gauge field $\tilde{A}_\mu(\boldsymbol{k}) = \ln U_\mu(k_l)$. Then the structure is equivalent to the former approach. The advantage of the latter approach is that Eq. (3.89) is gauge invariant because the phases of a U(1) gauge transformation will always cancel out. Furthermore, it is shown that Eq. (3.91) is always an integer independent of the lattice spacing [260]. It is also shown that the method reproduces the correct Chern number even for coarsely grained discretizations of the BZ.

The described method can be used to compute Chern numbers, i.e., to characterize topologically nontrivial states with explicitly broken TRS. In order to compute $\mathbb{Z}_2$ numbers, the method must be modified with the help of twisted boundary conditions (TBC). TBC were introduced in the context of topological insulators [261,262] as an equivalent to Laughlin's Gedankenexperiment [263]. Let us take a moment to understand this statement. In

Laughlin's Gedankenexperiment, we look at a 2d sample in cylinder geometry with electron reservoirs at each edge of the cylinder. A magnetic field is penetrating the cylinder radially which induces the IQH in the sample. Furthermore, a solenoid is arranged axially inside the cylinder much like in the Aharonov-Bohm effect. A flux Φ is adiabatically inserted into the cylinder through the solenoid by increasing it from 0 to 2π. From the Maxwell-Faraday law we find an electromotive force around the cylinder. Subsequently, because of the IQH in the sample, this leads to a transverse current along the cylinder. Since the bulk is insulating, the current will pump electrons from one edge to the other. Gauge invariance requires the initial and final states to be identical leading to a quantized number of pumped electrons. In the picture of TBC, the wavefunction is periodic with an additional phase factor. Consider, e.g., the boundary conditions $c_{x+N_x,y} = c_{x,y}$ and $c_{x,y+N_y} = e^{i\theta_y} c_{x,y}$, i.e., PBC in x direction and TBC in the y direction. This corresponds to the same cylinder geometry as the one treated in Laughlin's Gedankenexperiment with the mapping $\Phi = \theta_x/(2\pi)$.

Let us continue with the TRS case. Here, the TBC are applied to Fukui's method, which we explained above [264]. With the analog of Laughlin's Gedankenexperiment, we have recognized the connection of topologically nontrivial states and pumping, i.e., the change of polarization. In the TRS case, the charge polarization vanishes. Thus, one has to consider the *time-reversal polarization* [265]. This features a spin-dependent phase which the wavefunction will acquire at the boundary and results in the following spin-dependent TBC:

$$\hat{\boldsymbol{c}}_{x+N_x,y} = \hat{\boldsymbol{c}}_{x,y} e^{i\theta_x \mathbb{1}} \quad \text{and} \quad \hat{\boldsymbol{c}}_{x,y+N_y} = \hat{\boldsymbol{c}}_{x,y} e^{i\theta_y \sigma^z}, \tag{3.92}$$

where $N_x \times N_y$ is the 2d sample size and we again used the spinor representation $\hat{\boldsymbol{c}}_{x,y} = (\hat{c}_{\uparrow,x,y}, \hat{c}_{\downarrow,x,y})$. θ_x and θ_y are the *twist angles*. Note that for $\theta_x = 0$ and $\theta_y = 0$, the boundary conditions in Eq. (3.92) become PBC. For the computation of the $\mathbb{Z}_2$ number, Fukui's method is now applied onto the twist angles instead of originally the momenta. To this end, a real-space sample of $N_x \times N_y$ is computed for every value of θ_x and θ_y. This means, we have another grid of size $N_{\theta_x} \times N_{\theta_y}$ of discretized values of the twist angles $\{\theta_l\}$. The Eqs. (3.89) to (3.91) then become

$$\tilde{\Omega}(\theta_l) = \ln \left[U_x(\theta_l) U_y(\theta_l + \delta\theta_x) U_x^{-1}(\theta_l + \delta\theta_y) U_y^{-1}(\theta_l) \right] \tag{3.93}$$

with

$$U_\mu(\theta_l) = \frac{\langle \psi(\theta_l) | \psi(\theta_l + \delta\theta_\mu) \rangle}{|\langle \psi(\theta_l) | \psi(\theta_l + \delta\theta_\mu) \rangle|}, \tag{3.94}$$

where the $|\psi(\theta_l)\rangle$ are the respective eigenstates of the $N_x \times N_y$ sample. The $\mathbb{Z}_2$ number is given as

$$\nu_{2\mathrm{d}} = \frac{1}{2\pi i} \sum_l \tilde{\Omega}(\theta_l). \tag{3.95}$$

In practice, a well-quantized result for Eq. (3.95) can be obtained already for small values of N_x and N_y, e.g., twice the unit cell, and sufficiently large values for N_{θ_x} and N_{θ_y}.

3.6 Wilson loops

The original Wilson loop originates from gauge-field calculations in high-energy physics [266]. Here, in the condensed-matter context, it is used for the generalization of the Zak phase [267] to multiband systems [268]. The Zak phase φ corresponds to the Berry phase [35] applied to a lattice which is exposed to a gauge field. The definition related to the Berry connection in Eq. (3.84) reads

$$\varphi_{\mathcal{C}} = \oint_{\mathcal{C}} d\boldsymbol{k} \boldsymbol{A}(\boldsymbol{k}), \tag{3.96}$$

where $\mathcal{C}$ is some closed 1d path within the BZ. As a generalization, the Wilson loop constitutes a 1d topological invariant for multiband systems. In our case, it is interesting because of TRS which necessarily implies multiple bands.

In the following, we introduce the Wilson loop technique which is derived from the transfer matrix method in Ref. [268] in which also the TRS case is discussed. The technique can also be used for inversion symmetric systems [269] and a scheme for the detection in cold atom setup has been developed [270]. We define the position operator in the Wannier basis $|j\alpha\rangle$, where j denotes the lattice site index and α is an internal degree of freedom as

$$\hat{X} = \sum_{j\alpha} e^{-2\pi i j/N} |j\alpha\rangle\langle j\alpha|, \tag{3.97}$$

where N is the number of lattice sites. We note that the complex phases j/N of the eigenvalues of $\hat{X}$ refer to the positions normalized to the lattice size N. This will be used to determine the polarization, which also in the TRS case [265], plays an important role in the topological classification of a many-body state. We also define $\Delta k = 2\pi/(Na)$ being the stepsize between two neighboring k values and a is the lattice constant. Of course, only occupied bands will contribute to the polarization. Consequently, we consider the projected position operator, see Eq. (3.81):

$$\hat{P}\hat{X}\hat{P} = \sum_{nk} |\psi_{nk}\rangle\langle\psi_{nk}| \sum_{j\alpha} e^{-i\Delta k j a} |j\alpha\rangle\langle j\alpha| \sum_{mk'} |\psi_{mk'}\rangle\langle\psi_{mk'}|. \tag{3.98}$$

Now we rewrite the Bloch states in the center in terms of their cell-periodic parts $|\psi_{nk}\rangle = e^{ikx}|u_{nk}\rangle$

$$\begin{aligned}\hat{P}\hat{X}\hat{P} &= \sum_{nmkk'} |\psi_{nk}\rangle\langle u_{nk}|e^{-ikx}\sum_{j\alpha} e^{-i\Delta kja}|j\alpha\rangle\langle j\alpha|e^{ik'x}|u_{mk'}\rangle\langle\psi_{mk'}| \\ &= \sum_{nmkk'} |\psi_{nk}\rangle\sum_{j\alpha} e^{-ikx}e^{-i\Delta kja}e^{ik'x}\langle u_{nk}|j\alpha\rangle\langle j\alpha|u_{mk'}\rangle\langle\psi_{mk'}|.\end{aligned} \tag{3.99}$$

A central assumption in Ref. [268, Eq. (8)] is now that the states $|j\alpha\rangle$ are perfectly localized $|j\alpha\rangle = |\alpha\rangle\delta(x - ja)$. Hence, we find

$$\hat{P}\hat{X}\hat{P} = \sum_{nmkk'} |\psi_{nk}\rangle\sum_{j} e^{-ikja-i\Delta kja+ik'ja}\langle u_{nk}|\sum_{\alpha}|\alpha\rangle\langle\alpha|u_{mk'}\rangle\langle\psi_{mk'}|. \tag{3.100}$$

Here, the j sum results in a δ function and the α sum yields an identity since we assume the spin basis $|\alpha\rangle$ to be complete:

$$\hat{P}\hat{X}\hat{P} = \sum_{nmkk'} |\psi_{nk}\rangle\delta(k + \Delta k - k')\langle u_{nk}|u_{mk'}\rangle\langle\psi_{mk'}|. \tag{3.101}$$

We can write this expression as a matrix X in the k, k' basis, where the matrix elements $F^{nm}_{kk'}$ are matrices by themselves

$$X = \begin{pmatrix} 0 & F_0 & 0 & & & 0 \\ & 0 & F_1 & 0 & & \\ & & 0 & \ddots & & \\ & & & & & \\ & & & & \ddots & 0 \\ 0 & & & & 0 & F_{N-2} \\ F_{N-1} & 0 & & & & 0 \end{pmatrix} \tag{3.102}$$

with $F^{nm}_i = \langle u_{n,k_i}|u_{m,k_i+\Delta k}\rangle$. Remember that k runs from 0 to $2\pi/a$ with steps size $\Delta k = 2\pi/(Na)$ and the band index runs over the occupied bands. The resulting matrix F has thus size $N \cdot N_o \times N \cdot N_o$, where N_o is the number of occupied bands. Due to its block structure, the eigenproblem of X can also be solved by a transfer matrix method [268]. To this end, we define the ordered product of the F_i

$$D = F_0 F_1 F_2 \cdots F_{N-1}, \tag{3.103}$$

which is a matrix of size $N_o \times N_o$. The $N \cdot N_o$ eigenvalues λ^X_{nm} of X and the N_o eigenvalues λ^D_m of D are related through

$$\lambda^X_{nm} = N\sqrt{\lambda^D_m}e^{i(\theta_m+2\pi n)/N} \tag{3.104}$$

with $n = 0, 1, \ldots N - 1$ and $m = 0, 1, \ldots N_o - 1$. Here, θ_m are the complex phases of the eigenvalues of D. As we mentioned above, these phases are related to the position in real space. What is now left to do is that during a topological pump cycle, i.e., k performs a loop from 0 to 2π, one has to follow these positions in real space and determine whether their winding number is trivial or not. We will discuss how to numerically handle this winding number in the context of 3d topological insulators in Sec. 4.4.

Chapter 4

Results

This chapter constitutes a collection of new results which were obtained during the study of interacting tight-binding models for topological states in optical lattices by means of DMFT. Since tight-binding models are very well resembled by cold atom experiments in optical lattices, we do not only study the topological states but discuss possible detection methods in cold atom setups as well. Moreover, the discussion covers different generalizations to the Hofstadter model as well as the Haldane model which were introduced in Sec. 2. We start this section with the main part of this work, the inhomogeneous topological states studied with real-space DMFT.

4.1 Interacting, inhomogeneous topological states in optical lattices

Cold atom setups possess an intrinsic inhomogeneity due to the trapping potential which is commonly harmonic [101, 104, 106]. There has been considerable effort to overcome the harmonic trap, going onward to arbitrary trapping potentials using digital mirror devices [121] or light sheets [120], see Sec. 1.4. These techniques, however, can so far not create potentials with a resolution on the scale of the lattice spacing. The intrinsic inhomogeneity is still present and, within this work, we tackle the problem using real-space DMFT in the context of topological states.

4.1.1 Interacting Hofstadter interface

Besides cold atom experiments, topological insulators have various implementations in solid states, photonic crystals and even mechanical systems. The latter shows that topological phases do not necessarily require quantum physics. As explained in Sec. 1.2.3, most topologically non-trivial phases demand the existence of robust conducting edge states. In solid state systems, edge states could be observed at the step edge of layered $ZrTe_5$

by making use of atomic force microscopy and angle-resolved photoemission spectroscopy (ARPES) [271] as well as scanning tunneling microscopy (STM) [272]. In Ref. [273], edge states could be observed in artificial graphene realized by a photonic crystal. In the classical case, a lattice model of two mechanical pendula per site, which are coupled to neighboring sites in a special manner, showed edge states [274]. This raises the question for edge state detection in cold atom setups. In this context, an intrinsic problem is that cold atom setups, in contrast to solid state materials, do not have a well-defined edge since they rather constitute clouds. The cloud structure originates from the smooth trapping potential which causes the density of the gas to decrease continuously towards the boundary. In the noninteracting case, a harmonic trap seems to destroy the localization of the edge states and no clear distinction between bulk and edge can be made [41,275]. In the interacting bosonic case, however, the localization of the edge states can be recovered as it was investigated in the Thomas-Fermi approximation [276]. Despite the difficulties of the smooth trap, there exist diverse proposals for the experimental detection of edge states. One method proposes to relieve trapped edge states into formerly forbidden regions in the trap and to observe them by direct imaging of the time evolution [277]. Other works propose Bragg scattering and finding signatures of the edge states in the measured spectra [41,275,278]. Finally, the idea of interfaces between two topologically different phases is promising. In Ref. [279], a driving beam of finite waist creates a topologically nontrivial Floquet system in the center of the configuration and edge states emerge at the phase boundary. Another approach to create a topological phase boundary is by varying a staggered potential spatially. This has beeen studied in the noninteracting Haldane model [280]. Here, we follow this approach applied to the TRS Hofstadter model we introduced in Sec. 2.2. We are especially interested in the influence of two-body interactions on the edge state since Feshbach resonances can be used to tune the on-site interaction between atoms in the lattice.

The Hamiltonian we investigate is an inhomogeneous version of the TRS Hofstadter-Hubbard model introduced in Sec. 2.2 and reads

$$\begin{aligned}\hat{H} = &-t\sum_{x,y}\left[\hat{\boldsymbol{c}}^{\dagger}_{x+1,y}e^{2\pi i\gamma\sigma^{x}}\hat{\boldsymbol{c}}_{x,y}+\hat{\boldsymbol{c}}^{\dagger}_{x,y+1}e^{2\pi i\alpha x\sigma^{z}}\hat{\boldsymbol{c}}_{x,y}+\text{h.c.}\right]\\ &+\sum_{x,y}\left[\lambda(x)\hat{\boldsymbol{c}}^{\dagger}_{x,y}\hat{\boldsymbol{c}}_{x,y}+U\hat{c}^{\dagger}_{\uparrow,x,y}\hat{c}_{\uparrow,x,y}\hat{c}^{\dagger}_{\downarrow,x,y}\hat{c}_{\downarrow,x,y}\right],\end{aligned}\tag{4.1}$$

where we used again the spinor representation $\hat{\boldsymbol{c}}_{x,y} = (\hat{c}_{\uparrow,x,y}, \hat{c}_{\downarrow,x,y})$. The amplitude $\lambda(x)$ of the staggered potential is now spatially dependent. We set $\alpha = 1/6$ and $\gamma = 1/4$ and focus on the half-filled case corresponding to the phase diagram in Fig. 2.4(c). The size of the lattice is $N_x \times N_y$. In order to create a topological phase boundary in real space, we apply a staggered

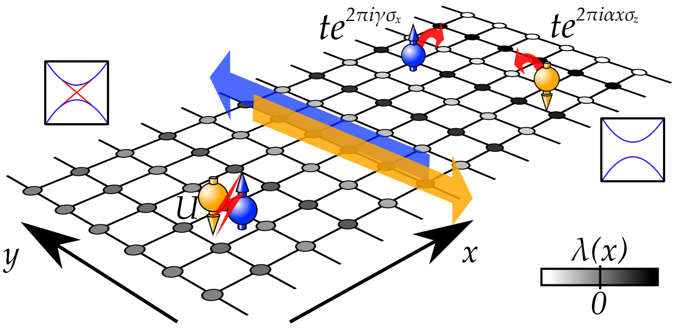

Figure 4.1: Schematic of the topological interface: spin-1/2 fermions described by the Hamiltonian in Eq. (4.1) in a 2d lattice. The spatially dependent staggered potential Eq. (4.2) is implemented and depicted as a gray scale. This induces a topological phase separation and a boundary which should feature helical edge states which is represented by blue/orange arrows. Reprinted with permission from Ref. [255]. Copyright (2020) by the American Physical Society.

potential of the form

$$\lambda(x) = \left[\lambda_L + (\lambda_R - \lambda_L)\frac{x}{N_x}\right](-1)^x, \tag{4.2}$$

where λ_L and λ_R correspond to the amplitudes of the staggered potential at the left and the right boundary of the system. We chose this form of the potential since it could be realized by superponing two standing-wave laser beams with slightly shifted wavevectors. The result would be a beads profile which could be tuned such that the envelope is approximately linear and matches the form of Eq. (4.2).

The present system is depicted schematically in Fig. 4.1. The parameters λ_R and λ_L are chosen such that the critical value $\lambda_c \approx 1.25$ is reached in the center of the system, where we expect a topological phase boundary and hence an edge state. See Sec. 2.2 for details.

Spin decoupling

For the present case of $\gamma = 1/4$, i.e., for maximal spin mixing such that a spin is exactly flipped when hopping one lattice site in x direction, the problem can be simplified. To this end, we introduce new fermion operators

$$\hat{d}_{\sigma,x,y} = \begin{cases} \hat{c}_{\sigma,x,y} \text{ if } x \text{ is even} \\ \hat{c}_{\bar{\sigma},x,y} \text{ if } x \text{ is odd} \end{cases} \tag{4.3}$$

which represent decoupled, virtual spins. Here, the bar notation again flips a spin, i.e., $\bar{\uparrow} = \downarrow$ and $\bar{\downarrow} = \uparrow$. Rewriting Eq. (4.1) in terms of $\hat{d}$ operators we find

$$\begin{aligned}\hat{H} = &-t\sum_{x,y}\left[\hat{\boldsymbol{d}}^{\dagger}_{x+1,y}\hat{\boldsymbol{d}}_{x,y} + \hat{\boldsymbol{d}}^{\dagger}_{x,y+1}e^{2\pi i\alpha(-1)^{x}x\sigma^{z}}\hat{\boldsymbol{d}}_{x,y} + \text{h.c.}\right] \\ &+\sum_{x,y}\left[\lambda(x)\hat{\boldsymbol{d}}^{\dagger}_{x,y}\hat{\boldsymbol{d}}_{x,y} + U\hat{d}^{\dagger}_{\uparrow,x,y}\hat{d}_{\uparrow,x,y}\hat{d}^{\dagger}_{\downarrow,x,y}\hat{d}_{\downarrow,x,y}\right],\end{aligned} \tag{4.4}$$

where we once again use the spinor representation $\hat{\boldsymbol{d}}_{x,y} = (\hat{d}_{\uparrow,x,y}, \hat{d}_{\downarrow,x,y})$. We observe that under this transformation the spin-mixing phase, which was originally acquired in the x hopping process in Eq. (4.1), vanishes completely in Eq. (4.4). However, the flux α becomes a staggered flux $(-1)^{x}\alpha$ similar to the flux pattern of the very early realization of the Hofstadter model in a cold atom experiment [112]. Now we want to argue that the transformation in Eq. (4.3) is unitary, that it does not change the physics, and hence does not change the topological state of the system. To this end, we make use of topological field theory since any interactions can be straightforwardly included in stark contrast to topological band theory [281]. Here, the $\mathbb{Z}_2$ number is expressed by the extended momentum-frequency integral

$$P_2 = \frac{\epsilon^{\mu\nu\rho\sigma\tau}}{120(2\pi)^3}\int d^3k\,du\,dv\,\text{Tr}\left[\hat{G}\partial_{\mu}\hat{G}^{-1}\hat{G}\partial_{\nu}\hat{G}^{-1}\hat{G}\partial_{\rho}\hat{G}^{-1}\hat{G}\partial_{\sigma}\hat{G}^{-1}\hat{G}\partial_{\tau}\hat{G}^{-1}\right]. \tag{4.5}$$

Herein, $\epsilon^{\mu\nu\rho\sigma\tau}$ is the five-dimensional anti-symmetric tensor. Furthermore, $k = (i\omega_n, k_x, k_y)$ is the generalized momentum which contains the Matsubara frequency ω_n and the physical 2d momentum. u and v are residual variables from dimensional reduction [282], and the greek indices run over $i\omega_n, k_x, k_y, u, v$. Moreover, $\hat{G} = \hat{G}(k, u, v)$ represents the extended Green's function operator which satisfies $\hat{G}(k, 0, 0) = \hat{G}(k) = \hat{G}(i\omega_n, k_x, k_y)$. The 4+1-dimensional integral stems from the second Chern number in 4+1 dimensions which is said to be *fundamental*. Here, 'fundamental' means that the topological properties of the system can be classified by an integer, e.g., the second Chern number in 4+1 dimensions or the first Chern number in 2+1 dimensions, see Refs. [30, 31]. The TRS cases in 3+1 and 2+1 dimensions can be derived from the 4+1 dimensional system by dimensional reduction [282]. The residual dimensions remain as Wess-Zumino-Witten terms [283] inside the integrals [281]. This is why we find five integration variables in Eq. (4.5). We will now show that the number P_2 in Eq. (4.5) can be expressed in the basis of the transformation in Eq. (4.3). This yields the same form which shows that its value is independent of the basis. We introduce the unitary transformation $\hat{\mathcal{U}}$ such that $\hat{d} = \hat{\mathcal{U}}\hat{c}$. By interpreting the position inside a unit cell as an internal degree of freedom, we find that $\mathcal{U}$ is position-independent and consequently momentum-independent. The Green's function in the Fourier-transformed $\hat{d}$ basis reads

$$\tilde{G}(i\omega_n, k_x, k_y) = \langle T_{\tau}\hat{\boldsymbol{d}}_{k_x,k_y}(\tau)\hat{\boldsymbol{d}}^{\dagger}_{k_x,k_y}(0)\rangle = \mathcal{U}G(i\omega_n, k_x, k_y)\mathcal{U}^{\dagger}, \tag{4.6}$$

where T_τ is imaginary-time ordering operator. The extended Green's function operator follows directly satisfying $\hat{\tilde{G}}(k,0,0) = \hat{\tilde{G}}(k) = \hat{\tilde{G}}(i\omega_n, k_x, k_y)$. We can now rewrite Eq. (4.5) in terms of this new extended Green's function operator simply by using $\hat{G} = \hat{\mathcal{U}}^\dagger \hat{\tilde{G}} \hat{\mathcal{U}}$ which follows from Eq. (4.6). Then we exploit the properties of the trace, i.e., cyclicly permuting the order of the operators to get:

$$P_2 = \frac{\epsilon^{\mu\nu\rho\sigma\tau}}{120(2\pi)^3} \int d^3k du dv \mathrm{Tr} \left[\tilde{G}\partial_\mu \tilde{G}^{-1} \tilde{G}\partial_\nu \tilde{G}^{-1} \tilde{G}\partial_\rho \tilde{G}^{-1} \tilde{G}\partial_\sigma \tilde{G}^{-1} \tilde{G}\partial_\tau \tilde{G}^{-1} \right]. \tag{4.7}$$

Thus, the number P_2 can readily be expressed in terms of the new fermionic operators and we find that it is invariant under the transformation defined in Eq. (4.3). The advantage of this is that the newly introduced fermions are spin-conserved, i.e., $\hat{d}_\uparrow$ and $\hat{d}_\downarrow$ are decoupled. As a consequence, we can compute Chern numbers of each species and the $\mathbb{Z}_2$ number is determined as the difference of both, see Sec. 1.3. This means we only need to compute Chern numbers instead of $\mathbb{Z}_2$ numbers which is easier to do. The drawback is that we are restricted to a maximal spin mixing of $\gamma = 1/4$.

Edge states at the interface

Edge states between topologically different many-body phases can generally not be observed in the particle density but rather through transport properties, i.e., their conduction behavior. This can be quantified by, e.g, the spectral density or the compressibility at the Fermi level $\omega = 0$. The spectral density is obtained from the imaginary part of the Green's function, see Sec. 1.7. In this particular instance, we consider the cylinder geometry, i.e., the system possesses OBCs in the x direction, associated with the real-space variable x, and PBCs in the y direction, associated with the momentum space variable k_y. Consequentially, due to the Fourier transform, the Green's function is diagonal in k_y. On the other hand, it is not diagonal in the variable x, i.e., it exhibits nonlocal components. For the spectral density, nonlocal contributions are neglected. To emphasize this, we use the symbol ρ instead of A as in Sec. 1.7. The k_y-momentum-integrated spectral density of a particle in spin state σ at the Fermi level reads

$$\rho_x^\sigma = -\frac{1}{\pi} \int dk_y \mathrm{Im} G_{xx}^{\sigma\sigma}(\omega = 0, k_y). \tag{4.8}$$

Here, the Green's function in cylinder geometry is expressed as

$$G_{xx'}^{\sigma\sigma'}(\omega, k_y) = \left[\omega + i\eta + \mu - H(k_y) - \Sigma(\omega)\right]^{-1}\Big|_{xx'}^{\sigma\sigma'} \tag{4.9}$$

Here, ω is the real frequency, η is a small broadening factor, μ is the chemical potential, $H(k_y)$ is the noninteracting Hamiltonian matrix in spin and x

coordinate basis, and $\Sigma(\omega)$ is the selfenergy in spin-position basis. We consider a system of 48 lattice sites along the x direction, i.e., $H(k_y)$ and $\Sigma(\omega)$ are of the size 96×96.

Another quantity for determination of the conduction properties is the compressibility. It quantifies whether particles can be added to the system if the chemical potential is slightly increased. If so and if additionally there is no disorder, the system is in the metallic state; otherwise it is insulating. We are interested in a version of the compressibility in cylinder geometry: Generally speaking, the particle density of a system can be calculated through the energy integral over the spectral density times the distribution function. This translates in our case to

$$\begin{aligned} n_x^\sigma(k_y) &= \int d\omega n_F(\omega) \rho_x^\sigma(\omega, k_y) && (4.10) \\ &= -\frac{1}{\pi} \int d\omega n_F(\omega) \mathrm{Im} G_{xx}^{\sigma\sigma}(\omega + i\eta, k_y), && (4.11) \end{aligned}$$

where the η term makes sure that one does not integrate over poles. $n_F(\omega)$ is the Fermi-Dirac distribution function which can be expressed as [157, (3.5)]

$$n_F(\omega) = \frac{1}{e^{\beta(\omega-\mu)} + 1} = \frac{1}{2} + \frac{1}{\beta} \sum_n \frac{1}{i\omega_n - \omega + \mu}. \tag{4.12}$$

We insert Eq. (4.12) into Eq. (4.10) and find

$$\begin{aligned} n_x^\sigma(k_y) &= \frac{1}{2} \int d\omega \rho_x^\sigma(\omega, k_y) + \frac{1}{\beta} \sum_n \int d\omega \frac{\rho_x^\sigma(\omega, k_y)}{i\omega_n - \omega + \mu} \\ &= \frac{1}{2} + \frac{1}{\beta} \sum_n G_{xx}^{\sigma\sigma}(i\omega_n, k_y), \end{aligned} \tag{4.13}$$

where we have used for the second equality that the spectral function is normalized as well as the spectral representation of the Matsubara Green's function [157, Eq. (3.118)]. The formula in Eq. (4.13) shows a direct relation between the particle density and the Matsubara Green's function.

The compressibility now follows as the derivative of the particle density with respect to the chemical potential $\kappa = \partial n / \partial \mu$ at constant temperature and volume:

$$\begin{aligned} \kappa_x^\sigma(k_y) = \frac{\partial n_x^\sigma(k_y)}{\partial \mu} &= \frac{1}{\beta} \sum_n \frac{\partial}{\partial \mu} G_{xx}^{\sigma\sigma}(i\omega_n, k_y) && (4.14) \\ &= -\frac{1}{\beta} \sum_{n, x', \sigma'} G_{xx'}^{\sigma\sigma'}(i\omega_n, k_y) \left[\frac{\partial}{\partial \mu} G^{-1}(i\omega_n, k_y) \right]_{x'x'}^{\sigma'\sigma'} G_{x'x}^{\sigma'\sigma}(i\omega_n, k_y) && (4.15) \end{aligned}$$

where we have used that $\partial A = -A \left(\partial A^{-1} \right) A$ in Eq. (4.15) which applies for an invertible matrix A since $A^{-1} A = 1$. In order to perform the remaining derivative, we consult Eq. (4.9) and make the assumption that the selfenergy does only weakly depend on μ, i.e., $\partial\Sigma/\partial\mu \ll 1$ is negligible. We are then left with

$$\kappa_x^\sigma(k_y) = -\frac{1}{\beta} \sum_{n,x',\sigma'} G_{xx'}^{\sigma\sigma'}(i\omega_n, k_y) G_{x'x}^{\sigma'\sigma}(i\omega_n, k_y). \tag{4.16}$$

This expression has the advantage that it contains only Matsubara Green's functions which are directly obtained in DMFT. Thus, the local compressibility as a measure to find edge states is straightforwardly obtained from the DMFT results through Eq. (4.16). On the other hand, an expression for the compressibility can be found in the following way [284–286]: In the grand-canonical ensemble the particle density in cylinder geometry reads

$$n_x^\sigma(k_y) = \langle \hat{n}_x^\sigma(k_y) \rangle = \frac{\mathrm{Tr}\ \hat{n}_x^\sigma(k_y) e^{-\beta(\hat{H}-\mu\hat{N})}}{\mathrm{Tr} e^{-\beta(\hat{H}-\mu\hat{N})}}, \tag{4.17}$$

where the operator measuring the total number of particles is defined as $\hat{N} = \sum_{\sigma,x} \hat{n}_x^\sigma(k_y)$. Performing the derivative with respect to μ, we find the compressibility as

$$\kappa_x^\sigma(k_y) = \beta \sum_{\sigma',x'} \left[\langle \hat{n}_x^\sigma(k_y) \hat{n}_{x'}^{\sigma'}(k_y) \rangle - \langle \hat{n}_x^\sigma(k_y) \rangle \langle \hat{n}_{x'}^{\sigma'}(k_y) \rangle \right], \tag{4.18}$$

which corresponds to nonlocal correlations between site x and all sites of the lattice x'. We claim that this is a quantity which could actually be measured in cold atom experiments by using a quantum gas microscope. Here, the idea is to extract the averages in Eq. (4.18) from cold atom measurements. For the average density, this is done by sampling over many quantum gas microscope images. The correlation term, on the other hand, is more tricky to obtain. Here, in every image the product of the density of every site x with every other site x' has to be computed. To this end, one needs to develop an algorithm which finds the correct position of the site in the image. Also, care must be taken for influences from noises and drifts during the experiment. Topological states and quantum gas microscopes have been combined in an experiment [147], however, in this instance the focus was on the trajectory of the particles rather than on measuring correlations.

We show the spectral function as well as the local compressibility as functions of the site index x in Fig. 4.2(c) for the noninteracting case in blue and the moderately interacting case with $U = 2$ from DMFT results in orange. Note that the tilde refers to the virtual spin basis of Eq. (4.3) discussed above. The first observation is that the spectral function as well as the local compressibility coincide up to small deviations which can be attributed to the small, rather arbitrarily chosen, parameter η in Eq. (4.9). We show that these two quantities should indeed coincide: Recalling Eq. (4.10)

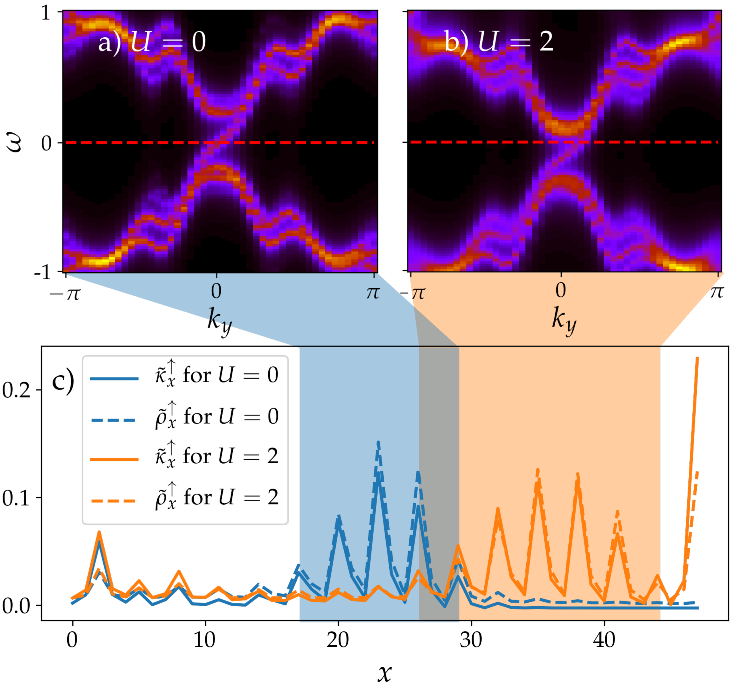

Figure 4.2: Spectral density as well as local compressibility as functions of x in (c). Edge state spectra for the noninteracting and moderately interacting case in (a) and (b), respectively. Contributions are taken from the highlighted areas in (c). The parameters for the potential in Eq. (4.2) are $\lambda_L = 0$ and $\lambda_R = 2.5$. Reprinted with permission from Ref. [255]. Copyright (2020) by the American Physical Society.

at zero temperature $T = 0$ and inserting Eq. (4.9) yields

$$\begin{aligned} n_x^{\sigma}(k_y) &= -\frac{1}{\pi}\int_{-\infty}^{0} d\omega \mathrm{Im}\left[\omega + i\eta + \mu - H(k_y) - \Sigma(\omega)\right]^{-1}\Big|_{xx}^{\sigma\sigma} \\ &= -\frac{1}{\pi}\int_{-\infty}^{\mu} d\omega \mathrm{Im}\left[\omega + i\eta - H(k_y) - \Sigma(\omega - \mu)\right]^{-1}\Big|_{xx}^{\sigma\sigma} \end{aligned} \tag{4.19}$$

where we have performed the shift $\omega + \mu \to \omega$. Performing the derivative with respect to μ gives the compressibility

$$\kappa_x^{\sigma}(k_y) = -\frac{1}{\pi}\mathrm{Im}\left[\omega + i\delta + \mu - H(k_y) - \Sigma(0)\right]^{-1}\Big|_{xx}^{\sigma\sigma} + \mathcal{O}\left(\frac{\partial\Sigma}{\partial\mu}\right), \tag{4.20}$$

which exactly corresponds to the spectral density at the Fermi level, i.e. $\omega = 0$, $\rho_x^{\sigma}(\omega = 0, k_y)$. Note that particle conservation is required for the two quantities to coincide. In superconducting systems, e.g., they can deviate [286].

Coming back to the result in Fig. 4.2(c), we observe for the noninteracting case a peak of the envelope function of the compressibility in the middle of the system at $x \approx 24$. Since we have chosen $\lambda_L = 0$ and $\lambda_R = 2.5$ in our potential in Eq. (4.2), this is where we expect the critical value of $\lambda(x \approx 24) \approx 1.25$. Thus, the edge state is indeed found from the compressibility. The spiky appearance of the compressibility is explained in the following way: In the normal Hofstadter model, see Sec. 2.1, the flux is constant throughout the lattice, i.e., every plaquette is pierced by the same amount of flux α. However, if we perform the transformation of Eq. (4.3) the system is mapped onto spin-decoupled fermions subject to a staggered flux $\alpha(-1)^x$ as explained above. For the used value of $\alpha = 1/6$, the plaquette flux is now position-dependent and has a magnitude of $2\pi(2x+1)/6$ which has a periodicity of 3. This inhomogeneous flux pattern is the reason for the spiky profile of the compressibility which only emerges due to the spin-mixing process. The envelope function is approximately Gaussian which we understand as an increased extent of the edge state into the bulk due to the underlying linearly increasing staggered potential amplitude: An edge state decays off a sharp edge in an exponential fashion with respect to x. Since in the present consideration the edge is smooth, i.e., linear in x, this gives another contribution which results in an Gaussian decay of the edge state into the insulating bulk.

The spectrum of the edge state in the noninteracting case is made visible by plotting out the spectral function as a function of k_y and ω. This is shown in Fig. 4.2(a). The edge state crosses the band gap once with positive group velocity $\partial\omega/\partial k_y$. There are no states with negative group velocity such that backscattering is impossible and consequently the edge state is robust. We capture the full contribution of the extended edge to the spectral function by including a certain region of x values. This is highlighted as a blue shaded area in Fig. 4.2(c).

In the interacting case, with $U = 2$, we observe in Fig. 4.2(c) that the peak in the compressibility is shifted to the right $x \approx 36$ as compared to the noninteracting case. Here, we can also compute the spectral density by analytically continuing the selfenergy from DMFT via the maximum entropy method which we discussed in Sec. 3.2. The x values of the Green's function which contribute to the spectral function of this edge state are highlighted as an orange shaded are in Fig. 4.2(c). Plotting the spectral density as shown in Fig. 4.2(b), shows almost the same picture as in the noninteracting case. This shows that the edge state is robust against Hubbard interactions and just shifts its location towards higher values of $\lambda(x)$. This is consistent since the band gap has not been closed between $U = 0$ and $U = 2$ and thus no topological phase transition could take place. At larger interactions, the gap could close if the system undergoes either a band insulator to AFM transition or a band insulator to Mott insulator transition. Complementary to the results in Fig. 4.2, we show the compressibility as function of x and

U for three different sets of λ_L and λ_R in Fig. 4.3. We observe that with increasing difference $\lambda_R - \lambda_L$ the edge state becomes more pronounced as the edge itself becomes sharper. Also, the edge state is shifted towards the right side as interactions are increased. The edge state is surrounded by dark regions which correspond to vanishing compressibility and therefore to insulating phases.

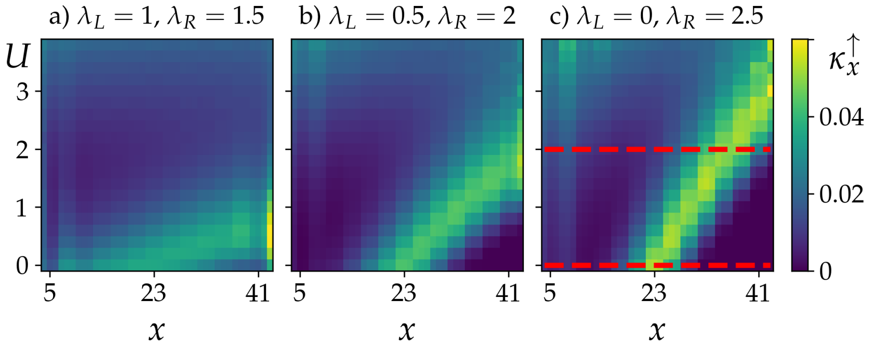

Figure 4.3: Compressibility as function of x and U for different potentials as defined in Eq. (4.2). The red lines in (c) correspond to the cases discussed in Figs. 4.2 and 4.4. Reprinted with permission from Ref. [255]. Copyright (2020) by the American Physical Society.

Topological pumping

So far, we have argued that there are two insulating many-body phases separated by a gapless edge state in between. We shall now argue that these phases are indeed topologically different, i.e., they carry different topological invariants. One approach is to look at the Hall response of the system also known as topological pumping. In particular, we look at the transverse shift a particle experiences if it is moved in the longitudinal direction. In our case, we change k_y. The Hall response is then read out from the shift in the x direction. After a full pump cycle of 2π the particle is pumped further by a quantized amount. The idea of measuring Hall response in optical lattices in the cylinder geometry is proposed by Ref. [287]. The Hall response, also dubbed anomalous velocity, was also measured in Ref. [143] for the first experimental determination of the Chern number in artificial systems. Topological pumping is furthermore used in 1d topological systems [288,289]. This is referred to the Thouless pump [290] which can be mapped to a 2d static system via the Rice-Mele model [288,291,292]. In Fig. 4.4, we show the line particle density as a function of x with changing k_y for the noninteracting case in (a) and with interactions of $U = 2$ in (b). For (a), we observe, following a full pump cycle of k_y, that on the left-hand side of the system, $0 \lesssim x \lesssim 20$, the shift in x of the particle density is 6 which corresponds to the size of the unit cell corresponding to a topologically nontrivial phase. On the right-hand side, $30 \lesssim x \lesssim 48$, however, the particles are not pumped during one pump cycle corresponding to a topologically trivial phase. This nicely shows how the transition region, $20 \lesssim x \lesssim 30$, in the center of the system separates the two topologically different phases. In the interacting case (b), the topologically nontrivial region extends more to the right, $0 \lesssim x \lesssim 25$, compared to the noninteracting case in (a) which is consistent with the shift of the edge state through interactions as seen from Figs. 4.2 and 4.3.

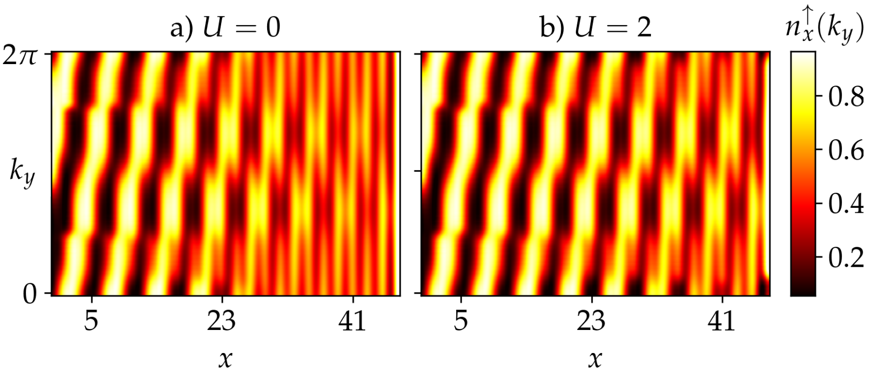

Figure 4.4: Topological pumping: particle density as function of x and k_y for the noninteracting case as well as the interacting case with $U = 2$. The parameters for the potential in Eq. (4.2) are $\lambda_L = 0$ and $\lambda_R = 2.5$. Reprinted with permission from Ref. [255]. Copyright (2020) by the American Physical Society.

Local spin Chern marker

Even though the pumping behavior in Fig. 4.4 nicely reflects the topological phase separation and the connection between topological states and the Hall response, the results are quite complicated and one desires a simpler function of the variable x only. This brings us to the concept of real-space interpretations of topological indices. In Sec. 3.4, we have introduced the local Chern marker (LCM) by Bianco and Resta [251]. In the present case, we can directly apply it in our virtual spin basis defined in Eq. (4.3) since it contains two decoupled spin species. We also have shown that the $\mathbb{Z}_2$ number does not depend on the basis and that it can be simply obtained from the difference of the two Chern numbers in the virtual spin basis. By exploiting TRS, it is even sufficient to compute only one of the Chern numbers.

Before we look at the results for the LCM, we have to consider some subtleties concerning the LCM in cylinder geometry. Since the LCM can

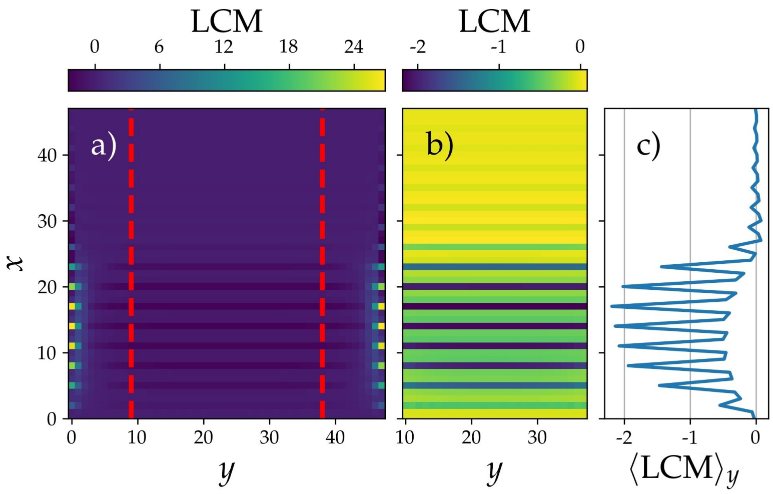

Figure 4.5: Local Chern marker in cylinder geometry: (a) on the full lattice, (b) on the cut-off lattice corresponding to the red cut-off marks in (a), and (c) the y average $\langle\mathrm{LCM}\rangle_y$ of the LCM on the cut-off system depicted in (b) for $U = 0$, $\lambda_L = 0$, and $\lambda_R = 2.5$. Reprinted with permission from Ref. [255]. Copyright (2020) by the American Physical Society.

be written in the form of a commutator, its trace must always vanish. In practice, this implies that the LCM will have nonphysical boundary effects which compensate the bulk value of the LCM. In particular, these boundary effects depend on the size of the system. The boundary will be cut off in the results to get rid of the unphysical boundary effects. Interestingly, boundary effects emerge also for PBC. The reason for that is, that the position operator in the expression of the LCM in Eq. (3.82) is not well-defined with PBC in a finite system. There is no labeling for the matrix elements of the position operator such that it could smoothly connect the last site with the first site. As a result, boundary effects occur for PBC as well. In Fig. 4.5, we show the LCM for the full system in (a). Then the result is cut at the red lines shown in (a) and one obtains the LCM for the cut-off system shown in (b). Finally, the average in y direction is taken in order to get a function of x only, as shown in (c). The spiky profile arises due to the same reason as the spiky profile of the compressibility, as we explained above. Consequently, we smoothen our data by applying an average over 3 lattice sites. This corresponds to half of a unit cell, but is sufficient to achieve a smooth result.

In order to investigate finite interactions, we make use of the topological Hamiltonian approach which we introduced in Sec. 3.3. It is a very general technique and can be straightforwardly applied to our system. In Fig. 4.6, we present the line average of the LCM for one of the decoupled virtual spin states as a function of x and U computed with the topological Hamiltonian. We observe that the LCM is well quantized in regions where we

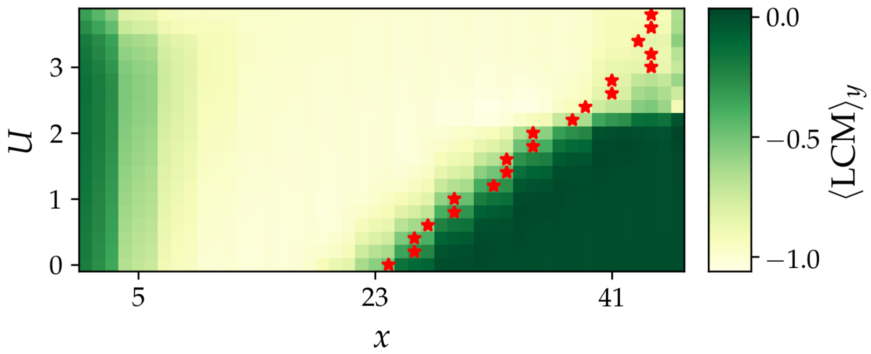

Figure 4.6: Local Chern marker line average as a function of interaction strength U for $\lambda_L = 0$ and $\lambda_R = 2.5$. The red stars denote the position of the maxima of the compressibility corresponding to the result in Fig. 4.3(c). Reprinted with permission from Ref. [255]. Copyright (2020) by the American Physical Society.

expect the system to be insulating. Light regions correspond to the topologically nontrivial phase, where the LCM is nonzero, and dark regions to the topologically trivial one, where the LCM is zero. In the transition region, the LCM has no physical meaning since the system is gapless here. We also plot the maxima of the compressibility corresponding to the result of Fig. 4.3 as red stars to provide an estimate of where the edge state is located. Here, we find excellent agreement between the two results. The change of a topological invariant has to coincide with the existence of a gapless state. This confirms the bulk-boundary correspondence with interactions [249] at the smooth interface.

4.1.2 Local Chern marker of smoothly confined, interacting Hofstadter fermions

Another application of our framework for real-space DMFT combined with the topological Hamiltonian are cold atom systems confined by a trapping potential. Trapping potentials in the context of topological states have been widely discussed: noninteracting topological states within trapped optical lattices [275], the trapped Hofstadter model [41], possible detection of edge states in traps using quench dynamics [277], single-particle dynamics in the trap [293], trapping effects in periodically driven systems in 1d [294] as well as 2d [295], and trapped interacting bosons [276].

Here, we are interested in interacting fermions in the TRS Hofstadter model confined to a harmonic trap. The Hamiltonian for this system reads

$$\begin{aligned}\hat{H} = &-t\sum_{x,y}\left[\hat{\boldsymbol{c}}^{\dagger}_{x+1,y}e^{2\pi i\gamma\sigma^{x}}\hat{\boldsymbol{c}}_{x,y}+\hat{\boldsymbol{c}}^{\dagger}_{x,y+1}e^{2\pi i\alpha x\sigma^{z}}\hat{\boldsymbol{c}}_{x,y}+\text{h.c.}\right]\\ &+\sum_{x,y}\left[\lambda(-1)^{x}\hat{\boldsymbol{c}}^{\dagger}_{x,y}\hat{\boldsymbol{c}}_{x,y}+V(x)\hat{\boldsymbol{c}}^{\dagger}_{x,y}\hat{\boldsymbol{c}}_{x,y}+U\hat{c}^{\dagger}_{\uparrow,x,y}\hat{c}_{\uparrow,x,y}\hat{c}^{\dagger}_{\downarrow,x,y}\hat{c}_{\downarrow,x,y}\right],\end{aligned} \tag{4.21}$$

where we have introduced the trapping potential $V(x) = V(x - x_0)^2$ which is chosen to be harmonic with x_0 being the position of trap center. The potential is constant in y since we will again consider the cylinder geometry. The trapping potential depth V is chosen such that the potential assumes a value of 10 in units of hopping energies at the boundaries of the system. We choose this value since it exceeds the total bandwidth of the Hofstadter model with the flux set to $\alpha = 1/6$ [192] which energetically suppresses the probability for the occupation of a state at the boundary.

In the system described by Eq. (4.21), there are three competing energy scales, with $t = 1$, being the staggered potential amplitude λ, the trapping potential depth V, and the interaction strength U. Since V is fixed as explained above and U should vary, we are left with choosing a proper regime for λ. Our aim is to investigate the stability of topological states in the presence of the trap. Under the assumption that in the center of the system the particles obey the bulk physics we choose λ such that the particles in the trap center remain in the topologically nontrivial phase. To this end, we consult the phase diagram of Ref. [193] which is reproduced in Fig. 2.4(c) and rescale $\lambda = \lambda(U)$ with the interaction strength as

$$\lambda(U) = \frac{1}{2} + \frac{U}{3}, \tag{4.22}$$

which ensures that in the trap center the system is in the QSH phase even for strong interactions and does not undergo a phase transition into a magnetically ordered but topologically trivial phase, according to Fig. 2.4(c).

A technical challenge for real-space DMFT applied to the trapped system is the determination the number of particles inside the trap. DMFT is generally formulated in the grand-canonical ensemble such that the chemical potential is fixed and the number of particles can fluctuate. However, from the experimental point of view, it is more feasible to look at a constant number of particles confined in the trap and to investigate the influence of interactions. Within DMFT, this can be achieved by applying an algorithm during the DMFT loop which readjusts the chemical potential. After each self-consistency iteration, the number of particles is computed and compared to the desired number of particles. If the actual number exceeds the desired number of particles, the chemical potential is reduced or the other way around, similar to a bisection method. As a result, the number of particles should converge to the desired value while the selfenergy converges

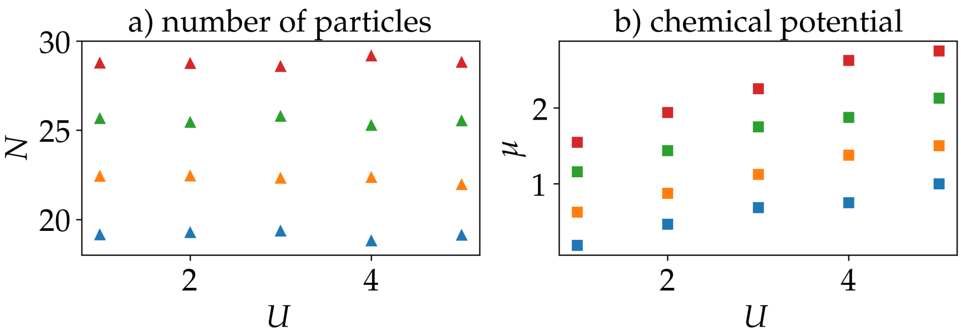

Figure 4.7: Results of the algorithm to fix the number of particles inside the trap. (a) four different values of the number of particles per line in x direction $\bar{N} = 19.2, 22.4, 25.6, 28.9$ averaged over the full range of interaction strengths U. (b) the corresponding chemical potentials as a result of the algorithm.

simultaneously. In order to guarantee convergence, one must be careful in different parameter regimes and in the implementation of this algorithm. It is recommended to find a chemical potential which is close to the final chemical potential by prior considerations. In Fig. 4.7, we show the results of this algorithm. The data is obtained from real-space DMFT with a QMC CT-AUX solver, see Sec. 3.1.4. Due to the cylindric geometry of the system, the total density profile $n_{x,y}$ does not depend on the coordinate y. We are thus only interested in the number of particles for an arbitrary value of y. Furthermore, we introduce the average number of particles for a set of interaction strengths

$$\bar{N} = \left\langle \sum_x n_{x,y=0} \right\rangle_U \tag{4.23}$$

In Fig. 4.7(a), we show the result for fixing the average number of particles to four different values of $\bar{N} = 19.2, 22.4, 25.6, 28.9$ represented in different colors. Figure 4.7(b) shows the corresponding adjusted chemical potentials. The fluctuations in the data stem from the QMC sampling.

We show the total line density profile $n_x = n_x^{\uparrow} + n_x^{\downarrow}$ of the trapped system as a function of x and U in Fig. 4.8. First, we observe that the width of the profile as well as the occupation in the trap center increase with increasing average particle number $\bar{N}$. Secondly, the width increases with increasing interaction strength and at the same time the profile becomes flatter, i.e., the occupation at the trap center decreases. The former mechanism stems from the competition of the Hubbard interaction U with the trapping potential V, the latter from the suppression of doubly occupied sites due to strong interactions U, which refers to bulk physics and is tuned through λ, see Eq. (4.22).

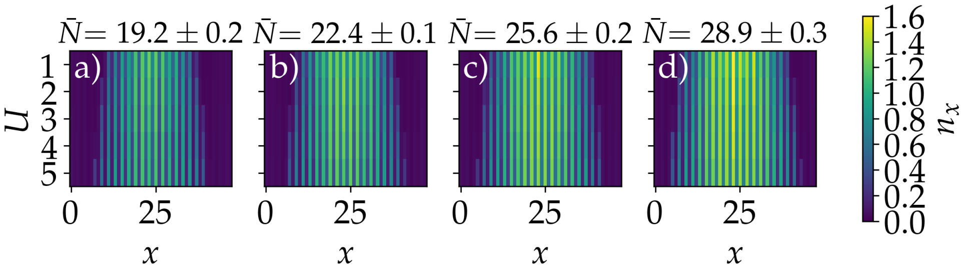

Figure 4.8: Line density profile as a function of x and U for different values of the total number of particles $\bar{N} = 19.2, 22.4, 25.6, 28.9$ defined in Eq. (4.23). Reprinted with permission from Ref. [257]. Copyright (2020) by the American Physical Society.

For strong interaction $U = 5$ and large number of particles $N = 29.2$, we find an interesting side effect which is a feature of the trapping potential. In Fig. 4.9, we plot the spin-resolved line density profiles n_x^σ, the magnetization $n_x^\uparrow - n_x^\downarrow$, and the spectral density ρ_x. We observe that the magnetization is constantly zero except for two very localized points in the system at $x \approx 9$ and $x \approx 37$. Here, the magnetization shows peaks which suggests a spatially small region of magnetic order. Another interpretation could be that there are very well-localized edge states, in contrast to the usually extended edge states in trap geometries [41,275]. For the sake of clarification, we plot the spectral density ρ_x as a red line in Fig. 4.9 and find that the edge states are still extended and decay into the trap center. The left edge state resides at $5 \lesssim x \lesssim 17$ and the right one at $30 \lesssim x \lesssim 43$. Moreover, the edge states are not influenced by the magnetic peaks. We conclude that these peaks are of purely magnetic nature. We explain their emergence as follows: The region

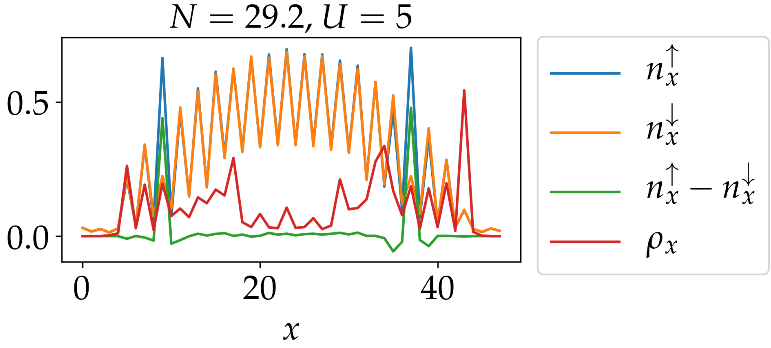

Figure 4.9: Magnetic state at the trap boundary for strong interactions: spin-resolved density profiles n_x^σ, magnetization $n_x^\uparrow - n_x^\downarrow$, and spectral density ρ_x. Reprinted with permission from Ref. [257]. Copyright (2020) by the American Physical Society.

$10 \lesssim x \lesssim 35$ is approximately half filled but protected by the topological gap and can thus not be magnetized through strong interactions. The outer regions $x < 5$ and $x > 37$ have small occupation and can therefore also not be magnetized. Only at specific points, i.e., at $x \approx 9$ and $x \approx 37$, the topological protection is lifted, because the system is gapless here according to the underlying band structure [257]. The occupation is still large enough to induce magnetic ordering.

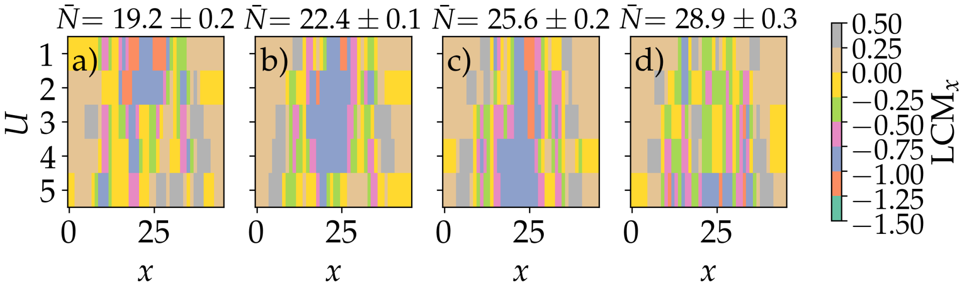

Figure 4.10: Local Chern marker (LCM) of the interacting, trapped system as a function of x and U for different average number of particles $\bar{N} = 19.2, 22.4, 25.6, 28.9$ defined in Eq. (4.23). Reprinted with permission from Ref. [257]. Copyright (2020) by the American Physical Society.

Let us now turn to the computation of the LCM, see Sec. 3.4, for the interacting, trapped system. We again apply the topological Hamiltonian technique, see Sec. 3.3, first which reduces the interacting problem to an effectively noninteracting one and the LCM can directly be applied. In order to find the selfenergy at zero frequency, we perform a polynomial fit for the smallest Matsubara frequencies in magnitude. Through this simple estimate the application of the rather complicated maximum entropy method, which was introduced in Sec. 3.2, can be avoided. As in the section before, we apply the unitary transformation of Eq. (4.3) since we focus on $\gamma = 1/4$ and the transformation simplifies the $\mathbb{Z}_2$ problem to a Chern problem, see Sec. 1.3. We show the LCM as a function of x and U for different numbers of particles in Fig. 4.10. First, we find that in the outer regions, where no particles are present, the LCM is zero which is expected for the vacuum. Secondly, the LCM can be very spiky in the gapless regimes, however, in those, the LCM has no physical meaning. So we can safely ignore these large fluctuations of the LCM. The interesting regions in Fig. 4.10 are the blue ones. Here, the LCM assumes the quantized value -1 which corresponds to a topologically nontrivial QSH phase. These regions appear at larger values of U for a large average number of particles $\bar{N}$. This is because the bulk in the center of the system needs to have a proper filling in order to be in the gapped QSH state. As we explained above, interactions change the density profile because of the suppression of doubly occupied sites.

Concluding this section, we have developed a framework for studying topological phases of matter with Hubbard interactions in inhomogeneous systems. Hence, we are able to analyze and characterize the topological interface even if the phase separation is smooth. Also trapping potentials are smooth in cold atom setups and we studied the competition between the confining trap and the interaction in the system which gives rise to interaction-induced topological phase transitions within the trap.

4.2 Tomography of the local Chern marker

In the previous section, we encountered the local Chern marker (LCM) and learned that it is very useful for the investigation of topologically nontrivial states in systems where the translational lattice symmetry is broken. This is frequently the case for cold atom experiments since they are built from laser potentials which usually vary smoothly in space. This prompted the question whether the LCM is a quantity which can be observable in cold atom setups. In the following, we show that the LCM can be rewritten in terms of the single-particle density matrix for which we then propose a tomographic scheme for its measurement. We recall Eq. (3.82) for the LCM, $C(\boldsymbol{r}) = -4\pi \mathrm{Im}\langle \boldsymbol{r}|\hat{P}\hat{x}\hat{P}\hat{y}\hat{P}|\boldsymbol{r}\rangle$, which is of course only applicable for gapped systems. We now insert the definition of the projector, Eq. (3.80), onto the occupied eigenstates $\hat{P} = \mathcal{N}\sum_{n\in O}\int d\boldsymbol{k}|\psi_n(\boldsymbol{k})\rangle\langle\psi_n(\boldsymbol{k})|$ with the normalization constant $\mathcal{N}$, such that

$$\begin{aligned} C(\boldsymbol{r}) =& -4\pi\mathcal{N}^3 \mathrm{Im}\sum_{nmq}\int d\boldsymbol{k}d\boldsymbol{k}'d\boldsymbol{k}'' \\ &\times \langle \boldsymbol{r}|\psi_n(\boldsymbol{k})\rangle\langle\psi_n(\boldsymbol{k})|\hat{x}|\psi_n(\boldsymbol{k}')\rangle\langle\psi_n(\boldsymbol{k}')|\hat{y}|\psi_n(\boldsymbol{k}'')\rangle\langle\psi_n(\boldsymbol{k}'')|\boldsymbol{r}\rangle. \end{aligned} \tag{4.24}$$

We now introduce two complete sets of eigenstates of the position operator $\mathbb{1} = \sum_{\boldsymbol{r}}|\boldsymbol{r}\rangle\langle\boldsymbol{r}|$ yielding

$$\begin{aligned} C(\boldsymbol{r}) = -4\pi\mathcal{N}^3 \mathrm{Im}\sum_{\boldsymbol{r}'\boldsymbol{r}''}\sum_{nmq}\int & d\boldsymbol{k}d\boldsymbol{k}'d\boldsymbol{k}'' \\ & \times \langle \boldsymbol{r}|\psi_n(\boldsymbol{k})\rangle\langle\psi_n(\boldsymbol{k})|\hat{x}|\boldsymbol{r}'\rangle\langle\boldsymbol{r}'|\psi_n(\boldsymbol{k}')\rangle \\ & \times \langle\psi_n(\boldsymbol{k}')|\hat{y}|\boldsymbol{r}''\rangle\langle\boldsymbol{r}''|\psi_n(\boldsymbol{k}'')\rangle\langle\psi_n(\boldsymbol{k}'')|\boldsymbol{r}\rangle. \end{aligned} \tag{4.25}$$

Using $\hat{x}|\boldsymbol{r}\rangle = x|\boldsymbol{r}\rangle$, and analogously $\hat{y}|\boldsymbol{r}\rangle = y|\boldsymbol{r}\rangle$, this leads to

$$\begin{aligned} C(\boldsymbol{r}) = -4\pi\mathcal{N}^3 \mathrm{Im}\sum_{\boldsymbol{r}'\boldsymbol{r}''}\sum_{nmq}\int & d\boldsymbol{k}d\boldsymbol{k}'d\boldsymbol{k}''x'y'' \\ & \times \langle \boldsymbol{r}|\psi_n(\boldsymbol{k})\rangle\langle\psi_n(\boldsymbol{k})|\boldsymbol{r}'\rangle\langle\boldsymbol{r}'|\psi_n(\boldsymbol{k}')\rangle \\ & \times \langle\psi_n(\boldsymbol{k}')|\boldsymbol{r}''\rangle\langle\boldsymbol{r}''|\psi_n(\boldsymbol{k}'')\rangle\langle\psi_n(\boldsymbol{k}'')|\boldsymbol{r}\rangle. \end{aligned} \tag{4.26}$$

We define the single-particle density matrix as

$$\rho(\boldsymbol{r},\boldsymbol{r}') = \mathcal{N}\sum_n \int d\boldsymbol{k} \langle \boldsymbol{r}|\psi_n(\boldsymbol{k})\rangle\langle\psi_n(\boldsymbol{k})|\boldsymbol{r}'\rangle, \tag{4.27}$$

with $\rho(\boldsymbol{r},\boldsymbol{r}) = n(\boldsymbol{r})$ being the on-site particle density. Then we find for the LCM [254,256]

$$C(\boldsymbol{r}) = -4\pi \mathrm{Im} \sum_{\boldsymbol{r}'\boldsymbol{r}''} x'y''\rho(\boldsymbol{r},\boldsymbol{r}')\rho(\boldsymbol{r}',\boldsymbol{r}'')\rho(\boldsymbol{r}'',\boldsymbol{r}). \tag{4.28}$$

Hence, the LCM can be rewritten in terms of the single-particle density matrix summed over to spatial variables running over the whole lattice. We understand that the word 'local' in LCM is therefore a misnomer, however, we will find that in some regimes the quantity is at least quasi-local, i.e., decays fast enough as $|\boldsymbol{r}-\boldsymbol{r}'| \to \infty$. Further, we find that the formula in Eq. (4.28) is a summation over triangles in real-space with the three corner points at $\boldsymbol{r}$, $\boldsymbol{r}'$, and $\boldsymbol{r}''$ and a nonvanishing area. The area does not vanish since all three corner points have to be different. If, e.g., $\boldsymbol{r} = \boldsymbol{r}' \neq \boldsymbol{r}''$, we find

$$\rho(\boldsymbol{r},\boldsymbol{r}')\rho(\boldsymbol{r}',\boldsymbol{r}'')\rho(\boldsymbol{r}'',\boldsymbol{r}) = n(\boldsymbol{r})\rho(\boldsymbol{r},\boldsymbol{r}'')\rho(\boldsymbol{r}'',\boldsymbol{r}). \tag{4.29}$$

Since $\rho(\boldsymbol{r},\boldsymbol{r}') = \rho^*(\boldsymbol{r}',\boldsymbol{r})$, the right-hand side is strictly real, thus, has no contribution in Eq. (4.28). Hence, only off-diagonal elements $\rho(\boldsymbol{r},\boldsymbol{r}')$ of different density matrices contribute. The idea is now to make the off-diagonal element of the single-particle density matrix experimentally accessible in order to find the LCM in Eq. (4.28). Since the summation of $\boldsymbol{r}'$ and $\boldsymbol{r}''$ run over the whole lattice, which includes an infinite number of triangles to be summed, a proper cut off should be determined. To this end, we reorder the summation in Eq. (4.28) into a summation of groups of equally shaped triangles. The shape is determined by the area and the perimeter of a triangle, which constitute the joint quantity $l = (\text{area}, \text{perimeter})$. The LCM is then computed by $C(\boldsymbol{r}) = \sum_l c_l$, where c_l is the contribution to the LCM from all the triangles which have the same l. These contributions are of course model-dependent. Here, we apply the scheme to the Harper-Hofstadter-Hatsugai (HHH) model introduced in Sec. 2.3. The benefit of this model is that the minimal model for nontrivial topological properties has a two-site unit cell which is achieved for the flux $\alpha = 1/2$. This is in contrast to the Hofstadter model, introduced in Sec. 2.1, where at least three sites in a unit cell are required to show nontrivial topological properties. We do not consider spin degrees of freedom to keep the system as simple as possible. It is described by the tight-binding Hamiltonian

$$\begin{aligned}\hat{H} = -t\sum_{x,y}\Big[&\hat{c}^\dagger_{x+1,y}\hat{c}_{x,y} + (-1)^x\hat{c}^\dagger_{x,y+1}\hat{c}_{x,y} + i(-1)^x\hat{c}^\dagger_{x+1,y+1}\hat{c}_{x,y} \\ &+ i(-1)^x\hat{c}^\dagger_{x,y+1}\hat{c}_{x+1,y} + \text{h.c.}\Big] + \lambda\sum_{x,y}(-1)^x\hat{c}^\dagger_{x,y}\hat{c}_{x,y}.\end{aligned} \tag{4.30}$$

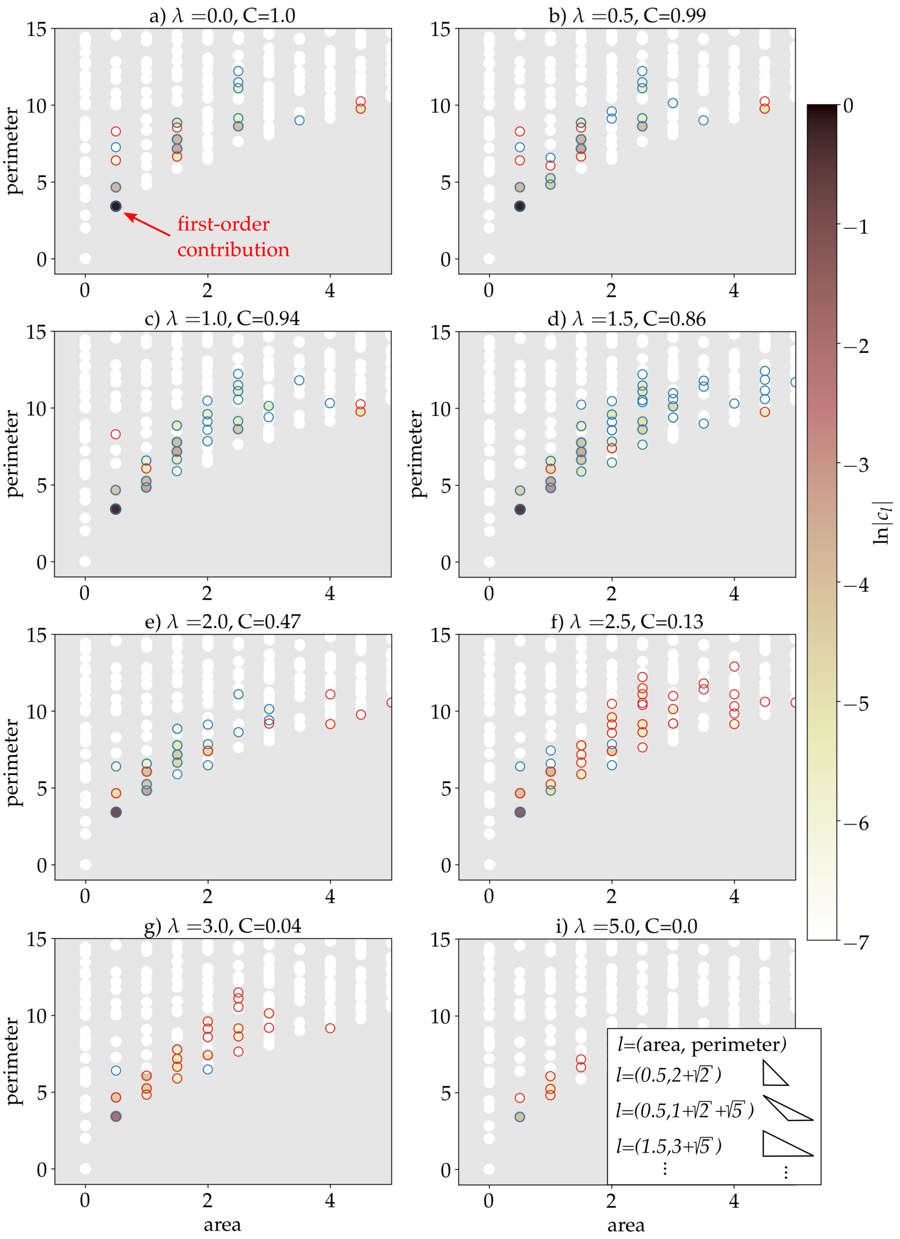

Figure 4.11: Contributions to the local Chern marker c_l as a function of $l = (\text{area}, \text{perimeter})$ for different values of the staggered potential λ in (a)-(i). The topological phase transition occurs at the critical value $\lambda_c = 2$ [195]. The colormap corresponds to the absolute value of c_l in log scale down to a cut off 10^{-7} for better visibility. The blue (red) circles denote the positive (negative) sign of the contribution c_l. C refers to the sum of all computed c_l. The data is obtained for the HHH model in Eq. (4.30) on a 40×40 lattice. Reprinted with permission from Ref. [256]. Copyright (2020) by the American Physical Society.

Here, we use the hopping energy as the unit of energy $t = 1$ and λ is the amplitude of the staggered potential which is a control parameter for the topological phase of the Hamiltonian in Eq. (4.30). There is a phase transition at $\lambda_c = 2$: For $0 \leq \lambda < 2$, the system is in a topologically nontrivial phase with Chern number $C = 1$ while for $\lambda > 2$ it is in a topologically trivial phase, $C = 0$ [195].

Microscopic contributions

We show the contributions to the LCM c_l as a function of the area and the perimeter in Fig. 4.11 for different values of the staggered potential λ. The absolute value of c_l is shown as a colorcode and the sign is depicted as a blue (red) circle for a positive (negative) sign. Furthermore, the C denotes the sum of all computed contributions c_l which should resemble the Chern number. We observe that all c_l with zero area vanish as we discussed above. Next, we see that in Fig. 4.11(a) the contribution from $l = (0.5, 2 + \sqrt{2})$ is the highest and two orders of magnitude larger than the remaining contributions. We will call the contribution from $l = (0.5, 2 + \sqrt{2})$ the *first-order contribution*. We will investigate whether this quantity is suitable to detect topological phase separations in ultracold quantum gases in optical lattices.

As we increase the staggered potential, the system will undergo a phase transition at the critical value for the staggered potential $\lambda_c = 2$. As λ approaches λ_c the first-order contribution decreases and more positive contributions from larger triangles emerge. Right after the phase transition, in Fig. 4.11(f), these contributions from larger triangles flip sign such that the summation with the first-order contribution vanishes. Increasing λ even further reduces the number of nonvanishing contributions.

As the results in Fig. 4.11 show, the first-order contribution is the largest and it might be sufficient to determine topological properties in inhomogeneous systems. We now focus on the first-order contribution which means that we only include triangles in Eq. (4.28) which contain off-diagonal elements of density matrices $\rho(\boldsymbol{r}, \boldsymbol{r'})$, where $\boldsymbol{r}$ is nearest or next-nearest neighbor of $\boldsymbol{r'}$. In the case of a square lattice with two sites in the unit cell, there exist eight such ρ_i which we label with numbers $i = 1, \dots 8$. This is shown in Fig. 4.12, where the two sites of the unit cell are labeled with A, marked in red, and B, marked in black, respectively. The eight ρ_i appear repeatedly according to the lattice symmetry. In x direction the lattice is periodic with period 2 and in y direction it is translationally symmetric. We only consider translational symmetries; mirror symmetries might even further reduce the number of different ρ_i. Since the density matrix is complex-valued the ρ_i possess an associated direction such that, e.g., ρ_1 connects (x, y) with $(x + 1, y + 1)$ and ρ_1^* connects $(x + 1, y + 1)$ with (x, y) as shown in Fig. 4.12. The LCM $C(\boldsymbol{r}_A)$ of site $\boldsymbol{r}_A$ is now computed as the sum of all possible combinations of three connected ρ_i with $\boldsymbol{r}_A$ being the starting point. There are 48

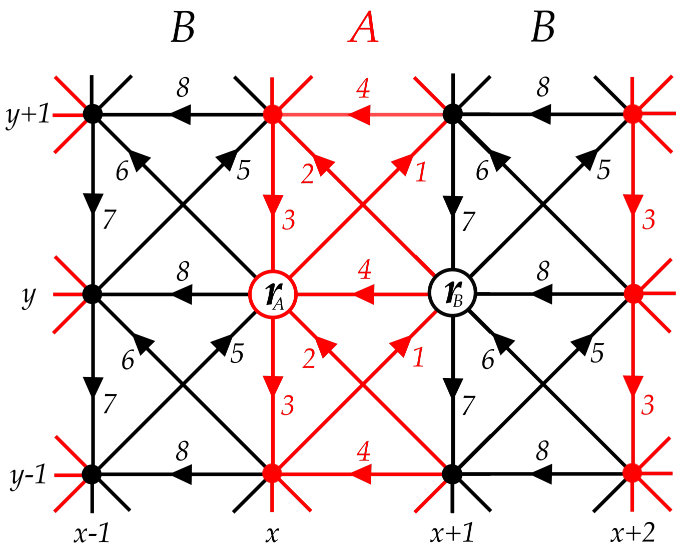

Figure 4.12: Schematic of the lattice of the Hamiltonian in Eq. (4.30) with the two-site unit cell (A, B). Sublattice A (B) is colored in red (black). The numbers label the density matrices connecting two sites, e.g., ρ_1 connects (x, y) and $(x+1, y+1)$, ρ_2 connects $(x+1, y)$ and $(x, y+1)$, and so on. Reprinted with permission from Ref. [256]. Copyright (2020) by the American Physical Society.

combinations of that. Starting with ρ_1, three exemplary terms are

$$\begin{aligned} C(\boldsymbol{r}_A) = -4\pi \mathrm{Im}\,[&(x_A+1)y_A\rho_1\rho_7\rho_4 + (x_A+1)(y_A+1)\rho_7^*\rho_4^*\rho_1^* \\ &+ (x_A+1)(y_A+1)\rho_1\rho_4\rho_3 + \dots, \end{aligned} \tag{4.31}$$

and analogously for $\boldsymbol{r}_B$

$$\begin{aligned} C(\boldsymbol{r}_B) = -4\pi \mathrm{Im}\,[&(x_B+1)y_B\rho_5\rho_3\rho_8 + (x_B+1)(y_B+1)\rho_8^*\rho_3^*\rho_5^* \\ &+ (x_B+1)(y_B+1)\rho_5\rho_8\rho_7 + \dots, \end{aligned} \tag{4.32}$$

with another 48 terms. The examples in Eqs. (4.31) and (4.32) can be retraced from Fig. 4.12 by applying Eq. (4.28) with only nearest and next-nearest neighbors. We define the unit cell average $\bar{C} = [C(\boldsymbol{r}_A) + C(\boldsymbol{r}_B)]/2$. Computing $\bar{C}$ and using that $\boldsymbol{r}_B = \boldsymbol{r}_A + \hat{e}_x$, we find that

$$\bar{C} = -4\pi(\rho_7 - \rho_3)(2\rho_5\rho_8 + 2\rho_6\rho_8^* - \rho_1\rho_4 - \rho_2\rho_4^*). \tag{4.33}$$

This formula is applicable for any square lattice model with a two-site unit cell. It is not specific for the HHH model.

Finite-size scaling

In Fig. 4.13(a), we show the bulk average $\bar{C}$ as well as the first-order contribution as functions of the staggered potential λ for different system sizes

$N \times N$. While we observe that the transition of $\bar{C}$ becomes sharper with increasing N, the first-order contribution is independent of N. This is because the first-order transition is almost local, i.e., it contains only contributions from a small neighborhood of nearest and next-nearest neighbors.

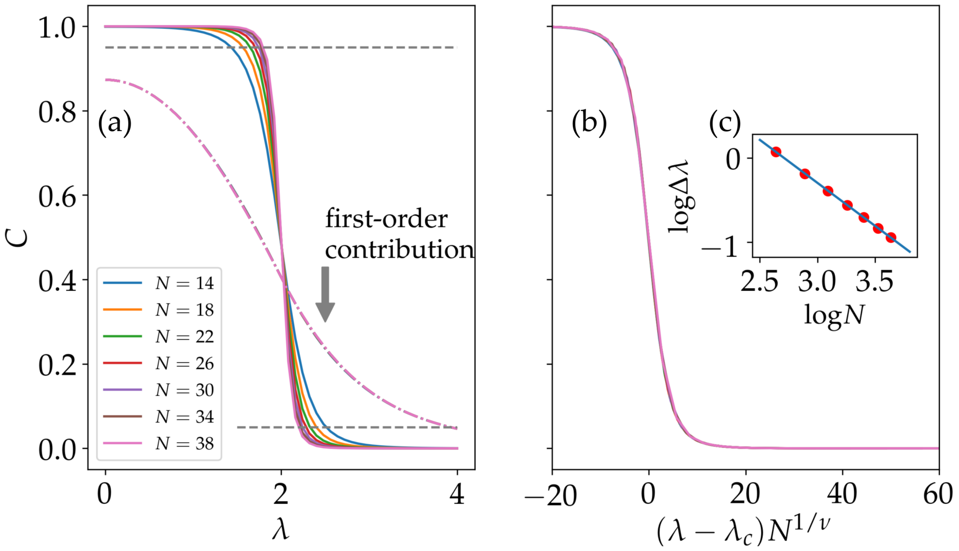

Figure 4.13: Topological phase transition of the system described by the Hamiltonian in Eq. (4.30) controlled through the staggered potential λ. (a) bulk average of the LCM $\bar{C}$ as a function of λ for different system sizes $N \times N$. (b) rescaled $\bar{C} \sim \tilde{f}([\lambda - \lambda_c]N^{1/\nu})$. (c) determination of the critical exponent of the topological phase transition ν. Reprinted with permission from Ref. [256]. Copyright (2020) by the American Physical Society.

Let us now look at the scaling of the LCM with the system size. In Ref. [254], the LCM for the Haldane model, see Sec. 2.4, has been investigated. Therein, a finite size analysis has been performed. We will now go along these lines for the HHH model. We assume that finite size effects occur if the bulk correlation length ξ is of the same order as the system size N, where we consider square lattices $N \times N$ and the lattice constant is set to unity. The bulk average of the LCM $\bar{C}$ thus should behave as a function of ξ/N. This leads us to $\bar{C} \sim f(\xi/N)$. We further assume that the correlation length is divergent obeying a power law at the topological phase transition at λ_c. This yields the relation $\xi \sim (\lambda - \lambda_c)^{-\nu}$. For the bulk average of the LCM we thus find the following scaling behavior:

$$\begin{aligned} \bar{C} &\sim f(\xi/N) \sim f([\lambda - \lambda_c]^{-\nu}/N) \\ &\sim \tilde{f}([(\lambda - \lambda_c)^{-\nu}/N]^{-1/\nu}) \sim \tilde{f}([\lambda - \lambda_c]N^{1/\nu}), \end{aligned} \tag{4.34}$$

where we have defined $\tilde{f}$ in the second line being a function of $(\xi/N)^{-1/\nu}$, in contrast to $f(\xi/N)$. In order to use this new function, we have to find an estimate for the exponent ν. To this end, we define $\Delta\lambda$, a window in which the phase transition happens, and look at its scaling. We assume that it is of the form $\log \Delta\lambda = -(1/\nu) \log N$. To check with the data, we define $\Delta\lambda = |\lambda_{0.95} - \lambda_{0.05}|$ with $\bar{C}(\lambda = \lambda_{0.95}) = 0.95$ and $\bar{C}(\lambda = \lambda_{0.05}) = 0.05$ for different values of N. This is shown in Fig. 4.13(a) with the grey dashed lines representing $\bar{C} = 0.95$ and $\bar{C} = 0.05$, respectively. The intersections with the actual curves of $\bar{C}$ then defines $\lambda_{0.95}$ and $\lambda_{0.05}$ and thus $\Delta\lambda$. We now plot $\log \Delta\lambda$ as a function of $\log N$ in Fig. 4.13(c) and a linear fit yields the critical exponent $\nu \approx 1.02$. With this value, we can now plot the rescaled $\bar{C}$ according to Eq. (4.34). This is shown in Fig. 4.13(b). We observe that all curves for different values of N collapse onto a single universal curve. In Ref. [254] it is suggested that this confirms that the LCM can be used to determine a topological phase transition, in a similar fashion like a local order parameter. Of course, the two perceptions of a topological phase transition and a local order parameter are contradictory since topological properties are global properties and cannot be reduced to local properties. Especially at the phase transition, the correlation length diverges and finite size effects play a role no matter how large the system is. However, it turns out that away from the topological phase transition the LCM can give a good idea of the topological properties of the system. This is because the contributions to the LCM become more localized away from the phase transition as we stressed while discussing Fig. 4.11.

As we have analyzed the contributions, the scaling, and the first-order contribution of the LCM in detail, let us now look at two examples. We have investigated the smooth topological interface as well as the harmonic trap in the context of interacting topological states in Sec. 4.1. We have seen the good applicability of the LCM in these systems and will now compare it to its first-order contribution, which we already introduced in this section. In Fig. 4.14(a), we show the LCM and the first-order contribution as a function of the spatial coordinate x for the half-filled HHH model described by the Hamiltonian in Eq. (4.30). The system confined through a harmonic trapping potential on a 40×40 lattice and we set $\lambda = 0$. We observe that the first-order contribution resembles the qualitative behavior of the LCM, but quantitatively does not reach the quantized value of 1 in the center of the system as the LCM does. As it was expected from the results in Fig. 4.11 the first-order contribution is responsible for the main contribution to the LCM but the remaining contribution from higher orders is still significant. On the other hand, the first-order contribution might act as an indicator for topological nontrivial spatial regions even without a quantized value since it well coincides with the drop off of the LCM when going from the trap center to the boundary of the system. We also plot the density profile in Fig. 4.14(a) and observe that the drop off is already resembled by the corresponding density profile in the trapped system. It is anticipated that the LCM as well as its first-order contribution vanish for a vanishing density

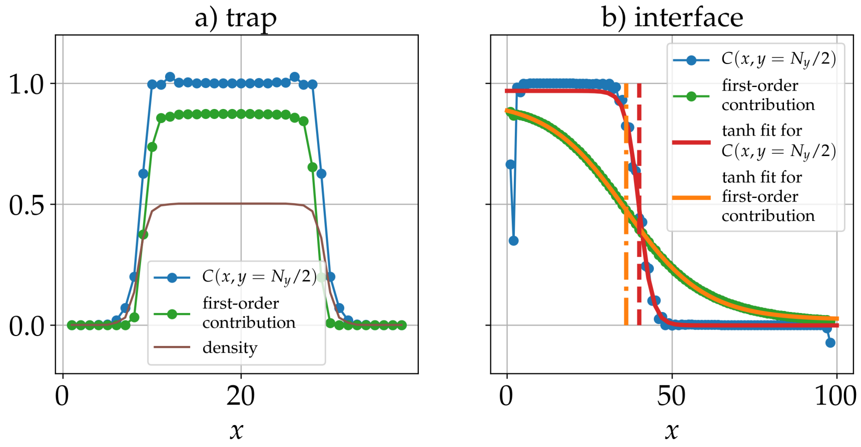

Figure 4.14: Examples for inhomogeneous systems: (a) harmonic trap and (b) smooth topological interface to apply the LCM and its first-order contribution. Reprinted with permission from Ref. [256]. Copyright (2020) by the American Physical Society.

of particles.

In Fig. 4.14(b), we show the results for the LCM and its first-order contribution for the smooth topological interface as it was already introduced in Sec. 4.1.1. The smooth interface is created by a staggered potential whose amplitude is linearly increased in space. We compute the HHH model on a lattice of size 100 × 20 and add a potential of the form $\lambda(x) = (-1)^x 5x/100$ such that we find $\lambda(0) = 0$ and $\lambda(100) = 5$. Thus, we expect that the critical value λ_c is reached at $x = 40$ so we expect the LCM to drop here from 1 to zero. This is indeed the case as shown in Fig. 4.14(b) and we can clearly identify the phase separation between the topologically trivial, $40 < x < 100$, and nontrivial phase, $0 < x < 40$. The first-order contribution, on the other hand, looks rather smooth and a phase transition, at first glance, cannot be read off easily. To circumvent this, we fit the data of the LCM and the first-order contribution with hyperbolic tangent functions according to $a \tanh(c\lambda - c\lambda') - b$. Here, a, b, c, and λ' are fitting parameters, where λ' directly gives an estimate of the critical value for the phase transition λ_c. The fit curves are shown in red for the LCM and in orange for the first-order contribution in Fig. 4.14(b). The dashed line of the respective curve shows the value for the fit parameter λ' and thus shows the estimated location of the phase transition. For the local Chern marker we find $\lambda' \approx 2$ which is exactly the expected value of the critical value λ_c. For the first-order contribution, we find $\lambda' \approx 1.8$ which underestimates λ_c by roughly 10%.

Let us now turn to the possible experimental measurement of the first-order contribution to the LCM. As we discussed, it contains off-diagonal matrix elements of the density matrix connecting two sites. Here, the sites are nearest neighbors or next-nearest neighbors. The aim is to quench the system into an effective two-level system and look at the time evolution of the density matrix to read out its off-diagonal elements. The two-site density matrix is defined as

$$\bar{\rho}(\boldsymbol{r},\boldsymbol{r}') = \begin{pmatrix} n(\boldsymbol{r}) & \rho(\boldsymbol{r},\boldsymbol{r}') \\ \rho(\boldsymbol{r}',\boldsymbol{r}) & n(\boldsymbol{r}') \end{pmatrix} = \begin{pmatrix} n(\boldsymbol{r}) & \rho(\boldsymbol{r},\boldsymbol{r}') \\ \rho^*(\boldsymbol{r},\boldsymbol{r}') & n(\boldsymbol{r}') \end{pmatrix}. \tag{4.35}$$

Here, the on-site densities $n(\boldsymbol{r})$ can be measured by means of time-of-flight measurements or quantum gas microscopes which we discussed in Sec. 1.4. The off-diagonal elements $\rho(\boldsymbol{r},\boldsymbol{r}')$, on the other hand, cannot be directly measured and one needs to measure them indirectly via the diagonal terms. This is done by effectively rotating $\bar{\rho}(\boldsymbol{r},\boldsymbol{r}')$ such that off-diagonal elements are rotated into the diagonal element. This is dubbed tomography and is a increasingly popular approach in cold atom setups [115,196,296–298].

We quench the system with a Hamiltonian $\hat{H}_Q$ which both enables hopping of particles between the two sites and imposes an on-site energy difference between the sites. In pseudo-spin representation, i.e., we use Pauli matrices, this reads

$$H_Q = J(\cos\theta\sigma^x + \sin\theta\sigma^z), \tag{4.36}$$

where the σ^x term corresponds to the hopping with energy $J\cos\theta$ and the σ^z term corresponds to the on-site energy difference with magnitude $J\sin\theta$. We chose the trigonometric expression to achieve an analytic result for the subsequent time evolution. A similar measurement which corresponds to $\theta = 0$ has been performed before in ladder systems [299]. The density matrix in Eq. (4.35) in pseudo-spin representation reads

$$\bar{\rho}(\boldsymbol{r},\boldsymbol{r}') = n(\boldsymbol{r})\frac{\mathbb{1}+\sigma^z}{2} + n(\boldsymbol{r}')\frac{\mathbb{1}-\sigma^z}{2} + \mathrm{Re}[\rho(\boldsymbol{r},\boldsymbol{r}')]\sigma^x + i\mathrm{Im}[\rho(\boldsymbol{r},\boldsymbol{r}')]\sigma^y. \tag{4.37}$$

The time evolution of $\bar{\rho}(\boldsymbol{r},\boldsymbol{r}')$ with H_Q is

$$\bar{\rho}(\boldsymbol{r},\boldsymbol{r}',t) = e^{iH_Qt}\bar{\rho}(\boldsymbol{r},\boldsymbol{r}')e^{-iH_Qt}, \tag{4.38}$$

where we can use now the Euler relation for Pauli matrices

$$e^{ia\boldsymbol{n}\cdot\boldsymbol{\sigma}} = \cos(a)\mathbb{1} + i\sin(a)\boldsymbol{n}\cdot\boldsymbol{\sigma}, \tag{4.39}$$

where $|\boldsymbol{n}| = 1$, in our case in Eq. (4.36) we have $\boldsymbol{n} = (\cos\theta, 0, \sin\theta)$. Hence, we find

$$e^{iH_Qt} = \cos(tJ)\mathbb{1} + i\sin(tJ)\cos(\theta)\sigma^x + i\sin(tJ)\sin(\theta)\sigma^z. \tag{4.40}$$

Combining Eqs. (4.35), (4.38), and (4.40) we find for the time evolution of the on-site density at $\boldsymbol{r}$

$$\begin{aligned} n(\boldsymbol{r},t) =& n(\boldsymbol{r}) - [n(\boldsymbol{r}) - n(\boldsymbol{r}')]\cos^2(\theta)\sin^2(tJ) \\ &+ \mathrm{Re}[\rho(\boldsymbol{r},\boldsymbol{r}')]\sin(2\theta)\sin^2(tJ) \\ &+ \mathrm{Im}[\rho(\boldsymbol{r},\boldsymbol{r}')]\cos(\theta)\sin(2tJ). \end{aligned} \tag{4.41}$$

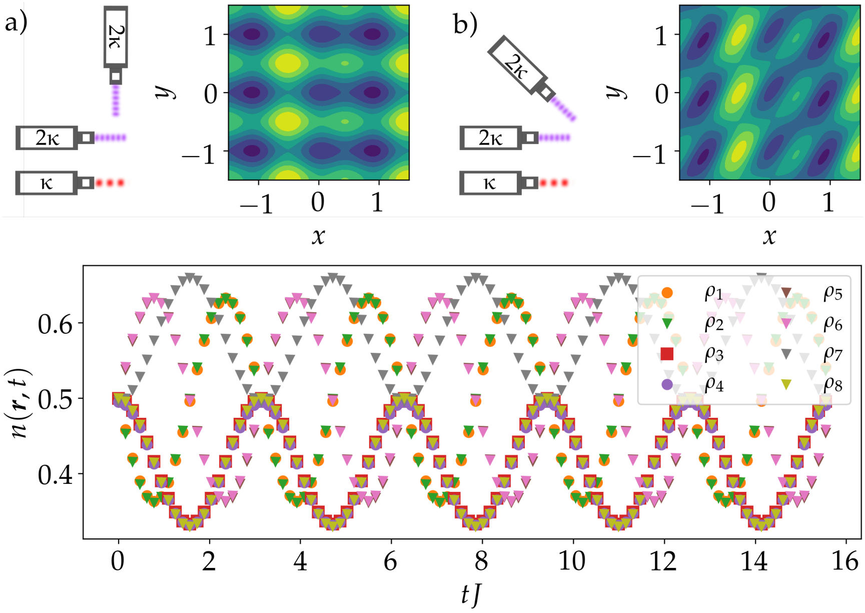

Figure 4.15: Quench potentials for the time evolution for the determination of the off-diagonal density matrix elements for (a) nearest neighbors and (b) next-nearest neighbors. Time evolution $n(\boldsymbol{r},t)$ is shown in (c). Reprinted with permission from Ref. [256]. Copyright (2020) by the American Physical Society.

Through measuring $n(\boldsymbol{r},t)$ at different points in time t and using Eq. (4.41) as a fit function for the measured data we get access to the off-diagonal elements of $\bar{\rho}(\boldsymbol{r},\boldsymbol{r}')$. $\mathrm{Re}[\rho(\boldsymbol{r},\boldsymbol{r}')]$ and $\mathrm{Im}[\rho(\boldsymbol{r},\boldsymbol{r}')]$ act as fit parameters. $n(\boldsymbol{r}')$ is either another fit parameter or can be measured. In Fig. 4.15(c) we examplarily show the time evolution in order to determine the eight off-diagonal density matrix elements ρ_i of the square lattice with a two-site unit cell presented in Fig. 4.12 for a value $\theta = \pi/6$.

Using a quantum gas microscope, $n(\boldsymbol{r},t)$ could be simultaneously accessed for all lattice sites $\boldsymbol{r}$ at once by performing snap shots after different evolution times t. The challenge here is to create a lattice potential which dimerizes the lattice such that one achieves locally the Hamiltonian H_Q from Eq. (4.36). We propose a lattice potential scheme in Fig. 4.15(a) for nearest-neighbor lattice sites and (b) next-nearest-neighbor lattice sites. The corresponding laser configuration is also shown. For nearest neighbors in x direction a laser with wavevector 2κ points in the y direction with π/κ matching the lattice constant of the original square lattice. In x direction two lasers with wavevectors 2κ and κ are applied which exhibit a small phase difference. This phase difference is necessary to create the on-site energy offset between the two dimer lattice sites. For next-nearest neighbors, the dimerization has to connect diagonally displaced lattice sites. A corresponding dimerization potential can be generated by rotating the 2κ laser in y direction by 45° into the $x - y$ direction. The resulting potential is shown in Fig. 4.15(b).

Even though the experimental implementation with the dimerization potential might be comparably simple, it is not clear that coupling to neighboring sites, which do not belong to the dimer, are sufficiently well suppressed. In a future study, this could be answered by explicitly computing the Wannier functions and subsequently the hopping matrix elements in the potential. Furthermore, one could try to optimize the hopping matrix elements as a function of the laser parameters such as intensities and phase shifts. An alternative approach to measure the density matrix is proposed in Ref. [298] where a quantum gas microscope is used to couple far distant lattice sites through a two-level Hamiltonian by engineering a coupling channel.

Concluding this section, we want to point out that approximating the LCM by its first-order contribution might be helpful in situations where the system is not close to a topological phase transition. It is then possible through tomographic measurements to compute this first-order contribution to the LCM. If a quantum gas microscope is implemented in the experimental setup for the detection of local densities it could also be used to measure higher contributions to the LCM according to Eq. (4.28). To this end, an automatized protocol would be necessary keeping track of all the contributions in Eq. (4.28). As we discussed for this example, the lattice symmetry significantly reduces the number of measurements. Quantum gas microscopes have already been combined with artificial gauge fields [147]. Such a real-space measurement with cold atoms would then complement a similar experiment in photonic systems [300] in which many different contributions to the topological index have been detected and collected to yield a well-quantized number. Recently, the LCM has been measured in a cold atom system with synthetic dimensions [150]. Synthetic dimensions are well-suited for such measurements since the synthetic sites can be coupled straightforwardly.

4.2.1 Tomography of the topological Hamiltonian

In the previous section, we have discussed the tomography of the LCM using real-space state tomography for noninteracting inhomogeneous systems. For extended noninteracting systems, theoretical works proposed fast Raman pulses [296] and quench dynamics [297] in order to map out the corresponding state properties. Experimentally, the proposal of Ref. [297] was realized in a shaken hexagonal lattice [115] and was improved though lattice modulation techniques [301].

Tomography of states of systems with finite two-body interactions requires a different, more complex theoretical framework. We embed the discussion of measuring the topological properties of many-body states into this section. In Sec. 4.1, we have seen that the topological Hamiltonian H_{top}, which we introduced in Sec. 3.3, is a convenient tool for computing topological invariants of interacting systems. Therefore, accessing the topological Hamiltonian of an interacting topological state experimentally would readily lead to a topological invariant of the interacting system. Of course, this applies only if the requirements for the topological Hamiltonian approach is fulfilled, see Sec. 3.3. Unfortunately, H_{top} is an effective Hamiltonian and does not describe a physical system. However, in the following, we discuss a particular case in which the topological Hamiltonian can be related to the single-particle density matrix. In the noninteracting case, the energy spectrum of a translationally invariant system consists of bands. If interactions between the particles is present, these bands become broadened and one has to consult the spectral function, see Sec. 1.7, as an analog to the energy spectrum. If the broadening is small compared to other energy scales in the system, we can still identify so-called quasiparticle bands. The broadening is then associated with the inverse lifetime of these quasiparticles.

In a system with two quasiparticle bands, e.g. two sublattices, the topological Hamiltonian can be related to the single-particle density matrix in the following way [196]:

$$H_{\text{top}}^{-1}(\boldsymbol{k}) \simeq \frac{\rho^T(\boldsymbol{k})}{\epsilon^+(\boldsymbol{k})} - \frac{\mathbb{1} - \rho^T(\boldsymbol{k})}{\epsilon^-(\boldsymbol{k})}, \tag{4.42}$$

where $\rho(\boldsymbol{k})$ is the single-particle density matrix and $\epsilon^{\pm}(\boldsymbol{k})$ correspond to the upper and lower quasiparticle band, respectively. The single-particle density matrix can be obtained from the full many-body density matrix

$$\mathcal{P}_{\text{MB}} = \sum_{\eta} p_{\eta} |\eta\rangle\langle\eta|, \tag{4.43}$$

where $|\eta\rangle$ is a many-body state and p_η is the distribution function with $\sum_\eta p_\eta = 1$. The single-particle density matrix follows as

$$\rho(\boldsymbol{k})|_{ij} = \text{Tr}\left[\hat{c}^{\dagger}_{\boldsymbol{k}i}\hat{c}_{\boldsymbol{k}j}\mathcal{P}_{\text{MB}}\right]. \tag{4.44}$$

Here, i and j label the internal state of the two-level system according to the sublattices A and B.

Coming back to Eq. (4.42), it is of course only valid if we can assign quasiparticle bands, i.e., the linewidth is small. Furthermore, we observe that the eigenstates of the inverse of $H_{\text{top}}(\boldsymbol{k})$ are the same as the eigenstates of the transpose of $\rho(\boldsymbol{k})$ because the identity will only provide an offset to the eigenvalues. We conclude that measuring the single-particle density matrix reveals all the information we need for the topological Hamiltonian which we can then use to compute the topological invariants.

A density matrix ρ for a two-level system can always be expressed in terms of Pauli matrices. This is true for its transpose as well. So, we find

$$\rho(\boldsymbol{k})^T = \frac{1}{2}\left[\mathbb{1} + \boldsymbol{a}(\boldsymbol{k})\cdot\boldsymbol{\sigma}\right], \tag{4.45}$$

where $\boldsymbol{\sigma} = (\sigma^x, \sigma^y, \sigma^z)$ is the Pauli vector. The components of $\boldsymbol{a}(\boldsymbol{k})$ can be accessed through

$$a_i(\boldsymbol{k}) = \mathrm{Tr}\left[\rho(\boldsymbol{k})^T\sigma^i\right] = \sum_\eta p_\eta \langle\eta|\hat{\boldsymbol{c}}_{\boldsymbol{k}}^\dagger\sigma^i\hat{\boldsymbol{c}}_{\boldsymbol{k}}|\eta\rangle, \tag{4.46}$$

where $i = x, y, z$. Here, we have used the two-sublattice pseudo-spinor notation $\hat{\boldsymbol{c}}_{\boldsymbol{k}}^\dagger = (\hat{c}_{A\boldsymbol{k}}^\dagger, \hat{c}_{B\boldsymbol{k}}^\dagger)$. Since $\boldsymbol{a}(\boldsymbol{k})$ fully determines $\rho(\boldsymbol{k})$ which subsequently determines $H_{\mathrm{top}}(\boldsymbol{k})$, we are interested in a method to measure $\boldsymbol{a}(\boldsymbol{k})$. Like in the previous section, this is done by means of state tomography. Therein, it was pointed out that direct measurements of the density distribution reveal only the diagonal components of the single-particle density matrix. Using a quench of the system to a new Hamiltonian then provides access to the off-diagonal elements of the single-particle density matrix. The quench two-level Hamiltonian should have the general form

$$\hat{H}_Q = \sum_{\boldsymbol{k}} \hat{\boldsymbol{c}}_{\boldsymbol{k}}^\dagger \boldsymbol{h}(\boldsymbol{k})\cdot\boldsymbol{\sigma}\hat{\boldsymbol{c}}_{\boldsymbol{k}}, \tag{4.47}$$

where $\boldsymbol{h}(\boldsymbol{k})$ is the quench protocol. The quench will put the system in a nonequilibrium state such that the field operators evolve as $e^{-i\hat{H}_{\mathrm{Q}}t}\hat{\boldsymbol{c}}_{\boldsymbol{k}}$ with evolution time t.

The tomography scheme will contain three steps. First, the interaction is switched off by tuning the respective Feshbach resonance, see Sec. 1.4. Secondly, the system is immediately quenched with the Hamiltonian in Eq. (4.47) with a finite evolution period $0 < t < \tau$. The components of $\boldsymbol{a}(\boldsymbol{k}, t)$ will evolve during this period as

$$a_i(\boldsymbol{k}, t) = \sum_\eta p_\eta \langle\eta|\hat{\boldsymbol{c}}_{\boldsymbol{k}}^\dagger e^{i\hat{H}_{\mathrm{Q}}t}\sigma^i e^{-i\hat{H}_{\mathrm{Q}}t}\hat{\boldsymbol{c}}_{\boldsymbol{k}}|\eta\rangle. \tag{4.48}$$

Finally, all potentials are switched off in order to perform a time-of-flight measurement.

Before we discuss the exact tomography protocol, i.e., the form of $\boldsymbol{h}(\boldsymbol{k})$, let us look at the measurement of the density distribution. In order to access the momentum distribution of the particle density, one typically uses time-of-flight measurements, see Sec. 1.4. According to Ref. [106], this distribution reads

$$\hat{n}_{\mathrm{TOF}}(\boldsymbol{k}) \propto \frac{1}{t_{\mathrm{TOF}}^3}\sum_{\boldsymbol{r}\boldsymbol{r}'} e^{ik(r-r')}\hat{c}_{\boldsymbol{r}}^\dagger\hat{c}_{\boldsymbol{r}'} \tag{4.49}$$

where t_{TOF} is the time-of-flight expansion time and $\hat{c}_{\boldsymbol{r}}$ is the field operator which annihilates a particle at site $\boldsymbol{r}$ in real space. We rewrite the right-hand side as

$$\begin{aligned}
\sum_{\boldsymbol{r}\boldsymbol{r}'} e^{i\boldsymbol{k}(\boldsymbol{r}-\boldsymbol{r}')}\hat{c}^{\dagger}_{\boldsymbol{r}}\hat{c}_{\boldsymbol{r}'} =& \sum_{\boldsymbol{r}} e^{i\boldsymbol{k}\boldsymbol{r}}\hat{c}^{\dagger}_{\boldsymbol{r}} \sum_{\boldsymbol{r}'} e^{-i\boldsymbol{k}\boldsymbol{r}'}\hat{c}_{\boldsymbol{r}'} \\
=& \left[\sum_{\boldsymbol{r}\in A} e^{i\boldsymbol{k}\boldsymbol{r}}\hat{c}^{\dagger}_{\boldsymbol{r}} + \sum_{\boldsymbol{r}\in B} e^{i\boldsymbol{k}\boldsymbol{r}}\hat{c}^{\dagger}_{\boldsymbol{r}}\right] \\
& \times \left[\sum_{\boldsymbol{r}'\in A} e^{-i\boldsymbol{k}\boldsymbol{r}'}\hat{c}_{\boldsymbol{r}'} + \sum_{\boldsymbol{r}'\in B} e^{-i\boldsymbol{k}\boldsymbol{r}'}\hat{c}_{\boldsymbol{r}'}\right] \\
\propto& (\hat{c}^{\dagger}_{A\boldsymbol{k}} + \hat{c}^{\dagger}_{B\boldsymbol{k}})(\hat{c}_{A\boldsymbol{k}} + \hat{c}_{B\boldsymbol{k}}),
\end{aligned} \tag{4.50}$$

where we have used in the second equation that the lattice in real space consists of two sublattices. In the last step, we performed a Fourier transformation. We obtain for the expectation value of Eq. (4.49):

$$n_{\text{TOF}}(\boldsymbol{k}) = \langle \hat{n}_{\text{TOF}}(\boldsymbol{k})\rangle \propto \left\langle (\hat{c}^{\dagger}_{A\boldsymbol{k}} + \hat{c}^{\dagger}_{B\boldsymbol{k}})(\hat{c}_{A\boldsymbol{k}} + \hat{c}_{B\boldsymbol{k}})\right\rangle, \tag{4.51}$$

which we also rewrite:

$$\begin{aligned}
\left\langle (\hat{c}^{\dagger}_{A\boldsymbol{k}} + \hat{c}^{\dagger}_{B\boldsymbol{k}})(\hat{c}_{A\boldsymbol{k}} + \hat{c}_{B\boldsymbol{k}})\right\rangle =& \left\langle \hat{c}^{\dagger}_{A\boldsymbol{k}}\hat{c}_{A\boldsymbol{k}} + \hat{c}^{\dagger}_{B\boldsymbol{k}}\hat{c}_{B\boldsymbol{k}}\right\rangle \\
& + \left\langle \hat{c}^{\dagger}_{A\boldsymbol{k}}\hat{c}_{B\boldsymbol{k}} + \hat{c}^{\dagger}_{B\boldsymbol{k}}\hat{c}_{A\boldsymbol{k}}\right\rangle \\
=& \left\langle \hat{\boldsymbol{c}}^{\dagger}_{\boldsymbol{k}}\mathbb{1}\hat{\boldsymbol{c}}_{\boldsymbol{k}}\right\rangle + \left\langle \hat{\boldsymbol{c}}^{\dagger}_{\boldsymbol{k}}\sigma^{x}\hat{\boldsymbol{c}}_{\boldsymbol{k}}\right\rangle \\
=& 1 + a_x(\boldsymbol{k}),
\end{aligned} \tag{4.52}$$

where we have used Eq. (4.46) in the last equation. In this we have dropped the time argument. Note, however, that this value corresponds to the value at the end of the quench, right at the beginning of the time-of-flight expansion:

$$n_{\text{TOF}}(\boldsymbol{k}) = 1 + a_x(\boldsymbol{k}, \tau). \tag{4.53}$$

As we read off Eq. (4.52), only the first component of $\boldsymbol{a}(\boldsymbol{k}, \tau)$ can be accessed through a time-of-flight measurement. The aim is now to set up quench protocols $\boldsymbol{h}(\boldsymbol{k})$ which map the other components onto $a_x(\boldsymbol{k}, \tau)$. Let us consider the specific quench $\boldsymbol{h}(\boldsymbol{k}) = (0, 0, 1)$. In an optical lattice experiment, this corresponds to suppressing all hopping processes and imposing a staggered potential. This is shown in Fig. 4.16(a) where all sites of sublattice A have an energy offset of J and all sites of sublattice B an energy offset of $-J$. Using Eq. (4.48) for $i = x$, the particular quench Hamiltonian leads to the

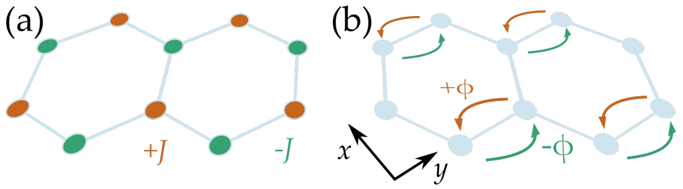

Figure 4.16: Schematics of quench protocols for the tomography of a two-level mixed state according to Eq. (4.47): (a) corresponds to $\boldsymbol{h}(\boldsymbol{k}) = (0, 0, 1)$ and (b) to $\boldsymbol{h}(\boldsymbol{k}) = (\cos(k_y + \phi), \sin(k_y + \phi), 0)$.

evolution:

$$\begin{aligned} e^{i\hat{H}_Q t}\sigma^x e^{-i\hat{H}_Q t} =& e^{itJ\sigma^z}\sigma^x e^{-itJ\sigma^z} \\ =& \left[\cos(tJ)\mathbb{1} + i\sin(tJ)\sigma^z\right]\sigma^x\left[\cos(tJ)\mathbb{1} - i\sin(tJ)\sigma^z\right] \\ =& \left[\cos^2(tJ) - \sin^2(tJ)\right]\sigma^x \\ &+ i\cos(tJ)\sin(tJ)\left[\sigma^z\sigma^x - \sigma^x\sigma^z\right] \\ =& \cos(2tJ)\sigma^x - \sin(2tJ)\sigma^y. \end{aligned} \tag{4.54}$$

Together with Eqs. (4.48), (4.51), and (4.52), we find that $a_x(\boldsymbol{k})$ and $a_y(\boldsymbol{k})$ are mapped onto $a_x(\boldsymbol{k}, \tau)$ in a periodic manner in τ. By fitting the experimental data of different evolution times τ, one can obtain $a_x(\boldsymbol{k})$ and $a_y(\boldsymbol{k})$.

For a pure state, this is sufficient since we know that $|\boldsymbol{a}(\boldsymbol{k})| = 1$. We are, however, interested in interacting systems such that we deal with a mixed state, i.e., $|\boldsymbol{a}(\boldsymbol{k})| < 1$. Thus, a second protocol is necessary. One possibility is to use $\boldsymbol{h}(\boldsymbol{k}) = (\cos(k_y + \phi), \sin(k_y + \phi), 0)$ which corresponds to hopping between nearest neighbors along the y axis only. The hopping process is also accompanied by phase shift ϕ. This is depicted schematically in Fig. 4.16(b) and can be engineered by periodic shaking [302,303]. Following the steps we performed for the first protocol, the second protocol leads to the mapping

$$\begin{aligned} a_x(\boldsymbol{k}, \tau) = & \left[\cos^2(tJ) + \sin^2(tJ)\cos(2k_y + 2\phi)\right] a_x(\boldsymbol{k}) \\ &+ \sin^2(tJ)\sin(2k_y + 2\phi)a_y(\boldsymbol{k}) \\ &+ \sin(2tJ)\sin(k_y + \phi)a_z(\boldsymbol{k}) \end{aligned} \tag{4.55}$$

Eventually, we have full access to the vector $\boldsymbol{a}(\boldsymbol{k})$ and subsequently to $H_{\text{top}}(\boldsymbol{k})$ via Eq. (4.42). The Chern number would then readily follow from Eq. (1.3) with the eigenstates of $H_{\text{top}}(\boldsymbol{k})$. It is, on the other hand, also possible to map out the Berry curvature and subsequently the Chern number directly. This can be seen from the following formula for the Chern number specialized to a two-level system:

$$C = -\frac{1}{4\pi}\int d\boldsymbol{k}\left[\partial_{k_x}\hat{\boldsymbol{a}}(\boldsymbol{k}) \times \partial_{k_y}\hat{\boldsymbol{a}}(\boldsymbol{k})\right] \cdot \hat{\boldsymbol{a}}(\boldsymbol{k}), \tag{4.56}$$

where $\hat{\tilde{\boldsymbol{a}}}(\boldsymbol{k}) = \tilde{\boldsymbol{a}}(\boldsymbol{k})/|\tilde{\boldsymbol{a}}(\boldsymbol{k})|$ and $\tilde{\boldsymbol{a}}(\boldsymbol{k})$ is a unitary transformation of $\boldsymbol{a}(\boldsymbol{k})$ such that the periodicity of the BZ is properly implemented. The particular form of Eq. (4.56) can be interpreted as a 2d winding number of the vector $\hat{\tilde{\boldsymbol{a}}}(\boldsymbol{k})$ [50]. Using this formula it is possible to map out directly the topological phase transition in interacting systems. This has be shown for the interaction-induced topological phase transition in the Haldane-Hubbard model [198] in Ref. [196].

4.3 Spin-imbalanced Hofstadter-Hubbard model

In this section, we present a study on the fermionic Hofstadter-Hubbard model with repulsive Hubbard interaction and an additional imbalance in the population of spin-up and down particles. The spin-imbalanced Hofstadter model has been investigated in the noninteracting case showing diverse Chern insulating phases depending on the filling and the amount of imbalance [304]. Also the attractive spin-imbalanced Hofstadter-Hubbard model has been investigated giving rise to exotic many-body phases such as striped supersolids [305]. What follows is the complementary study for repulsive interactions.

We are interested in this model since the two groundstates of the TRS Hofstadter-Hubbard model and the imbalanced Hubbard model are utterly different. This is schematically highlighted in Fig. 4.17(a)-(d). Let us start the discussion with the standard Hubbard model depicted in (a) which was already discussed in Sec. 1.7. Here, the Hamiltonian of the model exhibits the lattice symmetry L which contains translational, rotational, and inversion symmetries of the lattice. The spin symmetry stems from the present spin-1/2 fermions and its symmetry group is SU(2). Upon breaking the symmetry spontaneously through Hubbard interactions the groundstate is found to be AFM, see the subsection on the Heisenberg model in Sec. 1.7. Applying an additional Zeeman field $\boldsymbol{B}$, as shown in (c), the symmetry of the Hamiltonian as well as the symmetry of the groundstate is reduced compared to the case in (a). The Zeeman field induces a spin imbalance and the groundstate will be a canted AFM. We note that the canted AFM exhibits a finite net magnetization parallel to $\boldsymbol{B}$ which compensates the Zeeman field. For infinitesimal field strength $B = |\boldsymbol{B}|$, the spins remain completely in the plane perpendicular to $\boldsymbol{B}$. This is different when we go over to the balanced TRS Hofstadter-Hubbard model shown in (b). Here, the flux α, originating from the gauge field, breaks the SU(2) symmetry of case (a) and the groundstate becomes an AFM pointing strictly in z direction. We understand that the Zeeman field as well as the flux both break the spin symmetry of the standard Hubbard model, however, in very different ways. This leads to completely different groundstates and we are interested in what the combination of these two effects will yield. Of course, the spin

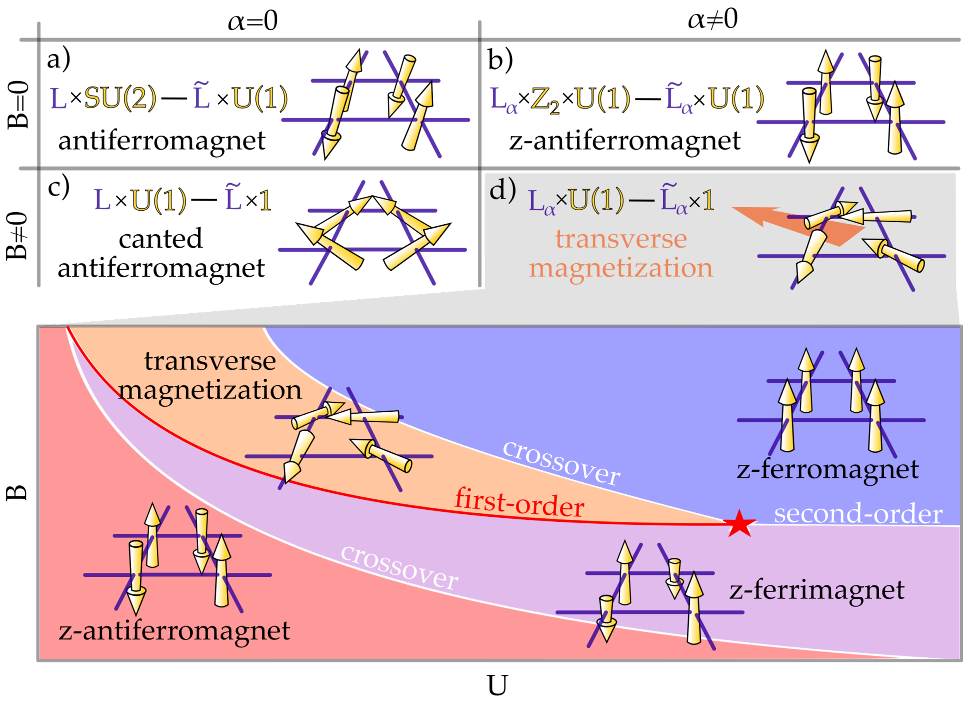
α=0
α≠0
B=0
B≠0
a)
L×SU(2)—L̃×U(1)
antiferromagnet
b)
L_α×Z_2×U(1)—L̃_α×U(1)
z-antiferromagnet
c)
L×U(1)—L̃×1
canted
antiferromagnet
d)
L_α×U(1)—L̃_α×1
transverse
magnetization
transverse
magnetization
crossover
z-ferromagnet
first-order
second-order
crossover
z-ferrimagnet
z-antiferromagnet
B
U

Figure 4.17: Symmetries of the Hamiltonians and the groundstates of the symmetry-broken phase as well as schematics of these groundstates for: (a) standard Hubbard model, (b) TRS Hofstadter-Hubbard model, (c) imbalanced Hubbard model, and (d) imbalanced Hofstadter-Hubbard model. Lattice symmetries are colored in purple and spin symmetries are colored in yellow. The phase diagram schematically shows the groundstate of the imbalanced Hofstadter-Hubbard model. Reprinted with permission from Ref. [306]. Copyright (2020) by the American Physical Society.

imbalance will break the TRS.

Before we proceed, it is worth mentioning that the discussed system has relevance in cold atomic experiments. Mazurenko et al. have measured AFM long-range correlations in an optical lattice filled with the two lowest hyperfine states of ^{6}Li atoms [81]. The work is also remarkable since it uses a technique to reshuffle entropy in the system, see Sec. 1.4, through which it is actually possible to reach such low temperatures required for fermionic superexchange. Shortly after, the canted AFM has been observed also with ^{6}Li atoms by Brown et al. [307]. Currently, successful experiments featuring artificial gauge fields and interactions are restricted due to enhanced heating rate in the quantum gas experiments [308, 309]. However, Görg et al. have measured magnetic correlations in driven systems and studied the interplay between driving and interactions [148]. This shows that there is a good chance for the realization of spin-imbalanced, interacting topological states in cold atom systems in the future. The Hamiltonian of the spin-imbalanced Hofstadter-Hubbard model reads

$$\begin{aligned}\hat{H} = &- t \sum_{x,y} \left[\hat{c}^{\dagger}_{x+1,y} \hat{c}_{x,y} + \hat{c}^{\dagger}_{x,y+1} e^{2\pi i \alpha x \sigma^z} \hat{c}_{x,y} + \text{h.c.} \right] \\ &+ U \sum_{x,y} \left[\hat{c}^{\dagger}_{\uparrow,x,y} \hat{c}_{\uparrow,x,y} \hat{c}^{\dagger}_{\downarrow,x,y} \hat{c}_{\downarrow,x,y} \right] ,\end{aligned} \tag{4.57}$$

where the flux is chosen in TRS manner due to the spin-selective field $\alpha\sigma^z$. TRS is preserved, as long as there is no Zeeman field $\boldsymbol{B}$. Also, there are no spin-mixing terms included such as in Sec. 4.1. We start investigating this model in the strong interaction limit where the charge degrees of freedom freeze out and the mapping to an effective Heisenberg model can be applied [190]:

$$\begin{aligned}\hat{H} = J \sum_{x,y} \Big\{ &\hat{S}^x_{x+1,y} \hat{S}^x_{x,y} + \hat{S}^y_{x+1,y} \hat{S}^y_{x,y} + \hat{S}^z_{x+1,y} \hat{S}^z_{x,y} \\ &+ \cos(4\pi\alpha x) \left[\hat{S}^x_{x,y+1} \hat{S}^x_{x,y} + \hat{S}^y_{x,y+1} \hat{S}^y_{x,y} \right] \\ &+ \sin(4\pi\alpha x) \left[\hat{S}^y_{x,y+1} \hat{S}^x_{x,y} - \hat{S}^x_{x,y+1} \hat{S}^y_{x,y} \right] + \hat{S}^z_{x,y+1} \hat{S}^z_{x,y} \Big\} ,\end{aligned} \tag{4.58}$$

with $J = U/t^2$ being the superexchange energy, $\hat{S}^i_{x,y} = \hat{c}^{\dagger}_{x,y} \sigma^i \hat{c}_{x,y}$ the spin operator at site x, y in coordinate space, and σ^i the ith Pauli matrix. Equation (4.58) is the effective spin Hamiltonian of the spin-balanced Hofstadter-Hubbard model. Before we start discussing the spin-imbalanced system, let us look at some of its features. By setting $\alpha = 1/2$, the Hamiltonian in Eq. (4.58) reduces to the usual Heisenberg model with an SU(2) degenerate AFM groundstate, see Sec. 1.7. For general α, there is always Heisenberg coupling between spins coupled along the x direction. For spins which are coupled along the y direction, however, the spin components, which lie in the $\hat{S}^x \hat{S}^y$ plane, possess a different coupling compared to the $\hat{S}^z$ component. This asymmetry was discussed in Fig. 4.17(b) leading to an AFM groundstate with a staggered magnetization pointing in the z direction, what we call z antiferromagnet in Fig. 4.17. The term proportional to the cosine corresponds to the scalar product of the two-dimensional in-plane spin vectors and is maximized in magnitude if the spins are parallel or anti-parallel. The term proportional to the sine corresponds to the z component of the cross product of the neighboring spin vectors. It is maximized if the spin vectors are in-plane and orthogonal to each other. This term corresponds to the so-called Dzyaloshinsky-Moriya interaction [310, 311]. So we recognize the competition between the cosine and the sine term. After $\alpha = 1/2$, the second most simple case is $\alpha = 1/4$. Here, the cosine becomes $(-1)^x$ and the sine vanishes completely. It is the easiest nontrivial case and will be the focus in what follows.

Classical Monte Carlo results

We now consider the classical limit of the Hamiltonian in Eq. (4.58), i.e., we are interested in the mean-field, or saddlepoint, solution $\langle \hat{S}_{x,y} \rangle$ and neglect fluctuations of $\hat{S}_{x,y}$. Thus, we substitute the operators in Eq. (4.58) by their respective expectation values $S^i_{x,y} = \langle \hat{S}^i_{x,y} \rangle$. Later, we will investigate fluctuations within DMFT. In the classical limit, the $S^i_{x,y}$ are just numbers and the groundstate of a finite system can be found by minimizing Eq. (4.58) with respect to the set of $S^i_{x,y}$. Also, in the classical limit, the spins are normalized, i.e., $|\mathbf{S}_{x,y}| = 1$. This simplifies the problem to two degrees of freedom per site. A system of $N_x \times N_y$ classical spins has therefore $2 \times N_x \times N_y$ degrees of freedom. PBC can reduce that number, however, in general, it is a large number which makes the minimization difficult. This problem can be tackled by means of Monte Carlo (MC) algorithms. Here, we use *annealing* MC in order to find the groundstate of this high-dimensional problem. Annealing MC algorithms are successful methods to find the global minimum of a function. A schematic example of a classical spin system is shown in Fig. 4.18. Out of an ensemble of spins (a) with total energy E_1 we randomly select one spin, shown in orange, which is then rotated in a random fashion, shown in (b). The total energy change $\Delta E = E_2 - E_1$ of the new configuration (b) with energy E_2 is measured. With the acceptance probability of the Metropolis sampling $\min\{1, \exp(-\beta \Delta E)\}$ [230], the new spin configuration is accepted and the loop starts over as explained earlier. Since the spin rotations are randomly performed, the total magnetization is not conserved during this procedure. The prefix 'annealing' stands for the slow cool down of the temperature $T = 1/\beta$. For large T the sampling can cover large areas of the state space. The temperature is then slowly reduced to very low values such that the acceptance rate of high-energy states is suppressed. This algorithm can be computationally costly but finds the global minimum with slow enough cooling of T.

We now introduce spin imbalance to the Hamiltonian in Eq. (4.58). This can be done by adding a Zeeman term $-B \sum_{x,y} S^z_{x,y}$. This, however, determines the imbalance $S^z := \sum_{x,y} S^z_{x,y}$ only approximately during the MC process and fluctuations will be present. In order to circumvent this problem, we make use of a method which allows us to set specific constraints on the groundstate, the so-called constrained MC introduced in Ref. [312]. Here, the MC procedure is not applied to a single spin within an ensemble of spins but rather to a pair of spins. The second spin is a compensation spin which is used to recover the desired magnetization. We schematically depict the constrained MC procedure in Fig. 4.18(c) and (d). Constrained MC is applied because we want to preserve the total magnetization of the possible sampled states, i.e., in our case S^z should be a fixed number. To this end, two spins out of the ensemble are randomly selected, shown in orange and green in (c). The orange spin is then randomly rotated as in normal MC

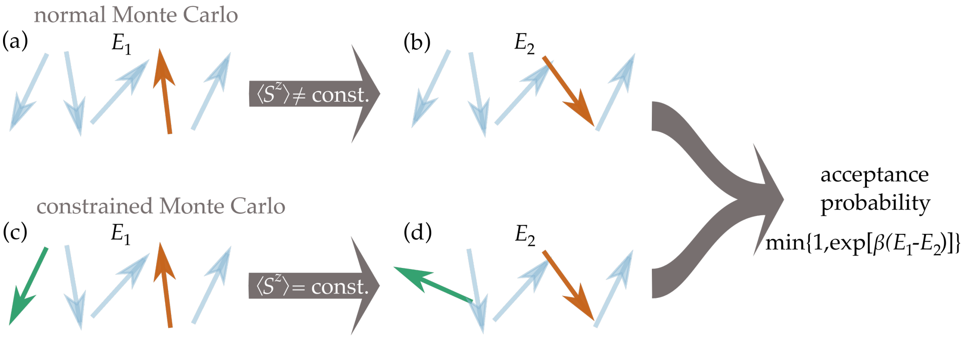

Figure 4.18: Schematic comparison between normal Monte Carlo and constrained Monte Carlo [312]: In normal Monte Carlo a random spin is randomly rotated from (a) to (b) and the energy difference determines the acceptance probability. In constrained Monte Carlo, two random spins are selected, while one (orange) is randomly rotated from (c) to (d), the other is (green) rotated in such a manner that the total magnetization, say S_z, is not changed.

and the green compensation spin used to match the correct value of the total S^z magnetization, shown in (d). This means, that the S^z component of the green spin is constrained by the sampling of the orange spin. The sampling of the orange spin has two degrees of freedom. Due to the constraint, the sampling of the green spin has just one degree of freedom. Thus a MC proposal in constrained MC samples three spin degrees of freedom in contrast to normal MC where there are only two degrees of freedom sampled.

We show the results for the spin Hamiltonian in Eq. (4.58) in the classical limit obtained with constrained annealing MC in Fig. 4.19 for $\alpha = 1/4$. In order to find the correct size of the unit cell, we perform calculations for different sizes of the unit cell $N_x \times N_y$ and compute the energy per spin. This is shown in Fig. 4.19(a) for $\alpha = 1/4$ and $S^z = 1/3$. We observe that multiples of $N_x \times N_y = 2 \times 2$ yield the same energy per spin which is smaller than sizes not being multiples of 2×2. This suggests that 2×2 is the correct size of the unit cell for the classical system. We show the corresponding spin configuration in Fig. 4.19(b) for $S^z = 1/3$. Here, the blue colormap stands for the on-site S^z component and the red arrows denote the on-site $S^x S^y$ components. Furthermore, the unit cell is labeled by A, B, A′, and B′. We note that A and A′ as well as B and B′ exhibit the same S^z values but differ in the respective S^x and S^y values. This results in a chequerboard pattern for $S^z_{x,y}$. The $S^x S^y$ components, however, possess a more complex pattern. Their direction is rotated by 90° between the A and the A′ sites. This 90° rotation also applies to the B and B′ sites. When summing up these contributions within one unit cell we find that the net in-plane magnetization is finite, in contrast to, e.g., a canted AFM.

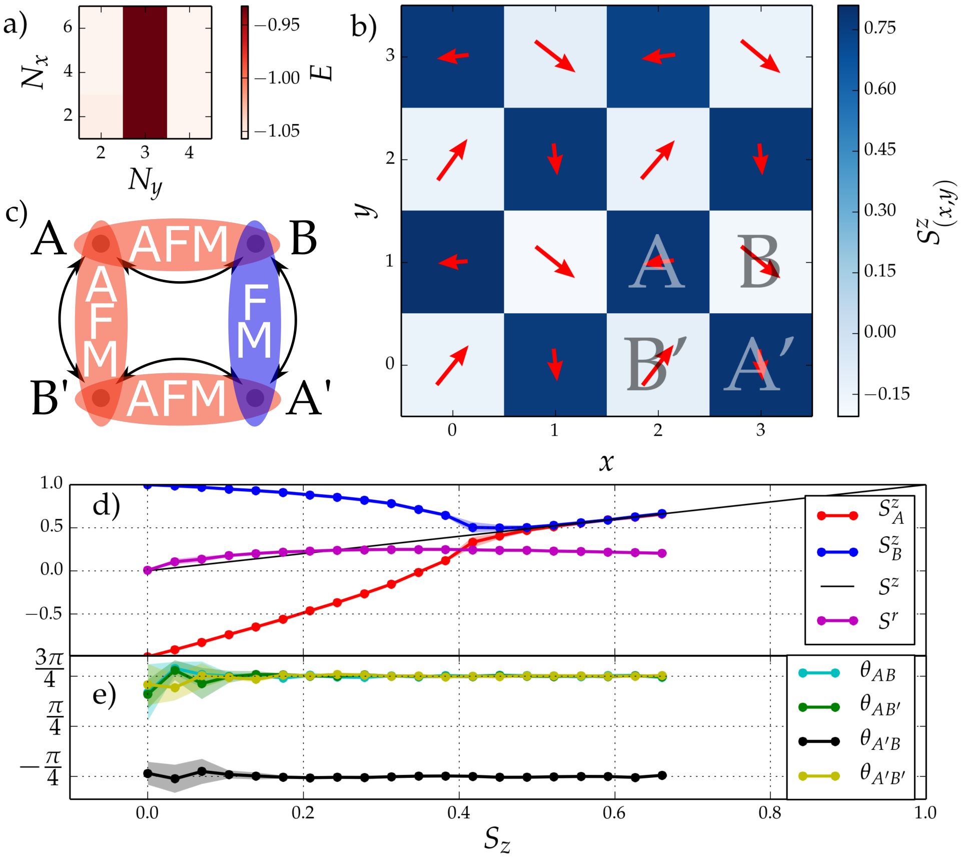

Figure 4.19: Constrained Monte Carlo results for the classical limit of the spin Hamiltonian in Eq. (4.58) for $\alpha = 1/4$: (a) energy per spin E as a function of the size of the unit cell $N_x \times N_y$, (b) spin configuration for $S^z = 1/3$, on-site S^z components in blue-white color scale and on-site $S^x S^y$ components as red arrows, (c) schematic pattern of spin-spin couplings in the unit cell for the Hamiltonian in Eq. (4.58) for $\alpha = 1/4$, (d) sublattice S^z components and transverse magnetization S^r as functions of the total magnetization S^z, and (e) angles between spins in the $S^x S^y$ plane within the unit cell. Reprinted with permission from Ref. [306]. Copyright (2020) by the American Physical Society.

We can explain the exotic spin pattern of Fig. 4.19(b) by looking closer at the Hamiltonian in Eq. (4.58) for $\alpha = 1/4$. For this value of the plaquette flux, the term proportional to the sine is always zero. The term proportional to the cosine, however, becomes an alternating function with respect to the lattice site index x: $\cos(4\pi\alpha x) \rightarrow (-1)^x$. This means that for even values of x the coupling in y direction is AFM and for odd x it is ferromagnetic (FM), as we depict schematically in Fig. 4.19(c). This scheme is reminiscent of the XY model proposed by Villain which was originally introduced to form a spin glass without disorder [313]. Here, three FM bonds and one AFM bond constitute the unit cell. As a result, the system is geometrically frustrated since it cannot fulfill the preferred configuration of all these bonds simultaneously. We can map the Villain model to our model through $J \to -J$. The Villain model in a broader context is also known as the fully frustrated XY model, a special case of the frustrated XY model. Its classical groundstate is known [313,314] and can be mapped to the spin configuration of the in-plane components of Fig. 4.19(b) via rotating every other spin by 180°. The frustrated XY model has attracted attention over many decades because of its two phase transitions which have similar critical temperatures. This made the problem complex and intriguing for theorists [314–316].

Coming back to the model in Eq. (4.58) for $\alpha = 1/4$ and finite magnetization $S^z \neq 0$, we are interested in the transition between the balanced and the imbalanced case. As we know from Ref. [192], the spin configuration of the classical groundstate for the Hamiltonian in Eq. (4.58) at $S^z = 0$ is a z AFM. This is because the gauge field, present through α, breaks the SU(2) symmetry of the normal Hubbard model, see Fig. 4.17. We show the S^z components of the A and the B sublattices, equivalent to the A′ and B′ sublattices, in Fig. 4.19(d) as a function of the magnetization S^z. For $S^z = 0$, we find the balanced case and $S^z_A = -S^z_B = -1$ corresponding to an AFM in z direction. For large S^z we find $S^z_A = S^z_B = S^z$ which corresponds to a FM in z direction. Note that for very large values of $S^z \gtrsim 0.7$ there are no data points. This is because constrained MC suffers from bad sampling since it becomes unlikely to find a proper compensation spin. At around $S^z \approx 0.4$ we find a phase transition between these two regimes. For small increasing values of S^z, the on-site value S^z_A increases from -1 while S^z_B decreases from 1. Since the spins are normalized in the classical limit, they must acquire finite S^x and S^y components if $S^z < 1$. As discussed above, these in-plane components sum up to a finite net magnetization which is inside the plane. We quantify this transverse magnetization through

$$S^r = \frac{1}{N_x N_y} \sqrt{\left(\sum_{x,y} S^x_{x,y} \right)^2 + \left(\sum_{x,y} S^y_{x,y} \right)^2} . \tag{4.59}$$

We observe that S^r is finite throughout the range $0 < S^z < 1$. Furthermore, we look at the angles between the in-plane spins of different sites of the unit cell θ_{ij} with $i, j \in \{\text{A, B, A}', \text{B}'\}$ in Fig. 4.19(e). We find that all angles are constant during the full range $0 \leq S^z \leq 1$ with some fluctuations at small values of S^z. These arise from MC sampling since the energy difference for different angles is very small in this regime.

DMFT results

After we have discussed the Hofstadter-Hubbard model in Eq. (4.58) in the classical limit for the general spin-imbalanced case, we now study the influence of quantum fluctuations leading to corrections to the classical limit or even to new phases. We use real-space DMFT with an ED solver with four bath sites, Sec. 3.1, in order to include all local quantum fluctuations. In contrast to the constrained MC scheme, we do not have the possibility to seek for solutions with an exactly determined magnetization S^z. Instead, we introduce the spin imbalance through a finite Zeeman field B. We are interested in the half-filled case, in which we can include the Zeeman field directly into the chemical potential $\mu_\sigma = U/2 \pm B$, where the plus applies for the spin-up, $\sigma = \uparrow$, and the minus for the spin-down particles, $\sigma = \downarrow$. This formula ensures that the lattice is half-filled at any value of B.

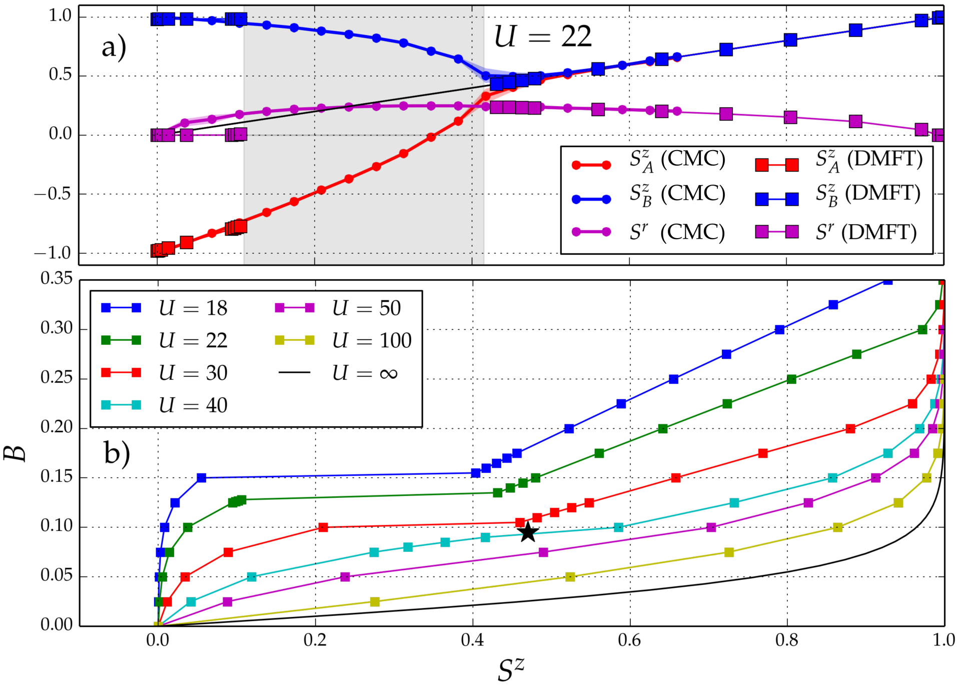

Figure 4.20: Comparison between constrained Monte Carlo and DMFT results in (a) and magnetization S^z as a function of the Zeeman field strength B for different values of the interaction strength U in (b) including Eq. (4.62).

We perform DMFT calculations with different chemical potentials μ_σ for the two spin species. We compare the DMFT results, exemplarily at $U = 22$, with the constrained MC results of Fig. 4.19(d), corresponding to the strong interaction limit, in Fig. 4.20(a). At $S^z = 0$ and $0.4 \lesssim S^z \lesssim 0.7$, we find perfect agreement between both the DMFT and the constrained MC results. In the range $0 < S^z \lesssim 0.1$, the two theories differ. Here, DMFT shows constantly $S^z_B = 1$ and $S^r = 0$, but an increasing S^z_A as a function of B. We will later see that this corresponds to a ferrimagnet, a state which cannot be obtained from the classical limit since it relaxes the strict spin normalization at a site $|\hat{S}_{x,y}| \leq 1$. We conclude that the many-body phase obtained with constrained MC partially breaks down in the presence of local quantum fluctuations. We also observe that there are no data points of DMFT in the grey shaded region in Fig. 4.20(a). This occurs because we obtain solutions for a fixed Zeeman field B. We go into more detail in Fig. 4.20(b), where we show the magnetization S^z as a function of the Zeeman field B. For $U = 22$, which is the green curve, we clearly find a jump in S^z when B passes over $B \approx 0.13$ corresponding to a first-order phase transition. The size of the jump, i.e., from $S^z \approx 0.1$ to $S^z \approx 0.4$, corresponds to the width of the shaded region in Fig. 4.20(a). For $U = 18$, the size of the jump is even larger. For $U = 30$, the size decreases until it vanishes at $U = 40$. This point is marked as a black star in the phase diagram. It is a critical point where the phase transition becomes a second-order instead of first-order. For higher interaction strengths, the phase transition remains a second-order phase transition. For infinite interaction strength, the energy scale for the superexchange $J = t^2/U$ is completely suppressed such that the Hamiltonian reads $\hat{H} = -B \sum_{x,y} \hat{S}^z_{x,y}$. Since there is no hopping, this Hamiltonian applies for a single site. We thus drop the site index and the Hamiltonian reads

$$\hat{H} = -B\hat{n}_\uparrow + B\hat{n}_\downarrow, \tag{4.60}$$

which is diagonal and has eigenstates $|\uparrow\rangle$ and $|\downarrow\rangle$. We find for the magnetization

$$S^z = \frac{\langle\uparrow|(+1)e^{-\beta\hat{H}}|\uparrow\rangle + \langle\downarrow|(-1)e^{-\beta\hat{H}}|\uparrow\rangle}{\langle\uparrow|e^{-\beta\hat{H}}|\uparrow\rangle + \langle\uparrow|e^{-\beta\hat{H}}|\uparrow\rangle} \tag{4.61}$$

$$= \frac{e^{+\beta B} - e^{-\beta B}}{e^{+\beta B} + e^{-\beta B}} = \frac{1}{1+e^{-2\beta B}} - \frac{1}{1+e^{2\beta B}}. \tag{4.62}$$

This solution is shown in Fig. 4.20(b) as solid black line and we find that is an asymptotic curve for the DMFT curves as expected.

We now show the phase diagram of the spin-imbalanced Hofstadter-Hubbard model. To this end, we define four different order parameters. We remember that the Hofstadter-Hubbard model does not have the SU(2) symmetry, so we keep track of magnetization in z direction only. The order parameter for the FM phase is the sublattice average of the on-site magnetization in z direction $(S^z_A + S^z_B)/2$. For the AFM order parameter, we compute the sublattice difference of the on-site S^z components $(S^z_A - S^z_B)/2$. Ferrimagnetism is quantified through the difference in length of the S^z components between the sublattices $|S^z_A| - |S^z_B|$. The new phase which we already found with constrained MC in Fig. 4.19(d) for $S^z \gtrsim 0.4$ is assigned to the order parameter S^r defined in Eq. (4.59). The four order parameters

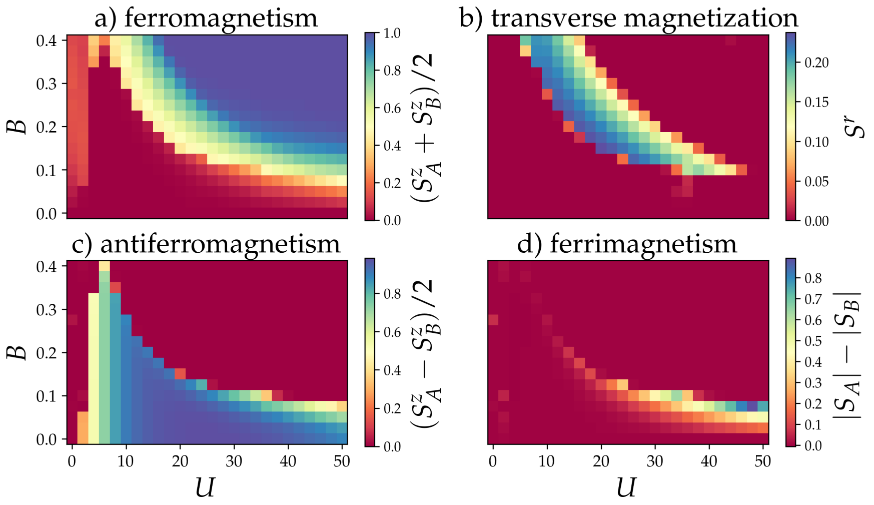

Figure 4.21: Order parameters for the four different magnetic phases of the spin-imbalanced Hofstadter-Hubbard model obtained from DMFT. Reprinted with permission from Ref. [306]. Copyright (2020) by the American Physical Society.

are depicted in Fig. 4.21. We observe that FM exists for a strong Zeeman field B and AFM for small B. This stems from the competition between the two energy scales of superexchange J and Zeeman field B. In the transition region where $J = t^2/U \sim B$, we find the transversely magnetized phase which we know from Fig. 4.19. Furthermore, for small $B \lesssim 0.1$ and strong interactions $U \gtrsim 30$, there exists a ferrimagnetic phase. In our results, the ferrimagnet is strongest at $U = 48$ and $B \approx 0.1$.

From the experimental perspective, spin correlations belong to the state-of-the-art measurements in cold atom systems [81,307] and the manipulation of spin correlations is possible as well [317]. Also quantum gas microscopes, see Sec. 1.4, are a feasible platform to read out spin order and subsequently magnetism for exotic phases as they appear in the present context [318,319]. Fermions, however, require very low temperatures in order to be below the superexchange temperature necessary to see magnetic order. A temperature of 0.25 hopping energies, e.g., was only achieved through elaborate methods such as the reshuffling of entropy within the system [81]. BECs, on the other hand, are already achieved at higher temperatures. Also they have a well-defined quantum phase corresponding to the broken U(1) symmetry. This phase can directly be mapped to a 2d spin what made it possible to investigate magnetism in a lattice of separated BECs [320,321].

4.4 $\mathbb{Z}_2$ characterization of the three-dimensional time-reversal-symmetric Hofstadter-Hubbard model

The Hofstadter model, Sec. 2.1, was originally proposed as a model for a 2d square lattice with a homogeneous magnetic flux piercing the 2d plane. Of course, generalizations to higher dimensions exist. For the TRS-breaking case, Halperin introduced the 3d generalization of the QHE in a periodic potential in 1987 [322] which has recently been observed in ZrTe_5 [32]. For the Hofstadter model itself, there are generalizations in even dimensions with Abelian gauge fields and in 4d with non-Abelian gauge fields [323]. Proposals for implementations in optical lattices which predict Weyl and nodal-line semimetals exist as well [324]. In the TRS case, a study of the 3d generalization of the TRS Hofstadter model has led to weak topological insulators (WTI) and strong topological insulators (STI) by studying the boundary states [325]. We focus on the particular 3d generalization of the TRS Hofstadter model to 3d which was introduced in Ref. [191]. The noninteracting tight-binding Hamiltonian for the 3d TRS Hofstadter model reads:

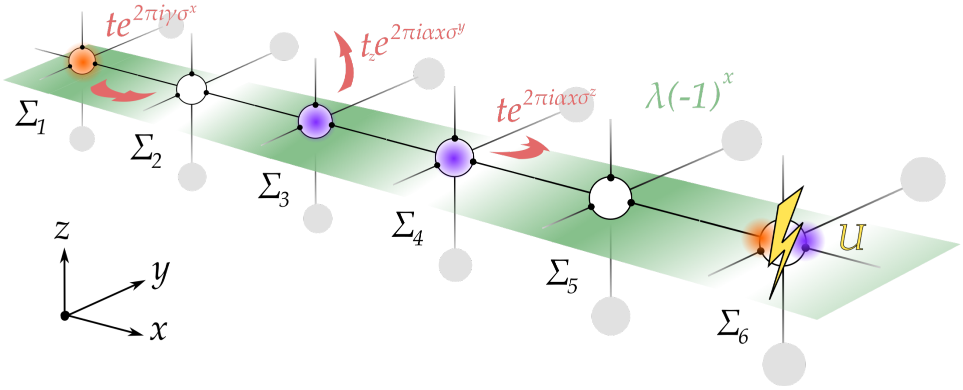
$te^{2\pi i\gamma\sigma^x}$
$t_z e^{2\pi i\alpha x\sigma^y}$
$te^{2\pi i\alpha x\sigma^z}$
$\lambda(-1)^x$
Σ_1
Σ_2
Σ_3
Σ_4
Σ_5
Σ_6
U
z
y
x

Figure 4.22: Schematic for the Hamiltonian in Eq. (4.63) for $\alpha = 1/6$. Particles hopping on the lattice acquire different complex phases $\boldsymbol{\theta}$ due to the non-Abelian gauge field. Hubbard interactions in DMFT will induce local selfenergies. For $\alpha = 1/6$, there are six of these selfenergies Σ_i. A staggered potential $(-1)^x\lambda$ along the x direction and the hopping amplitude along the z direction control the topological phase. Taken from Ref. [326].

$$\hat{H} = \sum_{\boldsymbol{j}} \left[\sum_{\mu=x,y,z} (-t_\mu) \left(\hat{\boldsymbol{c}}^\dagger_{\boldsymbol{j}+\hat{\mu}} e^{2\pi i \boldsymbol{\theta}_\mu} \hat{\boldsymbol{c}}_{\boldsymbol{j}} + \text{h.c.} \right) + (-1)^x \lambda \hat{\boldsymbol{c}}^\dagger_{\boldsymbol{j}} \hat{\boldsymbol{c}}_{\boldsymbol{j}} \right], \qquad (4.63)$$

in a compact notation, where $\boldsymbol{j} = (x, y, z)$ is the 3d lattice vector and μ runs over the three spatial variables. Here, $\hat{\mu}$ is the corresponding unit vector. The non-Abelian gauge field is chosen such that the complex matrix-valued quantum phase has the form $\boldsymbol{\theta} = (\gamma\sigma^x, \alpha x\sigma^z, \alpha x\sigma^y)$. We further set the hopping energies to $t_x = t_y = t = 1$ such that t_z is an independent parameter, tunable in cold atom experiments via the optical lattice laser intensity in z direction. Note that for $t_z = 0$, we recover decoupled layers of the 2d, TRS Hamiltonian in Eq. (2.10). A schematic figure describing the Hamiltonian in Eq. (4.63) is shown in Fig. 4.22 for $\alpha = 1/6$.

Noninteracting, three-dimensional phases

At first, we are interested in the nontinteracting phases of the Hamiltonian in Eq. (4.63) at half filling and we will later extend this to the Hubbard-interacting case. For $\alpha = 1/6$, the unit cell contains six lattice sites and the Fourier-transformed Hamiltonian of Eq. (4.63) reads

$$\mathcal{H}(\boldsymbol{k}) = \begin{pmatrix} O(1) & T & & & & T^\dagger e^{ik_x} \\ T^\dagger & O(2) & T & & & \\ & T^\dagger & O(3) & T & & \\ & & T^\dagger & O(4) & T & \\ & & & T^\dagger & O(5) & T \\ Te^{-ik_x} & & & & T^\dagger & O(6) \end{pmatrix}, \tag{4.64}$$

where we defined $T = te^{2\pi i\gamma\sigma^x}$ and

$$\begin{aligned} O(x) = & -2t\cos(k_y)\cos(2\pi\alpha x)\mathbb{1} \\ & -2t\sin(k_y)\sin(2\pi\alpha x)\sigma^z \\ & -2t_z\cos(k_z)\cos(2\pi\alpha x)\mathbb{1} \\ & -2t_z\sin(k_z)\sin(2\pi\alpha x)\sigma^y + \lambda(-1)^x\mathbb{1}. \end{aligned} \tag{4.65}$$

The Hamiltonian in Eq. (4.64) has 12 bands because of the size of the unit cell multiplied with two spin degrees of freedom. We compute the gap Δ at half filling through

$$\Delta = \min_{\boldsymbol{k}} E_+(\boldsymbol{k}) - \max_{\boldsymbol{k}} E_-(\boldsymbol{k}). \tag{4.66}$$

Here, $E_\pm(\boldsymbol{k})$ are the highest occupied (-) and the lowest empty (+) band, respectively. Since the Hamiltonian in Eq. (4.63) is particle-hole symmetric, there is no indirect band gap and we find

$$\Delta = \min_{\boldsymbol{k}}[E_+(\boldsymbol{k}) - E_-(\boldsymbol{k})] = 2\min_{\boldsymbol{k}}[E_+(\boldsymbol{k})]. \tag{4.67}$$

The band gap Δ is found numerically by minimization routines with random initial values for $\boldsymbol{k}$. We show the result in Fig. 4.23(i) as a function of λ and t_z for different γ. We observe for large λ that for any γ, there is always a gapped phase whose critical value increases with increasing t_z. This is expected since we anticipate a band insulator (BI) for a large staggered potential λ. This is because large λ will give rise to two groups of bands with the same number of states in the spectrum. One of these groups contains the high-energy bands and one the low-energy bands. Since we look at half filling, this will then lead to a BI. It competes with increasing interlayer coupling in the third dimension t_z which is represented by the increasing critical value of λ with increasing t_z in Fig. 4.23(i). For $\gamma = 0.2$, we observe a second gapped phase and for $\gamma = 0.22$ and 0.25 we observe, in total, three gapped phases. If $\gamma = 0.25$, the three phases are separated by thin gapless transition lines. For $\gamma = 0.22$, however, these transition lines expand into a gapless region between the three gapped phases. We go into more detail about that after we have discussed the topological characterization. Figure 4.23(i), column (e) coincides with Ref. [191, Fig. 1(b)].

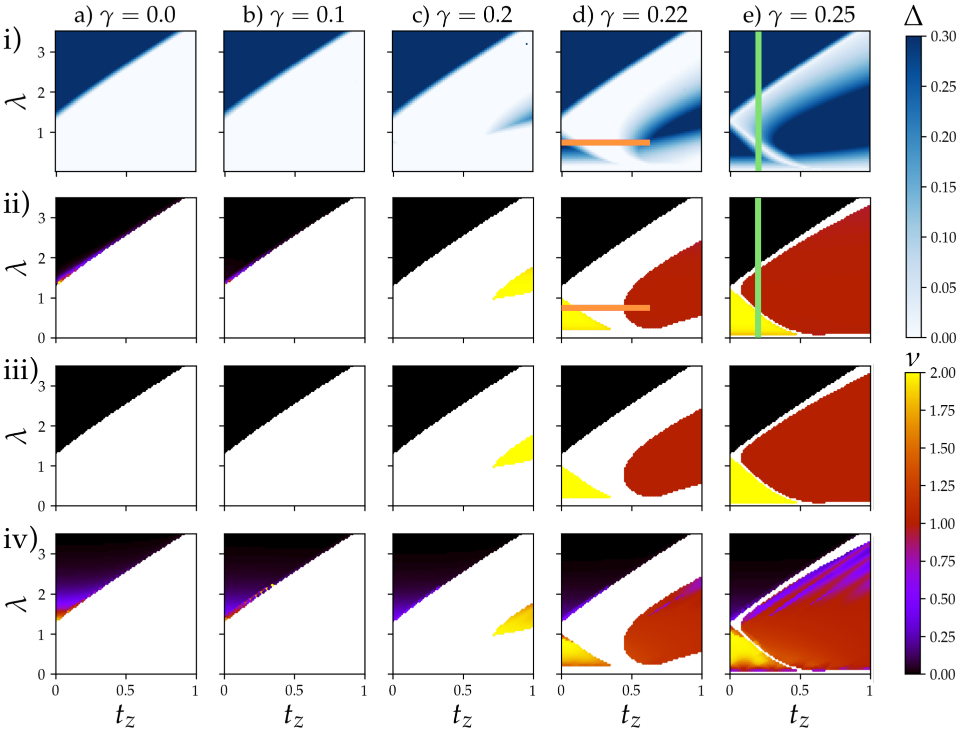

Figure 4.23: Noninteracting phases of the Hamiltonian in Eq. (4.63) for $\alpha = 1/6$: (i) gap Δ defined in Eq. (4.66) and topological index ν defined in Eq. (4.68) computed with (ii) twisted boundary conditions, (iii) Wilson loops, and (iv) the local $\mathbb{Z}_2$ marker as functions of λ and t_z for different γ. The light green and the orange lines correspond to the noninteracting values in Fig. 4.25. Taken from Ref. [326].

Three-dimensional phases with TRS are classified with $\mathbb{Z}_2$ invariants [30] and their characterization can be reduced to the characterization of 2d phases [47]. As in Ref. [191], we define a topological index which is especially useful for the present system since it exhibits the anisotropy $t_x = t_y \neq t_z$ which corresponds to decoupled layers in the xz plane if $t_z = 0$. A single layer is characterized by a single $\mathbb{Z}_2$ number $\nu_{2\mathrm{D}}$, computed with 2d methods. Finite coupling in z direction makes this number now k_z-dependent $\nu_{2\mathrm{D}}(k_z)$. This means that we can characterize all possible phases with $t_x = t_y \neq t_z$ with one topological index

$$\nu = \nu_{2\mathrm{D}}(k_z = 0) + \nu_{2\mathrm{D}}(k_z = \pi), \tag{4.68}$$

which can assume three different values: 0, 1, or 2. This is in contrast to the full classification with four different $\mathbb{Z}_2$ numbers which applies in the general case as explained in Sec. 1.2.6. If $\nu = 0$, the phase is topologically trivial corresponding to $(\nu_0; \nu_1, \nu_2, \nu_3) = (0; 0, 0, 0)$ being a BI. For $\nu = 1$, we find an STI with $(1; 0, 0, 0)$ and for $\nu = 2$ a WTI with $(0; 0, 0, 1)$. Again, the reason that we only find this particular WTI is the anisotropy $t_x = t_y \neq t_z$.

Twisted boundary conditions

We now characterize the topological properties of the insulating phases in Fig. 4.23(i). To this end, we utilize three different methods in order to benchmark them against each other. The first method is based on twisted boundary conditions (TBC) [193, 260, 262, 264] introduced in Sec. 3.5. Before we apply the TBC, we Fourier transform the z direction of the real-space Hamiltonian in Eq. (4.63). This yields the quantum number k_z. For the remaining xy plane we apply spin-dependent TBC as

$$\hat{\boldsymbol{c}}_{x+N_x,y,k_z} = \hat{\boldsymbol{c}}_{x,y,k_z} e^{i\vartheta_x \mathbb{1}} \quad \text{and} \quad \hat{\boldsymbol{c}}_{x,y+N_y,k_z} = \hat{\boldsymbol{c}}_{x,y,k_z} e^{i\vartheta_y \sigma^z}, \tag{4.69}$$

where $N_x \times N_y$ is the size of the 2d system. As explained in Sec. 3.5, the 2d $\mathbb{Z}_2$ invariant is computed by sampling the $(\vartheta_x, \vartheta_y)$ space. In contrast to the purely 2d case, here, this $\mathbb{Z}_2$ number is dependent on the parameter k_z. We can thus apply the formula in Eq. (4.68). We show the results of ν computed with spin-dependent TBC in Figs. 4.23(ii) as a function of λ and t_z for different γ. We observe that the three insulating phases in Fig. 4.23(i), column (d) and (e) are indeed topologically different as shown in Fig. 4.23(ii), column (d) and (e). Red regions correspond to the STI, yellow ones to the WTI, and black ones to the BI phase. Interestingly, at $\gamma = 0.2$, we find a WTI besides the BI in the region, $\lambda, t_z \approx 1$, where there was an STI at $\gamma = 0.22$. Therefore, between $\gamma = 0.2$ and 0.22 there must occur a gap closing at this region since there occurs a topological phase transition from a WTI to an STI.

Wilson loops

We benchmark the results obtained with TBC with the Wilson loop technique [268,270] introduced in Sec. 3.6. The Wilson loop is computed on a closed 1d contour $C_{\boldsymbol{k}}$ in the BZ which is 3d in the present case. The discretized Wilson loop reads

$$D(C_{\boldsymbol{k}}) = \prod_{\boldsymbol{k}_j \in C_{\boldsymbol{k}}} F_j, \quad \text{with} \quad F_j^{mn} = \langle u_m(\boldsymbol{k}_j) | u_n(\boldsymbol{k}_{j+1}) \rangle, \tag{4.70}$$

where $\boldsymbol{k}_j \in C_{\boldsymbol{k}}$, $j = 1, 2, \dots$ is the discretized contour with stepsize $\Delta\boldsymbol{k}$. The $2N_m \times 2N_m$ matrix F_j is calculated from the cell-periodic part of the Bloch functions $|u(\boldsymbol{k})\rangle$. Here, $2N_m$ corresponds to the number of occupied bands. This means that the filling of the system is implicitly contained in the definition of F_j. Note that in a TRS system of spin-1/2 fermions the filling must be even, thus, $2N_m$. As we see from Eq. (4.68), k_z is set to π or 0 since the topological indices can only change at the TRIM. We choose $C_{\boldsymbol{k}}$ to go along k_x such that the discretized Wilson loop in Eq. (4.70) is a parametric function of k_y only, i.e., $D(C_{\boldsymbol{k}}) = D(k_y)$. The matrix $D(k_y)$ has $2N_m$ eigenvalues $\lambda_m(k_y)$ with $m = 1, 2, \dots 2N_m$. The complex phases of the $\lambda_m(k_y)$ are as well functions of k_y and will perform trajectories on a cylinder in the (k_y, θ_m) space, where k_y runs from 0 to π [265] and θ_m, being a phase, goes from 0 to 2π. Because of the TRS, at $k_y = 0$, the θ_m are pairwise degenerate corresponding to Kramer pairs. For $0 < k_y < \pi$, these pairs can split. At $k_y = \pi$, there must again be degenerate pairs, however, these are not necessarily the same pairs as the ones at $k_y = 0$. The number of pairs changes during the parameter range $0 \leq k_y \leq \pi$, being even or odd, defines exactly the desired $\mathbb{Z}_2$ number, see Sec. 3.6. The question we have to answer numerically is now: how many times do the $\theta_m(k_y)$ wind around the cylinder (k_y, θ_m) when tuning k_y from 0 to π?

First, we sample $\theta_m(k_y)$ for different values $0 \leq k_y \leq \pi$. Then we divide the range of the values for $\theta_m(k_y)$ into three parts according to the following labels: I, where $0 < \theta_m(k_y) < 2\pi/3$; II, where $2\pi/3 < \theta_m(k_y) < 4\pi/3$, and III, where $4\pi/3 < \theta_m(k_y) < 2\pi$. Then we count the number n_i of data points $\theta_m(k_y)$ being in one of the three regions $i =$ I, II, III. We compute the change in n_i with respect to advancing k_y by one step Δk_y, defining Δn_i with $i =$ I, II, III and discard any values which are not a permutation of (-1,0,1). This kind of permutation corresponds to a single $\theta_m(k_y)$ changing from one region to another. If there is no change then $\Delta n_i = 0$ for all i, which does not carry any information. We now measure the permutation of the Δn_i by applying a Levi-Civita tensor. Summing these permutations yields an even or an odd number, where the former is topologically trivial the latter is topologically nontrivial. Let us look at two examples: In Fig. 4.24 we show the winding of the $\theta_m(k_y)$ for a topologically trivial case in blue and a topologically nontrivial case in orange. The data set for the blue curve

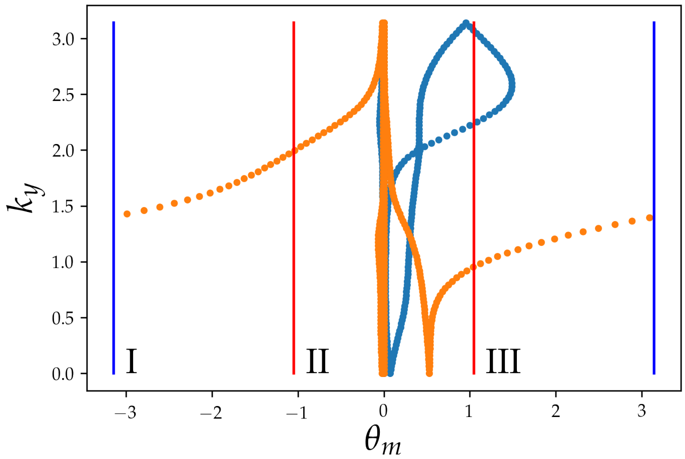

Figure 4.24: Examples to numerically determine the winding of the complex phases $\theta_m(k_y)$ of the eigenvalues of the Wilson loops $D(k_y)$, Eq. (4.70), across $0 \leq k_y \leq \pi$ applied to the model in Eq. (4.64) with $\gamma = 0.22$, $t_z = 0.6$, and $\lambda = 0.75$. The blue and orange dots correspond to $k_z = 0$ and π, respectively. Taken from Ref. [326].

would correspond to

$$\Delta n = [(0,-1,1),(0,1,-1)] \overset{\text{Levi-Civita}}{\rightarrow} (-1,1) \overset{\text{sum}}{\rightarrow} 0, \tag{4.71}$$

which is even, corresponding to a trivial winding. For the orange data, we have

$$\Delta n = [(0,-1,1),(1,0,-1),(-1,1,0)] \overset{\text{Levi-Civita}}{\rightarrow} (-1,-1,-1) \overset{\text{sum}}{\rightarrow} -3, \tag{4.72}$$

which is odd corresponding to a nontrivial winding. We show the results for the Wilson loop technique in Fig. 4.23(iii) as a function of λ and t_z for different γ and find exact agreement with the results obtained with the method using TBC in Fig. 4.23(ii).

Local $\mathbb{Z}_2$ marker

As a third method, we introduce the local $\mathbb{Z}_2$ marker as an TRS extension to the local Chern marker which we introduced in Sec. 3.4 as a 2d quantity. We then perform the extension to the 3d case according to Eq. (4.68). We define the band-projected Chern number as

$$C_{\zeta\xi}(x,y) = \langle x,y|\mathcal{P}_\zeta \hat{P}\hat{x}\hat{P}\hat{y}\hat{P}\mathcal{P}_\xi|x,y\rangle, \tag{4.73}$$

where ζ and ξ correspond to band indices of the {I,II} basis where II labels states which are the time-reversed partners of the states labeled by I. $\mathcal{P}_\zeta$

projects onto these states. The projector $\hat{P}$ projects onto occupied eigenstates of the Hamiltonian, see Sec. 3.4, and $|x, y\rangle$ is an eigenvecor of the 2d position operator. The expression in Eq. (4.73) determines a 2×2 matrix. In the basis of time-reversed partners {I,II}, this matrix is diagonal as the states of band I evolve exactly opposite compared to the ones of band II [265, Fig. 3]. Thus in the {I,II} basis the matrix determined by Eq. (4.73) has only two finite values corresponding to its eigenvalues. Since the eigenvalues are independent of the basis in which the matrix is represented, we do not have to find the states in the {I,II} basis but can use the spin basis $\{\uparrow, \downarrow\}$. The eigenvalues of this matrix correspond to real-space topological markers of the TRS system. Because of the TRS, one eigenvalue is the negative of the other. The generalization to 3d is similar to the one we performed for the TBC method. We first Fourier transform the z component of the Hamiltonian in Eq. (4.63). We are thus effectively left with a 2d real-space system which is parameterized by k_z. We can now apply the 2d local $\mathbb{Z}_2$ marker through the Eq. (4.68). We show the results of the bulk average of the local $\mathbb{Z}_2$ marker in Fig. 4.23(iv) as a function of λ and t_z for different γ computed on a 30×30 lattice. The bulk average is obtained by averaging the values of the local $\mathbb{Z}_2$ marker over a unit cell in the center of the system. We observe that the results qualitatively agree with the results in Figs. 4.23(ii) and (iii), however, there are some mismatches when the gap in Figs. 4.23(i) becomes small. This is expected since finite size effects will play an enhanced role if the gap is small which has already been shown for the local Chern marker [256]. For sufficiently large gaps, however, the local $\mathbb{Z}_2$ marker is well quantized providing a real-space tool to distinguish different topological phases in inhomogeneous TRS systems.

Three-dimensional time-reversal-symmetric Hofstadter-Hubbard model

The three methods we introduced are capable of computing invariants for an arbitrary value of γ referring to finite spin mixing. This is in stark contrast to the approach we followed in Sec. 4.1 where the method was specialized to values of $\gamma = 0$ or $1/4$. Indeed, the topological nontrivial gap is the largest at $\gamma = 1/4$ in 2d [189, 190] and 3d [191], which makes this parameter choice most interesting for the study of topologically insulating phases. However, in 3d there exist also gapless states which are topologically protected, as discussed in Sec. 1.2.6. These states have been found in the time-reversal broken case, in a generalized Hofstadter model [325]. By making use of the topological Hamiltonian approach, which we introduced in Sec. 3.3, we can also generalize the three methods to the interacting case with finite Hubbard interaction. This enlarges the parameter space to interacting states as long as the Green's function does not have a zero, e.g., in a Mott insulator. On the interaction strength itself, there is no restriction.

We now study the interacting phase diagram of the 3d, TRS Hofstadter-

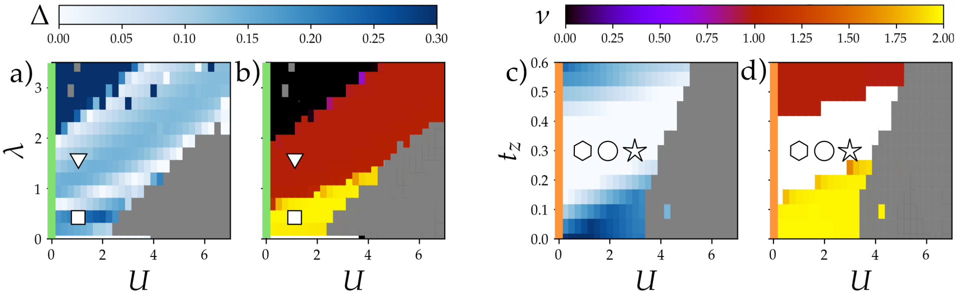

Figure 4.25: Phase diagrams of the 3d, TRS Hofstadter-Hubbard model. We show the gap of the topological Hamiltonian in (a) and (c) as well as the topological invariant ν, defined in Eq. (4.66), in (b) and (c) as functions of U and λ in (a) and (b) for $\gamma = 0.25$ and $t_z = 0.2$, and as functions of U and t_z in (c) and (d) for $\gamma = 0.22$ and $\lambda = 0.75$. The light green and the orange lines denote the parameter space for the noninteracting limit which coincides with the light green and the orange lines in Fig. 4.23. Taken from Ref. [326].

Hubbard model. Therefore, we add the Hubbard term $U \sum_j \hat{c}^\dagger_{\uparrow j}\hat{c}_{\uparrow j}\hat{c}^\dagger_{\downarrow j}\hat{c}_{\downarrow j}$ to the Hamiltonian in Eq. (4.63) and apply real-space DMFT, see Sec. 3.1. We are primarily interested in the symmetric phases, where there is no spontaneous symmetry breaking. Since the unit cell of the system contains six sites for the choice $\alpha = 1/6$, there are six different selfenergies to compute, see Fig. 4.22. Since nonlocal quantum fluctuations are suppressed for higher dimensions, we expect even more accurate results than the already successful studies for topological 2d systems with DMFT [190, 192, 193, 198, 253, 255, 257, 306]. In Fig. 4.25, we show the gap of the topological Hamiltonian Δ in (a) and (c) and the topological index defined in Eq. (4.66) in (b) and (d). Note that (a) and (b) are functions of U and λ for $\gamma = 0.25$ and $t_z = 0.2$, and (c) and (d) are functions of U and t_z for $\gamma = 0.22$ and $\lambda = 0.75$. The connection to the noninteracting case is given by the light green and the orange lines in Figs. 4.23 and 4.25. The grey regions in Fig. 4.25 correspond to many-body states where the DMFT procedure found spontaneous symmetry breaking. We go into more detail on this further below. The first observation we draw from Fig. 4.25 is that the closing of the gap of the topological Hamiltonian Δ always coincides with the topological phase transition. This is anticipated since even though the topological Hamiltonian is not a physical Hamiltonian but an effective one, its topological properties are the same as those of the full interacting Hamiltonian. Since a topological phase transition occurs only if the gap closes the topological as well as the full Hamiltonian have to have the same transition points where the gap closes. Note, however, that the topological Hamiltonian is not a legit low-energy Hamiltonian. So, as soon as its gap becomes finite, there is no physical meaning related to this quantity. Next, we observe that increasing the interaction strength U

shifts the transition points towards higher values of λ and t_z, respectively. The competition between U and λ can be explained quite generally on a mean-field level: Finite repulsive U creates an effective on-site potential from the real part of the selfenergy. This selfenergy is larger on doubly occupied sites. Those sites are the ones where the staggered potential is small. Thus the Hubbard interactions effectively smoothen the staggered potential, which results in a smaller effective staggered potential, which in turn results in a higher critical value for the actual staggered potential.

For the explanation of the interaction effect in Figs. 4.25(c) and (d), we have to go a detour via the staggered potential and again use mean-field arguments: As just discussed, increasing the Hubbard U results in a decrease of the effective staggered potential. If we look now at Fig. 4.23(ii), column (d), at the orange line, we see that a decrease of λ shifts the transition points toward higher values of t_z, as we can observe in Figs. 4.25(c) and (d). This, however, strongly depends on the position of the orange line and for other parameters the competition between U and t_z will differ.

Symmetry-broken phase

We will now have a brief look at symmetry-broken phases, i.e., magnetic order is present. The effective spin Hamiltonian for the Hamiltonian in Eq. (4.63) in the strong interaction limit is obtained from restricting the state space to the subspace of singly-occupied sites only [190], i.e., charge degrees of freedom are frozen but nearest-neighbor spin interactions can take place. In this limit, the spin Hamiltonian reads

$$\begin{aligned}\hat{H}_{\text{spin}} = \sum_j \sum_{\mu,\nu,\rho \text{ cyclic}} \frac{t_\mu^2}{U} \Big\{ & \hat{S}_j^\mu \hat{S}_{j+\hat{\mu}}^\mu \\ & + \cos(4\pi\theta_\mu) \left[\hat{S}_j^\nu \hat{S}_{j+\hat{\mu}}^\nu + \hat{S}_j^\rho \hat{S}_{j+\hat{\mu}}^\rho \right] \\ & + \sin(4\pi\theta_\mu) \left[\hat{S}_j^\nu \hat{S}_{j+\hat{\mu}}^\rho - \hat{S}_j^\rho \hat{S}_{j+\hat{\mu}}^\nu \right] \Big\} ,\end{aligned} \tag{4.74}$$

where we defined the spin operators as $\hat{S}_j^\mu = \hat{c}_j^\dagger \sigma^\mu \hat{c}_j$ with σ^μ being the μth Pauli matrix. The static gauge fields enter through $\theta = (\gamma, \alpha x, \alpha x)$. In 2d, it was possible to argue that the spin interaction energy is minimized through AFM ordering along the y direction with the magnetization direction pointing in S_z direction. Then one is left with a possibly enlarged unit cell in the x direction only because the ordering in y direction can be recovered from AFM order. This argument does not hold in 3d since the spin interactions are much more complex. Note, that the argument also does not hold in the spin-imbalanced case [306]. We thus have to find the correct size of the unit cell empirically by comparing the groundstate energy for different sizes of the unit cell $N_x \times N_y \times N_z$. This is very elaborate in the full quantum case

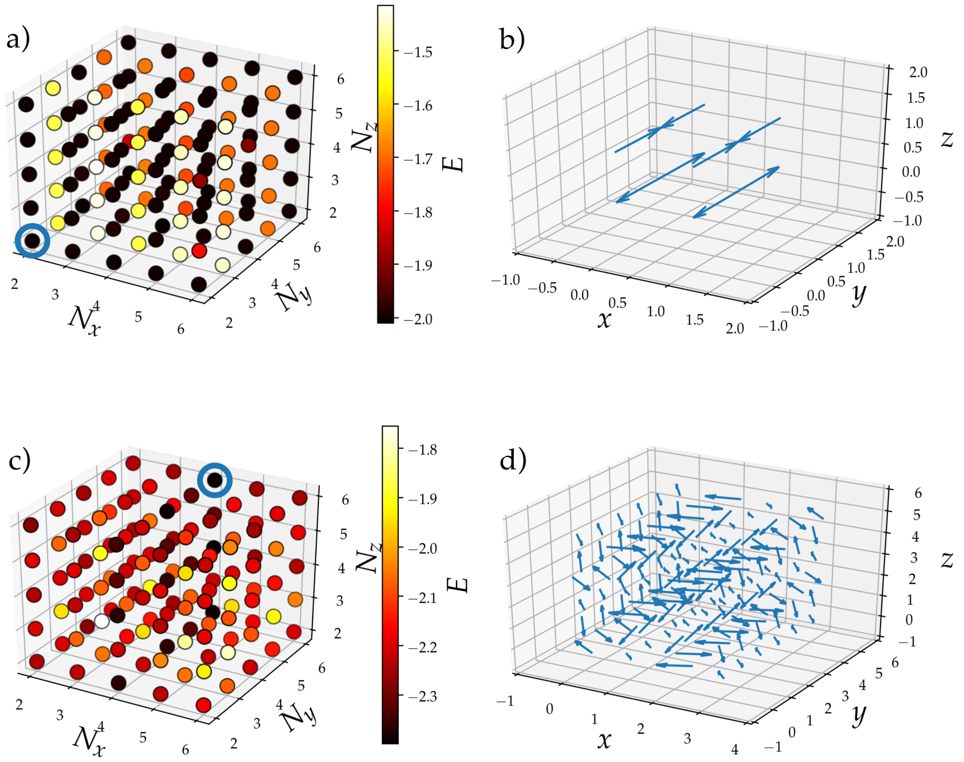

Figure 4.26: Classical groundstate energy E per spin of the spin Hamiltonian in Eq. (4.74) obtained from Monte Carlo studies for different sizes of the unit cell $N_x \times N_y \times N_z$ for (a) $\gamma = 0.25$ and $t_z = 0.2$ and (c) $\gamma = 0.22$ and $t_z = 1$. The state with the smallest energy is highlighted with a blue circle in (a) and (c), respectively. The corresponding spin configuration is shown in (b) and (d), respectively. Taken from Ref. [326].

including fluctuations. Here, we only focus on the classical limit, where the spin operators become numbers $\hat{S}_j^\mu \to S_j^\mu$ and $|\boldsymbol{S}_j| = 1$. The Hamiltonian then becomes an energy functional $E[\{\boldsymbol{S}_j\}]$ with $(3-1) \times N_x \times N_y \times N_z$ degrees of freedom, where the factor $3-1$ stems from the three directional spin degrees of freedom which are reduced by one due to the normalization condition $|\boldsymbol{S}_j| = 1$. We minimize $E[\{\boldsymbol{S}_j\}]$ via a Monte Carlo routine, the results are shown in Fig. 4.26 for unit cell sizes up to $N_x \times N_y \times N_z = 6 \times 6 \times 6$. In (a), we show the groundstate energy per spin E for $\gamma = 0.25$ and $t_z = 0.2$. We observe that all multiples $N_x \times N_y \times N_z = 2 \times 2 \times 2$ yield the same groundstate energy per spin which suggests that $2 \times 2 \times 2$ might indeed be the correct unit cell for this set of parameters. The spin configuration of the $2 \times 2 \times 2$ groundstate is shown in (b) revealing ferromagnetic ordering along the x direction and AFM ordering along the y and z directions. In Fig. 4.26(c) and (d), we show E and the spin configuration with lowest energy per spin, respectively, for $\gamma = 0.22$ and $t_z = 1$. We conclude that for different parameters the unit cell can be very large and the spin ordering can become very complicated.

Surface states

Let us now turn to the investigation of the surface states of the 3d, interacting topological states we found in Fig. 4.25. We use a configuration in which the system is finite in the x direction but extended in the y and z directions. The surface BZ is then spanned by the quantum numbers k_y and k_z from the PBC. k_x is not a good quantum number anymore since we have to apply OBC in the x direction. We visualize the surface states with the spectral density which is specialized to these boundary conditions as:

$$\begin{aligned} \rho_X(\omega, k_y, k_z) &= -\frac{1}{\pi} \sum_{\sigma, x \in X} \mathrm{Im} G^{\sigma\sigma}_{xx}(\omega, k_y, k_z) \\ G^{\sigma\sigma'}_{xx'}(\omega, k_y, k_z) &= \left[\left\{ \omega - \Sigma(\omega) - H_0(k_y, k_z) \right\}^{-1} \right]^{\sigma\sigma'}_{xx'}, \end{aligned} \tag{4.75}$$

where X defines a spatial region of x coordinates in which the spectral density should be computed. We set the extent of the system in x direction to $N_x = 60$ and define the left surface L for $1 \leq x \leq 3$, the bulk B as $25 \leq x \leq 36$, and the right surface R as $58 \leq x \leq 60$. Note that $G(\omega, k_y, k_z)$ in Eq. (4.75) is a $2N_x \times 2N_x$ matrix, as well as the selfenergy $\Sigma(\omega)$ and the Hamiltonian $H_0(k_y, k_z)$ which is the Fourier transform of the Hamiltonian in Eq. (4.63) in the y and z directions. Note, that within the DMFT calculations now 60 local selfenergies have to be calculated. We show the results for the surface states in Fig. 4.27. The white symbols correspond to the white symbols in Fig. 4.25 determining the parameter sets used. The red squares highlight the TRIM. We plot only a quarter of the surface BZ since the results are mirror symmetric with respect to the k_y and k_z axes. In (a) and (b) we show the topologically nontrivial insulating phases, where (a) corresponds to the surface states of the STI. We observe that the Fermi surface encircles exactly one TRIM as predicted by Ref. [47]. In contrast, in (b), the Fermi surface encloses two TRIM also in agreement with Ref. [47]. As these curves represent cuts through the 2d dispersion of the surface BZ $E_{\mathrm{surf}}(k_y, k_z) = E_F$, we have a notion of the propagation direction of the surface state via the group velocity through

$$\vec{v}_{\mathrm{surf}} = \vec{\nabla} E_{\mathrm{surf}}(k_y, k_z), \text{ with } \vec{\nabla} = (\partial_{k_y}, \partial_{k_z})^T. \tag{4.76}$$

We deduce from the curves in Fig. 4.27(a) and (b) that the surface state of the WTI in (b) will only propagate in y direction. The surface state of the STI in (a), on the other hand, can propagate in any direction in the yz plane. This is a typical property of an STI hosting a Dirac cone on its surface which is spin-momentum locked such that propagation is possible in any direction but no backscattering occurs.

Nodal-line semimetal

Let us now focus on the gapless region in the phase diagram presented in Fig. 4.25(c) and (d). As it was shown for the 3d generalization of the Kane-Mele model in Ref. [327], the gapless region between an STI and a WTI or BI can exhibit exotic features. In this particular case, a Weyl semimetal was found. In our case, we are in a similar situation as the gapless region we are interested in, is located between a WTI and an STI. We look at the surface states as well as the bulk state in three different instances in the phase diagram in Fig. 4.25(d) assigned through three white symbols. In Fig. 4.27(c), column R we find that the right surface state resembles that of a WTI as, e.g., shown in Fig. 4.27(b), column R. The left surface state, on the other hand, in Fig. 4.27(c), column L is more similar to a surface state of an STI, however, a piece is missing. This means that it does not completely perform a loop, as a cut at constant energy through a Dirac cone would do, but rather stops at a certain point $(k_y, k_z) \approx (3, 1)$ in the surface BZ. This reminds us of a Fermi arc, which is the surface state of a Weyl semimetal [56]. By looking at the bulk state in Fig. 4.27(c), column B, we find a small curve at $(k_y, k_z) \approx (3, 1)$ rather than a single point as it would be the case in a Weyl semimetal. An even closer view of the gapless state is shown in the full 3d BZ in Fig. 4.27(f) where the blue line denotes a finite spectral density in 3d and the red lines correspond to projections on the respective 2d BZ. Here, we clearly observe a nodal-loop which winds around the k_z axis at $(k_x, k_y) = (0, \pi)$. However, we first have to determine its topological properties in order to clarify whether this is indeed a nodal-line semimetal or just an accidental band touching. For the case without TRS, the Berry phase must assume a nonzero value if it is computed by integrating along a path linking the nodal line. This is the topological invariant which protects the nodal line from gapping out as a result of perturbations. On top of that, nodal lines can possess so-called topological charges like Weyl points which can be calculated from a 2d topological invariant which is computed from integrating over a surface completely enclosing the nodal line [55]. In our case, we have to use methods generalized to the TRS case. For the TRS generalization of the Berry phase θ_B we use the Wilson loop, introduced in Sec. 3.6, as

$$\theta_B = \mathrm{Im}\mathrm{Tr}\log \prod_j F_j, \quad F_j^{mn} = \langle u_m(\boldsymbol{k}_j) | u_n(\boldsymbol{k}_{j+1}) \rangle, \tag{4.77}$$

analogously to Eq. (4.70). Indeed, we find $\theta_B = \pi$ if the Wilson loop and the nodal line are linked and $\theta_B = 0$ if not. The gapless region in Figs. 4.23, column (d) and 4.25(c) and (d) is thus a nodal-line semimetal. We also

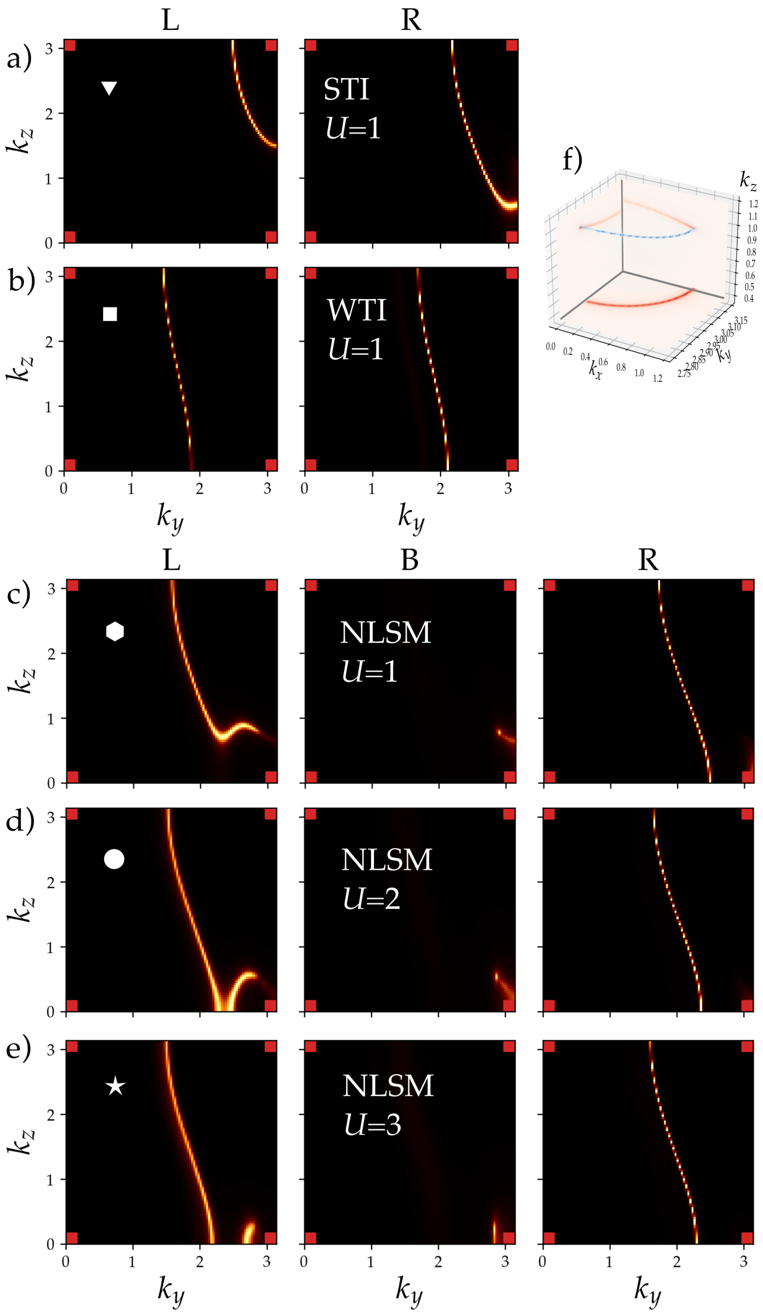

Figure 4.27: Surface states of 3d TRS Hofstadter-Hubbard model. The white symbols denote the parameter sets corresponding to the white symbols in Fig. 4.25. (a) and (b) show the surface BZ of insulating states and (c)-(e) those of gapless states. (f) shows the nodal line in the full 3d BZ. Taken from Ref. [326].

performed a calculation to compute the $\mathbb{Z}_2$ number on the surface of a box completely enclosing the nodal line. This, however, yields zero from which we conclude that the nodal line in the present case has no topological charge and could gap out if it shrinks to a point.

For increasing interaction strength, we see in Figs. 4.27(c)-(e) a transition of the left surface state but not of the right one. During the transition from $U = 1$ to $U = 3$ we see in Fig. 4.27(c)-(e), column L that the original curve of the spectral density splits up into two curves. One of them looks like the surface state of a WTI. This we can explain again from a mean-field argument. If we start with $U = 0$ at the point $t_z = 0.2$ and $\lambda = 0.75$ in Fig. 4.23(ii), column (d) and increase the interaction strength, the staggered potential λ is effectively reduced as explained above. The position in the phase diagram then effectively moves downwards in the phase diagram. At the same point, there is a phase transition to the WTI as it was anticipated from the form of the surface states. Increasing U even further leads to a spontaneously broken symmetry as shown in Fig. 4.25(c) such that the mean-field arguments we draw from the noninteracting phase diagrams in Fig. 4.23 do not hold anymore.

4.4.1 Topological proximity effect in layered systems

At this point of the manuscript, we have discussed 2d and 3d topological states of matter. We realized that the physics of both can be quite different. A straightforward way to think of the transition from 2d to 3d would be layering. This means, we stack samples of 2d systems on top of each other and allow them to couple. Repeated stacking of layers would eventually result in a 3d object.

It turns out, however, that interesting physics emerges already for stacking only two layers. Here, we refer to the *bulk topological proximity effect* (BTPE) [328]. Proximity effects are known in diverse fields of physics, e.g., in superconductivity. Herein, thin normal conductors can become superconducting when sandwiched between two superconductors [329,330]. In fact, the superconducting order parameter has a finite value in the normal conductor which decreases with some typical penetration depth.

In the context of topological states, we can make an analogous consideration. Let us think of two 2d systems. The first one is described by Hamiltonian $\hat{H}_A$ and is topologically trivial, the other is topologically nontrivial and obeys Hamiltonian $\hat{H}_B$. These two should be coupled via the third spatial dimension through a coupling operator $\hat{R}$. The total Hamiltonian then reads

$$\hat{H} = \begin{pmatrix} \hat{H}_A & \hat{R} \\ \hat{R}^\dagger & \hat{H}_B \end{pmatrix} . \tag{4.78}$$

If we consider the topologically nontrivial system B as a perturbation to the topologically trivial system A, the corrections to $\hat{H}_A$ would be of the form $-\hat{R}\hat{H}_B^{-1}\hat{R}^\dagger$. The topological properties of a system are encoded in its eigenstates, see, e.g., the Chern number in Eq. (1.3). Let us assume that the system B exhibits the Chern number $C_B = 1$. System A has a trivial Chern number $C_A = 0$, so all nontrivial topological properties come from the eigenstates of the perturbation from system B. If we assume that the coupling $\hat{R}$ changes the topological properties, the eigenstates of the perturbation are the same as the eigenstates of $\hat{H}_B$ with negative energies. In static systems the Chern numbers of the full set of bands have to add up to 0. This means that the eigenstates of the negative energies have to yield the negative Chern number. Concluding this consideration, the topologically trivial system A becomes topologically nontrivial with Chern number -1 when coupled to the System B with Chern number 1. This is the BTPE. Note that it is a phenomenon which originates from the bulk properties of the respective systems. It is as such to be distinguished from edge physics as it was discussed, e.g., in Sec. 4.1.1.

Originally, the BTPE was shown to exist in a topologically nontrivial spin-orbit-coupled layer coupled to a flat band in Ref. [328]. It has been measured in thin films coupled to a 3d topological insulator [331]. Theoretically, the BTPE has been considered as an application for topological invariants in open systems [332]. Moreover, it was discussed in great detail for layers of the Haldane model [333].

Here, we look at the BTPE in the multilayer case, i.e., more than two layers stacked upon each other [334]. We study this for L honeycomb lattices. The nontrivial topological properties enter through a Haldane layer, see Sec. 2.4, as the hth layer. The corresponding Hamiltonian reads

$$H(\boldsymbol{k}) = \begin{pmatrix} \ddots & & & & \\ & \vec{h}_{i-1}(\boldsymbol{k}) \cdot \boldsymbol{\sigma} & r\mathbb{1} & & \\ & r\mathbb{1} & \vec{h}_i(\boldsymbol{k}) \cdot \boldsymbol{\sigma} & r\mathbb{1} & \\ & & r\mathbb{1} & \vec{h}_{i+1}(\boldsymbol{k}) \cdot \boldsymbol{\sigma} & \\ & & & & \ddots \end{pmatrix}, \tag{4.79}$$

where $\boldsymbol{\sigma} = (\mathbb{1}, \sigma^x, \sigma^y, \sigma^z)$ is a four vector containing the 2×2 identity matrix and the Pauli matrices. The Hamiltonian in Eq. (4.79) has 2×2 Hamiltonians on its diagonal, one for the ith layer with $i = 1, ...L$. They are coupled through hopping with energy r. We furthermore use the pseudo spin-1/2 representation of the 2×2 Hamiltonians which we introduced in Eq. (2.13). The vector representation for the Hamiltonian of the Haldane layer reads

$$\vec{h}_h(\boldsymbol{k}) = \begin{pmatrix} -2t' \cos(\phi) \sum_i \cos(\boldsymbol{k} \cdot \boldsymbol{a}_i) \\ -t \sum_i \cos(\boldsymbol{k} \cdot \boldsymbol{a}_i) \\ -t \sum_i \sin(\boldsymbol{k} \cdot \boldsymbol{a}_{\boldsymbol{i}}) \\ -2t' \sin(\phi) \sum_i \sin(\boldsymbol{k} \cdot \boldsymbol{b}_i) \end{pmatrix}, \tag{4.80}$$

where we set the staggered potential to zero at the layer $i = h$. For the honeycomb layers, i.e. $i \neq h$ and $t' = 0$, we have the following vector representation for the Hamiltonian

$$\vec{h}_h(\boldsymbol{k}) = \begin{pmatrix} 0 \\ -t\sum_i \cos(\boldsymbol{k}\cdot\boldsymbol{a_i}) \\ -t\sum_i \sin(\boldsymbol{k}\cdot\boldsymbol{a_i}) \\ \lambda \end{pmatrix}. \tag{4.81}$$

Throughout the remaining discussion on layered systems, we will set $t' = 1$ as the unit of energy and set $\lambda = 1$, $\phi = \pi/2$, and $t = 4$.

Having defined our model system, we now come to the computation of topological invariants. First of all, one might wonder how to define a Chern number for a multilayer system since Chern numbers are defined in 2d. In fact, the Chern number of a single band is defined on a 2d torus. As we see in Eq. (1.3), the total Chern number of a system is the sum of the Chern numbers of all occupied bands. This is helpful for the present system as we can interpret the layer index as an additional degree of freedom in the unit cell, much like an orbital. Consequently, the Chern number is computed from the $2L$-dimensional eigenstates with associated energies below the Fermi level. Eventually, this yields the Chern number of the full system.

One might also wonder, whether a Chern number can be assigned to a single layer, as it was suggested in the beginning of this subsection on the weak perturbation. In Ref. [335], a topological invariant for a subsystem α based on the single-particle density matrix was introduced:

$$I_\alpha = \frac{i}{2\pi}\sum_{j=1}^{m}\int dk_x dk_y \left[\langle\partial_{k_x}\bar{\psi}_j(\boldsymbol{k})|\partial_{k_y}\bar{\psi}_j(\boldsymbol{k})\rangle - \langle\partial_{k_y}\bar{\psi}_j(\boldsymbol{k})|\partial_{k_x}\bar{\psi}_j(\boldsymbol{k})\rangle\right], \tag{4.82}$$

where $|\bar{\psi}_j(\boldsymbol{k})\rangle$ is the jth eigenstate of the reduced density matrix ρ_α and the summation runs over the eigenstates of the largest m eigenvalues. This is in contrast to the Chern number where the eigenstates of the smallest eigenvalues contribute. To determine m, we need to discuss a feature of open systems. As in the interacting case, which was discussed in Sec. 3.3, in open systems the Green's function not only exhibits poles but can also exhibit zeros. Bands associated with these zeros are called *blind* bands. They are absent in closed and nontinteracting system, but can also carry topological properties [249]. In an open system with N_{pole} conventional bands and N_{blind} blind bands, we find $m = N_{\text{pole}} - N_{\text{blind}}$.

Let us turn to a specific example of a multilayer system, the trilayer system, i.e., $L = 3$. Here, we find two distinct cases of how to assemble one Haldane layer (HL) and two honeycomb, or graphene, layers (GL). These cases are $h = 1$ and $h = 2$. In principle, we could also have $h = L = 3$ but this case is equivalent to $h = 1$ due to the symmetry of the system. We denote the case $h = 1$ as HGG as the HL is on top of the two GL. This is

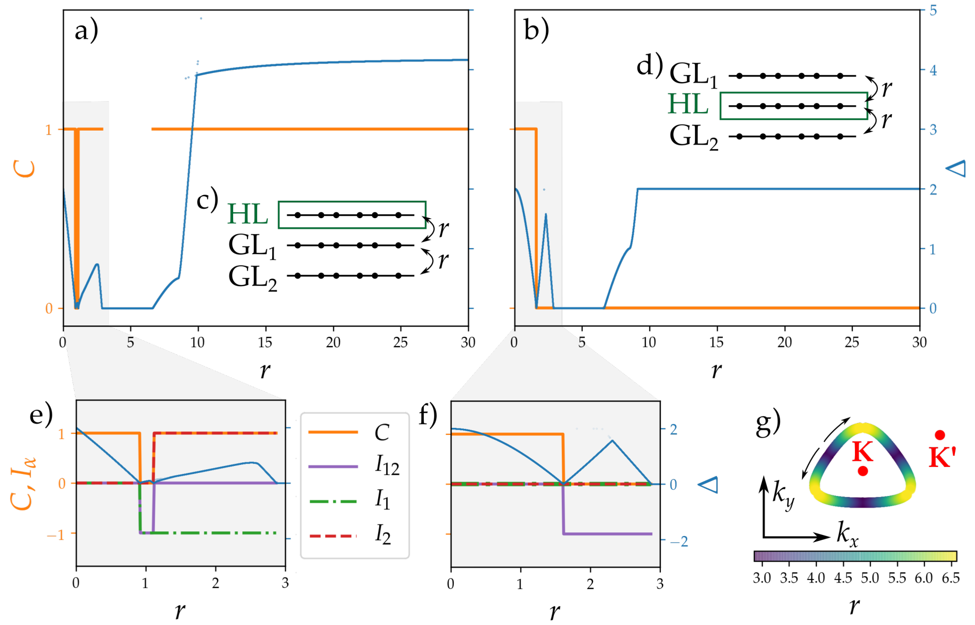

Figure 4.28: Band gap Δ, Chern number C, and layer-specific invariants I_α for the trilayer systems as functions of the inter-layer coupling r, where the Haldane layer is (a,c) on top of the graphene layers and (b,d) sandwiched between the graphene layers. (e) and (f) constitute zooms into the weak r regime of (a) and (b), respectively. (g) positions of Dirac cones in the BZ as a function of r inside the semimetallic regime. Reprinted with permission from Ref. [334]. Copyright (2020) by the American Physical Society.

schematically depicted in Fig. 4.28(c). The case $h = 2$ is referred to as GHG in which the HL is sandwiched between the two GL which is schematically shown in Fig. 4.28(d).

In Fig. 4.28, we present the band gap Δ of the full system, the Chern number C, and three different layer-specific invariants I_α as functions of the inter-layer coupling r for the two configurations HGG in (a) as well as GHG in (b). Generally, we note that topological phase transitions are always accompanied with a gap closing which is what we expect. Moreover, we observe in Fig. 4.28(a) that in the strong coupling regime $r \approx 30$ the system is gapped with $\Delta \approx 4$ and has a Chern number of $C = 1$. In contrast, in (b), the system is also gapped with $\Delta = 2$ but exhibits a trivial Chern number $C = 0$. Already at this stage, we note that the topological properties do not only depend on the number ratio of topologically nontrivial layers to trivial layers but also on the particular implementation. In the weak coupling regime $0 \leq r \leq 3$, the dependence of Δ and C on r is rather complicated. We zoom into this regime in Figs. 4.28(e) and (f) for the HGG and the GHG cases, respectively. We also plot the layer-specific invariants I_α in this regime.

Here, $\alpha = 1$ denotes that only the eigenstates of the reduced single-particle density matrix of subsystem GL_1 enter in Eq. (4.82). It thus is an topological invariant for GL_1 only. This applies analogously for $\alpha = 2$. When we write $\alpha = 12$, we mean that the subsystem is the combined system of both GL_1 and GL_2. In Fig. 4.28(e), we observe that C changes twice while r is tuned. This can be explained by two subsequent changes of I_1 and I_2, respectively. In particular, we find that $I_{12} = I_1 + I_2$, i.e., the layer-specific invariants obey some kind of sum rule. On the other hand, when looking at Fig. 4.28(f) there occurs only once a change of C. This change is by no means resembled in the layer-specific invariants I_1 and I_2 since they are constantly zero in the full range of r. Only I_{12} reflects the change of C up to a constant offset of 1. Clearly, the sum rule which applied in the HGG case is violated here in the GHG case. The system in the GHG rather behaves as the original BTPE of a bilayer system. This means, the BTPE, which is induced by the HL, emerges in the combined layer of both GL_1 and GL_2.

The discrepancy between the HGG and the GHG case can be explained with the emergence of *dark states* [336–338]. We note that the GHG configuration exhibits a mirror symmetry at the middle layer which is absent for the HGG configuration. Let us look at the Hamiltonian in Eq. (4.79) for $L = 3$ and $h = 2$. Out of the set of six-dimensional eigenvectors, there are two eigenvectors which can be written in the form

$$\left(v_1^{\pm}(\boldsymbol{k}), v_2^{\pm}(\boldsymbol{k}), 0, 0, v_1^{\pm}(\boldsymbol{k}), v_2^{\pm}(\boldsymbol{k})\right)^T, \tag{4.83}$$

where $\left(v_1^{\pm}(\boldsymbol{k}), v_2^{\pm}(\boldsymbol{k})\right)^T$ is an eigenvector of the 2×2 Hamiltonian $\vec{d}(\boldsymbol{k}) \cdot \boldsymbol{\sigma}$ corresponding to Eq. (4.81) and $\pm$ refers to the upper and lower band of this Hamiltonian. The important part here, is that the two eigenstates in Eq. (4.83) have vanishing amplitude at the middle layer which is the HL. They are thus completely decoupled from the HL and are referred to as dark states. In the presence of a dark state, the HL only couples to another pair of states. This is exactly the situation of a bilayer system since four states are involved. Remember that per layer two states are present because of the two-site unit cell.

Another observation of Figs. 4.28(a) and (b) is the gapless phase in the regime $3 \lesssim r \lesssim 6.5$. We find that the extent of this regime is identical between the cases HGG and GHG. In fact, we find a semimetal which exhibits six Dirac cones. In Fig. 4.28(g) we show the positions of these Dirac cones within the 2d BZ at the Fermi level. Herein, K and K' denote the high-symmetry points of the honeycomb BZ [197]. The color code reflects the values of the coupling r. At around $r \approx 3$, three pairs of Dirac cones are created. Increasing r causes the Dirac cones of one pair to separate which is highlighted by two arrows. At around $r \approx 6.5$, the Dirac points meet again in pairs, but this time with different partners, and annihilate. This phase is an instance of a quasi-2d semimetal. Other instances are reported in Refs. [190, 339], see also Ref. [52]. The pair creation and annihilation mechanism we described above when discussing Fig. 4.28(g) is reminiscent of a mechanism in 3d topological insulators [327, 340]. Therein, Weyl points are created in pairs, move within the 3d BZ, and are again annihilated in different pairs. This occurs in Weyl semimetals which emerge in the phase diagram between STI, WTI, and BI. Semimetals between 3d topologically insulating phases have been discussed in the previous section.

We now discuss results of the general multilayer system with L layers and the HL sitting at position h. Here, we will restrict ourselves to the discussion of the strong coupling limit where r is much larger than all other energy scales in the system. Using perturbation theory it was shown in Ref. [334] that the energy spectrum of the full system can be separated into L pairs of energy bands $\epsilon^{\pm}(\boldsymbol{k}, \kappa_z)$

$$E(\boldsymbol{k}) = -2r\cos(\kappa_z) + \epsilon^{\pm}(\boldsymbol{k}, \kappa_z), \tag{4.84}$$

where $\kappa_z = n\pi/(L+1)$ with $n = 1, ...L$ is a quantum number of a standing wave mode along the stacking direction of the layers. Since r is large, the pairs of energy bands are energetically separated from the other pairs with a scaling proportional to r. In fact, each pair resembles a separate effective set of Haldane bands with effective parameters

$$\lambda_{\text{eff}} = \left[1 - |\mathcal{N}|^2 \sin^2(\kappa_z h)\right] \lambda \quad \text{and} \quad t'_{\text{eff}} = |\mathcal{N}|^2 \sin^2(\kappa_z h) t'. \tag{4.85}$$

Here, the normalization constant $\mathcal{N}$ is determined from the amplitude of the wavefunction $|\mathcal{N}|^2 \sin^2(\kappa_z h)$ of the standing wave mode at the HL.

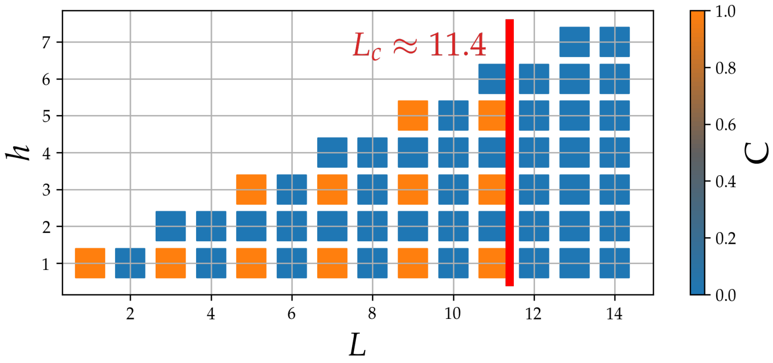

Figure 4.29: Strong coupling regime $r = 50$ for the general multilayer case. The color code refers to the numerical computation of C. The critical value L_c is defined in the text. Reprinted with permission from Ref. [334]. Copyright (2020) by the American Physical Society.

For a single pair of Haldane bands, we find the Chern insulating state only if the lower band is completely filled and the higher band is completely empty. For the multilayer system in the strong coupling regime, this means that only the two bands closest to the Fermi energy determine whether the full system is topologically trivial or not. Furthermore, only if these two bands, which are closest to the Fermi energy, belong to the same effective Haldane model, nontrivial topological properties can emerge. We conclude that only for odd values of L the system can be topologically trivial. In Fig. 4.29 we show the Chern number in the strong coupling regime $r = 50$ as a color scale. Here, C is determined numerically using Eq.(1.3). We observe that indeed if L is even, the multilayer system is always topologically trivial independent of h. We also see that if h is even, the multilayer system is again always topologically trivial independent of the value of L. This effect is attributed to the emergence of dark states as it was explained above for the trilayer system. Finally, we can determine a limit for the number of layers L the system can have, while remaining topologically nontrivial. This limit is determined from the effective parameters λ_{eff} and t'_{eff}. The Haldane model shows a Chern insulator state if $|\lambda|/t' < 3\sqrt{3}$ otherwise it is a band insulator. Computing this limit for the effective parameters, which depend on L, yields an upper bound L_c for the number of layers such that the system can still show nontrivial topological properties for any L and h. For $\lambda = 1$ and $t' = 1$, this yields $L_c \approx 11.4$ which we depict in Fig. 4.29. Indeed, we find from the numerical results for C that beyond L_c the system is always topologically trivial.

Concluding the section on layered systems in the context of the BTPE, we have found that the topological properties of the full multilayer system sensitively depend on the particular configuration. We have argued that the emergence of dark states in the multilayer system can cause the system to alter its topological properties. In fact, dark states are present even without the presence of any topologically nontrivial ingredients, such as the Haldane model in this case. Usually they do not have strong influence on global properties of the system. In the context of topological states, however, we show that dark states do matter. Experimentally, multilayer systems might be feasible to implement in cold atom systems with synthetic dimensions [333]. One would think of a 2d system in the real dimensions with atoms possessing many addressable hyperfine states. These hyperfine states act as layers and can be coupled via Raman transitions. In order to implement the BTPE, one would then have to impose an artificial gauge field on only one of these hyperfine states. This could be done through state-selective laser-assisted tunneling or lattice shaking as we have introduced the methods in Sec. 2.

Chapter 5

Conclusion

Within this work, we have introduced the reader to the field of topological states of matter and the possible experimental realization within the context of cold atomic gases in optical lattices. These highly tunable and well controlled systems allow one to built quantum simulators of tight-binding Hamiltonians. Among others, the on-site interaction between the atoms is tunable over a large range which makes it especially interesting to study Hubbard Hamiltonians. This work is dedicated to a variety of Hofstadter-Hubbard models, which generalize the seminal Hofstadter model. The difficult many-body problem, which arises due to the interparticle interaction, is treated by means of dynamical mean-field theory which is able to describe the full complexity of the metal-to-Mott-insulator transition.

The aim of this work is to theoretically describe cold atom systems hosting interacting, topologically nontrivial states of matter. These problems become very complex and require a numerical toolbox which is able to tackle problems originating from different fields of physics simultaneously. With this, we were able to investigate interacting, inhomogeneous, and spin-orbit-coupled states in two as well as in three dimensions.

This work can act as a starting point for future investigations of interacting topological states of matter in two and three dimensions [45,50,55,56] with numerical methods such as DMFT [211], as well as their possible realizations and probing in quantum simulators, especially in cold atom experiments [133,136]. The long-term aim could be the study of emergent topological states like topological Mott insulators [341] and other quantum spin liquid states [342] by means of the cluster extension to DMFT [343,344] and even quantum-classical DMFT as an application of quantum computing algorithms [345–347]. In the following, we recapitulate the results of this work and propose different projects as an outlook for further research:

Real-space DMFT study of inhomogeneous systems

Two-dimensional topological states are nowadays routinely engineered in cold atomic setups [112–115]. However, an obstacle for detecting, e.g., topological edge states, in these systems is their intrnisic inhomogeneity such that in many cases bulk and edge cannot be distinguished adequately. In order to circumvent this issue, we study the smooth interface between a quantum spin Hall and a band insulating phase in a 2d optical lattice and the effect of the Hubbard interaction [255]. Due to the high degree of inhomogeneity, we use the real-space version of DMFT [214, 215]. We characterize the topological properties of the interacting interface system by looking at topological pumping as well as the local Chern marker [251], generalized to the spinful case, in combination with the topological Hamiltonian approach [242]. The edge state itself is accessible from the local compressibility. We propose quantum gas microscopy to measure correlations and, subsequently, the edge state. Moreover, in another study [257], we analyze the competition between Hubbard interactions and a harmonic confining potential. In the bulk of the system, this gives rise to an interaction-induced topological phase transition similar to Refs. [193, 196] where the competing energy scales are the Hubbard interaction and the staggered potential. The underlying mechanism is the redistribution of the particle profile and the suppression of doubly occupied sites due to the interaction strength.

The used numerical methods could, e.g., be applied to twisted bilayer graphene (TBG) which shows insulating and superconducting behavior at different dopings [348] at the so-called magic twist angles [349]. Real-space DMFT could be used to study the effect of local quantum fluctuations in the whole range of interaction energies since it is nonperturbative. This enables the investigation of possible Mott regimes and thus goes beyond the Hartree-Fock approach to TBG [350, 351]. In cold atom systems, it is possible to tune the interaction energies freely by using Feshbach resonances. The study of TBG in cold atom setups is proposed in Ref. [352] and it is discussed that tunable interlayer hopping could increase the value of magic twist angles. This is helpful for a real-space DMFT study since a small twist angle yields a very large unit cell. Thus, for a DMFT study, one would start with a larger angle and use exact diagonalization methods to efficiently solve the impurity problems of the DMFT iterations.

Spin-imbalance-induced frustration

Canted antiferromagnetism [307] as well as the TRS Hofstadter model [112] can be realized in cold atom experiments. This leads to the study of the TRS Hofstadter-Hubbard model with additional TRS-breaking spin-population imbalance [306]. Here, we connect the two different groundstates of the spin-imbalanced Hubbard model and the Hofstadter-Hubbard model which are a canted antiferromagnet and a z-antiferromagnet, respectively. We find an exotic classical groundstate exhibiting a transverse net magnetization. Upon including local quantum fluctuations, this state is stable for some parameter regimes but breaks down into a ferrimagnet in different regimes of the phase diagram. The origin of frustration stems from the gauge field in the system, leading to a nontrivial modification of spin-spin interaction coefficients of the Heisenberg and Dyzaloshinskii-Moriya terms [190].

Here, it would be interesting to seek for emergent quantum phases, such as valence bond states and quantum spin liquids [342], arising from the nonlocal quantum fluctuations. Spin imbalance could serve as an experimentally accessible control parameter to tune the lattice frustration in cold atom systems. An interacting extension to the Harper-Hofstadter-Hatsugai model [194], which includes next-nearest neighbor hopping, is possible. This model is closely connected to the spin-1/2 J_1-J_2 Heisenberg model [353].

Tomography

Probing topological states in cold atom systems is an active research topic. Possible schemes base on Hall drifts [143], tomography [115, 272, 297], interferometry [270, 354], and depletion [355], among others. We develop tomographic schemes based on the single-particle density matrix in real space [256] as well as in momentum space [196], where the latter even enables the probing of interacting states.

3d topological states are much less abundant among cold atom experiments than 2d states. A reason for that is the difficulty to realize and probe these states. A recent setup successfully created a nodal-line semimetal [149] whose probing relies on a certain symmetry of the system. The demand for interacting schemes is still unabated which motivates the development of tomographic schemes based on the single-particle density matrix approach and reconstruction techniques [356].

Three-dimensional topological states

A 3d generalization of the TRS Hofstadter model was proposed [191] which hosts weak and strong topological insulator phases. We investigate this model by means of generalizations of methods based on twisted boundary conditions [264], Wilson loops [268], and the local Chern marker [251]. It appears that for finite spin mixing the gapless transition lines between the topological insulator regimes extend to gapless regions featuring a nodal-line semimetal. We study the bulk and surface states of these 3d topological states for finite interactions with real-space DMFT. The drumhead surface states of a NLSM have a diverging density of states which make them intriguing for interaction effects that strongly depend on the spin-orbit coupling [357].

The methods developed in Ref. [326] are suitable for any 3d multiband Hubbard model. It is thus attractive to apply them to models which preserve the surface flat band of the drumhead states. In Ref. [357] surface antiferromagnetism in a NLSM is predicted. Ref. [358] reports on a surface Chern insulator which emerges from the interplay of interactions and spin-orbit coupling. In combination with an interface configuration [255] these phenomena could be accessible in cold atom systems.

Layered systems

The topological proximity effect was introduced [328] as an analogue to the proximity effect in superconductivity. When a 2d topologically nontrivial system with Chern number $C = 1$ is coupled to a topologically trivial layer, the trivial layer becomes nontrivial with Chern number $C = -1$. In a further study [334], we investigated this effect for multilayer systems and find that the induced topological properties not only depend on the number of layers but also on their spatial configuration. This is explained by the emergence of dark states which effectively decouple from the nontrivial layer. Also a quasi-2d, semi-metallic phase emerges which persists even in the presence of spin-orbit coupling and a staggered potential. Within this phase we observe a creation and annihilation process of pairs of Dirac points which is reminiscent of Weyl points in 3d topological states [327]. The topological proximity effect has gained much attention since its first mention [328]. Bilayer systems are very promising candidates to host exotic quantum matter such as chiral and $\mathbb{Z}_2$ quantum spin liquids [359], an interaction-induced anomalous Hall insulator [360], and charge-ordered as well as spin-ordered Chern insulators [361]. The induced Chern number in the system of Ref. [328] has opposite Chern number compared to the inducing one. Hence, one could seek for systems in which both Chern numbers are equal. Moreover, the emerging semimetal in Ref. [334] suggests a connection to 3d gapless topological states. It might be interesting to study the transition from 2d to 3d physics using multilayer systems, especially in time-reversal-symmetric (TRS) systems, that may reveal possible connections to weak topological insulators.

Abbreviations

1d, 2d, 3d	one-, two-, three-dimensional/dimensions
AFM	antiferromagnetic/antiferromagnet
AIM	Anderson impurity model
BEC	Bose-Einstein condensate
BTPE	bulk topological proximity effect
BZ	Brillouin zone
BI	band insulator
CTQMC	continuous-time quantum Monte Carlo
DMFT	dynamical mean-field theory
DOS	density of states
ED	exact diagonalization
FM	ferromagnetic/ferromagnet
GL	graphene layer
HHH	Harper-Hofstadter-Hatsugai
HL	Haldane layer
IQH	integer quantum Hall effect
LCM	local Chern marker
MC	Monte Carlo
OBC	open boundary conditions
PBC	periodic boundary conditions
QMC	quantum Monte Carlo
QSH	quantum spin Hall effect
STI	strong topological insulator
TBC	twisted boundary conditions
TRIM	time-reversal-invariant momentum
TRS	time-reversal symmetric/symmetry
WTI	weak, topological insulator

Data, Software, and Permissions

Data and codes are archived at the Institute for Theoretical Physics of the Goethe University Frankfurt in Frankfurt am Main, Germany. Data and codes can be accessed by the Hofstetter group.

The results of this work were computed with codes written in Python and C++ including packages such as numpy, scipy, and matplotlib.

The author owns permissions from the journals of the peer-reviewed publications to reproduce Figs. 2.2(a), 2.2(b), 2.2(c), 2.2(d), 2.4(a), 2.4(b), 2.4(c), 4.1-4.6, 4.11-4.15, and 4.17-4.21. The Figs. 4.22-4.27 are published in Ref. [326] under the terms of the Creative Commons Attribution 4.0 International license and do not require a permission.

Journal title abbreviations correspond to the ones of the Caltech library at: www.library.caltech.edu/journal-title-abbreviations, March 2020

Acknowledgement

I want to thank the following people who accompanied me during my scientific career, for enlightening discussions, for their support. The order is randomized on purpose. I apologize for any forgotten mentions.

Ulrich Schollwöck, David Schneider, Francesca Ferlaino, Urs Gebert, Anna Sanpera, Cesar R. Cabrera, Axel Pelster, Jamir Marino, Cornelius Gahl, Nur Ünal, Václav Zatloukal, Tao Qin, Fabian Heidrich-Meißner, Etienne Wamba, Philippe Verkerk, Andreas Geißler, Walter Hofstetter, Roser Valentí, Denis Morath, Andrew L. C. Hayward, Matej Kanduč, Giovanna Morigi, Roland R. Netz, Constantin Meyer-Grant, Silvio Künstner, Kirill Plekhanov, Alexander Schnell, Mikhail Baranov, Peter Orth, Carlos Sa de Melo, Oleksandr Tsyplyatyev, Jürgen Bosse, Jaromir Panas, Mohsen Hafez-Torbati, Herwig Ott, Martin Kübler, Daniel Litinski, Irakli Titvinidze, Päivi Törmä, Karyn Le Hur, Maximilian Buser, Christof Weitenberg, Ivana Vasić, Sebastian Eggert, Nele Gluhovskij, Nathan Goldman, Sandro Gödtel, Maarten Grothus, Christian Schweizer, Randall Hulet, Michael Lohse, Nathan Schine, Marcel Goihl, Martin Weinelt, Dominik Straßel, Javed Akram, Frederic Sulzmann, Anand Sharma, Vladislav Borisov, Johannes Zeiher, Monika Aidelsburger, Martin Bonkhoff, Francisco Ednilson Alves dos Santos, Piet Brouwer, Ulrich Schneider, Antun Balaž, Michael Buchhold, Rudolf Grimm, Steven Winter, Eugene Zaremba, Botao Wang, Michael Pasek, Julius Schulz, Ana Hudomal, Arya Dhar, Fabian Grusdt, Alexander Schlaich, Fabrice Gerbier, Nicola Wurz, Nigel R. Cooper, Daniel Cocks, Mathieu Barbier, Fabrice Gerbier, Ulf Bissbort, Jan-Lennart Bönsel, Günter Steinert, Micheala Groll, Felix von Oppen, Hélène Perrin, Jason Ho, Michael Fleischhauer, Karen Wintersperger, Philipp W. Klein, Jun-Hui Zheng

The next page contains selected figures which arose within the scope of this work by mistake, be it from wrong theories, corrupt data, or failed plotting.

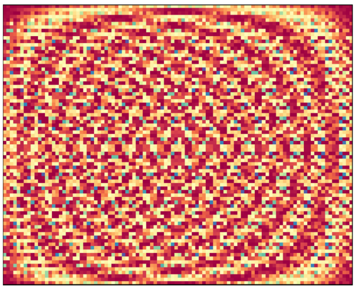

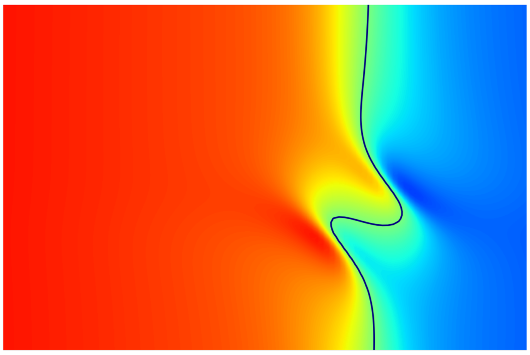

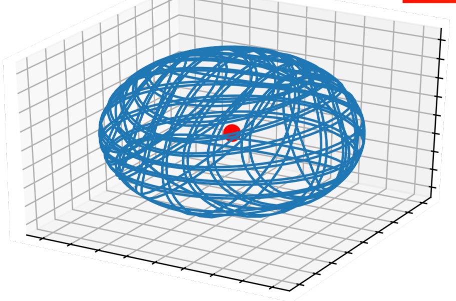

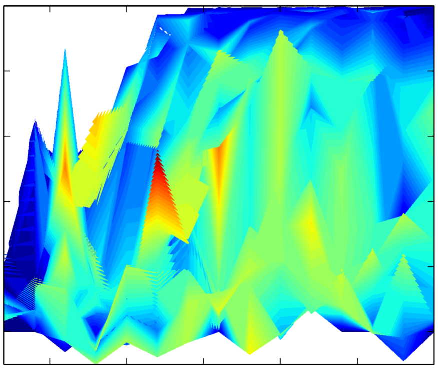

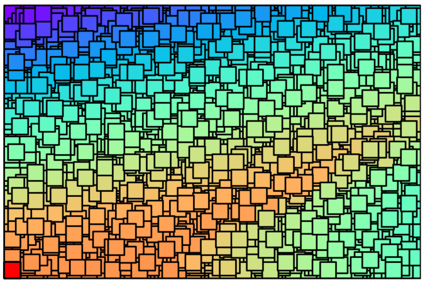

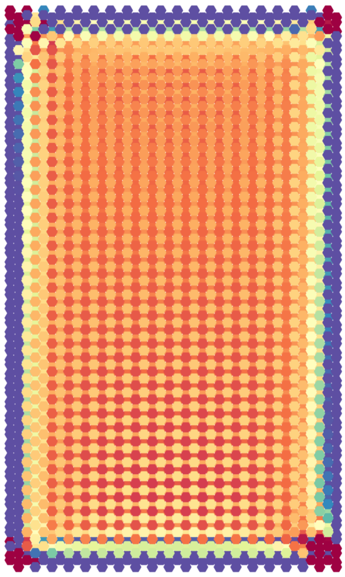

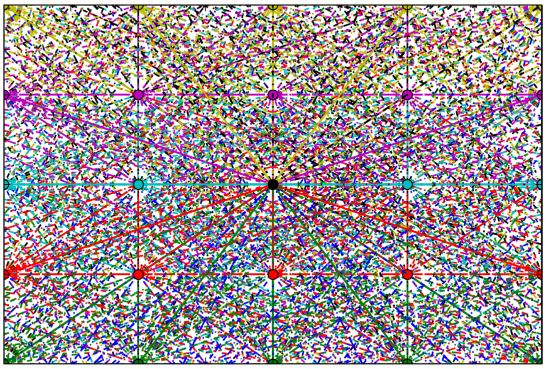

Bibliography

[1] E. H. Hall. On a new action of the magnet on electric currents. *Am. J. Math.*, 2:287, 1879.

[2] Z. F. Ezawa. *Quantum Hall Effects: Recent Theoretical and Experimental Developments Third Edition*. World Scientific Publishing Company, 2013.

[3] B. A. Bernevig and T. L. Hughes. *Topological Insulators and Topological Superconductors*. Princeton University Press, 2013.

[4] J. K. Asbóth, L. Oroszlány, and A. Pályi. *A Short Course on Topological Insulators*. Springer International Publishing, 2016.

[5] D. Tong. Lectures on the quantum hall effect. *arXiv:1606.06687*, 2016.

[6] K. von Klitzing, G. Dorda, and M. Pepper. New method for high-accuracy determination of the fine-structure constant based on quantized Hall resistance. *Phys. Rev. Lett.*, 45:494, 1980.

[7] T. Kinoshita. The fine structure constant. *Rep. Prog. Phys.*, 59:1459, 1996.

[8] D. R. Hofstadter. Energy levels and wave functions of Bloch electrons in rational and irrational magnetic fields. *Phys. Rev. B*, 14:2239, 1976.

[9] P. G. Harper. Single band motion of conduction electrons in a uniform magnetic field. *Prog. Phys. Soc. A*, 68:874, 1955.

[10] E. H. Hall. On the "rotational coefficient" in nickel and cobalt. *Philos. Mag.*, 12:157, 1881.

[11] R. Karplus and J. M. Luttinger. Hall effect in ferromagnetics. *Phys. Rev.*, 95:1154, 1954.

[12] N. Nagaosa, J. Sinova, S. Onoda, A. H. MacDonald, and N. P. Ong. Anomalous Hall effect. *Rev. Mod. Phys.*, 82:1539, 2010.

[13] C.-Z. Chang, J. Zhang, X. Feng, J. Shen, Z. Zhang, M. Guo, K. Li, Y. Ou, P. Wei, L.-L. Wang, Z.-Q. Ji, Y. Feng, S. Ji, X. Chen, J. Jia, X. Dai, Z. Fang, S.-C. Zhang, K. He, Y. Wang, L. Lu, X.-C. Ma, and Q.-K. Xue. Experimental observation of the quantum anomalous Hall effect in a magnetic topological insulator. *Science*, 340:167, 2013.

[14] F. D. M. Haldane. Model for a quantum Hall effect without Landau levels: Condensed-matter realization of the "parity anomaly". *Phys. Rev. Lett.*, 61:2015, 1988.

[15] M. I. Dyakonov and V. I. Perel. Current-induced spin orientation of electrons in semiconductors. *Phys. Lett. A*, 35:459, 1971.

[16] M. I. Dyakonov and V. I. Perel. Possibility of orienting electron spins with current. *JETP Lett.*, 13:467, 1971.

[17] J. Sinova, S. O. Valenzuela, J. Wunderlich, C. H. Back, and T. Jungwirth. Spin Hall effects. *Rev. Mod. Phys.*, 87:1213, 2015.

[18] S. Murakami, N. Nagaosa, and S.-C. Zhang. Spin-Hall insulator. *Phys. Rev. Lett.*, 93:156804, 2004.

[19] B. A. Bernevig and S.-C. Zhang. Quantum spin Hall effect. *Phys. Rev. Lett.*, 96:106802, 2006.

[20] C. L. Kane and E. J. Mele. Quantum spin Hall effect in graphene. *Phys. Rev. Lett.*, 95:226801, 2005.

[21] B. A. Bernevig, T. L. Hughes, and S.-C. Zhang. Quantum spin Hall effect and topological phase transition in HgTe quantum wells. *Science*, 314:1757, 2006.

[22] M. König, S. Wiedmann, C. Brüne, A. Roth, H. Buhmann, L. W. Molenkamp, X.-L. Qi, and S.-C. Zhang. Quantum spin Hall insulator state in HgTe quantum wells. *Science*, 318:766, 2007.

[23] M. König, H. Buhmann, L. W. Molenkamp, T. Hughes, C.-X. Liu, X.-L. Qi, and S.-C. Zhang. The quantum spin Hall effect: Theory and experiment. *J. Phys. Soc. Jpn.*, 77:031007, 2008.

[24] D. C. Tsui, H. L. Stormer, and A. C. Gossard. Two-dimensional magnetotransport in the extreme quantum limit. *Phys. Rev. Lett.*, 48:1559, 1982.

[25] R. B. Laughlin. Anomalous quantum Hall effect: An incompressible quantum fluid with fractionally charged excitations. *Phys. Rev. Lett.*, 50:1395, 1983.

[26] J. K. Jain. Composite-fermion approach for the fractional quantum Hall effect. *Phys. Rev. Lett.*, 63:199, 1989.

[27] G. Moore and N. Read. Nonabelions in the fractional quantum Hall effect. *Nucl. Phys. B*, 360:362, 1991.

[28] A. Kitaev and J. Preskill. Topological entanglement entropy. *Phys. Rev. Lett.*, 96:110404, 2006.

[29] K. Qian, D. J. Apigo, C. Prodan, Y. Barlas, and E. Prodan. Topology of the valley-Chern effect. *Phys. Rev. B*, 98:155138, 2018.

[30] S. Ryu, A. P. Schnyder, A. Furusaki, and A. W. W. Ludwig. Topological insulators and superconductors: tenfold way and dimensional hierarchy. *New J. Phys.*, 12:065010, 2010.

[31] M. Lohse, C. Schweizer, H. M. Price, O. Zilberberg, and I. Bloch. Exploring 4d quantum Hall physics with a 2d topological charge pump. *Nature*, 553:55, 2018.

[32] F. Tang, Y. Ren, P. Wang, R. Zhong, J. Schneeloch, S. A. Yang, K. Yang, P. A. Lee, G. Gu, Z. Qiao, and L. Zhang. Three-dimensional quantum Hall effect and metal-insulator transition in ZrTe5. *Nature*, 569:537, 2019.

[33] M. Nakahara. *Geometry, topology and physics*. CRC Press, 2003.

[34] D. J. Thouless, M. Kohmoto, M. P. Nightingale, and M. den Nijs. Quantized Hall conductance in a two-dimensional periodic potential. *Phys. Rev. Lett.*, 49:405, 1982.

[35] M. V. Berry. Quantal phase factors accompanying adiabatic changes. *Proc. Roy. Soc. A.*, 392:45, 1984.

[36] B. I. Halperin. Quantized Hall conductance, current-carrying edge states, and the existence of extended states in a two-dimensional disordered potential. *Phys. Rev. B*, 25:2185, 1982.

[37] Y. Hatsugai. Chern number and edge states in the integer quantum hall effect. *Phys. Rev. Lett.*, 71:3697, 1993.

[38] A. M. Essin and V. Gurarie. Bulk-boundary correspondence of topological insulators from their respective Green's functions. *Phys. Rev. B*, 84:125132, 2011.

[39] T. E. Lee. Anomalous edge state in a non-hermitian lattice. *Phys. Rev. Lett.*, 116:133903, 2016.

[40] K. Kawabata, K. Shiozaki, and M. Ueda. Anomalous helical edge states in a non-hermitian Chern insulator. *Phys. Rev. B*, 98:165148, 2018.

[41] M. Buchhold, D. Cocks, and W. Hofstetter. Effects of smooth boundaries on topological edge modes in optical lattices. *Phys. Rev. A*, 85:063614, 2012.

[42] S. Murakami. Two-dimensional topological insulators and their edge states. *J. Phys. Conf. Ser.*, 302:012019, 2011.

[43] B.-H. Chen and D.-W. Chiou. A detailed proof and investigation of the bulk-boundary correspondence in the generic two-band model of Chern insulators. *arXiv:1904.11671*, 2019.

[44] C. L. Kane and E. J. Mele. Z_2 topological order and the quantum spin Hall effect. *Phys. Rev. Lett.*, 95:146802, 2005.

[45] M. Z. Hasan and C. L. Kane. Colloquium: Topological insulators. *Rev. Mod. Phys.*, 82:3045, 2010.

[46] L. Fu. Topological crystalline insulators. *Phys. Rev. Lett.*, 106:106802, 2011.

[47] L. Fu, C. L. Kane, and E. J. Mele. Topological insulators in three dimensions. *Phys. Rev. Lett.*, 98:106803, 2007.

[48] J. E. Moore and L. Balents. Topological invariants of time-reversal-invariant band structures. *Phys. Rev. B*, 75:121306, 2007.

[49] R. Roy. Topological phases and the quantum spin hall effect in three dimensions. *Phys. Rev. B*, 79:195322, 2009.

[50] M. Z. Hasan and J. E. Moore. Three-dimensional topological insulators. *Annu. Rev. Conden. Ma. P.*, 2:55, 2011.

[51] Z. Ringel, Y. E. Kraus, and A. Stern. Strong side of weak topological insulators. *Phys. Rev. B*, 86:045102, 2012.

[52] S. M. Young, S. Zaheer, J. C. Y. Teo, C. L. Kane, E. J. Mele, and A. M. Rappe. Dirac semimetal in three dimensions. *Phys. Rev. Lett.*, 108:140405, 2012.

[53] B. Sbierski, M. Schneider, and P. W. Brouwer. Weak side of strong topological insulators. *Phys. Rev. B*, 93:161105, 2016.

[54] A. Amaricci, J. C. Budich, M. Capone, B. Trauzettel, and G. Sangiovanni. Strong correlation effects on topological quantum phase transitions in three dimensions. *Phys. Rev. B*, 93:235112, 2016.

[55] C. Fang, H. Weng, X. Dai, and Z. Fang. Topological nodal line semimetals. *Chinese Phys. B*, 25:117106, 2016.

[56] N. P. Armitage, E. J. Mele, and A. Vishwanath. Weyl and Dirac semimetals in three-dimensional solids. *Rev. Mod. Phys.*, 90:015001, 2018.

[57] R. P. Feynman. Simulating physics with computers. *Int. J. Theor. Phys.*, 21:467, 1982.

[58] I. Buluta and F. Nori. Quantum simulators. *Science*, 326:108, 2009.

[59] P. Hauke, F. M. Cucchietti, L. Tagliacozzo, I. Deutsch, and M. Lewenstein. Can one trust quantum simulators? *Rep. Prog. Phys.*, 75:082401, 2012.

[60] I. M. Georgescu, S. Ashhab, and F. Nori. Quantum simulation. *Rev. Mod. Phys.*, 86:153, 2014.

[61] A. Acín, I. Bloch, H. Buhrman, T. Calarco, C. Eichler, J. Eisert, D. Esteve, N. Gisin, S. J. Glaser, F. Jelezko, S. Kuhr, M. Lewenstein, M. F. Riedel, P. O. Schmidt, R. Thew, A. Wallraff, I. Walmsley, and F. K. Wilhelm. The quantum technologies roadmap: a european community view. *New J. Phys.*, 20:080201, 2018.

[62] S. Lloyd. Universal quantum simulators. *Science*, 273:1073, 1996.

[63] L. Lamata, A. Parra-Rodriguez, M. Sanz, and E. Solano. Digital-analog quantum simulations with superconducting circuits. *Adv. Phys.*, 3:1457981, 2018.

[64] R. Blatt and C. F. Roos. Quantum simulations with trapped ions. *Nat. Phys.*, 8:277, 2012.

[65] A. A. Houck, H. E. Türeci, and J. Koch. On-chip quantum simulation with superconducting circuits. *Nat. Phys.*, 8:292, 2012.

[66] A. Aspuru-Guzik and P. Walther. Photonic quantum simulators. *Nat. Phys.*, 8:285, 2012.

[67] J. Tangpanitanon and D. G. Angelakis. Many-body physics and quantum simulations with strongly interacting photons. *arXiv:1907.05030*, 2019.

[68] I. Bloch, J. Dalibard, and S. Nascimbène. Quantum simulations with ultracold quantum gases. *Nat. Phys.*, 8:267, 2012.

[69] S. Raeisi, N. Wiebe, and B. C. Sanders. Quantum-circuit design for efficient simulations of many-body quantum dynamics. *New J. Phys.*, 14:103017, 2012.

[70] C. Gross and I. Bloch. Quantum simulations with ultracold atoms in optical lattices. *Science*, 357:995, 2017.

[71] W. Hofstetter and T. Qin. Quantum simulation of strongly correlated condensed matter systems. *J. Phys. B*, 51:082001, 2018.

[72] U.-J. Wiese. Ultracold quantum gases and lattice systems: quantum simulation of lattice gauge theories. *Ann. Phys.-Berlin*, 525:777, 2013.

[73] E. Zohar, J. I. Cirac, and B. Reznik. Quantum simulations of gauge theories with ultracold atoms: Local gauge invariance from angular-momentum conservation. *Phys. Rev. A*, 88:023617, 2013.

[74] C. Hempel, C. Maier, J. Romero, J. McClean, T. Monz, H. Shen, P. Jurcevic, B. P. Lanyon, P. Love, R. Babbush, A. Aspuru-Guzik, R. Blatt, and C. F. Roos. Quantum chemistry calculations on a trapped-ion quantum simulator. *Phys. Rev. X*, 8:031022, 2018.

[75] J. Argüello-Luengo, A. González-Tudela, T. Shi, P. Zoller, and J. I. Cirac. Analogue quantum chemistry simulation. *Nature*, 574:215, 2019.

[76] M. Greiner, O. Mandel, T. Esslinger, T. W. Hänsch, and I. Bloch. Quantum phase transition from a superfluid to a Mott insulator in a gas of ultracold atoms. *Nature*, 415:39, 2002.

[77] R. Jördens, N. Strohmaier, K. Günter, H. Moritz, and T. Esslinger. A Mott insulator of fermionic atoms in an optical lattice. *Nature*, 455:204, 2008.

[78] C. A. Regal, M. Greiner, and D. S. Jin. Observation of resonance condensation of fermionic atom pairs. *Phys. Rev. Lett.*, 92:040403, 2004.

[79] M. W. Zwierlein, C. A. Stan, C. H. Schunck, S. M. F. Raupach, A. J. Kerman, and W. Ketterle. Condensation of pairs of fermionic atoms near a Feshbach resonance. *Phys. Rev. Lett.*, 92:120403, 2004.

[80] A. G. Truscott, K. E. Strecker, W. I. McAlexander, G. B. Partridge, and R. G. Hulet. Observation of Fermi pressure in a gas of trapped atoms. *Science*, 291:2570, 2001.

[81] A. Mazurenko, C. S. Chiu, G. Ji, M. F. Parsons, M. Kanász-Nagy, R. Schmidt, F. Grusdt, E. Demler, D. Greif, and M. Greiner. A cold-atom Fermi-Hubbard antiferromagnet. *Nature*, 545:462, 2017.

[82] C. Schweizer, F. Grusdt, M. Berngruber, L. Barbiero, E. Demler, N. Goldman, I. Bloch, and M. Aidelsburger. Floquet approach to Z_2 lattice gauge theories with ultracold atoms in optical lattices. *Nat. Phys.*, 15:1168, 2019.

[83] W. Hofstetter, J. I. Cirac, P. Zoller, E. Demler, and M. D. Lukin. High-temperature superfluidity of fermionic atoms in optical lattices. *Phys. Rev. Lett.*, 89:220407, 2002.

[84] D. Porras and J. I. Cirac. Effective quantum spin systems with trapped ions. *Phys. Rev. Lett.*, 92:207901, 2004.

[85] R. Blatt and D. Wineland. Entangled states of trapped atomic ions. *Nature*, 453:1008, 2008.

[86] T. Orell, A. A. Michailidis, M. Serbyn, and M. Silveri. Probing the many-body localization phase transition with superconducting circuits. *Phys. Rev. B*, 100:134504, 2019.

[87] F. Dreisow, M. Heinrich, R. Keil, A. Tünnermann, S. Nolte, S. Longhi, and A. Szameit. Classical simulation of relativistic Zitterbewegung in photonic lattices. *Phys. Rev. Lett.*, 105:143902, 2010.

[88] L. Pitaevskii and S. Stringari. *Bose-Einstein Condensation*. Clarendon Press, 2003.

[89] C. J. Pethick and H. Smith. *Bose-Einstein Condensation in Dilute Gases*. Cambridge University Press, 2008.

[90] S. Giorgini, L. P. Pitaevskii, and S. Stringari. Theory of ultracold atomic Fermi gases. *Rev. Mod. Phys.*, 80:1215, 2008.

[91] S. Chu. Nobel lecture: The manipulation of neutral particles. *Rev. Mod. Phys.*, 70:685, 1998.

[92] C. N. Cohen-Tannoudji. Nobel lecture: Manipulating atoms with photons. *Rev. Mod. Phys.*, 70:707, 1998.

[93] W. D. Phillips. Nobel lecture: Laser cooling and trapping of neutral atoms. *Rev. Mod. Phys.*, 70:721, 1998.

[94] S. Bose. Plancks Gesetz und Lichtquantenhypothese. *Z. Phys.*, 26:178, 1924.

[95] A. Einstein. Quantentheorie des einatomigen idealen Gases - Zweite Abhandlung. *Sitzber. preuss. Akad.*, 1925:3, 1925.

[96] M. H. Anderson, J. R. Ensher, M. R. Matthews, C. E. Wieman, and E. A. Cornell. Observation of Bose-Einstein condensation in a dilute atomic vapor. *Science*, 269:198, 1995.

[97] K. B. Davis, M. O. Mewes, M. R. Andrews, N. J. van Druten, D. S. Durfee, D. M. Kurn, and W. Ketterle. Bose-Einstein condensation in a gas of sodium atoms. *Phys. Rev. Lett.*, 75:3969, 1995.

[98] C. C. Bradley, C. A. Sackett, J. J. Tollett, and R. G. Hulet. Evidence of Bose-Einstein condensation in an atomic gas with attractive interactions. *Phys. Rev. Lett.*, 75:1687, 1995.

[99] C. C. Bradley, C. A. Sackett, J. J. Tollett, and R. G. Hulet. Evidence of Bose-Einstein condensation in an atomic gas with attractive interactions [Phys. Rev. Lett. 75, 1687 (1995)]. *Phys. Rev. Lett.*, 79:1170, 1997.

[100] A. Ashkin. Acceleration and trapping of particles by radiation pressure. *Phys. Rev. Lett.*, 24:156, 1970.

[101] R. Grimm, M. Weidemüller, and Y. B. Ovchinnikov. Optical dipole traps for neutral atoms. In *Advances In Atomic, Molecular, and Optical Physics*, page 95. Elsevier, 2000.

[102] D. Jaksch, C. Bruder, J. I. Cirac, C. W. Gardiner, and P. Zoller. Cold bosonic atoms in optical lattices. *Phys. Rev. Lett.*, 81:3108, 1998.

[103] T. Giamarchi A. Georges. Strongly correlated bosons and fermions in optical lattices. In C. Salomon, G. V. Shlyapnikov, and L. F. Cugliandolo, editors, *Many-Body Physics with Ultracold Gases*. Oxford University Press, 2012.

[104] I. Bloch. Ultracold quantum gases in optical lattices. *Nat. Phys.*, 1:23, 2005.

[105] M. Lewenstein, A. Sanpera, V. Ahufinger, B. Damski, A. Sen(De), and U. Sen. Ultracold atomic gases in optical lattices: mimicking condensed matter physics and beyond. *Adv. Phys.*, 56:243, 2007.

[106] I. Bloch, J. Dalibard, and W. Zwerger. Many-body physics with ultracold gases. *Rev. Mod. Phys.*, 80:885, 2008.

[107] U. Schneider, L. Hackermueller, S. Will, Th. Best, I. Bloch, T. A. Costi, R. W. Helmes, D. Rasch, and A. Rosch. Metallic and insulating phases of repulsively interacting fermions in a 3d optical lattice. *Science*, 322:1520, 2008.

[108] Z. Hadzibabic, C. A. Stan, K. Dieckmann, S. Gupta, M. W. Zwierlein, A. Görlitz, and W. Ketterle. Two-species mixture of quantum degenerate Bose and Fermi gases. *Phys. Rev. Lett.*, 88:160401, 2002.

[109] G. Roati, F. Riboli, G. Modugno, and M. Inguscio. Fermi-Bose quantum degenerate ^{49}K-^{87}Rb mixture with attractive interaction. *Phys. Rev. Lett.*, 89:150403, 2002.

[110] S. Taie, R. Yamazaki, S. Sugawa, and Y. Takahashi. An SU(6) Mott insulator of an atomic Fermi gas realized by large-spin Pomeranchuk cooling. *Nat. Phys.*, 8:825, 2012.

[111] C. Chin, R. Grimm, P. Julienne, and E. Tiesinga. Feshbach resonances in ultracold gases. *Rev. Mod. Phys.*, 82:1225, 2010.

[112] M. Aidelsburger, M. Atala, M. Lohse, J. T. Barreiro, B. Paredes, and I. Bloch. Realization of the Hofstadter Hamiltonian with ultracold atoms in optical lattices. *Phys. Rev. Lett.*, 111:185301, 2013.

[113] H. Miyake, G. A. Siviloglou, C. J. Kennedy, W. C. Burton, and W. Ketterle. Realizing the Harper Hamiltonian with laser-assisted tunneling in optical lattices. *Phys. Rev. Lett.*, 111:185302, 2013.

[114] G. Jotzu, M. Messer, R. Desbuquois, M. Lebrat, T. Uehlinger, D. Greif, and T. Esslinger. Experimental realization of the topological Haldane model with ultracold fermions. *Nature*, 515:237, 2014.

[115] N. Fläschner, B. S. Rem, M. Tarnowski, D. Vogel, D.-S. Lühmann, K. Sengstock, and C. Weitenberg. Experimental reconstruction of the Berry curvature in a Floquet Bloch band. *Science*, 352:1091, 2016.

[116] Y.-J. Lin, K. Jiménez-García, and I. B. Spielman. Spin-orbit-coupled Bose-Einstein condensates. *Nature*, 471:83, 2011.

[117] M. Schreiber, S. S. Hodgman, P. Bordia, H. P. Luschen, M. H. Fischer, R. Vosk, E. Altman, U. Schneider, and I. Bloch. Observation of many-body localization of interacting fermions in a quasirandom optical lattice. *Science*, 349:842, 2015.

[118] K. Singer, M. Reetz-Lamour, T. Amthor, S. Fölling, M. Tscherneck, and M. Weidemüller. Spectroscopy of an ultracold Rydberg gas and signatures of Rydberg-Rydberg interactions. *J. Phys. B*, 38:S321, 2005.

[119] A. L. Gaunt, T. F. Schmidutz, I. Gotlibovych, R. P. Smith, and Z. Hadzibabic. Bose-Einstein condensation of atoms in a uniform potential. *Phys. Rev. Lett.*, 110:200406, 2013.

[120] B. Mukherjee, Z. Yan, P. B. Patel, Z. Hadzibabic, T. Yefsah, J. Struck, and M. W. Zwierlein. Homogeneous atomic Fermi gases. *Phys. Rev. Lett.*, 118:123401, 2017.

[121] G. Gauthier, I. Lenton, N. McKay Parry, M. Baker, M. J. Davis, H. Rubinsztein-Dunlop, and T. W. Neely. Direct imaging of a digital-micromirror device for configurable microscopic optical potentials. *Optica*, 3:1136, 2016.

[122] D. C. McKay and B. DeMarco. Cooling in strongly correlated optical lattices: prospects and challenges. *Rep. Prog. Phys.*, 74:054401, 2011.

[123] T. W. Hänsch and A. L. Schawlow. Cooling of gases by laser radiation. *Opt. Commun.*, 13:68, 1975.

[124] C. Savage. Introduction to light forces, atom cooling, and atom trapping. *Aust. J. Phys.*, 49:745, 1996.

[125] K. Günter, T. Stöferle, H. Moritz, M. Köhl, and T. Esslinger. Bose-Fermi mixtures in a three-dimensional optical lattice. *Phys. Rev. Lett.*, 96:180402, 2006.

[126] T.-L. Ho and Q. Zhou. Universal cooling scheme for quantum simulation. *arXiv:0911.5506*, 2009.

[127] W. S. Bakr, J. I. Gillen, A. Peng, S. Fölling, and M. Greiner. A quantum gas microscope for detecting single atoms in a Hubbard-regime optical lattice. *Nature*, 462:74, 2009.

[128] E. Haller, J. Hudson, A. Kelly, D. A. Cotta, B. Peaudecerf, G. D. Bruce, and S. Kuhr. Single-atom imaging of fermions in a quantum-gas microscope. *Nat. Phys.*, 11:738, 2015.

[129] K. D. Nelson, X. Li, and D. S. Weiss. Imaging single atoms in a three-dimensional array. *Nat. Phys.*, 3:556, 2007.

[130] C. Weitenberg, M. Endres, J. F. Sherson, M. Cheneau, P. Schauß, T. Fukuhara, I. Bloch, and S. Kuhr. Single-spin addressing in an atomic Mott insulator. *Nature*, 471:319, 2011.

[131] S. L. Cornish, N. R. Claussen, J. L. Roberts, E. A. Cornell, and C. E. Wieman. Stable ^{85}Rb Bose-Einstein condensates with widely tunable interactions. *Phys. Rev. Lett.*, 85:1795, 2000.

[132] A. J. Moerdijk, B. J. Verhaar, and A. Axelsson. Resonances in ultracold collisions ^{6}Li, ^{7}Li, and ^{23}Na. *Phys. Rev. A*, 51:4852, 1995.

[133] J. Dalibard, F. Gerbier, G. Juzeliūnas, and P. Öhberg. Colloquium: Artificial gauge potentials for neutral atoms. *Rev. Mod. Phys.*, 83:1523, 2011.

[134] N. Goldman, G. Juzeliūnas, P. Öhberg, and I. B. Spielman. Light-induced gauge fields for ultracold atoms. *Rep. Prog. Phys.*, 77:126401, 2014.

[135] N. Goldman, J. C. Budich, and P. Zoller. Topological quantum matter with ultracold gases in optical lattices. *Nat. Phys.*, 12:639, 2016.

[136] M. Aidelsburger, S. Nascimbene, and N. Goldman. Artificial gauge fields in materials and engineered systems. *Compt. Rend. Phys.*, 19:394, 2018.

[137] N. R. Cooper. Rapidly rotating atomic gases. *Adv. Phys.*, 57:539, 2008.

[138] V. Schweikhard, I. Coddington, P. Engels, V. P. Mogendorff, and E. A. Cornell. Rapidly rotating Bose-Einstein condensates in and near the lowest Landau level. *Phys. Rev. Lett.*, 92:040404, 2004.

[139] V. Bretin, S. Stock, Y. Seurin, and J. Dalibard. Fast rotation of a Bose-Einstein condensate. *Phys. Rev. Lett.*, 92:050403, 2004.

[140] Y.-J. Lin, R. L. Compton, K. Jiménez-García, J. V. Porto, and I. B. Spielman. Synthetic magnetic fields for ultracold neutral atoms. *Nature*, 462:628, 2009.

[141] O. Boada, A. Celi, J. I. Latorre, and M. Lewenstein. Quantum simulation of an extra dimension. *Phys. Rev. Lett.*, 108:133001, 2012.

[142] M. Houbiers, R. Ferwerda, H. T. C. Stoof, W. I. McAlexander, C. A. Sackett, and R. G. Hulet. Superfluid state of atomic ^{6}Li in a magnetic trap. *Phys. Rev. A*, 56:4864, 1997.

[143] M. Aidelsburger, M. Lohse, C. Schweizer, M. Atala, J. T. Barreiro, S. Nascimbène, N. R. Cooper, I. Bloch, and N. Goldman. Measuring the Chern number of Hofstadter bands with ultracold bosonic atoms. *Nat. Phys.*, 11:162, 2015.

[144] M. Mancini, G. Pagano, G. Cappellini, L. Livi, M. Rider, J. Catani, C. Sias, P. Zoller, M. Inguscio, M. Dalmonte, and L. Fallani. Observation of chiral edge states with neutral fermions in synthetic Hall ribbons. *Science*, 349:1510, 2015.

[145] B. K. Stuhl, H.-I. Lu, L. M. Aycock, D. Genkina, and I. B. Spielman. Visualizing edge states with an atomic Bose gas in the quantum Hall regime. *Science*, 349:1514, 2015.

[146] T. Li, L. Duca, M. Reitter, F. Grusdt, E. Demler, M. Endres, M. Schleier-Smith, I. Bloch, and U. Schneider. Bloch state tomography using Wilson lines. *Science*, 352:1094, 2016.

[147] M. E. Tai, A. Lukin, M. Rispoli, R. Schittko, T. Menke, D. Borgnia, P. M. Preiss, F. Grusdt, A. M. Kaufman, and M. Greiner. Microscopy of the interacting Harper-Hofstadter model in the two-body limit. *Nature*, 546:519, 2017.

[148] F. Görg, M. Messer, K. Sandholzer, G. Jotzu, R. Desbuquois, and T. Esslinger. Enhancement and sign change of magnetic correlations in a driven quantum many-body system. *Nature*, 553:481, 2018.

[149] B. Song, C. He, S. Niu, L. Zhang, Z. Ren, X.-J. Liu, and G.-B. Jo. Observation of nodal-line semimetal with ultracold fermions in an optical lattice. *Nat. Phys.*, 15:911, 2019.

[150] T. Chalopin, T. Satoor, A. Evrard, V. Makhalov, J. Dalibard, R. Lopes, and S. Nascimbene. Probing chiral edge dynamics and bulk topology of a synthetic Hall system. *Nat. Phys.*, 16:1017, 2020.

[151] M. Bukov, L. D'Alessio, and A. Polkovnikov. Universal high-frequency behavior of periodically driven systems: from dynamical stabilization to Floquet engineering. *Adv. Phys.*, 64:139, 2015.

[152] J. H. Shirley. Solution of the Schrödinger equation with a Hamiltonian periodic in time. *Phys. Rev.*, 138:B979, 1965.

[153] A. Eckardt. Colloquium: Atomic quantum gases in periodically driven optical lattices. *Rev. Mod. Phys.*, 89:011004, 2017.

[154] J. Hubbard. Electron correlations in narrow energy bands. *Proc. Roy. Soc. A*, 276:238, 1963.

[155] J. Kanamori. Electron correlation and ferromagnetism of transition metals. *Prog. Theor. Phys.*, 30:275, 1963.

[156] M. C. Gutzwiller. Effect of correlation on the ferromagnetism of transition metals. *Phys. Rev. Lett.*, 10:159, 1963.

[157] G. D. Mahan. *Many-Particle Physics*. Springer, Boston, MA, 2000.

[158] A. Amaricci, J. C. Budich, M. Capone, B. Trauzettel, and G. Sangiovanni. First-order character and observable signatures of topological quantum phase transitions. *Phys. Rev. Lett.*, 114:185701, 2015.

[159] L. Crippa, A. Amaricci, N. Wagner, G. Sangiovanni, J. C. Budich, and M. Capone. Nonlocal annihilation of Weyl fermions in correlated systems. *Phys. Rev. Res.*, 2:012023, 2020.

[160] J. E. Hirsch. Quasiparticle undressing: A new route to collective effects in solids. In A. C. Hewson and V. Zlatić, editors, *Concepts in Electron Correlation*. Springer, Dordrecht, 2003.

[161] R. Staudt, M. Dzierzawa, and A. Muramatsu. Phase diagram of the three-dimensional Hubbard model at half filling. *Eur. Phys. J. B*, 17:411, 2000.

[162] P. R. C. Kent, M. Jarrell, T. A. Maier, and T. Pruschke. Efficient calculation of the antiferromagnetic phase diagram of the three-dimensional Hubbard model. *Phys. Rev. B*, 72:060411, 2005.

[163] F. Werner, O. Parcollet, A. Georges, and S. R. Hassan. Interaction-induced adiabatic cooling and antiferromagnetism of cold fermions in optical lattices. *Phys. Rev. Lett.*, 95:056401, 2005.

[164] X. Dai, K. Haule, and G. Kotliar. Strong-coupling solver for the quantum impurity model. *Phys. Rev. B*, 72:045111, 2005.

[165] J. E. Hirsch. Simulations of the three-dimensional Hubbard model: Half-filled band sector. *Phys. Rev. B*, 35:1851, 1987.

[166] Y. Kakehashi and H. Hasegawa. Magnetic phase diagram of the half-filled Hubbard model for a simple cubic lattice. *Phys. Rev. B*, 36:4066, 1987.

[167] D. J. Scalapino, R. L. Sugar, S. R. White, N. E. Bickers, and R. T. Scalettar. Numerical simulations: some results for the 2- and 3-d Hubbard models and a 2-d electron phonon model. *Phys. Scr.*, 1989:101, 1989.

[168] G. S. Rushbrooke, G. A. Baker Jr., and P. J. Wood. Heisenberg model. In C. Domb and M.S. Green, editors, *Phase Transitions and Critical Phenomena. Vol. 3; Series Expansions for Lattice Models*, volume 3. Academic Press, 1974.

[169] E. V. Gorelik, I. Titvinidze, W. Hofstetter, M. Snoek, and N. Blümer. Néel transition of lattice fermions in a harmonic trap: A real-space dynamic mean-field study. *Phys. Rev. Lett.*, 105:065301, 2010.

[170] J. C. Slater. Magnetic effects and the Hartree-Fock equation. *Phys. Rev.*, 82:538, 1951.

[171] M. Jarrell and T. Pruschke. Magnetic and dynamic properties of the Hubbard model in infinite dimensions. *Z. Phys. B*, 90:187, 1993.

[172] N. F. Mott. The basis of the electron theory of metals, with special reference to the transition metals. *Proc. Phys. Soc. Lond. A*, 62:416, 1949.

[173] A. Georges. Strongly correlated electron materials: Dynamical mean-field theory and electronic structure. *arXiv:cond-mat/0403123*, 2004.

[174] G. Kotliar, S. Y. Savrasov, K. Haule, V. S. Oudovenko, O. Parcollet, and C. A. Marianetti. Electronic structure calculations with dynamical mean-field theory. *Rev. Mod. Phys.*, 78:865, 2006.

[175] M. Imada, A. Fujimori, and Y. Tokura. Metal-insulator transitions. *Rev. Mod. Phys.*, 70:1039, 1998.

[176] V. Galitski and I. B. Spielman. Spin-orbit coupling in quantum gases. *Nature*, 494:49, 2013.

[177] R. Peierls. Zur Theorie des Diamagnetismus von Leitungselektronen. *Z. Phys.*, 80:763, 1933.

[178] D. Nakamura, A. Ikeda, H. Sawabe, Y. H. Matsuda, and S. Takeyama. Record indoor magnetic field of 1200 T generated by electromagnetic flux-compression. *Rev. Sci. Instrum.*, 89:095106, 2018.

[179] I. Vasić, A. Petrescu, K. Le Hur, and W. Hofstetter. Chiral bosonic phases on the Haldane honeycomb lattice. *Phys. Rev. B*, 91:094502, 2015.

[180] T. Qin and W. Hofstetter. Spectral functions of a time-periodically driven Falicov-Kimball model: Real-space Floquet dynamical mean-field theory study. *Phys. Rev. B*, 96:075134, 2017.

[181] P. Roushan, C. Neill, J. Tangpanitanon, V. M. Bastidas, A. Megrant, R. Barends, Y. Chen, Z. Chen, B. Chiaro, A. Dunsworth, A. Fowler, B. Foxen, M. Giustina, E. Jeffrey, J. Kelly, E. Lucero, J. Mutus, M. Neeley, C. Quintana, D. Sank, A. Vainsencher, J. Wenner, T. White, H. Neven, D. G. Angelakis, and J. Martinis. Spectroscopic signatures of localization with interacting photons in superconducting qubits. *Science*, 358:1175, 2017.

[182] D. Osadchy and J. E. Avron. Hofstadter butterfly as quantum phase diagram. *J. Math. Phys.*, 42:5665, 2001.

[183] L. Du, Q. Chen, A. D. Barr, A. R. Barr, and G. A. Fiete. Floquet Hofstadter butterfly on the Kagome and triangular lattices. *Phys. Rev. B*, 98:245145, 2018.

[184] P. Roushan, C. Neill, A. Megrant, Y. Chen, R. Babbush, R. Barends, B. Campbell, Z. Chen, B. Chiaro, A. Dunsworth, A. Fowler, E. Jeffrey, J. Kelly, E. Lucero, J. Mutus, P. J. J. O'Malley, M. Neeley, C. Quintana, D. Sank, A. Vainsencher, J. Wenner, T. White, E. Kapit, H. Neven, and J. Martinis. Chiral ground-state currents of interacting photons in a synthetic magnetic field. *Nat. Phys.*, 13:146, 2017.

[185] D. Jaksch and P. Zoller. Creation of effective magnetic fields in optical lattices: the Hofstadter butterfly for cold neutral atoms. *New J. Phys.*, 5:56, 2003.

[186] F. Gerbier and J. Dalibard. Gauge fields for ultracold atoms in optical superlattices. *New J. Phys.*, 12:033007, 2010.

[187] M. Aidelsburger. Artificial gauge fields and topology with ultracold atoms in optical lattices. *J. Phys. B*, 51:193001, 2018.

[188] M. Aidelsburger. *Artificial gauge fields with ultracold atoms in optical lattices*. PhD thesis, Ludwig-Maximilians-Universität München, 2015.

[189] N. Goldman, I. Satija, P. Nikolic, A. Bermudez, M. A. Martin-Delgado, M. Lewenstein, and I. B. Spielman. Realistic time-reversal invariant topological insulators with neutral atoms. *Phys. Rev. Lett.*, 105:255302, 2010.

[190] D. Cocks, P. P. Orth, S. Rachel, M. Buchhold, K. Le Hur, and W. Hofstetter. Time-reversal-invariant Hofstadter-Hubbard model with ultracold fermions. *Phys. Rev. Lett.*, 109:205303, 2012.

[191] M. S. Scheurer, S. Rachel, and P. P. Orth. Dimensional crossover and cold-atom realization of topological Mott insulators. *Sci. Rep.*, 5:8386, 2015.

[192] P. P. Orth, D. Cocks, S. Rachel, M. Buchhold, K. Le Hur, and W. Hofstetter. Correlated topological phases and exotic magnetism with ultracold fermions. *J. Phys. B*, 46:134004, 2013.

[193] P. Kumar, T. Mertz, and W. Hofstetter. Interaction-induced topological and magnetic phases in the Hofstadter-Hubbard model. *Phys. Rev. B*, 94:115161, 2016.

[194] Y. Hatsugai and M. Kohmoto. Energy spectrum and the quantum Hall effect on the square lattice with next-nearest-neighbor hopping. *Phys. Rev. B*, 42:8282, 1990.

[195] J.-H. Zheng, T. Qin, and W. Hofstetter. Interaction-enhanced integer quantum Hall effect in disordered systems. *Phys. Rev. B*, 99:125138, 2019.

[196] J.-H. Zheng, B. Irsigler, L. Jiang, C. Weitenberg, and W. Hofstetter. Measuring an interaction-induced topological phase transition via the single-particle density matrix. *Phys. Rev. A*, 101:013631, 2020.

[197] A. H. Castro Neto, F. Guinea, N. M. R. Peres, K. S. Novoselov, and A. K. Geim. The electronic properties of graphene. *Rev. Mod. Phys.*, 81:109, 2009.

[198] T. I. Vanhala, T. Siro, L. Liang, M. Troyer, A. Harju, and P. Törmä. Topological phase transitions in the repulsively interacting Haldane-Hubbard model. *Phys. Rev. Lett.*, 116:225305, 2016.

[199] W. Yao, A. H. MacDonald, and Q. Niu. Optical control of topological quantum transport in semiconductors. *Phys. Rev. Lett.*, 99:047401, 2007.

[200] T. Oka and H. Aoki. Photovoltaic Hall effect in graphene. *Phys. Rev. B*, 79:081406, 2009.

[201] T. Kitagawa, T. Oka, A. Brataas, L. Fu, and E. Demler. Transport properties of nonequilibrium systems under the application of light: Photoinduced quantum Hall insulators without Landau levels. *Phys. Rev. B*, 84:235108, 2011.

[202] N. H. Lindner, G. Refael, and V. Galitski. Floquet topological insulator in semiconductor quantum wells. *Nat. Phys.*, 7:490, 2011.

[203] H. Min, J. E. Hill, N. A. Sinitsyn, B. R. Sahu, L. Kleinman, and A. H. MacDonald. Intrinsic and rashba spin-orbit interactions in graphene sheets. *Phys. Rev. B*, 74:165310, 2006.

[204] Y. Yao, F. Ye, X.-L. Qi, S.-C. Zhang, and Z. Fang. Spin-orbit gap of graphene: First-principles calculations. *Phys. Rev. B*, 75:041401, 2007.

[205] I. Boustani. Systematic ab initio investigation of bare boron clusters: Determination of the geometry and electronic structures B_n ($n = 2 - 14$). *Phys. Rev. B*, 55:16426, 1997.

[206] A. J. Mannix, X.-F. Zhou, B. Kiraly, J. D. Wood, D. Alducin, B. D. Myers, X. Liu, B. L. Fisher, U. Santiago, J. R. Guest, M. J. Yacaman, A. Ponce, A. R. Oganov, M. C. Hersam, and N. P. Guisinger. Synthesis of borophenes: Anisotropic, two-dimensional boron polymorphs. *Science*, 350:1513, 2015.

[207] B. Feng, J. Zhang, Q. Zhong, W. Li, S. Li, H. Li, P. Cheng, S. Meng, L. Chen, and K. Wu. Experimental realization of two-dimensional boron sheets. *Nat. Chem.*, 8:563, 2016.

[208] W. Metzner and D. Vollhardt. Correlated lattice fermions in $d = \infty$ dimensions. *Phys. Rev. Lett.*, 62:324, 1989.

[209] E. Müller-Hartmann. Correlated fermions on a lattice in high dimensions. *E. Z. Physik B*, 74:507, 1989.

[210] G. Kotliar and D. Vollhardt. Strongly correlated materials: Insights from dynamical mean-field theory. *Phys. Today*, 57:53, 2004.

[211] A. Georges, G. Kotliar, W. Krauth, and M. J. Rozenberg. Dynamical mean-field theory of strongly correlated fermion systems and the limit of infinite dimensions. *Rev. Mod. Phys.*, 68:13, 1996.

[212] M. Potthoff and W. Nolting. Surface metal-insulator transition in the Hubbard model. *Phys. Rev. B*, 59:2549, 1999.

[213] S. Okamoto and A. J. Millis. Spatial inhomogeneity and strong correlation physics: A dynamical mean-field study of a model Mott-insulator–band-insulator heterostructure. *Phys. Rev. B*, 70:241104, 2004.

[214] R. W. Helmes, T. A. Costi, and A. Rosch. Mott transition of fermionic atoms in a three-dimensional optical trap. *Phys. Rev. Lett.*, 100:056403, 2008.

[215] M. Snoek, I. Titvinidze, C. Tőke, K. Byczuk, and W. Hofstetter. Antiferromagnetic order of strongly interacting fermions in a trap: real-space dynamical mean-field analysis. *New J. Phys.*, 10:093008, 2008.

[216] I. Titvinidze. *Dynamical Mean-Field Theory Approach for Ultracold Atomic Gases*. PhD thesis, Goethe-Universität in Frankfurt am Main, 2009.

[217] I. Titvinidze, A. Schwabe, N. Rother, and M. Potthoff. Dynamical mean-field theory of indirect magnetic exchange. *Phys. Rev. B*, 86:075141, 2012.

[218] I. Titvinidze, A. Dorda, W. von der Linden, and E. Arrigoni. Transport through a correlated interface: Auxiliary master equation approach. *Phys. Rev. B*, 92:245125, 2015.

[219] H. Jeschke. Dynamical mean-field theory. http://www.physics.okayama-u.ac.jp/jeschke_homepage/CMSST2016/chapter6.pdf, 2016.

[220] D. Vollhardt. Dynamical mean-field theory of electronic correlations in models and materials. *arXiv:1004.5069*, 2010.

[221] M. Kollar. Introduction to dynamical mean-field theory. In E. Pavarini, E. Koch, D. Vollhardt, and A. Lichtenstein, editors, *The LDA+DMFT approach to strongly correlated materials*. Forschungszentrum Jülich, 2011.

[222] P. W. Anderson. Localized magnetic states in metals. *Phys. Rev.*, 124:41, 1961.

[223] A. Georges and G. Kotliar. Hubbard model in infinite dimensions. *Phys. Rev. B*, 45:6479, 1992.

[224] K. G. Wilson. The renormalization group: Critical phenomena and the Kondo problem. *Rev. Mod. Phys.*, 47:773, 1975.

[225] W. Hofstetter. Generalized numerical renormalization group for dynamical quantities. *Phys. Rev. Lett.*, 85:1508, 2000.

[226] M. Caffarel and W. Krauth. Exact diagonalization approach to correlated fermions in infinite dimensions: Mott transition and superconductivity. *Phys. Rev. Lett.*, 72:1545, 1994.

[227] J. E. Hirsch and R. M. Fye. Monte Carlo method for magnetic impurities in metals. *Phys. Rev. Lett.*, 56:2521, 1986.

[228] E. Gull, A. J. Millis, A. I. Lichtenstein, A. N. Rubtsov, M. Troyer, and P. Werner. Continuous-time Monte Carlo methods for quantum impurity models. *Rev. Mod. Phys.*, 83:349, 2011.

[229] C. Lanczos. An iteration method for the solution of the eigenvalue problem of linear differential and integral operators. *J. Res. Natl. Bur. Stand.*, 45:255, 1950.

[230] N. Metropolis, A. W. Rosenbluth, M. N. Rosenbluth, A. H. Teller, and E. Teller. Equation of state calculations by fast computing machines. *J. Chem. Phys.*, 21:1087, 1953.

[231] J. E. Hirsch. Discrete Hubbard-Stratonovich transformation for fermion lattice models. *Phys. Rev. B*, 28:4059, 1983.

[232] A. N. Rubtsov, V. V. Savkin, and A. I. Lichtenstein. Continuous-time quantum Monte Carlo method for fermions. *Phys.l Rev. B*, 72:035122, 2005.

[233] P. Werner, A. Comanac, L. de' Medici, M. Troyer, and A. J. Millis. Continuous-time solver for quantum impurity models. *Phys. Rev. Lett.*, 97:076405, 2006.

[234] M. Buchhold. Topological phases of interacting fermions in optical lattices with artificial gauge fields. Master's thesis, Goethe-Universität Frankfurt, 2012.

[235] J. Panas. *Investigation of the Bose-Hubbard model using dynamical mean-field theory*. PhD thesis, University of Warsaw, 2017.

[236] S. M. A. Rombouts, K. Heyde, and N. Jachowicz. Quantum Monte Carlo method for fermions, free of discretization errors. *Phys. Rev. Lett.*, 82:4155, 1999.

[237] E. Gull, P. Werner, O. Parcollet, and M. Troyer. Continuous-time auxiliary-field Monte Carlo for quantum impurity models. *Europhys. Lett.*, 82:57003, 2008.

[238] N. V. Prokof'ev, B. V. Svistunov, and I. S. Tupitsyn. Exact quantum Monte Carlo process for the statistics of discrete systems. *JETP Lett.*, 64:911, 1996.

[239] E. Gull, P. Werner, A. Millis, and M. Troyer. Performance analysis of continuous-time solvers for quantum impurity models. *Phys. Rev. B*, 76:235123, 2007.

[240] M. Jarrell and J. E. Gubernatis. Bayesian inference and the analytic continuation of imaginary-time quantum Monte Carlo data. *Phys. Rep.*, 269:133, 1996.

[241] M. Kollar. The maximum entropy method:analytic continuation of QMC data. In E. Pavarini, E. Koch, F. Anders, and M. Jarrel, editors, *Correlated Electrons: From Models to Materials*. Forschungszentrum Jülich, 2012.

[242] Z. Wang and S.-C. Zhang. Simplified topological invariants for interacting insulators. *Phys. Rev. X*, 2:031008, 2012.

[243] Z. Wang, X.-L. Qi, and S.-C. Zhang. Topological invariants for interacting topological insulators with inversion symmetry. *Phys. Rev. B*, 85:165126, 2012.

[244] K. Ishikawa and T. Matsuyama. Magnetic field induced multi-component QED$_3$ and quantum Hall effect. *Z. Phys. C*, 33:41, 1986.

[245] O. Viyuela, A. Rivas, and M. A. Martin-Delgado. Symmetry-protected topological phases at finite temperature. *2D Mater.*, 2:034006, 2015.

[246] F. Grusdt. Topological order of mixed states in correlated quantum many-body systems. *Phys. Rev. B*, 95:075106, 2017.

[247] A. A. Markov, G. Rohringer, and A. N. Rubtsov. Robustness of the topological quantization of the Hall conductivity for correlated lattice electrons at finite temperatures. *Phys. Rev. B*, 100, 2019.

[248] R. Unanyan, M. Kiefer-Emmanouilidis, and M. Fleischhauer. Finite-temperature topological invariant for interacting systems. *Phys. Rev. Lett.*, 125:215701, 2020.

[249] V. Gurarie. Single-particle Green's functions and interacting topological insulators. *Phys. Rev. B*, 83:085426, 2011.

[250] Z. Wang and B. Yan. Topological hamiltonian as an exact tool for topological invariants. *J. Physics-Condens. Mat.*, 25:155601, 2013.

[251] R. Bianco and R. Resta. Mapping topological order in coordinate space. *Phys. Rev. B*, 84:241106, 2011.

[252] D.-T. Tran, A. Dauphin, N. Goldman, and P. Gaspard. Topological Hofstadter insulators in a two-dimensional quasicrystal. *Phys. Rev. B*, 91:085125, 2015.

[253] A. Amaricci, L. Privitera, F. Petocchi, M. Capone, G. Sangiovanni, and B. Trauzettel. Edge state reconstruction from strong correlations in quantum spin Hall insulators. *Phys. Rev. B*, 95:205120, 2017.

[254] M. D. Caio, G. Möller, N. R. Cooper, and M. J. Bhaseen. Topological marker currents in Chern insulators. *Nat. Phys.*, 15:257, 2019.

[255] B. Irsigler, J.-H. Zheng, and W. Hofstetter. Interacting Hofstadter interface. *Phys. Rev. Lett.*, 122:010406, 2019.

[256] B. Irsigler, J.-H. Zheng, and W. Hofstetter. Microscopic characteristics and tomography scheme of the local Chern marker. *Phys. Rev. A*, 100:023610, 2019.

[257] U. Gebert, B. Irsigler, and W. Hofstetter. Local Chern marker of smoothly confined Hofstadter fermions. *Phys. Rev. A*, 101:063606, 2020.

[258] R. Bianco. *Chern invariant and orbital magnetization as local quantities*. PhD thesis, Università degli studi di Trieste, 2011.

[259] U. Gebert. Local chern number for noninteracting fermions in the Harper-Hofstadter model. Master's thesis, Goethe University of Frankfurt, 2018.

[260] T. Fukui, Y. Hatsugai, and H. Suzuki. Chern numbers in discretized Brillouin zone: Efficient method of computing (spin) hall conductances. *J. Phys. Soc. Jpn.*, 74:1674, 2005.

[261] D. N. Sheng, L. Sheng, Z. Y. Weng, and F. D. M. Haldane. Spin Hall effect and spin transfer in a disordered Rashba model. *Phys. Rev. B*, 72:153307, 2005.

[262] D. N. Sheng, Z. Y. Weng, L. Sheng, and F. D. M. Haldane. Quantum spin-Hall effect and topologically invariant Chern numbers. *Phys. Rev. Lett.*, 97:036808, 2006.

[263] R. B. Laughlin. Quantized hall conductivity in two dimensions. *Phys. Rev. B*, **23**:5632, (1981).

[264] T. Fukui and Y. Hatsugai. Topological aspects of the quantum spin-Hall effect in graphene: Z_2 topological order and spin Chern number. *Phys. Rev. B*, 75:121403, 2007.

[265] L. Fu and C. L. Kane. Time reversal polarization and a z_2 adiabatic spin pump. *Phys. Rev. B*, 74:195312, 2006.

[266] K. G. Wilson. Confinement of quarks. *Phys. Rev. D*, 10:2445, 1974.

[267] J. Zak. Berry's phase for energy bands in solids. *Phys. Rev. Lett.*, 62:2747, 1989.

[268] R. Yu, X. L. Qi, A. Bernevig, Z. Fang, and X. Dai. Equivalent expression of Z_2 topological invariant for band insulators using the non-Abelian Berry connection. *Phys. Rev. B*, 84:075119, 2011.

[269] A. Alexandradinata, X. Dai, and B. A. Bernevig. Wilson-loop characterization of inversion-symmetric topological insulators. *Phys. Rev. B*, 89:155114, 2014.

[270] F. Grusdt, D. Abanin, and E. Demler. Measuring Z_2 topological invariants in optical lattices using interferometry. *Phys. Rev. A*, 89:043621, 2014.

[271] R. Wu, J.-Z. Ma, S.-M. Nie, L.-X. Zhao, X. Huang, J.-X. Yin, B.-B. Fu, P. Richard, G.-F. Chen, Z. Fang, X. Dai, H.-M. Weng, T. Qian, H. Ding, and S. H. Pan. Evidence for topological edge states in a large energy gap near the step edges on the surface of $ZrTe_5$. *Phys. Rev. X*, 6:021017, 2016.

[272] X.-B. Li, W.-K. Huang, Y.-Y. Lv, K.-W. Zhang, C.-L. Yang, B.-B. Zhang, Y. B. Chen, S.-H. Yao, J. Zhou, M.-H. Lu, L. Sheng, S.-C. Li, J.-F. Jia, Q.-K. Xue, Y.-F. Chen, and D.-Y. Xing. Experimental observation of topological edge states at the surface step edge of the topological insulator $ZrTe_5$. *Phys. Rev. Lett.*, 116:176803, 2016.

[273] M. C. Rechtsman, Y. Plotnik, J. M. Zeuner, D. Song, Z. Chen, A. Szameit, and M. Segev. Topological creation and destruction of edge states in photonic graphene. *Phys. Rev. Lett.*, 111:103901, 2013.

[274] R. Süsstrunk and S. D. Huber. Observation of phononic helical edge states in a mechanical topological insulator. *Science*, 349:47, 2015.

[275] T. D. Stanescu, V. Galitski, and S. Das Sarma. Topological states in two-dimensional optical lattices. *Phys. Rev. A*, 82:013608, 2010.

[276] B. Galilo, D. K. K. Lee, and R. Barnett. Topological edge-state manifestation of interacting 2d condensed boson-lattice systems in a harmonic trap. *Phys. Rev. Lett.*, 119:203204, 2017.

[277] N. Goldman, J. Dalibard, A. Dauphin, F. Gerbier, M. Lewenstein, P. Zoller, and I. B. Spielman. Direct imaging of topological edge states in cold-atom systems. *Proc. Natl. Acad. Sci. USA*, 110:6736, 2013.

[278] N. Goldman, J. Beugnon, and F. Gerbier. Detecting chiral edge states in the Hofstadter optical lattice. *Phys. Rev. Lett.*, 108:255303, 2012.

[279] M. D. Reichl and E. J. Mueller. Floquet edge states with ultracold atoms. *Phys. Rev. A*, 89:063628, 2014.

[280] N. Goldman, G. Jotzu, M. Messer, F. Görg, R. Desbuquois, and T. Esslinger. Creating topological interfaces and detecting chiral edge modes in a two-dimensional optical lattice. *Phys. Rev. A*, 94:043611, 2016.

[281] Z. Wang, X.-L. Qi, and S.-C. Zhang. Topological order parameters for interacting topological insulators. *Phys. Rev. Lett.*, 105:256803, 2010.

[282] X.-L. Qi, T. L. Hughes, and S.-C. Zhang. Topological field theory of time-reversal invariant insulators. *Phys. Rev. B*, 78:195424, 2008.

[283] E. Witten. Global aspects of current algebra. *Nucl. Phys. B*, 223:422, 1983.

[284] Q. Zhou and T.-L. Ho. Universal thermometry for quantum simulation. *Phys. Rev. Lett.*, 106:225301, 2011.

[285] J. H. Drewes, E. Cocchi, L. A. Miller, C. F. Chan, D. Pertot, F. Brennecke, and M. Köhl. Thermodynamics versus local density fluctuations in the metal-mott-insulator crossover. *Phys. Rev. Lett.*, 117:135301, 2016.

[286] D. Nozadze and N. Trivedi. Compressibility as a probe of quantum phase transitions in topological superconductors. *Phys. Rev. B*, 93:064512, 2016.

[287] L. Wang, A. A. Soluyanov, and M. Troyer. Proposal for direct measurement of topological invariants in optical lattices. *Phys. Rev. Lett.*, 110:166802, 2013.

[288] M. Lohse, C. Schweizer, O. Zilberberg, M. Aidelsburger, and I. Bloch. A Thouless quantum pump with ultracold bosonic atoms in an optical superlattice. *Nat. Phys.*, 12:350, 2015.

[289] S. Nakajima, T. Tomita, S. Taie, T. Ichinose, H. Ozawa, L. Wang, M. Troyer, and Y. Takahashi. Topological Thouless pumping of ultracold fermions. *Nat. Phys.*, 12:296, 2016.

[290] D. J. Thouless. Quantization of particle transport. *Phys. Rev. B*, 27:6083, 1983.

[291] M. J. Rice and E. J. Mele. Elementary excitations of a linearly conjugated diatomic polymer. *Phys. Rev. Lett.*, 49:1455, 1982.

[292] A. Hayward, C. Schweizer, M. Lohse, M. Aidelsburger, and F. Heidrich-Meisner. Topological charge pumping in the interacting bosonic Rice-Mele model. *Phys. Rev. B*, 98:245148, 2018.

[293] A. R. Kolovsky, F. Grusdt, and M. Fleischhauer. Quantum particle in a parabolic lattice in the presence of a gauge field. *Phys. Rev. A*, 89:033607, 2014.

[294] P. Nevado, S. Fernández-Lorenzo, and D. Porras. Topological edge states in periodically driven trapped-ion chains. *Phys. Rev. Lett.*, 119:210401, 2017.

[295] Z. Yan, B. Li, X. Yang, and S. Wan. A general time-periodic driving approach to realize topological phases in cold atomic systems. *Sci. Rep.*, 5:16197, 2015.

[296] E. Alba, X. Fernandez-Gonzalvo, J. Mur-Petit, J. K. Pachos, and J. J. Garcia-Ripoll. Seeing topological order in time-of-flight measurements. *Phys. Rev. Lett.*, 107:235301, 2011.

[297] P. Hauke, M. Lewenstein, and A. Eckardt. Tomography of band insulators from quench dynamics. *Phys. Rev. Lett.*, 113:045303, 2014.

[298] L. A. Peña Ardila, M. Heyl, and A. Eckardt. Measuring the single-particle density matrix for fermions and hard-core bosons in an optical lattice. *Phys. Rev. Lett.*, 121:260401, 2018.

[299] M. Atala, M. Aidelsburger, M. Lohse, J. T. Barreiro, B. Paredes, and I. Bloch. Observation of chiral currents with ultracold atoms in bosonic ladders. *Nat. Phys.*, 10:588, 2014.

[300] N. Schine, M. Chalupnik, T. Can, A. Gromov, and J. Simon. Electromagnetic and gravitational responses of photonic landau levels. *Nature*, 565:173, 2019.

[301] M. Tarnowski, M. Nuske, N. Fläschner, B. Rem, D. Vogel, L. Freystatzky, K. Sengstock, L. Mathey, and C. Weitenberg. Observation of topological Bloch-state defects and their merging transition. *Phys. Rev. Lett.*, 118:240403, 2017.

[302] P. Hauke, O. Tieleman, A. Celi, C. Ölschläger, J. Simonet, J. Struck, M. Weinberg, P. Windpassinger, K. Sengstock, M. Lewenstein, and A. Eckardt. Non-Abelian gauge fields and topological insulators in shaken optical lattices. *Phys. Rev. Lett.*, 109:145301, 2012.

[303] J. Struck, C. Ölschläger, M. Weinberg, P. Hauke, J. Simonet, A. Eckardt, M. Lewenstein, K. Sengstock, and P. Windpassinger. Tunable gauge potential for neutral and spinless particles in driven optical lattices. *Phys. Rev. Lett.*, 108:225304, 2012.

[304] M. H. Yau and C. A. R. Sá de Melo. Chern-number spectrum of ultracold fermions in optical lattices tuned independently via artificial magnetic, Zeeman, and spin-orbit fields. *Phys. Rev. A*, 99:043625, 2019.

[305] M. Iskin. Attractive Hofstadter-Hubbard model with imbalanced chemical and vector potentials. *Phys. Rev. A*, 91:053606, 2015.

[306] B. Irsigler, J.-H. Zheng, M. Hafez-Torbati, and W. Hofstetter. Spin-imbalance-induced transverse magnetization in the Hofstadter-Hubbard model. *Phys. Rev. A*, 99:043628, 2019.

[307] P. T. Brown, D. Mitra, E. Guardado-Sanchez, P. Schauß, S. S. Kondov, E. Khatami, T. Paiva, N. Trivedi, D. A. Huse, and W. S. Bakr. Spin-imbalance in a 2d fermi-hubbard system. *Science*, 357:1385, 2017.

[308] L. D'Alessio and M. Rigol. Long-time behavior of isolated periodically driven interacting lattice systems. *Phys. Rev. X*, 4:041048, 2014.

[309] M. Bukov, S. Gopalakrishnan, M. Knap, and E. Demler. Prethermal Floquet steady states and instabilities in the periodically driven, weakly interacting Bose-Hubbard model. *Phys. Rev. Lett.*, 115:205301, 2015.

[310] I. Dzyaloshinsky. A thermodynamic theory of 'weak' ferromagnetism of antiferromagnetics. *J. Phys. Chem. Solids*, 4:241, 1958.

[311] T. Moriya. Anisotropic superexchange interaction and weak ferromagnetism. *Phys. Rev.*, 120:91, 1960.

[312] P. Asselin, R. F. L. Evans, J. Barker, R. W. Chantrell, R. Yanes, O. Chubykalo-Fesenko, D. Hinzke, and U. Nowak. Constrained Monte Carlo method and calculation of the temperature dependence of magnetic anisotropy. *Phys. Rev. B*, 82:054415, 2010.

[313] J. Villain. Spin glass with non-random interactions. *J. Phys. C*, 10:1717, 1977.

[314] M. Yosefin and E. Domany. Phase transitions in fully frustrated spin systems. *Phys. Rev. B*, 32:1778, 1985.

[315] S. Teitel and C. Jayaprakash. Phase transtions in frustrated two-dimensional *XY* models. *Phys. Rev. B*, 27:598, 1983.

[316] P. Olsson. Two phase transitions in the fully frustrated *XY* model. *Phys. Rev. Lett.*, 75:2758, 1995.

[317] N. Wurz, C. F. Chan, M. Gall, J. H. Drewes, E. Cocchi, L. A. Miller, D. Pertot, F. Brennecke, and M. Köhl. Coherent manipulation of spin correlations in the Hubbard model. *Phys. Rev. A*, 97:051602, 2018.

[318] M. Boll, T. A. Hilker, G. Salomon, A. Omran, J. Nespolo, L. Pollet, I. Bloch, and C. Gross. Spin- and density-resolved microscopy of antiferromagnetic correlations in Fermi-Hubbard chains. *Science*, 353:1257, 2016.

[319] L. W. Cheuk, M. A. Nichols, K. R. Lawrence, M. Okan, H. Zhang, E. Khatami, N. Trivedi, T. Paiva, M. Rigol, and M. W. Zwierlein. Observation of spatial charge and spin correlations in the 2D Fermi-Hubbard model. *Science*, 353:1260, 2016.

[320] A. Eckardt, P. Hauke, P. Soltan-Panahi, C. Becker, K. Sengstock, and M. Lewenstein. Frustrated quantum antiferromagnetism with ultracold bosons in a triangular lattice. *Europhys. Lett.*, 89:10010, 2010.

[321] J. Struck, M. Weinberg, C. Ölschläger, P. Windpassinger, J. Simonet, K. Sengstock, R. Höppner, P. Hauke, A. Eckardt, M. Lewenstein, and L. Mathey. Engineering ising-XY spin-models in a triangular lattice using tunable artificial gauge fields. *Nat. Phys.*, 9:738, 2013.

[322] B. I. Halperin. Possible states for a three-dimensional electron gas in a strong magnetic field. *Jpn. J. Appl. Phys.*, 26:1913, 1987.

[323] T. Kimura. Hofstadter problem in higher dimensions. *Prog. Theor. Exp. Phys.*, 2014:103B05, 2014.

[324] D.-W. Zhang, R.-B. Liu, and S.-L. Zhu. Generalized Hofstadter model on a cubic optical lattice: From nodal bands to the three-dimensional quantum Hall effect. *Phys. Rev. A*, 95:043619, 2017.

[325] Y. Li. Time-reversal invariant $\mathrm{SU}(2)$ Hofstadter problem in three-dimensional lattices. *Phys. Rev. B*, 91:195133, 2015.

[326] B. Irsigler, J.-H. Zheng, F. Grusdt, and W. Hofstetter. Z_2 characterization for three-dimensional multiband Hubbard models. *Phys. Rev. Res.*, 2:013299, 2020.

[327] S. Murakami and S.-i. Kuga. Universal phase diagrams for the quantum spin Hall systems. *Phys. Rev. B*, 78:165313, 2008.

[328] T. H. Hsieh, H. Ishizuka, L. Balents, and T. L. Hughes. Bulk topological proximity effect. *Phys. Rev. Lett.*, 116:086802, 2016.

[329] R. Holm and W. Meissner. Messungen mit hilfe von flüssigem helium. XIII. *Z. Phys.*, 74:715, 1932.

[330] H. Meissner. Superconductivity of contacts with interposed barriers. *Phys. Rev.*, 117:672, 1960.

[331] T. Shoman, A. Takayama, T. Sato, S. Souma, T. Takahashi, T. Oguchi, K. Segawa, and Y. Ando. Topological proximity effect in a topological insulator hybrid. *Nat. Commun.*, 6:6547, 2015.

[332] J.-H. Zheng and W. Hofstetter. Topological invariant for two-dimensional open systems. *Phys. Rev. B*, 97:195434, 2018.

[333] P. Cheng, P. W. Klein, K. Plekhanov, K. Sengstock, M. Aidelsburger, C. Weitenberg, and K. Le Hur. Topological proximity effects in a Haldane graphene bilayer system. *Phys. Rev. B*, 100:081107, 2019.

[334] J. Panas, B. Irsigler, J.-H. Zheng, and W. Hofstetter. Bulk topological proximity effect in multilayer systems. *Phys. Rev. B*, 102:075403, 2020.

[335] J.-H. Z. and W. Hofstetter. Topological invariant for 2d open systems. *Phys. Rev. B*, 97:195434, 2018.

[336] A. Griessner, A. J. Daley, S. R. Clark, D. Jaksch, and P. Zoller. Dark-state cooling of atoms by superfluid immersion. *Phys. Rev. Lett.*, 97:220403, 2006.

[337] B. Kraus, H. P. Büchler, S. Diehl, A. Kantian, A. Micheli, and P. Zoller. Preparation of entangled states by quantum Markov processes. *Phys. Rev. A*, 78:042307, 2008.

[338] M. Lacki, J. Zakrzewski, and N. Goldman. A dark state of Chern bands: Designing flat bands with higher Chern number. *arXiv:2002.05089*, 2020.

[339] S. M. Young and C. L. Kane. Dirac semimetals in two dimensions. *Phys. Rev. Lett.*, 115:126803, 2015.

[340] S. Murakami, M. Hirayama, R. Okugawa, and T. Miyake. Emergence of topological semimetals in gap closing in semiconductors without inversion symmetry. *Sci. Adv.*, 3:e1602680, 2017.

[341] D. Pesin and L. Balents. Mott physics and band topology in materials with strong spin-orbit interaction. *Nat. Phys.*, 6:376, 2010.

[342] P. W. Anderson. The resonating valence bond state in La2CuO4 and superconductivity. *Science*, 235:1196, 1987.

[343] G. Kotliar, S. Y. Savrasov, G. Pálsson, and G. Biroli. Cellular dynamical mean field approach to strongly correlated systems. *Phys. Rev. Lett.*, 87:186401, 2001.

[344] T. Zhu, C. A. Jiménez-Hoyos, J. McClain, T. C. Berkelbach, and G. K.-L. Chan. Coupled-cluster impurity solvers for dynamical mean-field theory. *Phys. Rev. B*, 100:115154, 2019.

[345] B. Bauer, D. Wecker, A. J. Millis, M. B. Hastings, and M. Troyer. Hybrid quantum-classical approach to correlated materials. *Phys. Rev. X*, 6:031045, 2016.

[346] J. M. Kreula, S. R. Clark, and D. Jaksch. Non-linear quantum-classical scheme to simulate non-equilibrium strongly correlated fermionic many-body dynamics. *Sci. Rep.*, 6:32940, 2016.

[347] T. Keen, T. Maier, S. Johnston, and P. Lougovski. Quantum-classical simulation of two-site dynamical mean-field theory on noisy quantum hardware. *Quantum Sci. Technol.*, 5:035001, 2020.

[348] Y. Cao, V. Fatemi, A. Demir, S. Fang, S. L. Tomarken, J. Y. Luo, J. D. Sanchez-Yamagishi, K. Watanabe, T. Taniguchi, E. Kaxiras, R. C. Ashoori, and P. Jarillo-Herrero. Correlated insulator behaviour at half-filling in magic-angle graphene superlattices. *Nature*, 556:80, 2018.

[349] G. Tarnopolsky, A. J. Kruchkov, and A. Vishwanath. Origin of magic angles in twisted bilayer graphene. *Phys. Rev. Lett.*, 122:106405, 2019.

[350] M. Xie and A. H. MacDonald. Nature of the correlated insulator states in twisted bilayer graphene. *Phys. Rev. Lett.*, 124:097601, 2020.

[351] S. Liu, E. Khalaf, J. Y. Lee, and A. Vishwanath. Nematic topological semimetal and insulator in magic angle bilayer graphene at charge neutrality. *arXiv:1905.07409*, 2019.

[352] A. González-Tudela and J. I. Cirac. Cold atoms in twisted-bilayer optical potentials. *Phys. Rev. A*, 100:053604, 2019.

[353] E. Dagotto and A. Moreo. Phase diagram of the frustrated spin-1/2 Heisenberg antiferromagnet in 2 dimensions. *Phys. Rev. Lett.*, 63:2148, 1989.

[354] L. Duca, T. Li, M. Reitter, I. Bloch, M. Schleier-Smith, and U. Schneider. An aharonov-bohm interferometer for determining bloch band topology. *Science*, 347(6219):288, 2014.

[355] L. Asteria, D. T. Tran, T. Ozawa, M. Tarnowski, B. S. Rem, N. Fläschner, K. Sengstock, N. Goldman, and C. Weitenberg. Measuring quantized circular dichroism in ultracold topological matter. *Nat. Phys.*, 15:449, 2019.

[356] Y. Shin, C. H. Schunck, A. Schirotzek, and W. Ketterle. Tomographic rf spectroscopy of a trapped Fermi gas at unitarity. *Phys. Rev. Lett.*, 99:090403, 2007.

[357] J. Liu and L. Balents. Correlation effects and quantum oscillations in topological nodal-loop semimetals. *Phys. Rev. B*, 95:075426, 2017.

[358] W. Chen and J. L. Lado. Interaction-driven surface Chern insulator in nodal line semimetals. *Phys. Rev. Lett.*, 122:016803, 2019.

[359] T. H. Hsieh, Y.-M. Lu, and A. W. W. Ludwig. Topological bootstrap: Fractionalization from Kondo coupling. *Sci. Adv.*, 3:e1700729, 2017.

[360] S. Sorn. Bilayer Haldane model: From trivial band insulator to fractionalized quantum anomalous Hall insulator. *Phys. Rev. B*, 98:125145, 2018.

[361] A. Mishra and S. B. Lee. Stacking sensitive topological phases in a bilayer Kane-Mele-Hubbard model at quarter filling. *Phys. Rev. B*, 100:045146, 2019.

Bernhard Julius Irsigler

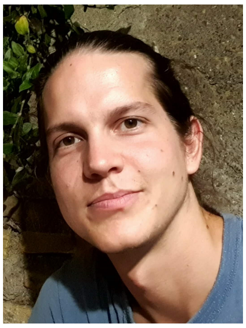

geboren am 29.01.1991 in Berlin

Marbachweg 341
60320 Frankfurt am Main

Ausbildung

2010	Abitur, Schadow-Gymnasium, Berlin
2010 - 2013	Bachelor-Studium der Physik, Freie Universität Berlin
2013 - 2014	Master-Studium der Physik, Università di Bologna
2014 - 2016	Master-Studium der Physik, Freie Universität Berlin
seit 2017	Doktorand an der Johann Wolfgang Goethe-Universität

Abschlussarbeiten

2013	*Effective interaction between ion-adsorbing plates: Poisson-Boltzmann theory*, Bachelor-Arbeit bei Prof. Dr. Roland Netz
2016	*Dimensional phase transition in ultracold Bose gases*, Master-Arbeit bei Priv.-Doz. Dr. Axel Pelster

Konferenzen und Schulen

2015	*Arctic science* Kiruna (Schweden), *Introductory course to ultracold quantum gases* Innsbruck, *Photonica* Belgrad, Serbien
2016	*DPG Frühjahrstagung* Hannover, *Thermal, quantum, and topological phase transitions* Bayern, *Ultracold quantum gases - current trends and future perspectives* Bad Honnef
2017	*Kickoff meeting DFG FOR 2414* München, *DPG Frühjahrstagung* Mainz, *From static to dynamical gauge fields with ultracold atoms* Florenz, *Cold atoms and quantum transport* Les Houches (Frankreich), *Annual meeting DFG FOR 2414* Hamburg
2018	*Topological matter in artificial gauge fields* Dresden, *DPG Frühjahrstagung* Erlangen, *Annual meeting DFG FOR 2414* Frankfurt, *Task force meeting DFG FOR 2414* Göttingen, *Research frontiers in ultracold quantum gases* Bad Honnef
2019	*Solvay workshop* Brüssel, *Task force meeting DFG FOR 2414* München, *DPG Frühjahrstagung* Rostock, *Task Force Meeting DFG FOR 2414* Paris, *Task Force Meeting DFG FOR 2414* Göttingen